University of Ioannina
School of Sciences
Department of Physics

Mechanisms of electron capture and ionization in fast ion-atom collisions

Ph.D. Dissertation

Stefanos Nanos

Ioannina, 2023

Πανεπιστημιο Ιωαννινων

Σχολη Θετικων Επιστημων

Τμημα Φυσικης

Μηχανισμοί ηλεκτρονικής σύλληψης και ιονισμού σε ταχείες κρούσεις ιόντων-ατόμων

Διδακτορικη Διατριβη

Στεφανος Νανος

Ιωάννινα, 2023

Ph.D. Committee

Three-member Ph.D. advisory committee

- E.P. Benis (Supervisor), Associate Professor, University of Ioannina
- S. Cohen, Professor, University of Ioannina
- A. Dubois, Professor, Sorbonne Université

Seven-member Ph.D. examination committee

- E.P. Benis (Supervisor), Associate Professor, University of Ioannina
- S. Cohen, Professor, University of Ioannina
- A. Dubois, Professor, Sorbonne Université
- K. Kosmidis, Professor, University of Ioannina
- J.M. Monti, Professor, Instituto de Física Rosario
- S. Kaziannis, Assistant Professor, University of Ioannina
- D. Sofikitis, Assistant Professor, University of Ioannina

Χόρεψε πάνω στο φτερό του καρχαρία...
Dance atop the shark's fin...
By N. Kavvadias

To those who have encouraged and supported me throughout my journey, allowing me to soar to new heights and dance fearlessly atop the shark's fin.
This work is dedicated to you, with deep gratitude for your belief in me.

Acknowledgments

It is with great pleasure that I express my sincere gratitude to all those who have supported me throughout my doctoral journey. Reflecting on the last years and the many challenges I faced along this journey, I am deeply thankful for the support of so many individuals who have helped me reach my goals. Without their guidance, patience, and encouragement, I would not have been able to accomplish all that I have.

First and foremost, I would like to express my heartfelt gratitude to my supervisor, Associate Professor E.P. Benis, whose unwavering support and guidance has been invaluable throughout my academic journey. Professor Benis has been instrumental in shaping my scientific career, generously sharing his extensive knowledge and expertise with me, and constantly challenging me to reach my full potential. He has provided me with numerous opportunities to participate in international collaborations, allowing me to expand my horizons and gain invaluable experience. Without his guidance and encouragement, I would not have been able to achieve what I have today, and for that, I will always be grateful.

My gratitude is extended to the members of my Advisory Committee, Professors S. Cohen and A.L. Dubois, for their invaluable contributions and insights throughout my work. Their immense expertise and invaluable knowledge have played a pivotal role in shaping and guiding my research journey.

My deepest appreciation goes to the seven-member examination committee for proofreading my thesis and providing constructive feedback that improved the quality of my work. Their valuable input and suggestions helped me to refine my ideas and present them effectively.

I cannot express enough gratitude to Professors T.J.M. Zouros, S. Hagmann, R.D. Rivarola, and Associate Professor J.M. Monti for their support, immense passion for my research, and invaluable knowledge. I have been incredibly fortunate to have had the opportunity to work with such inspiring individuals, and their contributions have been invaluable to my success.

My sincere appreciation goes to my colleagues, Dr. I. Madesis and A. Laoutaris, for their support during my work in the Tandem Accelerator Laboratory. They helped me to learn the experimental setup and how to properly conduct experiments while providing me with valuable scientific input. Along with A. Biniskos, they were my closest experimental mates, spending many hours of exhausting experiments and nightshifts. Their support and friendship have been invaluable to me, and I am grateful for the laughter and good times we shared.

I feel obliged to mention my sincere gratitude to the Tandem personnel. Specifically, I would like to acknowledge Dr. S. Harissopulos for his support during my Ph.D. studies, Dr. M. Axiotis for his invaluable knowledge and insightful discussions, and technicians B. Andreopoulos and M. Tsopanakis for their technical insights and

assistance throughout these years. I cannot forget to mention M. Andriannis, the tandem accelerator operator, who not only helped me gain knowledge and experience in operating the machine, which is difficult for a Ph.D. student to attain but also made me feel at home during my first days in the Tandem Laboratory. His warm welcome and friendly demeanor created a positive and inclusive environment that made me feel comfortable and at ease. Finally, I would like to thank Dr. A. Lagoyannis, who was not only a key player in my involvement with valuable scientific and technical input but also for being a great support during the difficult times of my Ph.D.

My heartfelt appreciation goes to Dr. N. Petridis and Dr. P.-M. Hillenbrand for their exceptional scientific input and assistance. N. Petridis's training in vacuum technology and gas targets has been invaluable, while P.-M. Hillenbrand's knowledge and expertise in Atomic Physics have been a constant source of inspiration. Also, I would like to mention their efforts to create a beautiful environment during my stays in Germany, which have left a memorable mark on me.

I would also like to express my gratitude to S. Nikolaou, N.J. Esponda, Dr. S. Passalidis and Dr. M.A. Quinto for their invaluable feedback and discussion on many theoretical aspects of my research. Their insights and perspectives have been significant for my work and have greatly enriched my understanding of the subject matter. Their contributions have been immeasurable, and I am fortunate to have had the opportunity to work with such a dedicated and talented group of scholars.

I cannot thank enough Eleni Mitsi, Stefanos Papagiannis, Kalliopi Tsampa, Evaggelia Taimpiri, Anastasia Ziagova, Christos Andrikopoulos and Anastasia Kotsovolou, the students working in the Tandem Laboratory. They have all created a beautiful environment, shared a lot of nice moments, and made all these years working with them an unexpected journey, fun, and enriching.

I firmly believe that friendship is one of life's greatest gifts, and I am fortunate to have had the support of some truly amazing friends during my Ph.D. journey. For that, I would like to express my graditude to Sofoklis Nikolaou, Lampros Trifyllis, Anastasios Koukos, Dimitris Katrisiotis, Eleni Trevlopoulou and Georgios Rattas who have supported me through all the highs and lows of this journey. Their friendship and presence in my life are treasures that I will always cherish.

My deepest gratitude is extended to my girlfriend, Sofia Konstantopoulou, for her support and encouragement. Her belief in my abilities, her understanding, and her constant motivation have been invaluable to my success. Her presence in my life has been a source of inspiration and strength, pushing me to overcome obstacles and pursue my academic goals with determination.

Finally, I want to express my heartfelt gratitude to my family, namely my brothers Stergios and Panagiotis, my parents Dimitris and Dimitria, my grandparents Stergios and Sofia and my aunt Stefania. Their constant love, support, and encouragement have been the foundation of my success. I could not have done this without them, and I am forever grateful for their unwavering belief in me.

Financial Support

I acknowledge support by the project "Cluster of Accelerator Laboratories for Ion-Beam Research and Applications - CALIBRA" (MIS 5002799), which is implemented under the Action "Reinforcement of the Research and Innovation Infrastructure", funded by the Operational Programme “Competitiveness, Entrepreneurship and Innovation" (NSRF 2014-2020) and co-financed by Greece and the European Union (European Regional Development Fund).

I acknowledge support by the program "Strengthening and supporting the operation of developmental, research and educational activities of the University of Ioannina".

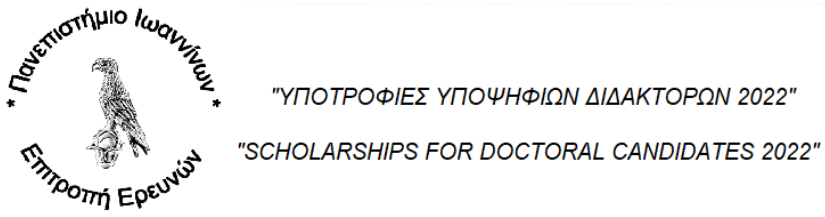

I acknowledge support by the project "IKYDA2020" of the IKY-DAAD Greek-German collaboration.

Contents

List of Figures

List of Tables

Preface

This dissertation concerns research related to the intricate atomic mechanisms of electron capture and ionization in fast ion-atom collisions. Particularly, focus was given to the unique opportunities presented by multi-electron open-shell ions, i.e., He-like, $1s2s\ ^3S$, and Be-like, $1s2s^22p\ ^3P$, ions. These pre-excited ion beams, having initially a K-shell vacancy, offer the opportunity of studying dynamic collision processes in ionic environments that depart from the usual ground state. Experiments on collision systems with pre-excited ions serve as an excellent laboratory for studying atomic physics phenomena, including electron capture/loss to the continuum of the projectile and single electron capture. This thesis investigates these processes in detail, offering a platform to test advanced collision theories and uncover the fundamental physics involved.

Our cusp electron studies involved collision systems with both bare and dressed projectiles of various ion species. Our investigations were focused on understanding the role of multielectronic target subshells, as well as the role of open-shell projectiles in the production of cusp electrons. The measurements were accompanied by state-of-the-art distorted wave theories. These studies unveiled intriguing physical phenomena related to the processes of electron capture and loss to the continuum of the projectile, exposing the role of the target $2p$ electron in collisions of bare projectiles with multielectronic Ne and Ar targets. In addition, our studies captured, both experimentally and theoretically, for the first time, the cusp electron peak originating solely from collisions of pre-excited ions with He targets, on the double differential cross section level. A key highlight of our work was the identification of a small peak on the low-energy wing of the cusp peak, with an energy smaller than the cusp maximum by the ionization potential of the target. This novel phenomenon suggests an effectively new electron loss to the continuum process with simultaneous target ionization through a correlated electron-electron interaction.

Furthermore, our research is also focused on studies related to the single electron capture process in collisions of fast (few MeV/u) He-like mixed-state ($1s^2\ ^1S,\ 1s2s\ ^3S$) projectiles with He. This study builds upon a recent work carried out by our team involving He-like carbon projectiles. In continuation of this, we undertook an isoelectronic investigation employing He-like oxygen and boron projectiles. Our results exposed the presence of strong electron correlations, further supporting the findings of previous studies performed with He-like projectiles. Moreover, the single differential cross sections of $1s2s2p\ ^4P,\ ^2P_{\pm}$ states from both the ground, $1s^2$, and metastable, $1s2s\ ^3S$, configurations of the incident beam were determined for a wide range of collision energies. These findings offer invaluable insights, serving as an important benchmark for the refinement and validation of advanced three-active electron theories, such as the 3eAOCC, which is critically compared to our results.

Finally, we introduced an alternative method for determining the energy width of

ion beams in tandem Van de Graaff accelerators, an important parameter as it affects the experimental resolution in general. In our approach, we employed measurements of KLL Auger spectra along with corresponding Monte Carlo simulations performed within the SIMION ion optics package. This new approach allows for an in-situ determination of the ion beam energy width directly from the KLL Auger spectra under study, thus eliminating the need for additional measurements.

Περίληψη - Preface in Greek

Η παρούσα διατριβή μελετά τους πολύπλοκους ατομικούς μηχανισμούς της σύλληψης και ιονισμού ηλεκτρονίου σε ταχείες κρούσεις ιόντων-ατόμων. Ειδικότερα, επικεντρωθήκαμε σε σχετικές μελέτες αξιοποιώντας προ-διεγερμένες ιοντικές δέσμες, όπως ηλιοειδείς, $1s2s\ ^3S$, και βηρυλλιοειδείς $1s2s^22p\ ^3P$ δέσμες ιόντων. Αυτές οι προ-διεγερμένες ιοντικές δέσμες, που έχουν αρχικά μια κενή θέση στη K-στιβάδα, προσφέρουν τη δυνατότητα να μελετήσουμε δυναμικές ατομικές διεργασίες σε ιοντικά περιβάλλοντα που απέχουν από τη βασική κατάσταση. Πειράματα σε συστήματα κρούσεων με προδιεγερμένα ιόντα αποτελούν εξαιρετικό εργαλείο για τη μελέτη ατομικών φαινομένων, συμπεριλαμβανομένης της σύλληψης/απώλειας ηλεκτρονίων στο συνεχές της δέσμης ιόντων και της απλής σύλληψης ηλεκτρονίου. Αυτή η διατριβή μελετά τους συγκεκριμένους μηχανισμούς λεπτομερώς, προσφέροντας σημαντικές πληροφορίες για τον έλεγχο προηγμένων θεωριών και την κατανόηση της θεμελιώδους φυσικής που εμπλέκεται.

Για τις μελέτες μας στα cusp ηλεκτρόνια αξιοποιήθηκαν συστήματα κρούσεων με πλήρως και μερικώς απουγυμνωμένες δέσμες ιόντων. Οι έρευνές μας επικεντρώθηκαν στην κατανόηση του ρόλου των τροχιακών πολυ-ηλεκτρονικών στόχων, καθώς και του ρόλου της δομής προ-διεγερμένων ιοντικών δεσμών στην παραγωγή cusp ηλεκτρονίων. Οι πειραματικές μετρήσεις συνοδεύονται από θεωρίες γνωστές ως distorted wave θεωρίες. Αυτές οι μελέτες έδειξαν ενδιαφέροντα φυσικά φαινόμενα που σχετίζονται με τις διαδικασίες της σύλληψης και απώλειας ηλεκτρονίων στο συνεχές των ιόντων δέσμης, αποκαλύπτοντας τον ρόλο του $2p$ ηλεκτρονίου του στόχου σε κρούσεις πλήρως απογυμνωμένων ιόντων δέσμης με πολυ-ηλεκτρονιακούς στόχους νέου και αργού. Επιπλέον, οι μελέτες μας κατέγραψαν, τόσο πειραματικά όσο και θεωρητικά, για πρώτη φορά, την cusp κορυφή προερχόμενη αποκλειστικά από κρούσεις προ-διεγερμένων ιόντων με στόχους ηλίου, σε επίπεδο διπλά διαφορικής ενεργού διατομής (DDCS). Ένα σημαντικό στοιχείο των μελετών μας ήταν η εντοπισμός μιας μικρής κορυφής στο αριστερό φτερό της cusp κορυφής, με ενέργεια μικρότερη από το μέγιστο της cusp κορυφής ίση με το δυναμικό ιονισμού του στόχου. Αυτό το νέο φαινόμενο σηματοδοτεί μία πιθανώς νέα διαδικασία απώλειας ηλεκτρονίων στο συνεχές μέσω υψηλά συσχετιζόμενης αλληλεπίδρασης ηλεκτρονίων (correlated electron-electron interaction).

Επιπλέον, η έρευνά μας επικεντρώθηκε σε μελέτες που σχετίζονται με τη διαδικασία σύλληψης ενός ηλεκτρονίου σε κρούσεις ταχέων (λίγων MeV/u) ηλιοειδών ιόντων δέσμης ($1s^2\ ^1S$, $1s2s\ ^3S$) με στόχους ηλίου. Αυτή η μελέτη έρχεται ως φυσικό επακόλουθο σε μία πρόσφατη εργασία που πραγματοποιήθηκε από την ομάδα μας με ηλιοειδής δέσμες ιόντων άνθρακα. Οι μελέτες που παρουσιάζονται στην εν λόγω διατριβή αφορούν μία ισο-ηλεκτρονική έρευνα αξιοποιώντας ηλιοειδής δέσμες ιόντων οξυγόνου και βορίου. Τα αποτελέσματά μας αποκάλυψαν την παρουσία ισχυρών ηλεκτρονικών συσχετισμών, υποστηρίζοντας περαιτέρω τα ευρήματα των προηγούμενων μελετών. Επιπλέον, ήταν εφικτός ο προσδιορισμός των απλά διαφορικών ενεργών διατομών (SDCS) των καταστάσεων $1s2s2p\ ^4P$, $^2P_\pm$ για κρούσεις ιόντων οξυγόνου, με

ηλεκτρονική δομή $O^{6+}(1s^2)$ και $O^{6+}(1s2s\ ^3S)$, με στόχους ηλίου, για ένα μεγάλο εύρος ενεργειών. Αυτά τα ευρήματα προσφέρουν σημαντική γνώση, καθώς αποτελούν σημείο αναφοράς για τη βελτίωση προηγμένων θεωριών τριών ενεργών ηλεκτρονίων, όπως η θεωρία 3eAOCC, που συγκρίνεται με τα πειραματικά αποτελέσματά μας.

Τέλος, εισαγάγαμε μια εναλλακτική μέθοδο για τον προσδιορισμό του εύρους ενέργειας των δεσμών ιόντων που παράγονται σε επιταχυντές τύπου tandem Van de Graaff. Το εύρος ενέργειας της δέσμης αποτελεί μία σημαντική παράμετρο καθώς επηρεάζει την πειραματική ανάλυση γενικότερα. Στην προσέγγισή μας, χρησιμοποιήσαμε μετρήσεις KLL Auger ηλεκτρονίων μαζί με αντίστοιχες προσομοιώσεις τύπου Monte Carlo που πραγματοποιήθηκαν στο πακέτο προσομοίωσης SIMION. Αυτή η νέα προσέγγιση επιτρέπει τον προσδιορισμό του εύρους ενέργειας της δέσμης ιόντων απευθείας από τα φάσματα KLL Auger ηλεκτρονίων, εξαλείφοντας έτσι την ανάγκη για επιπρόσθετες μετρήσεις.

Prologue

"Life is what happens when you're busy making other plans". These timeless words, immortalized by the legendary John Lennon, hold a profound truth that resonates with the unpredictable nature of our existence. It's a symphony of random events, chance encounters, and unforeseen twists that shape the course of our lives in ways we could never anticipate. These seemingly inconsequential moments, like seeds scattered by a gust of wind, take root and flourish into beautiful, unexpected journeys that define us. In this spirit, I would like to share a story that began with a spontaneous childish statement, meandered through the corridors of academia, and led me down a path of passion, perseverance, and discovery. A journey that has brought me to this pivotal moment, where the culmination of years of dedication and the unyielding support of loved ones are reflected in the pages of this Ph.D. dissertation.

When I was just six years old, before the world of formal education had fully embraced me, I embarked on a memorable journey with my parents to city of Ioannina. My father's work had brought us there for the summer, and little did I know that this trip would plant the seeds of a profound aspiration in my young heart.

In the waning days of August, with the impending start of schools, my mother and I visited a local school to inquire about the opening dates. As we conversed with the kind teacher, fate presented an unexpected question: "Why not enroll the young one in our school"? Then, my mother, explained the situation, and we continued on our way. Yet, a curious thought had taken root within me. As we strolled away from the school, I turned to my mother, my eyes full of wonder, and asked, "Does Ioannina have Universities"? To my delight, she replied with a smile, "Yes, it does, my dear". In that very moment, I made a bold declaration: "Then I will go to study in Ioannina"! My mother laughed, charmed by the innocence of my proclamation. Little did she know, and perhaps neither did I at that tender age, that this dream of studying in a distant city would eventually blossom into a steadfast passion for knowledge and a relentless pursuit of understanding the world around me.

As fate would have it, the dream of my six-year-old self found a way to intertwine with the path of my adulthood. When the time came to take exams to enter the university, there was no doubt in my heart about what I wanted to study. Physics had already claimed my curiosity and fascination. Almost accidentally, I found myself stepping through the doors of the University of Ioannina, and it was then that my mother gently reminded me of that long-forgotten childhood declaration.

An excited journey awaited me, filled with outstanding classes that unveiled the wonders of the universe and introduced me to a diverse group of friends who shared not only their passion for Physics but also formed strong bonds through spirited late-night conversations fueled by the warmth of tsipouro. Throughout my early academic years, I knew that I aspired to a career in research, but the precise field

that would ignite the fire within me remained elusive. That is until I had the fortune of crossing paths with an extraordinary mentor — Professor E.P. Benis. Under his guidance, a cascade of events unfurled, leading me ever closer to the realization of my dream.

Yet, no journey, especially one as profound as this, is without its challenges. During these pivotal years, life tested my resolve with a series of unhappy events, which left a void where beloved individuals once stood. Among them, my guiding light, my beloved mother, whose unwavering support and love had always fueled my ambitions. Although she might not have fully comprehended the intricacies of my research, she gave her best self to understand and encourage me. Her memory remains etched in my mind, a constant reminder of the strength and determination she instilled in me. In her honor, I took an oath: *to continue striving to understand Physics as deeply as I had longed to explain to her, and to embrace every challenge that research presented.*

Through trials, I found solace and purpose in the world of Physics. The pursuit of knowledge, the unraveling of the universe's mysteries, and the camaraderie of fellow scholars have sustained me throughout this challenging but immensely rewarding journey. So, as I pen these words as a testament to my Ph.D. dissertation, I offer my heartfelt gratitude to all who have supported and inspired me along the way. May the knowledge unveiled within these pages ignite new inquiries and spark the same wonder in others that has illuminated my own path.

Let the journey begin.

Stefanos Nanos
Athens, 2023

Chapter 1

Introduction

1.1 Accelerator-based Physics and Applications

Accelerator-based physics has played a pioneering role in the study of fundamental processes, unraveling the intricacies of particle interactions and shedding light on the building blocks of our universe. Beyond its contributions to our understanding of the cosmos, the development of particle accelerators has led to an array of practical applications that have profoundly impacted our daily lives. This progress has extended to diverse fields, showcasing how particle accelerators has transformed into a source of tangible benefits that enhance the well-being and progress of society as a whole.

The history of particle accelerators used for experiments can be traced back to the early 20th century. Linear accelerators, or linacs, were among the first designs. Linacs accelerate particles in a straight line using alternating electric fields. One of the earliest linacs was the Cockcroft-Walton accelerator, shown in Fig. 1.1. This type of accelerator was built in the early 1930s at the University of Cambridge by John Cockcroft and Ernest Walton, to accomplish the first artificial splitting of the atom [32]. This accelerator used an electric circuit that generates a high DC voltage from a low-voltage AC input to accelerate protons, marking a significant step forward in the field of nuclear physics.

In parallel, in the 1930s, physicist Ernest Lawrence invented the cyclotron, a circular particle accelerator that uses a magnetic field to bend particle trajectories and a varying electric field to accelerate particles as they circulate [33]. By the 1940s, cyclotrons were being used to produce high-energy particles for nuclear physics research.

The Van de Graaff accelerator, invented by American physicist Robert J. Van de Graaff in the early 1930s, marked a significant breakthrough in particle acceleration technology [34]. It utilized an innovative electrostatic generator design, employing a moving belt to transport electric charges to a high-voltage terminal, creating a powerful electric field for accelerating charged particles. Initially, capable of reaching energies around 1 MeV, Van de Graaff accelerators quickly found applications in nuclear physics research during World War II. In the post-war era, they continued to evolve and found new applications in various scientific and industrial fields. In response to the demand for greater particle energies, tandem Van de Graaff accelerators were developed in the 1950s [35]. Unlike traditional linear accelerators, tandem accelerators consist of two or more stages linked together. These stages acceler-

Figure 1.1: The Cockcroft-Walton accelerator terminal in the Grand Gallery at the National Museum of Scotland. Taken from [1].

ate charged particles, typically ions, in multiple steps, boosting their energy with each stage. Tandem Van de Graaff accelerators are particularly effective for producing high-energy ion beams for experiments in nuclear structure studies, material analysis, and atomic physics studies.

As researchers aimed to accelerate particles to even higher energies, the synchrocyclotron and synchrotron designs emerged. Synchrocyclotrons, like the Cosmotron at Brookhaven National Laboratory (1952) [36], shown in Fig. 1.2, combined cyclotron and synchrotron principles to achieve higher energies. By the 1950s and 1960s, full synchrotrons were developed, such as the Bevatron at Lawrence Berkeley National Laboratory (1954) [37], which could accelerate particles to energies exceeding those of cyclotrons.

Synchrotrons, with their ability to accelerate particles to relativistic speeds, paved the way for a new era of particle physics research. These circular accelerators use strong magnetic fields and radiofrequency cavities to maintain particle orbits and boost their energy. One of the most famous synchrotron facilities is CERN's Proton Synchrotron [38], schematically shown in Fig. 1.3, which played a crucial role in the discovery of new particles like the W and Z bosons [39]. Synchrotron facilities have also become vital sources of synchrotron radiation, high-intensity electromagnetic radiation produced when charged particles are accelerated in a curved path. These sources provide extremely bright X-rays that have revolutionized various fields, from materials science to biology. Examples include the SLAC [40] and the Advanced Photon Source (APS) [41] in the United States, the European XFEL and the Free-Electron Laser FLASH [42] in Germany, and the European Synchrotron Radiation Facility (ESRF) in France [43].

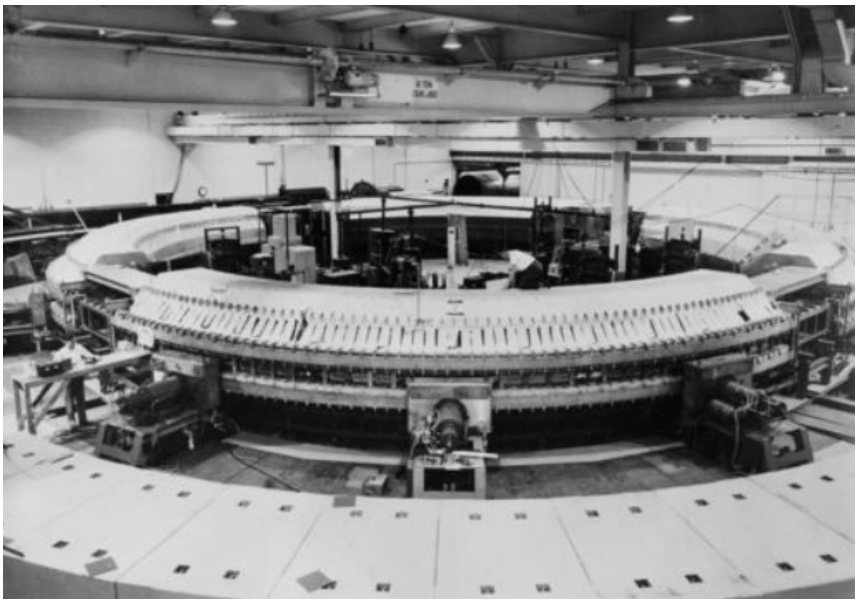

Figure 1.2: The Cosmotron synchrocyclotron of Brookhaven National Laboratory.

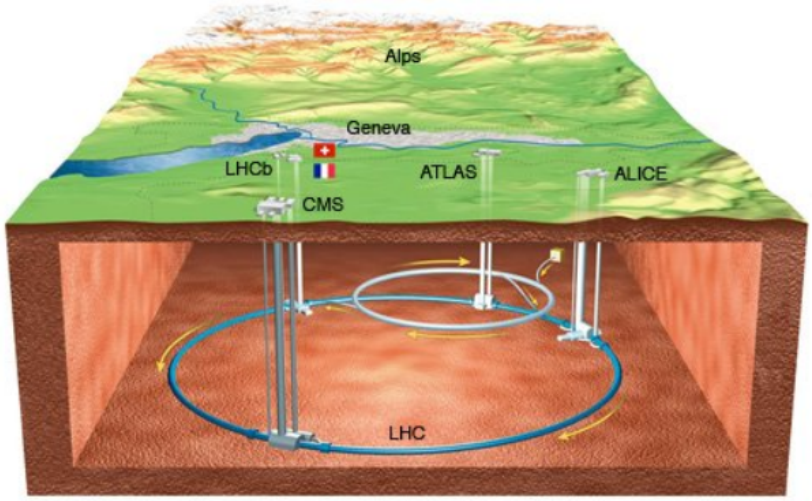

Figure 1.3: An underground schematic showing the CERN's large hadron collider (LHC) and its four main experiments.

The synchrotron principle led to the development of storage rings, a type of particle accelerator used to maintain a continuous stream of charged particles in a circular path using strong magnetic fields. These particles can be accelerated up to near-light speeds and then circulated around the ring. The GSI Helmholtz Centre for Heavy Ion Research, located in Darmstadt, Germany, is renowned for its prominent storage ring facilities [44]. One of its notable achievements is the operation of the heavy-ion storage ring (SIS), which plays an important role in advancing our understanding of nuclear structure, atomic physics in the near-relativistic domain, astrophysics, exotic particles, and fundamental forces.

In the ever-evolving landscape of accelerator-based research, Electron Beam Ion Sources (EBIS) and Electron Beam Ion Traps (EBIT) represent cutting-edge innovations that have revolutionized our ability to create and manipulate highly charged ions with precision and control [45]. Both EBIS and EBIT create highly charged ions by subjecting neutral atoms or ions to an intense electron beam under strong magnetic and electric fields. When ions are delivered outside the accelerator tank then it is called EBIS, while when they are only trapped inside the tank for studying then it is called EBIT. EBISs are of small dimensions and can accelerate high-Z highly charged ions up to energies up to hundreds keV/u. Thus, they are suitable for small laboratories but are also used as input sources for larger accelerators. Of similar use as EBIS is also the Electron Cyclotron Source (ECR), which uses radiofrequencies to create the highly charged ions [46].

Concluding our discussion of accelerator technologies, we turn our attention to laser-based accelerators, which leverage ultra-intense laser pulses [2]. These lasers generate extremely strong electric fields, exceeding the TV/m scale. Upon interaction of the laser beam with a gas medium, the gas is converted into plasma and triggers the formation of bubble-shaped plasma waves trailing behind the laser pulse. Inside these plasma bubbles, electric fields on the order of hundreds GV/m accelerate electrons from the surrounding plasma to relativistic speeds, akin to surfers riding sea waves. This process, known as laser wakefield acceleration (LWFA), occurs within a short distance of just a few millimeters. The LWFA principle is illustrated in Fig. 1.4.

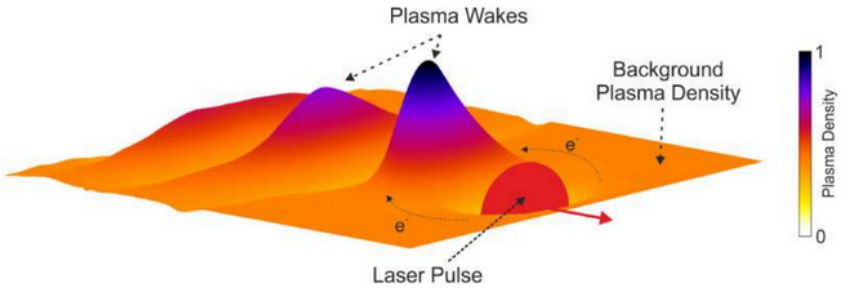

Figure 1.4: The LWFA principle: An ultra-intense laser pulse races through the plasma medium at nearly the speed of light, driving electrons towards its rear edge. This dynamic process gives rise to plasma wakes, capable of trapping background electrons and accelerating them to relativistic kinetic energies. Taken from [2]

The development of accelerator-based physics has led to numerous practical applications that extend beyond the study of fundamental processes. Here are several cases highlighting the importance of accelerator-based physics in our everyday lives.

Particle accelerators are important to medical facilities, delivering precise radiation beams for cancer treatment. Techniques like proton therapy and carbon ion therapy use accelerators to target tumors with minimal damage to healthy tissue, enhancing the effectiveness of cancer treatment [47]. Accelerators are also used in medical imaging, as seen in positron emission tomography (PET) scans, aiding disease diagnosis and treatment monitoring [48, 49].

In material science and industry, accelerators generate intense X-ray beams through synchrotron radiation. This capability enables researchers to analyze materials at the atomic level, contributing to advancements in industries like electronics, aerospace, and energy [50]. Accelerators are also used to implant ions into semiconductors, an important step in modern electronics production, enhancing performance and efficiency [51, 52].

Environmental monitoring benefits from accelerators through techniques like particle-induced X-ray emission (PIXE) and particle-induced gamma-ray emission (PIGE). These methods analyze environmental samples for trace elements and pollutants, aiding in pollution control and understanding natural processes [53, 54]. Furthermore, accelerators assist in studying archaeological artifacts. Several techniques are used to trace the origins of ancient materials, offering insights into historical trade routes, cultural interactions, and human migrations [55].

Another field where accelerators are used is food safety and preservation by irradiating food products to sterilize and extend shelf life [56]. This practice reduces foodborne illnesses, prevents spoilage, and enhances overall food security. Also, accelerators play an important role in non-destructive testing, providing high-energy beams that inspect materials without causing damage. This technology ensures safety and reliability in critical infrastructure such as pipelines, bridges, and aircraft components. Last but not least, accelerators are integrated into cargo and baggage inspection systems at transportation hubs. This enhances security by identifying hidden threats and contraband items, contributing to safer transportation, and thus to national security [57].

1.2 Accelerator-based Atomic Physics

Energetic ion beams, a cornerstone of atomic physics for the last decades, have propelled our exploration into the heart of the atomic realm. In the annals of modern science, accelerators have emerged as invaluable tools, delivering a diverse array of ion species and charge states, from keV/u protons to exotic projectiles such as bare uranium with velocities that reach the relativistic regime. Accelerator-based atomic physics has contributed to our understanding about the atomic structure and the dynamics involved during energetic ion-atom collisions. To an extent, this knowledge has found important practical applications in various research areas, such as thermonuclear fusion, astrophysics, and tumor therapy.

Accelerator-based atomic physics has reached significant milestones that illuminate the intricacies of the atomic world. Ion-atom collisions, have yielded insights into fundamental processes such as electron capture, excitation, and ionization, as well as the examination of exotic atoms for precision measurements of fundamental constants. Among numerous breakthrough studies, a few stand out as windows into the profound importance of this domain.

In the early 1960s, a significant development occurred as tandem Van de Graaff accelerators extended from nuclear to atomic physics studies. This extension allowed projectile ions to excite atomic states beyond the reach of photon and electron impact methods. This period marked the start of systematic investigations into auto-ionization effects, enhancing our understanding of atomic structure and collision dynamics. Simultaneously, pioneering works led to the discoveries of fundamental processes, such as the binary encounter and cusp electron peaks, challenging our understanding and paving the way for the development of sophisticated theories.

Building on early successes, accelerator-based atomic physics has witnessed transformative advancements. Amongst others, focus has been given to collision systems involving H-like and bare projectiles, such as Xe^{53+} and Xe^{54+}, considered as preliminary studies towards future experiments with supercritical fields within transient superheavy quasimolecules [58]. The study of the $1s\sigma$ molecular orbital and its evolution in collision systems with significant atomic numbers is central to this pursuit. This focus on the $1s\sigma$ remains persistent since the prediction of its diving into the Dirac sea for transient supercritical systems with $Z_{system} = Z_{Projectile} + Z_{Target} \geq 173$.

Optical atomic clocks, have proven essential in both fundamental scientific studies and technological innovations. Incorporating highly charged ions into these clocks offers a novel avenue for precision tests of fundamental physics [59]. The intrinsic properties of highly charged ions, coupled with their reduced sensitivity to external electric and magnetic fields, make them ideal candidates for precision measurements of hyperfine structure, quantum electrodynamics tests, and high-sensitivity searches for physics beyond the standard model.

While contemporary high-energy physics experiments, like those at CERN, focus on ion-ion interactions, the exploration of ion-ion collisions within atomic physics has primarily occurred at low velocities, typically a few keV/u. More recently, attention has shifted to the intermediate velocity regime, where MeV/u ions collide with keV/u ions [60]. Advances in accelerator technology have enabled the study of these collision systems, presenting complex challenges. In this regime, electron processes like capture, loss, and excitation, reach their maximum probabilities. These studies not only allow examination of the pure three-body problem involving a bare ion and a hydrogenic target but also enable step-by-step inclusion of additional electrons. This approach unveils insights into phenomena like electron-electron interactions across a wide spectrum of collision systems, enhancing our understanding of these interactions.

1.3 processes of Electron Capture and Ionization

Electron capture and ionization are amongst the most fundamental atomic processes inherent in ion-atom/molecule collisions. These processes, governed by complex dynamics, are difficult to theoretically describe due to the interplay of several factors, including the atomic numbers of the collision partners, i.e., Z_T and Z_p for the target and projectile respectively, the incoming ion charge, q, and the projectile velocity, V_p. It is worth mentioning that ion-atom collisions are commonly categorized into three, velocity regimes, characterized by the relative velocity of the projectile to the classical orbiting velocity of the active electron, v_e. These regimes are the adiabatic or slow regime, where $V_p << v_e$, the intermediate regime, where $V_p \simeq v_e$, and the high-energy or fast regime, where $V_p >> v_e$ [61]. Subsequently, we proceed to a

discussion related to the processes of electron capture and ionization, which stand as the primary focus of this thesis.

1.3.1 Charge Transfer Process

In ion-atom collisions, charge transfer processes involve the transfer of an electron from the target to the projectile, i.e.:

$$P^{q+} + T \rightarrow P^{(q-1)+*}(nl) + T^{+} \, . \tag{1.1}$$

Cross sections of reaction channels, as those described in Eq. 1.1, are of major importance in various fields of physics, including Atomic Physics, Astrophysics, Plasma Physics, and Accelerator Physics. The cross sections for SEC, describing the probability of capturing an electron during ion-atom collisions, can vary significantly based on several factors. One factor influencing SEC cross sections is the velocity of the projectile ion. At high velocities, particularly beyond the intermediate energy regime, the interaction time between the projectile and the target atom becomes relatively short. In these cases, one might expect the cross sections for SEC to decrease as the collision energy increases. This behavior is partially observed and can be roughly approximated using Schlachter's universal empirical scaling rule for SEC [62]. However, the cross sections for charge transfer are intricately influenced by multiple other factors. These include the atomic number (Z_T) of the target atom, the atomic number (Z_p) of the projectile ion, and the charge state (q) of the incoming ion. Each of these parameters can significantly impact the SEC cross sections, making charge transfer a complex and multifaceted phenomenon. Researchers in the field continue to explore and refine our understanding of these cross sections, considering these factors and their interplay in various collision scenarios.

In addition to the Z_T, Z_p, and q factors, it is worth to acknowledge the important role played by dynamic electron correlation effects in the charge exchange process. The influence of strong electron correlation effects, which naturally emerge from the complex multielectronic nature of collision systems, presents a compelling challenge to our comprehension of the charge exchange process [9, 23]. In the context of this thesis, we will detail the intricate interplay between these correlation effects and charge transfer phenomena, shedding light on their complex dynamics.

The process of charge transfer has attracted the attention of the scientific community for several decades. Originating in the early 1960s investigating proton collisions with hydrogen molecules, these studies initially aimed to test the scattering theories [63–66]. This initial foray paved the way for broader exploration, with heavier gas targets coming into play [67]. Notably, during the same period, experiments showed a distinctive electron energy spectrum resulting from ion impact on neon [68]. This presence of well-defined, sharp structures superimposed on a continuum background, further supported the idea that ionization in collisions of heavy particles involves the formation of multi-excited states, subsequently leading to autoionization.

Employing projectile ions brought about certain advantages, enabling the excitation of states inaccessible via photon or electron impact. This approach coincided with the introduction of heavier projectiles into the experiments, representing the next level of sophistication [69–72]. This progress has significantly contributed to understanding charge exchange processes between multiply charged ions and atoms,

which was of considerable interest due to their relevance in overcoming the impurity problem in thermonuclear plasma.

The potential to extract multiple electrons in a single collision has paved the way for high-resolution Auger spectroscopy of few-electron systems. In the early 1970s, a series of experiments focused on measuring high-resolution Auger electrons from fast-moving projectiles. During this period, the ejection of projectile Auger electrons following charge transfer in gas targets captured considerable attention [73, 74] (and references therein). While electron capture to excited states of highly ionized atoms had previously been important for studying plasma energy-loss processes and diagnostics in fusion-energy programs, such investigations mostly relied on high-resolution X-ray studies. However, projectile Auger electron spectroscopy emerged to address two main challenges faced during these earlier studies, i.e., significant attenuation of photons leading to substantial reduction in their intensity, and the relatively feeble radiative decay rate in comparison to the Auger decay rate, for low Z_p ions [75].

Even higher resolution on Auger electron measurements was achieved by observing electrons at forward angles of a few degrees. This was possible since the broadening effect stemming from the finite acceptance angle of the analyzer diminishes as the observation angle decreases, eventually vanishes in first order at zero degrees. In light of this, zero-degree Auger projectile spectroscopy (ZAPS) emerged as a valuable tool that captured the scientific community's attention [74, 76]. In the subsequent years, ZAPS has demonstrated its instrumental role through numerous groundbreaking studies in the field.

One of the most important milestones in related studies, is the use of pre-excited ion beams. In ion accelerators, the extracted ionic beam is typically magnetically selected for specific charge states and kinetic energies. Yet, this magnetic selection cannot separate the electronic configurations of particular ionic charge states. Consequently, mixed-state ionic beams are delivered that extend beyond the ground state. These additional metastable components offer a unique opportunity to investigate dynamic collision processes within ionic environments already having an initial K-shell vacancy [77]. The utilization of pre-excited, long-lived states has yielded success particularly in high-resolution projectile electron spectroscopy studies involving, amongst others, charge transfer investigations. Today, these pre-excited states continue to serve as an important tool for studying various collision processes, consistently revealing intriguing phenomena that contribute to our understanding of complex dynamics occurring during ion-atom collisions [22, 23, 78].

It is worth mentioning that not only experimental efforts, but also significant theoretical advancements have been made to further expand our understanding [9]. Initially, methods like the classical trajectory Monte Carlo (CTMC) [79] and the classical overbarrier model (COM) [80] have been employed to address charge transfer and ionization. CTMC involves a macroscopic classical representation of the system, integrating Newton's equations for electrons numerically. On the other hand, COM predicts electron capture by equating the potential energy barrier between the projectile and the target to the Stark shifted ionization energy.

Recently, approaches like the two centre basis generator method (TCBGM) [81] and the atomic orbital close coupling (AOCC) [82] have gained attention. Both techniques involve non-perturbative solutions of the time-dependent Schrödinger equation (TDSE), blending semiclassical descriptions of the collision partners with

a fully quantum mechanical description for electrons. These methods differ in their basis states and their applicability to various collision velocity regimes. AOCC, for instance, treats the initial electron configuration as *un-frozen* during the collision, taking into account a set of configurations with all the possible final combinations, forming the *basis* states.

It is noteworthy that the computational demand for solving TDSE limits the number of active electrons involved. Initially, these calculations were typically performed involving up to two active electrons, mainly focusing on the single electron capture (SEC) process to bare or single-electron projectiles. However, as the field progressed and the need to describe more complex systems arose, particularly those involving multi-electron final states with three or more electrons, it prompted the next level of sophistication in theoretical advancements, driven by the exponential growth of computer power.

1.3.2 Electron Capture to the Projectile's Continuum from Projectile/Target Ionization

Studies of the cross sections for ionization resulting from ion-atom collisions has remained a persistent challenge, compelling both experimental efforts and the advancement of theoretical frameworks. This challenge primarily stems from the intricate nature of the reaction channels. In this context, electrons ionized from the target atom are not only present in the target's continuum, which becomes the dominant channel for swift collisions and weak perturbations, but they also populate bound states or even low-energy continuum states of the projectile in cases of stronger perturbations.

The observation of a wide energy continuum peak, where emitted electron velocities match the velocity of the projectile, i.e., $v_e \simeq V_p$, marked a new field of research in atomic physics [83]. This phenomenon was quickly attributed to electrons becoming trapped within low-lying continuum states of the projectile. Depending on the collision system, these electrons could arise from two competing processes. In the first case, the active electron is ionized from the target atom and subsequently captured into the low-lying continuum states of the projectile. This ionization process may occur with or without the emission of a photon. The former process is termed electron capture to the continuum (ECC), while the latter is referred to as radiative electron capture to the continuum (RECC). The second case, relevant only to non-bare projectiles, involves the emitted electron originating from the dressed ion and being ionized into the projectile's continuum during the collision with a target atom. This process is known as electron loss to the continuum (ELC). Both processes result in a sharp peak in the electron spectrum measured around the emission angle of zero-degree with respect to the projectile velocity, and termed "cusp peak" and the corresponding electrons "cusp electrons".

Given the complexity of comprehending the concept of an electron being captured to the projectile's continuum, rather than to a bound state, a more accessible understanding can be achieved through the lens of the Coulombic centers framework [84]. This approach replaces the intricate dynamics of a many-body system with interactions of the heavy nuclei with the active electron in the final state. In the case where the final state involves two interactions, i.e., one between the active electron and the projectile nucleus, and a second between the same electron and the target

nucleus, a case of two-center electron emission arises.

The ECC process serves as a characteristic example of a two-center phenomenon. The initial theoretical attempts using the first-order Born approximation, which describes a single-center collision case, failed to replicate the cusp electron peak observed in ionization reactions, as shown in Fig. 1.5 for a typical ECC spectrum. Only when the initial and final wavefunctions were both subjected to distortion due to the projectile's Coulombic potential was the cusp feature successfully reproduced.

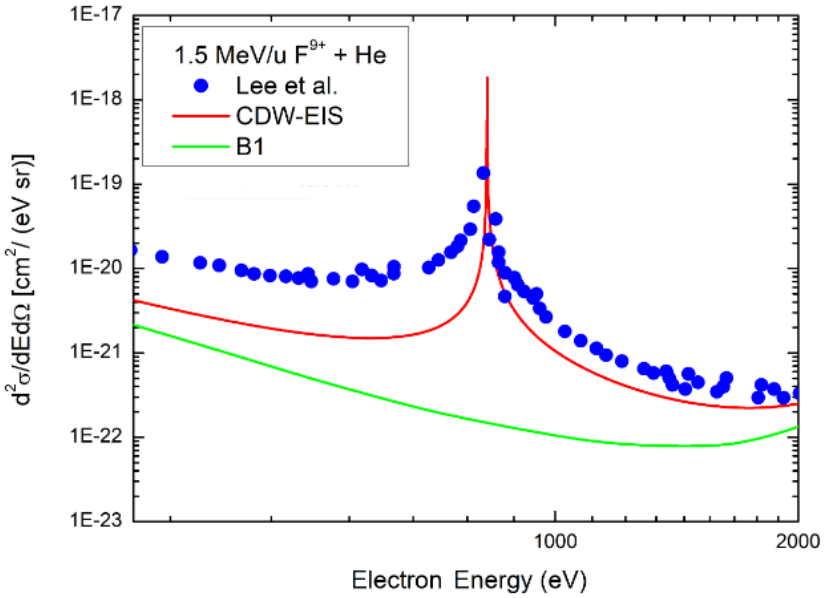

Figure 1.5: Example of a cusp electron spectrum demonstrating the difference between the CDW-EIS and B1 approximations. The data refer to electron emission at 0° in collisions of 1.5 MeV F^{9+} + He taken from [3]: (Red line) the CDW-EIS approximation calculated with the Ion-Atom/Argon Program and (Green line) B1 calculations taken from [4]. Taken from [5].

To even better visualize this, we could think of it from a classical perspective, through the framework of the double scattering process introduced by Thomas [85]. Consider a projectile travelling at a velocity of V_p toward a target atom. It has been demonstrated, as shown in Eq. 1.2, that within a binary collision, the velocity of the scattered electron from the target aligns with that of the projectile, given a scattering angle of 60 degrees with respect to the projectile's trajectory. Subsequently, if this electron undergoes elastic backscattering within the field of the target nucleus, it may be scattered following a trajectory nearly parallel to that of the projectile, thus increasing the probability for capture of the scattered electron into low energy continuum states of the projectile. The situation is illustrated in Fig. 1.6.

$$\mathrm{v}_e = 2V_p \cos\theta_e \Rightarrow \mathrm{v}_e \simeq V_p \ , \quad \text{for} \ \ \theta_e = 60^\circ \ . \tag{1.2}$$

It is important to note that while the Thomas scattering may not significantly contribute to ECC, the double scattering process is employed for qualitative discussions. This approach, effectively illustrates the significance of both the target and projectile nuclei in shaping the cusp electron peak. Moreover, it emphasizes the extended duration of interaction between the emitted electron and the projectile, providing valuable insights into the underlying dynamics.

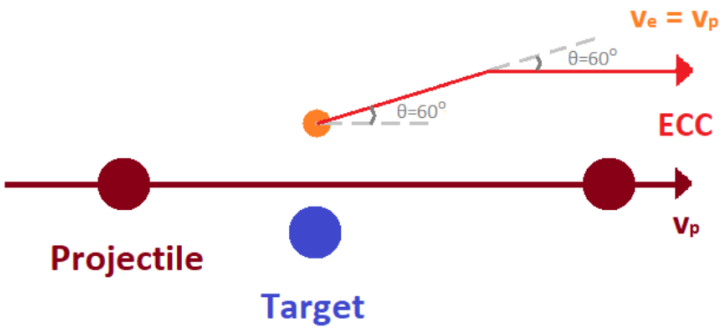

Figure 1.6: Schematic illustration of the ECC process under the Thomas's classical double scattering picture. Taken from [5].

Extensive research has been dedicated on the cusp electron peak, with diverse collision systems employed in experimental studies. Experiments conducted at tandem Van de Graaff accelerators featuring low-Z projectile ions and collision energies of a few MeV/u, have facilitated the exploration of contributions from both ECC and ELC processes to the cusp peak. These studies have been further refined through approaches considering factors such as the electron solid angle acceptance [86], impact parameter [87], and target recoil-ion momentum [88]. The emergence of heavy-ion accelerators has provided the means to delve even deeper into the collision dynamics of these processes [89–92]. This not only challenged the boundaries of existing theories but also motivated the development of new approximations, including fully relativistic treatments.

Despite the significant advancements made over the years, there still remaining several aspects that warrant deeper investigation, even within the non-relativistic domain. Presently, the most extensively employed theoretical frameworks are the distorted wave theories [93]. Originally, the concept of a continuum distorted wave (CDW) emerged as a quantum mechanical representation of a Coulomb wave linked to the motion of an electron associated with one ion/atom relative to, and simultaneously within, the continuum of another ion. This concept initially pertained to charge transfer phenomena. It was subsequently expanded to encompass the electron continuum, and later to ionization within ion-atom collisions. Building upon these developments, the CDW-EIS (eikonal initial state) approximation was introduced, effectively ensuring the unitarity of the propagating initial state.

In recent times, both experimental and theoretical endeavors persist in unveiling the intricacies of cusp electrons. In this thesis, we detail our efforts to further the exploration of cusp electron phenomena within collision systems, marking a significant step forward by incorporating open-shell projectiles for the first time.

1.4 Dissertation Goals

The goal of this thesis is to systematically study the intricate processes underlying electron capture and ionization in fast ion-atom collisions. In this research, we employ a recently introduced the double measurement technique to distinguish the contributions of specific reaction channels originating from both ground and excited state components of the mixed-state incident beam, which also allows the deter-

mination of the metastable content important for cross section determinations.. In pursuit of this objective, we have outlined two primary goals.

Our first primary goal is the investigation of cusp electron production during collisions of deuterons as well as mixed-state beams with gas targets. Through these studies, we expose the role played by the target subshells and the configuration of the incoming projectile during the collision process. Our investigations serve as a rigorous testing ground for theories based on distorted wave approximations, which accompany our measurements, thus advancing their models and the understanding of the underlying processes involved.

Our second primary goal is the systematic study of the SEC process in collisions of multielectron open-shell ions with atomic targets. For this study we employ KLL Auger electron spectroscopy, aiming to underscore the significance of strong correlation effects inherent in the SEC process, an area recently highlighted by our research team. To accomplish this goal, we have adopted a multidisciplinary approach that combines high-resolution experimental measurements with state-of-the-art 3eAOCC calculations, a three-active-electron theory. Our intention is to rigorously test and refine this theoretical framework within the context of our isoelectronic study. Ultimately, this goal aims to shed light on the intricate dynamics underlying the SEC process and contribute to the ever-evolving understanding of electron behavior in ion-atom collisions.

These two goals are the core objectives of this dissertation, collectively seeking to expand the knowledge in the field of fast ion-atom collisions. By achieving these objectives, we aspire to contribute to the scientific community's understanding of the fundamental processes governing electron capture and ionization, thereby advancing both theoretical models and practical applications in this dynamic domain.

1.5 Dissertation Outline

In this section, we present an overview of the structure of this dissertation. Each of the eight chapters is briefly described to offer a glimpse into their content.

In Chapter 2, we discuss the Zero-degree Auger projectile spectroscopy (ZAPS) technique. We commence with an exploration of its historical context, highlighting how ZAPS has emerged as a powerful tool for high-resolution measurements. Subsequently, the kinematics of Auger spectroscopy are elucidated, followed by an examination of broadening effects that can influence the precision of our measurements. This chapter is complemented by Appendix A, where all the formulas employed in our analysis are rigorously proven.

In Chapter 3, we present in detail the experimental setup utilized in our research. We begin by introducing the 5.5 MV tandem Van de Graaff accelerator, followed by an overview of the atomic physics experimental setup, elucidating the functionality and significance of each critical component. Furthermore, we touch upon the upgrades made to our setup, eventually enabling the incorporation of coincidence techniques to enhance the capabilities of our future research endeavors.

In Chapter 4, we discuss the intricacies of data analysis. There, we elucidate the step-by-step process by which raw data are analysed to derive absolute double differential cross-section (DDCS) spectra. We detail the energy calibration process and the DDCS formula, providing insight into all the parameters involved. Additionally, we discuss the effective solid angle correction factor, which plays an important role

in accounting for long-lived states. Moreover, we explore the determination of the metastable beam fraction through our double measurement technique. Finally, the chapter ends by explaining how single differential cross-sections (SDCS), which are integral to our studies, are determined.

In Chapter 5, we introduce SIMION, a software package used for the study of electrostatic fields and the orbits of charged particles within these fields. We present how SIMION can be harnessed as an analysis and diagnostic tool in our research. Specifically, we discuss its application in determining Auger electron yields and validating the process of recording overlapping electron spectra. Furthermore, we explore how SIMION serves as a robust approach for detailed studies, including the determination of the effective solid angle correction factor through Monte Carlo simulations.

In Chapter 6, we present the details and findings of our cusp electron studies. Starting with an introduction about the background and motivation for this research, we continue by discussing the distorted wave theories employed in our investigations. Subsequently, we present our cusp electron studies, starting with bare projectiles and multielectronic targets. There, we elucidate the significant role of target subshells in the formation of the cusp electron peak. We then proceed to discuss cusp electron studies utilizing dressed projectiles, where we isolate the cusp electron peak originating from collisions of pre-excited projectiles, $1s2s$, with He targets at a DDCS level, highlighting the importance of incoming configuration during cusp electron formation. Furthermore, we explore studies involving Be-like projectiles, and conclude this chapter by examining a small peak evident in the low-energy wing of the cusp electron peak. Through systematic investigations using multiple projectiles and target species, we aim to shed light on the nature of this new finding, proposing a novel electron-correlated process, i.e., electron loss to the continuum with simultaneous target ionization.

In Chapter 7, we present the details and findings of the isoelectronic study of the SEC process in collisions of multielectron open-shell ions with atomic targets. We place significant emphasis on the ratio R_m, of the ^4P peak to the two $^2P_\pm$ peaks, which provides important insights into spin statistics and collision dynamics of the SEC process. The chapter starts with an introduction providing background and motivation. We then present the 3eAOCC theory, a state-of-the-art approach involving three active electrons, which is critically compared to our measurements. We proceed to present our results for collision systems involving He-like oxygen and boron projectiles. For oxygen, a detailed study involving measurements at various collision energies enables us to also present SDCS contributions for collisions of O^{6+} (1s2s) and O^{6+} ($1s^2$) with He. Finally, we conclude this chapter with a detailed discussion that highlights the role of the $^2P_\pm$ states, demonstrating the presence of strong electron correlation effects in the SEC process during fast ion-atom collisions.

In Chapter 8, we propose a new method for the determination of the ion beam energy width using KLL Auger electron spectroscopy. Our in situ method allows for the convolution of the ion beam energy width within the Auger electron spectra, eliminating the need for additional measurements. Furthermore, it offers the flexibility to vary parameters such as the stripping location and accelerator settings for each experiment, enabling accurate determination of the energy width under specific conditions.

In Chapter 9, we present a summary of all the results and findings presented

throughout this dissertation. Additionally, we explore the future prospects of the Atomic Physics setup operating at the INPP of NCSR "Demokritos", highlighting its potential for further advancements and applications in the field of fast ion-atom collisions.

Chapter 2

Zero-Degree Auger Projectile Spectroscopy (ZAPS)

2.1 Background and Context

Auger electron spectroscopy has proven a valuable tool in studying inner-shell vacancy production in energetic ion-atom collisions. Auger spectroscopy has extensively utilized light projectiles, such as protons and helium ions, which induce minimal perturbation to the outer shells of the atom. Consequently, the Auger spectra obtained from these collisions are predominantly characterized by singly ionized systems [11, 94]. However, as the nuclear charge of the projectiles increases, additional outer-shell ionization becomes significantly enhanced. This phenomenon becomes more pronounced with heavy projectiles, where almost all outer-shell electrons are ionized under single collision conditions. Thus, Auger states of few-electron systems become predominantly excited, leading to complex Auger spectra with numerous satellite lines, difficult to analyze due to significant line blending [95].

An alternative approach widely known as Auger electron projectile spectroscopy offers distinct advantages when studying energetic ion-atom collisions [74]. By preparing highly ionized ion beams in a pure charge state before the collision process, light target atoms can be used as projectile inner-shell exciters, minimizing additional outer-shell ionization or excitation. This approach enables the preservation of the outer-shell electronic configurations of the incident ions during the production of inner vacancies. Consequently, Auger states of various charge states can be studied individually by varying the incident ionic charge state. This technique holds significant potential for in-depth investigations into Auger processes in ion-atom collisions (see [96] and references therein).

Furthermore, the technique known as zero-degree Auger projectile spectroscopy (ZAPS) offers a solution to mitigate the kinematic line-broadening effects by observing the Auger electrons emitted at zero degrees with respect to the projectile trajectory [76]. This technique has emerged as a valuable tool for enhancing the resolution in Auger spectroscopy, making it particularly advantageous for state-selective double differential cross section studies. Subsequently, ZAPS enables us to obtain precise and detailed insights into the electronic structure of atoms and molecules, and gain valuable knowledge regarding various production mechanisms of complex systems.

An illustrative example highlighting the enhanced resolution at zero-degree ob-

servation angle is depicted in Fig. 2.1. The spectra exhibit Auger electron emission resulting from 60 keV C^{6+} + He collisions for three different observation angles [6]. Each peak corresponds to the decay of Auger states associated with a configuration $2lnl'$, where n ranges from 3 to 6, produced by double electron capture. It is evident that as the observation angle increases, the kinematic broadening becomes more pronounced, thereby imposing limitations to the resolution of the Auger spectrum. It should be noted that this kinematic broadening becomes much more severe at the higher energies studied in this thesis.

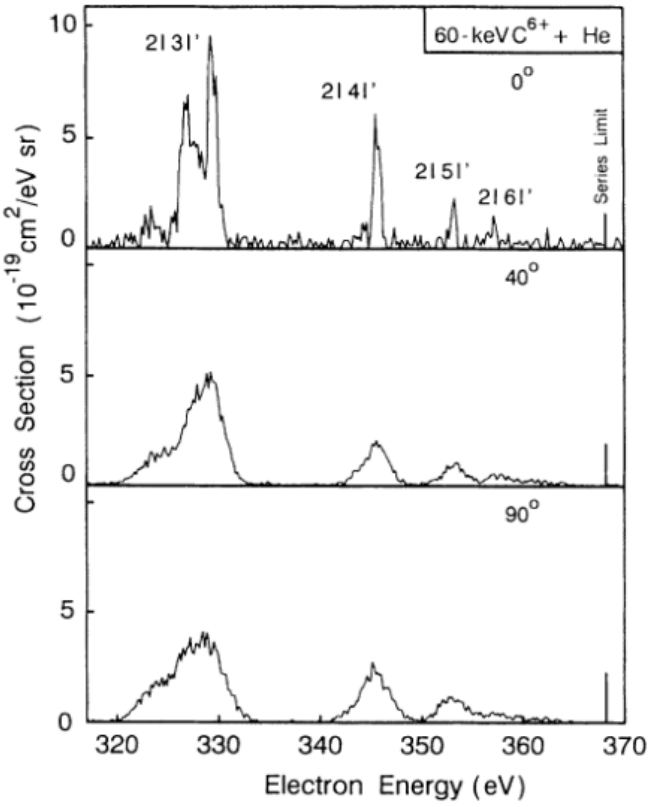

Figure 2.1: Auger electron emission spectra obtained in collisions of 60 keV C^{6+} + He for three different observation angles: [top] $\theta = 0°$; [middle] $\theta = 40°$; [bottom] $\theta = 90°$. Each peak corresponds to the decay of Auger states associated with the configuration $2lnl'$, where $n = 3 - 6$. Taken from [6].

Beyond its application in Auger electron projectile spectroscopy, ZAPS technique finds additional utility in two-center electron emission (TCEE) studies [84]. TCEE phenomena gain significance when the outgoing electron experiences the combined influence of both target and projectile nuclei fields. At zero-degree emission angle, TCEE processes are particularly pronounced, with a characteristic example being the production of cusp electrons resulting from electron capture or loss to the continuum (i.e., ECC and ELC processes). By employing ZAPS, the most sensitive characteristics of cusp electrons can be exposed unraveling, among others, the intricate interplay between the target and projectile fields [21].

The pioneering implementation of the ZAPS spectrometer can be credited to A. Itoh and N. Stolterfoht who introduced it in 1983. They employed a tandem configuration consisting of two consecutive 90-degree parallel plate analyzers (PPA)

with a deceleration stage composed of two parallel grids between the two PPAs. [96, 97]. The ZAPS technique quickly gained recognition and sparked interest among researchers worldwide. The extensive body of work generated during this era showcases the versatility and significance of the ZAPS technique in various scientific investigations. For more details and notable studies conducted during this time, readers are encouraged to refer to the cited references [3, 98–108].

The experimental studies conducted in this work utilized the ZAPS technique. The ZAPS experimental setup, located at the tandem van de Graaff accelerator laboratory of the Institute of Nuclear and Particle Physics (INPP) of the National Center for Scientific Research (NCSR) "Demokritos", was employed for these experiments. This setup, which is extensively described in Chapter 3, was initially developed at the J.R. Macdonald laboratory of Kansas State University [109–111], and since 2014 transferred to "Demokritos", initiating atomic physics studies using energetic ion-atom collisions.

The ZAPS setup at the INPP of NCSR "Demokritos" is a unique, state-of-the-art, experimental station worldwide. It offers significantly improved efficiency compared to the more traditional tandem PPA spectrometer, with approximately two orders of magnitude higher efficiency [111]. This enhanced efficiency enables accurate measurements of double differential cross sections (DDCS) of fundamental processes such as single electron capture (SEC), excitation, transfer and excitation (TE), electron capture to the continuum (ECC) and electron loss to the continuum (ELC), of interest in this dissertation. These DDCSs provide stringent tests for atomic collision theories and related modeling. Furthermore, our ZAPS setup has recently undergone upgrades, enhancing its capabilities and expanding its arsenal for future research studies.

2.2 Kinematics of Auger Spectroscopy

Auger electrons emitted by scattered projectiles experience kinematic influences that can complicate their analysis. However, in the case of energetic collisions studied in this dissertation, where the projectile ions are scattered at very small angles (∼mrads) due to their high energy (a few MeV/u), the effects on energy loss and projectile electron trajectories are negligible. Consequently, for simplicity, it is safe to assume a scattering angle of zero degrees for swift collisions. Under this assumption, a straightforward model based on vector addition of velocities is adequate for determining the transformation from the projectile frame to the laboratory frame and addressing related kinematic effects, without considering ion-recoil effects.

In the laboratory frame, the velocity $\mathbf{v}$ of the Auger electron is obtained by adding the projectile velocity $\mathbf{V_p}$ to the velocity $\mathbf{v}'$ of the electron in the projectile rest frame, as illustrated in Fig. 2.2 (primed symbols are reserved for the projectile rest frame). The kinetic energy ϵ of the electron in the laboratory frame can then be related to its corresponding rest frame kinetic energy ϵ' as:

$$\epsilon = \epsilon' + t_p + 2\sqrt{\epsilon' t_p}\cos\theta' \tag{2.1}$$

or equivalently

$$\epsilon' = \epsilon + t_p - 2\sqrt{\epsilon t_p}\cos\theta \tag{2.2}$$

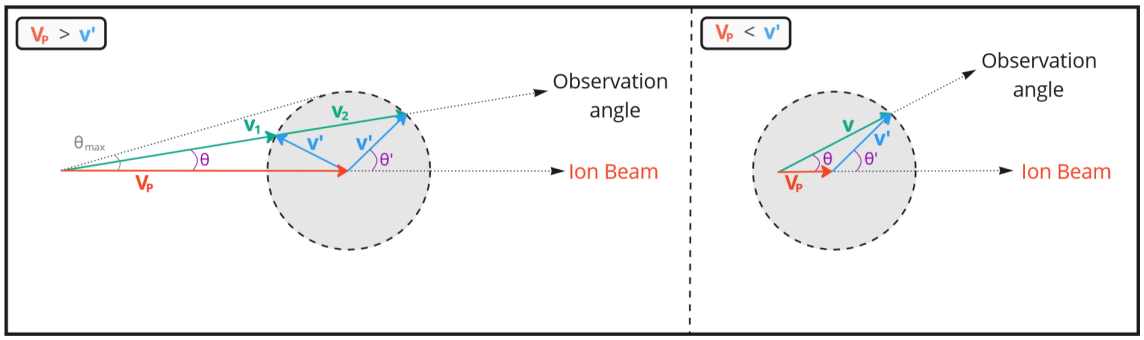

Figure 2.2: Velocity addition diagram showing the projectile velocity $\mathbf{V_p}$, the electron velocity in the laboratory frame $\mathbf{v}$ and the electron velocity in the projectile rest frame $\mathbf{v}'$. The case is depicted for emitter velocity larger than the electron velocity $\mathbf{V_p} > \mathbf{v}'$ (left) and for emitter velocity smaller than the electron velocity $\mathbf{V_p} < \mathbf{v}'$ (right). Transformation of the electron velocity from the projectile to the laboratory frame, and vice versa, becomes according to the vector addition rule as $\mathbf{v} = \mathbf{v}' + \mathbf{V_p}$.

where

$$t_p = \frac{1}{2} m V_p^2 = \frac{m}{M} E_p = 548.58 \, \frac{E_p(\mathrm{MeV})}{M(\mathrm{u})} (\mathrm{eV}) \tag{2.3}$$

is the reduced projectile energy known also as the *cusp* energy. E_p is the kinetic energy of the projectile in MeV and M the projectile's mass in atomic mass units (u), while m is the electron mass.

To facilitate a systematic examination of the kinematic transformation properties of the experimentally measurable quantities, it is advantageous to employ the universal dimensionless parameter ζ [76]:

$$\zeta \equiv \sqrt{\frac{t_p}{\epsilon'}} = \frac{V_p}{\mathrm{v}'} \, . \tag{2.4}$$

Furthermore, it proves beneficial to establish the connection between energies in the rest and the laboratory frames by formulating a function that incorporates the laboratory observation angle θ and the introduced ζ parameter [76]:

$$\epsilon_{\pm}(\theta) = \epsilon' \left(\zeta \cos\theta \pm \sqrt{1 - \zeta^2 \sin^2\theta} \right)^2 \qquad \left(\zeta > 1, \; 0^\circ \leq \theta \leq \arcsin \frac{1}{\zeta} \right) , \tag{2.5}$$

$$\epsilon(\theta) = \epsilon_+(\theta) \qquad (\zeta \leq 1, \; 0^\circ \leq \theta \leq 180^\circ) \, . \tag{2.6}$$

It is worth noting that in the case of fast emitters ($\zeta > 1$), there exists a maximum attainable observation angle θ_{max} as illustrated in Fig. 2.2. This comes naturally from the fact that the expression under the square root in Eq. 2.5 should be greater than or equal to zero. This limitation poses a critical constraint on non-zero degree Auger projectile spectroscopy, as it necessitates specific electron energies to correspond to distinct maximum detection angles, thereby imposing a lower limit on the range of accessible electron energies for the spectrometer. However, in the case of ZAPS, the entire range of projectile electron energies remains accessible. This represents one of the most significant advantages of measuring electron spectra at zero degrees. Eqs. 2.5, 2.6 are reduced for zero-degree observation to

$$\epsilon_+(\theta = 0^\circ) = \epsilon'(1+\zeta)^2 = (\sqrt{\epsilon'} + \sqrt{t_p})^2 \qquad (\text{All } \zeta,\ \theta' = 0^\circ), \tag{2.7}$$

$$\epsilon_-(\theta = 0^\circ) = \epsilon'(1-\zeta)^2 = (\sqrt{\epsilon'} - \sqrt{t_p})^2 \qquad (\zeta > 1,\ \theta' = 180^\circ). \tag{2.8}$$

It is important to highlight that for fast emitters there are two distinct solutions, as it is indicated in Eqs. 2.7, 2.8. This aspect is also depicted in the vector diagram presented in Fig. 2.2, illustrating the presence of two possible outcomes. In detail, Eqs. 2.7 and 2.8 represent the solution for forward ($\theta' = 0^\circ$) and backward ($\theta' = 180^\circ$) emission from the ion, respectively.

2.3 Kinematic Transformation Effects

The analysis presented in Section 2.2 depicts the presence of several kinematic effects that can significantly affect the position, energy width, and intensity of an Auger line. A comprehensive examination of these effects has been extensively discussed in [8, 9, 74, 76]. However, a brief discussion will be given here for completeness purposes. The equations used in the previous analysis, as well as those presented in the following, can be found in Appendix A, where their proofs are detailed.

2.3.1 Doubling

The above analysis has shown the presence of two distinct solutions for the laboratory electron energy ϵ, resulting in two peaks in the laboratory frame that correspond to the same Auger energy. This phenomenon, is further discussed in Chapter 6. There, it is demonstrated that the Auger peaks, originating from the inelastic scattering of quasi-free target electrons by ions, exhibit a symmetrical distribution around the cusp peak. This symmetry is in accordance to Eqs. 2.7, 2.8.

2.3.2 Shifting

Eqs. 2.7, 2.8 depict that an electron emitted with energy ϵ' in the projectile rest frame, will be observed in the laboratory frame at an energy ϵ. In the case of forward electron emission ($\theta' = 0^\circ$), the resulting laboratory energy ϵ is larger than ϵ'. Backward electron emission ($\theta' = 180^\circ$) can yield laboratory energy values that are either larger or smaller than ϵ', depending on the value of ζ. The ability to detect an Auger line at an energy larger than its rest frame value holds significant importance in ZAPS, as it allows for the easier detection of low-energy electrons ($\epsilon' < 10$ eV), since it shifts their energies to much higher values more accessible to electrostatic spectrometers and less influenced by the Earth's magnetic field..

2.3.3 Stretching

The energy width $\Delta\epsilon$ of an Auger line detected in the laboratory frame exhibits variations compared to the corresponding width $\Delta\epsilon'$ in the projectile frame, e.g., the natural line width of the Auger line. Upon differentiating Eqs. 2.7, 2.8 with respect to ϵ', the following expression is obtained:

$$\frac{\Delta\epsilon}{\Delta\epsilon'} \simeq \frac{d\epsilon}{d\epsilon'} \Rightarrow \begin{cases} \left.\frac{\Delta\epsilon}{\Delta\epsilon'}\right|_{+} = 1+\zeta & (\text{All } \zeta,\ \theta' = 0°, \theta = 0°) \\ \left.\frac{\Delta\epsilon}{\Delta\epsilon'}\right|_{-} = |1-\zeta| & (\zeta > 1,\ \theta' = 180°, \theta = 0°) \end{cases} \tag{2.9}$$

Eq. 2.9 clearly demonstrates that, in the case of forward electron emission ($\theta' = 0°$), line stretching occurs, while for backward electron emission ($\theta' = 180°$), line stretching or compression is observed, depending on the value of ζ. It is significant to emphasize that the spectral stretching does not increase the overlap between closely neighboring Auger lines. As a result, intrinsic structures within the spectrum remain unaffected. However, it is worth noting that the energy resolution $\Delta\epsilon/\epsilon$ experiences changes, as evident from Eq. 2.10:

$$\frac{\Delta\epsilon}{\epsilon} = \sqrt{\frac{\epsilon'}{\epsilon}}\frac{\Delta\epsilon'}{\epsilon'} \tag{2.10}$$

2.3.4 Angular Compression

Electrons emitted in the projectile rest frame undergo an angular compression when observed in the laboratory frame, leading to their detection within a narrower solid angle. This phenomenon is particularly pronounced for forward emission ($\theta' = 0°$), while for backward emission ($\theta' = 180°$), it occurs only when $\zeta > 2$. This behavior is mathematically described by the following equation, while the underlying geometric explanation is illustrated in Fig. 2.3.

$$\frac{\Delta\Omega}{\Delta\Omega'} \simeq \frac{d\Omega}{d\Omega'} \Rightarrow \begin{cases} \left.\frac{\Delta\Omega}{\Delta\Omega}\right|_{+} = \frac{1}{(1+\zeta)^2} & (\text{All } \zeta,\ \theta' = 0°, \theta = 0°) \\ \left.\frac{\Delta\Omega}{\Delta\Omega}\right|_{-} = \frac{1}{(1-\zeta)^2} & (\zeta > 1,\ \theta' = 180°, \theta = 0°) \end{cases} \tag{2.11}$$

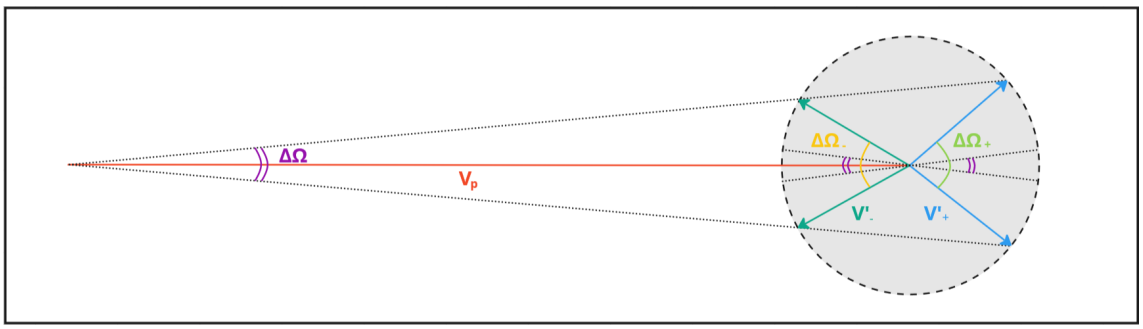

Figure 2.3: Angular compression of electrons emitted from fast emitters.

2.3.5 Enhancement

The measured height of an Auger peak in the laboratory frame deviates from its height in the projectile rest frame. This effect can be comprehended through the

transformation of the DDCS from the projectile to the laboratory frame at zero degrees, as:

$$\frac{d^2\sigma}{d\Omega d\epsilon} = \sqrt{\frac{\epsilon'}{\epsilon}}\frac{d^2\sigma}{d\Omega' d\epsilon'} \Rightarrow \begin{cases} \left.\frac{d^2\sigma}{d\Omega d\epsilon}\right|_+ = (1+\zeta)\frac{d^2\sigma}{d\Omega' d\epsilon'} & (\text{All } \zeta,\ \theta' = 0°, \theta = 0°) \\ \left.\frac{d^2\sigma}{d\Omega d\epsilon}\right|_- = |1-\zeta|\frac{d^2\sigma}{d\Omega' d\epsilon'} & (\zeta > 1,\ \theta' = 180°, \theta = 0°) \end{cases} \tag{2.12}$$

For forward emission (+ solution for all ζ values) and backward emission (- solution and $\zeta > 2$), an amplification of the peak heights in the laboratory frame is observed. Conversely, for backward emission (- solution and $1 < \zeta < 2$), a reduction in the laboratory peak heights is observed.

2.4 Line Broadening Effects

According to Eqs. 2.5, 2.6, electrons emitted in the projectile rest frame with the same velocity will be detected in the laboratory frame with different velocities, depending on the observation angle θ. Consequently, two electrons with identical energies in the projectile frame but emitted at different angles θ'_1 and θ'_2, they will be observed in the laboratory frame with distinct energies $\epsilon_1(\theta_1)$ and $\epsilon_2(\theta_2)$, respectively. In the case where the emission angles correspond to the angular width $\Delta\theta$ of the spectrometer's acceptance angle ($\Delta\theta = \theta_2 - \theta_1$), the observed energy difference ΔE can be expressed as $\Delta E = \epsilon_2(\theta_2) - \epsilon_1(\theta_1)$. This is illustrated in Fig. 2.4, where it is graphically shown that zero-degree observation angle ($\theta = 0°$) significantly reduces the observed energy width ΔE.

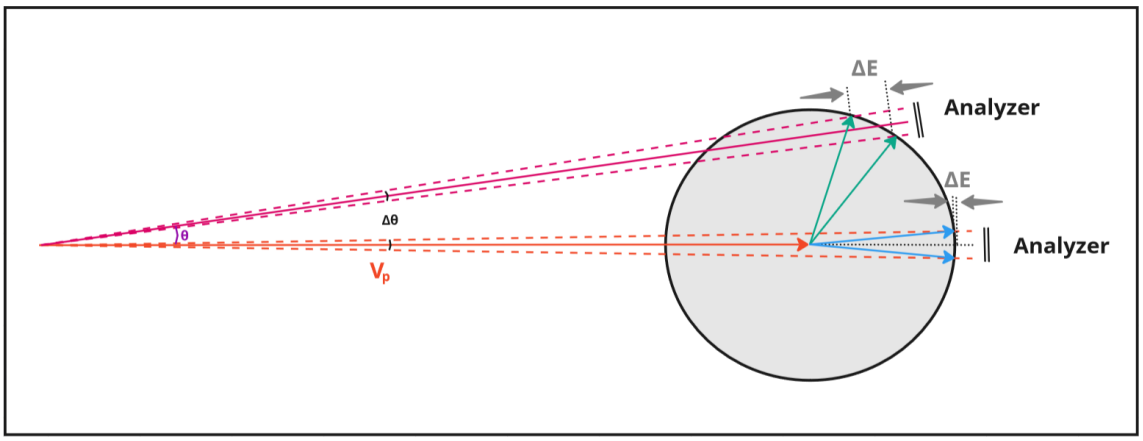

Figure 2.4: Geometrical interpretation of the broadening effect due to the observation angle θ.

The phenomenon of broadening can be comprehended mathematically by considering the uncertainties associated with two variables: the laboratory observation angle θ and the cusp energy t_p. The broadening caused by the observation angle θ can be accurately calculated for each experimental configuration, as it is determined geometrically by the size of the effective spectrometer acceptance aperture and the distance between this aperture and the target. While a straightforward calculation

of broadening can be performed for any spectrometer, employing an algebraic approach offers deeper insights. For that, one can employ a Taylor series expansion of Eq. 2.5 in powers of $\Delta\theta$ as [76]:

$$\Delta B_\theta \simeq \left| \sum_n \frac{\partial^n \epsilon(\theta)}{\partial \theta^n} \frac{(\Delta\theta)^n}{n!} \right| \equiv \left| \sum_n \Delta B_\theta^{(n)} \right| \tag{2.13}$$

Upon closer examination, it becomes evident that the first term of the expansion series in Eq. 2.13 is directly proportional to $\sin\theta$. As a consequence, when the observation angle is at zero degrees ($\theta = 0°$), this term vanishes. To an extent, the second order term coefficient, shown in Eq. 2.14, is negligible for high energy electrons, e.g., for KLL Auger electrons [8]. Thus, the broadening effect is significantly reduced under these conditions.

$$\Delta B_\theta^{(2)} = \begin{cases} \epsilon'(1 \pm \zeta)^2 \zeta \left(\frac{\Delta\theta}{2}\right)^2 & (\text{All } \zeta,\ \theta' = 0°, \theta = 0°) \\ \\ \epsilon'(1 - \zeta)^2 \zeta \left(\frac{\Delta\theta}{2}\right)^2 & (\zeta > 1,\ \theta' = 180°, \theta = 0°) \end{cases} \tag{2.14}$$

The line broadening attributed to the beam energy width can be realized when expanding Eq. 2.2 in a Taylor series, as:

$$\Delta B_{t_p} \simeq \left| \sum_n \frac{\partial^n \epsilon(t_p)}{\partial t_p^n} \frac{(\Delta t_p)^n}{n!} \right| \equiv \left| \sum_n \Delta B_{t_p}^{(n)} \right| \tag{2.15}$$

Notably, for a zero-degree observation angle, the first-order coefficient can be expressed as:

$$\Delta B_{t_p}^{(1)} = \begin{cases} \left(1 + \frac{1}{\zeta}\right) \Delta t_p & (All\ \zeta,\ \theta' = 0°, \theta = 0°) \\ \\ \left|1 - \frac{1}{\zeta}\right| \Delta t_p & (\zeta > 1,\ \theta' = 180°, \theta = 0°) \end{cases} \tag{2.16}$$

The line broadening observed in high-resolution Auger projectile spectroscopy provides valuable information about the beam energy uncertainty, which is the factor that most significantly contributes to the broadening effect. To gain a better insight, let us visualize this with an example. The angular broadening, determined for an ion beam energy of 1 MeV/u (equivalent to 548.58 eV according to Eq. 2.3) in conjunction with a typical Auger energy of $\epsilon' = 430$ eV, leads to a minimal contribution to the broadening of the Auger peak. According to Eq. 2.14, the broadening effect is calculated using the minus sign, since $\epsilon' < t_p$. The estimated contribution is only $\frac{\Delta B_\theta^{(2)}}{\epsilon'} \simeq 3{\times}10^{-3}\,\%$. The estimated contribution is approximately two orders of magnitude smaller than the broadening caused by the beam energy width. This highlights the potential of Auger spectroscopy as an accurate method for ion beam diagnostics [16], a topic that will be further discussed in Section 8.

Chapter 3

Experimental Setup

3.1 The 5.5 MV tandem Van de Graaff accelerator facility

The experiments were conducted at the 5.5 MV tandem Van de Graaff accelerator facility [7], located at NCSR "Demokritos" in Athens. It hosts the only ion accelerator operating in Greece (see Fig. 3.1), mainly used for nuclear physics experiments. A CAD (computer-aided design) view of the main accelerator components and beamlines is shown in Fig. 3.2. The low- and high-energy parts of the accelerator are marked with "LE" and "HE", respectively.

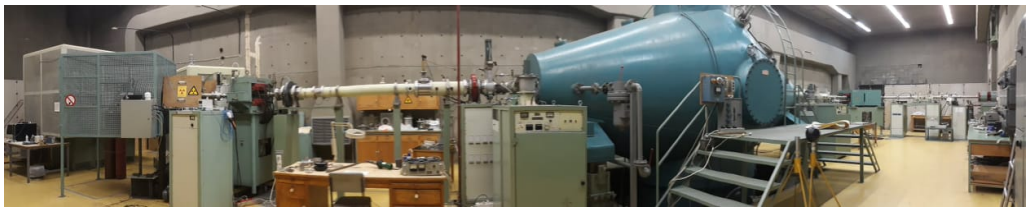

Figure 3.1: Panoramic view of the 5.5 MV tandem Van de Graaff accelerator facility located at NCSR "Demokritos".

Recently the tandem Van de Graaff accelerator was upgraded under the CALIBRA program (Cluster of Accelerator Laboratories for Ion-Beam Research and Applications). The upgrade included, amongst others (see Ref. [7] for details):

- Replacement of the existing belt at the tank's terminal with a triple pelletron chain.
- Installation of a new terminal potential stabilization system (TPS) at the high-voltage terminal.
- Replacement of the stripping system with a new one.
- Replacement of the ion sources with a TORVIS (H^- and He^- injection) and a SNICS II sputter (negative ions including species of higher atomic number) ion source.
- Replacement of the old vacuum system (oil diffusion pumps and controllers) with a new one (turbomolecular pumps).

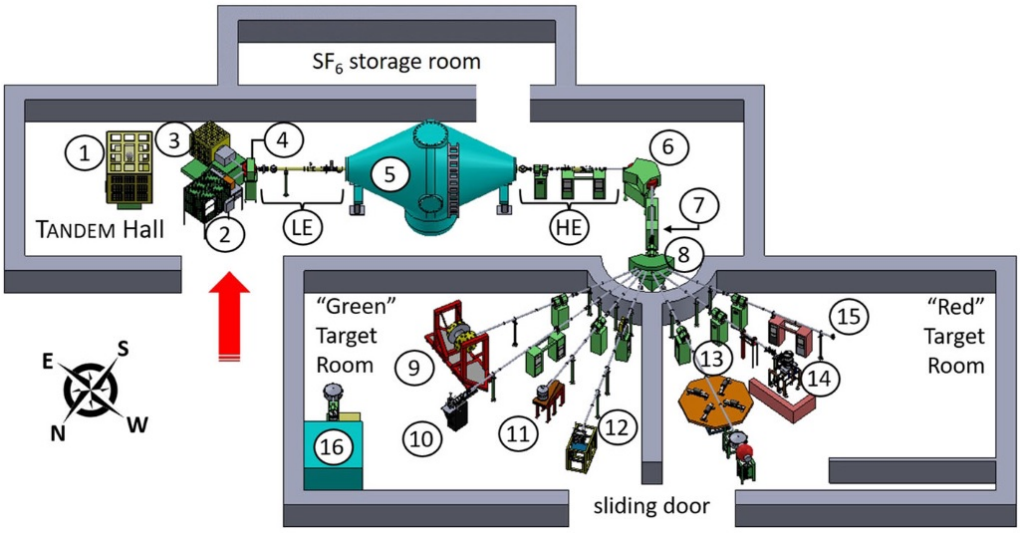

Figure 3.2: CAD view of the TANDEM accelerator facility. (1) Electronics faraday cage. (2) Duoplasmatron ion source. (3) Sputter ion source. (4) 30° inflector magnet. (5) Tank hosting the generator (terminal). (6) 90° Analyzing magnet. (7) Post-stripper. (8) Switching magnet. (9 - 15) Experimental beamlines. (16) PAPAP accelerator. Taken from Ref. [7].

Note that both the old system (mostly) and the upgraded one were used for the experiments of this dissertation.

The number of electrons the projectile caries during the collision process plays a crucial role in atomic collision experiments since it determines the initial/final atomic states and the underlying processes to be studied. The production of charged ions in tandem Van de Graaff accelerators is typically attainable by passing the initially negatively charged ion beam through a gas or thin foil medium, termed *stripper*, located inside the terminal (terminal stripper). Upon collision with the stripping medium, several electrons are removed from the ion, resulting in a distribution of positively charged ions, further boosted in energy in the second stage of acceleration. The kinetic energy of the positively charged ions upon exiting the accelerator terminal is given by

$$E = (q + 1)V \ , \tag{3.1}$$

where q corresponds to the charge state of the ion, and V is the maximum voltage of the accelerator. Depending on the medium, gas or foil, the stripping process is known as gas terminal stripping (GTS) or foil terminal stripping (FTS), respectively.

The charge states obtained from the stripping process follow Gaussian-like distributions, with the maximum value and width depending on factors such as the initial charge state, the stripping energy, and the stripping medium. Higher charge states, located towards the high end of the distribution, can be achieved by applying a second stripping process known as *post-stripping*. This additional process takes place between the analyzing and the switching magnets of the accelerator (see #7 in Fig. 3.2). It results in a new charge state distribution shifted to higher charge state values compared to the initial one, since the stripping occurs at a much higher energy after acceleration of the ion beam. The post-stripping process is then termed as gas post-stripping (GPS) or foil post-stripping (FPS), depending on the medium

used [112].

For experimental design purposes, it is essential to estimate the ion beam current at a specific charge state and energy. Several software packages have been developed based on semiempirical models and approaches to accurately estimate charge state distributions. An example of such software extensively used in this work is the TARDIS program, which is detailed in Appendix B. Ion beam current estimations can be obtained by varying the incoming charge state, the stripping energy, the stripping medium, and the stripping location. These parameters play a crucial role in determining the ion beam current and are valuable for planning and conducting experiments.

3.2 The Atomic Physics Installation

Since the transfer of the ZAPS setup to "Demokritos", a dedicated beamline for atomic physics studies was assigned at the tandem Van de Graaff accelerator facility. The establishment of the ZAPS setup in "Demokritos" initiated the field of atomic physics with accelerators in Greece [10, 76]. The installation received substantial financial support by the Greek Ministry of Education program "Thales", under the APAPES project (Atomic physics with accelerators: Projectile electron spectroscopy), securing its smooth development and operation. Further funding was given via the "CALIBRA" project of the "Large-Scale Research Infrastructure for the Greek Roadmap of Research Infrastructures" program, which substantially helped in the full development of the installation and the financial support of the Master and PhD students involved in the project. Recently, the atomic physics installation has been upgraded to include coincidences techniques for ion-atom and ion-molecule collisions, detailed in Section 3.3, receiving support form the IKYDA 2020 program, which promotes scientific cooperation between Greece and Germany.

The beamline is located at 45° downstream of the switching magnet in the "Red" Target Room (#14 in Fig. 3.2). A picture of the initial installation, encompassing the ZAPS setup, is shown in Fig. 3.3. The main parts of the ZAPS setup are the target gas cell and the hemispherical deflector analyzer (HDA) spectrograph. During the collision process, when the projectile ion beam interacts with the target atoms in the gas cell, electrons are produced either from the target or the projectile. The electrons emitted at zero-degree with respect to the ion beam are focused by the lens at the entry of the HDA, energy analyzed inside the HDA and recorded at the imaging detector. The projectile traverses the spectrometer in a straight line due to its higher energy, ending in a Faraday cup where the beam current is collected and measured for calibration purposes [113, 114].

Below, we present a description of the beamline components, instrumentation, and their operational principles. A detailed guide on the beamtime preparation and the data acquisition process can be found in Appendix C.

3.2.1 The Beamline

The beamline has a comprehensive arrangement designed to facilitate the precise delivery of the ion beam from its entrance point to the final collection at the last Faraday cup (FC2). The sequence begins with the 4-jaw slits, known as the upstream slits, positioned to ensure the appropriate collimation of the ion beam. Following

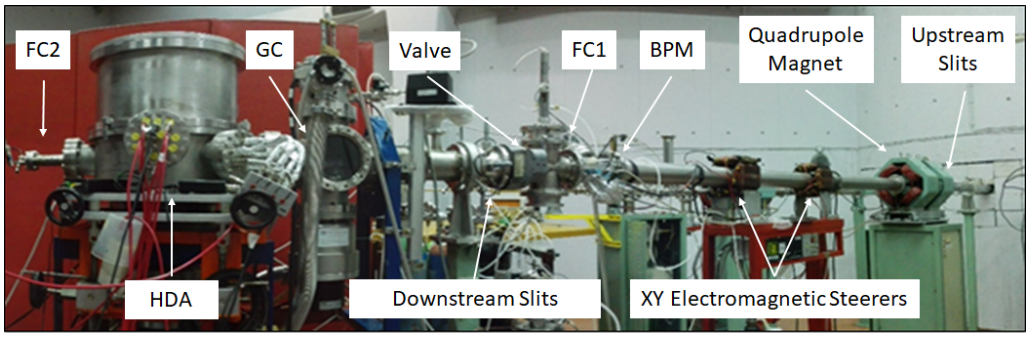

Figure 3.3: The Atomic Physics beamline operating at the tandem Van de Graaff accelerator of "Demokritos".

these slits, a quadrupole magnet is placed to focus the ion beam at the target area. Beyond this, there is a pair of XY electromagnetic steerers, for a fine-tuning of the ion beam trajectory. In front of the gas cell (GC) there is another set of 4-jaw slits, referred to as the downstream slits, which define the ion beam propagation axis and further reduces the beam's cross section to a minimum of 1×1 mm^2. The separation between the upstream and downstream slits is about 4.5 meters. Typical slit sizes used during the experiments are given in Table 3.1.

Table 3.1: Typical slit values. The first and second value correspond to the vertical and the horizontal axes, respectively.

Slit	Dimension (mm^2)
Upstream	4.0-6.0×4.0-8.0
Downstream	1.5-2.5×1.5-2.5

It is worth mentioning that the upstream slits are intentionally set wider than the downstream slits, due to their proximity to the switching magnet. The vertical slit dimension is larger than the horizontal one due to the focusing properties of the switching magnet. The downstream slit sizes are usually marginally smaller than the gas cell apertures to prevent any direct beam impact on the gas cell, thereby minimizing secondary electron production and reducing background signal in the spectra. During setup for optimal ion path, larger slit sizes are employed to maximize the current, while smaller sizes are chosen for use during the actual experiment.

A very helpful instrument of the beamline is the beam profile monitor (BPM), which provides real-time monitoring of the beam's shape and position in both the X and Y coordinates. The setup also includes two Faraday cups, one positioned before the gas cell and the other at the endpoint of the beamline. The Faraday cup upstream (FC1) is used in combination with the BPM for maximizing the beam current and fine-tuning the ion beam path. The downstream Faraday cup (FC2), serves also as a beam diagnostic tool, confirming the passage of the ionic beam through the gas cell, where the collisions take place. The current measured at

FC2 is used for normalization purposes in the data analysis presented below. The ion beam intensities achieved during the measurements were typically in the range between 0.1 to 20 nA on target.

Lastly, an isolation valve is located in front of the gas cell for isolating the HDA and the gas cell from the rest of the beamline. This valve is notably useful during gas cell loading, effectively preventing contamination of the tandem beamline and maintaining optimal vacuum pressures throughout the process.

3.2.2 The Gas Cell

Maintenance of the beamline pressure at low values, even with a fully loaded target gas cell (up to 40 mTorr for H_2), is crucial for safe operation of the spectrograph and for obtaining high-quality, low-background electron spectra. Thus, the gas cell is doubly differentially pumped, to avoid significant gas contamination of the beamline. More specifically, the gas cell consists of two concentric cells: an inner cell, where the gas target is loaded, and an outer cell encompassing the inner one and straightforwardly being connected with an 80 l/s turbomolecular pump as shown in Fig. 3.4. A stainless steel ISO-160 6-way cross hosts the doubly differentially pumped gas cell, which is supported by an XYZ translation stage [112] for alignment purposes. The 6-way cross is pumped by a 500 l/s turbomolecular pump. Specifics on the dimensions of the gas cell are given in Table 3.2.

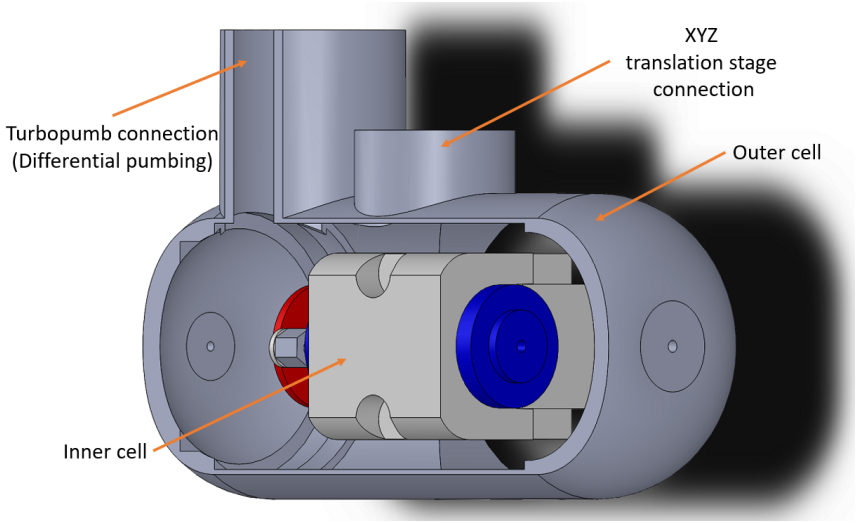

Figure 3.4: CAD view of the doubly differentially pumped gas cell.

The inner cell of the system can be voltage biased. Applying a voltage to the inner cell can be helpful for various tests and troubleshooting since the kinetic energy of the electrons generated inside it can be varied. Thus, the electrons generated outside the gas cell can be distinguished from the electrons originating from the gas cell area [115]. Note that in case of biasing, the gas cell acts as a lens since the outer cell is grounded. Thus, this voltage biasing technique is not appropriate for cross section measurements.

Table 3.2: Specifics of the gas cell system.

Part	Dimension (mm)
Apertures diameter	2.5
Inner cell diameter	25
Outer cell diameter	63
Inner cell length	49.8
Outer cell length	140

3.2.3 The Spectrograph

The spectrograph consists of a paracentric hemispherical deflector analyzer (HDA) equipped with a 4-element focusing/deceleration entry lens as well as a 2-dimensional position sensitive detector (2D-PSD). The 2D-PSD consists of a chevron style multichannel plates (MCP) with a diameter of 40 mm and a resistive anode encoder (RAE) [109, 116]. A schematic view of the HDA is shown in Fig. 3.5.

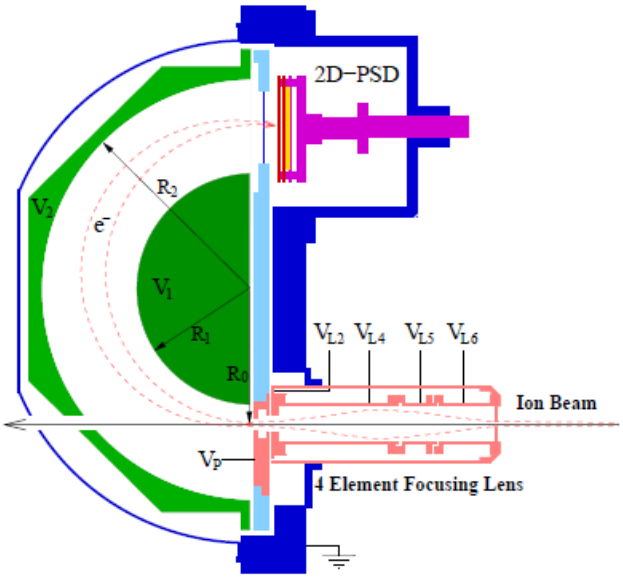

Figure 3.5: Schematic view of the paracentric HDA. Notation of the various voltages, HDA's shell radii, and asymmetric entrance position is included.

The term *paracentric* derives from the fact that the entrance aperture R_0 is optimized to have an offset from the central position $R_0 \neq (R_1 + R_2)/2$, where R_1 and R_2 are the radii of the inner and outer shell of the HDA, respectively. The advantage of this arrangement is the improved electron energy resolution, as opposed to conventional HDAs with central entry [117–120]. The 4-element focusing/deceleration entry lens acts as a virtual slit focusing the incoming electrons at the HDA entry,

thus the term *focusing*, improving the energy resolution. The term *deceleration* comes from the fact that further improvement of the energy resolution is possible, as low as 0.15%, by decelerating the electrons just before entry to the HDA itself. The HDA and the entry lens are made of aluminum and their inner surfaces are soot-coated to reduce secondary electron emission [121]. Also, a μ-metal shield surrounds the whole spectrometer and gas cell chambers, thus isolating the detection area from the earth's magnetic field [122].

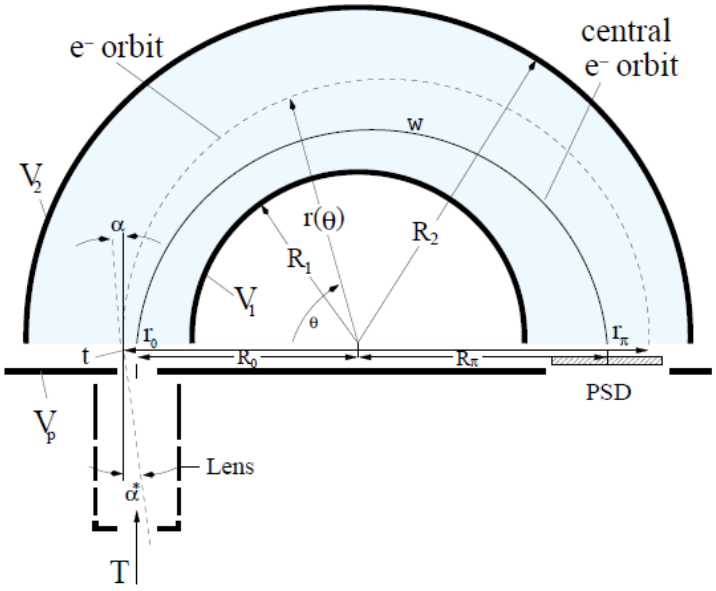

Figure 3.6: Schematic diagram of the paracentric HDA geometry and related notation. Taken from [8].

The HDA has been extensively studied in the literature [109, 116, 118, 123–126]. From the analysis of the general trajectory equation for an ideal HDA, the voltages of the inner and outer hemispheres must satisfy the following equation for a central electron trajectory of energy W [127]:

$$qV_{R_i} = \frac{W}{F}\left\{F - \gamma\left(\frac{R_0}{R_\pi}\right)\left[\frac{R_0 + R_\pi}{R_i} - 1\right]\right\} \ (i = 1, 2) \ , \tag{3.2}$$

where $q = -|e|$ is the electron charge, $F = w/W$ is the *deceleration factor*, W is the *tuning energy* of the HDA, which is equal to the energy of the central electron trajectory, and w is the *pass energy*, which is equal to the energy of the decelerated central electron trajectory. R_0 and R_π are the entry and exit radii, respectively. The parameter γ sets the value of the potential at the paracentric entry, $V(R_0)$, and it is defined as [117, 128]

$$\gamma \equiv 1 - \frac{qV(R_0)}{w} \tag{3.3}$$

The deceleration factor F sets the voltage value of the plate electrode V_p as given by Eq. 3.4.

$$V_p = w - W = W\left(\frac{1}{F} - 1\right) \leq 0 \ . \tag{3.4}$$

The base energy resolution R_B (i.e., 2× FWHM), for the ideal HDA is determined by the following formula:

$$R_B \equiv \frac{\Delta E_B}{w} = \frac{\Delta r_0 + \Delta r_\pi}{D_\gamma} + \alpha_{max}^{*2} \, . \tag{3.5}$$

The parameter α_{max}^{*2} is the maximum angle of incidence at the HDA entry. The parameter Δr_0 is the diameter of the HDA entry aperture. The diameter of the HDA entry is 6 mm, however, in experimental conditions it is smaller (virtual aperture) due the focusing of the lens of the spectrograph. The parameter Δr_π corresponds to the exit slit of the HDA, which in our case corresponds to the spatial resolution of the 2D-PSD, which is about 0.4 mm. The dispersion length, D_γ, for the HDA is determined as

$$D_\gamma = \left(\frac{R_\pi + R_0}{\gamma} \right) \frac{R_\pi}{R_0} \, . \tag{3.6}$$

In high-resolution applications, deceleration is commonly employed to enhance the energy resolution of the HDA by slowing down the electron beam prior to its entry into the HDA. In this case, the overall base resolution $\mathfrak{R}_B$, which is the actual experimental resolution, is given as [116]:

$$\mathfrak{R}_B \equiv \frac{\Delta E_B}{W} = \frac{1}{F} \left(\frac{\Delta E_B}{w} \right) = \frac{1}{F} \times R_B \, . \tag{3.7}$$

The energy window of the analyzer is the energy range that can be simultaneously detected on the active area of the 2D-PSD. For spectrometers that use exit slit, the energy acceptance window corresponds to the base energy width [116]. However, for PSD-equipped spectrographs with an effective diameter d_{PSD}, the energy acceptance window, denoted as ΔT_{window}, is defined as [8]:

$$\Delta T_{window} = \frac{\gamma}{1+\xi} \frac{d_{DSP}}{R_\pi} \frac{W}{F} \, , \tag{3.8}$$

with $\xi = R_\pi / R_0$ being the HDA paracentricity.

The energy acceptance window, ΔT_{window}, exhibits an inverse proportionality with the deceleration factor F. When $F = 1$, i.e., undecelerated electron beam, the estimated energy acceptance window of our HDA spectrograph is approximately $W \pm$ 15%. As the deceleration factor F increases, this percentage decreases accordingly, as indicated by Eq. 3.8.

A critical aspect for high resolution spectra is finding the optimum lens voltages. For our spectrograph, extended electron trajectory simulations using the SIMION ion optics package [8, 127, 129, 130], as well as experimental studies [8, 9] have been employed to determine the optimum voltage values for the lens elements V_{L4} and V_{L5}. In Figs. 3.7 and 3.8 the lens voltages adopted in the experiments of this thesis are presented for $F = 1$ and $F = 4$, i.e., for low and high resolution measurements, respectively.

3.2.4 The 2D-PSD Imaging Detector

The HDA is equipped with a 2-dimensional PSD [131], consisting of a pair of microchannel plates (MCP) of 40 mm diameter in a chevron-style arrangement, acting

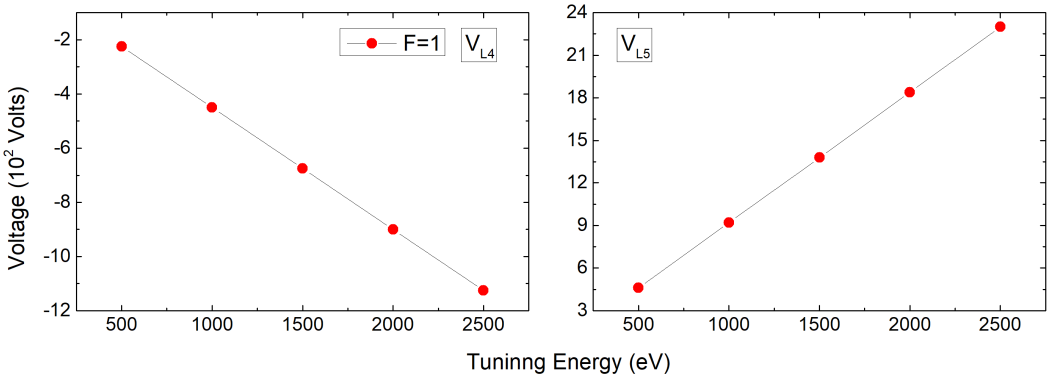

Figure 3.7: Lens voltages for F=1.

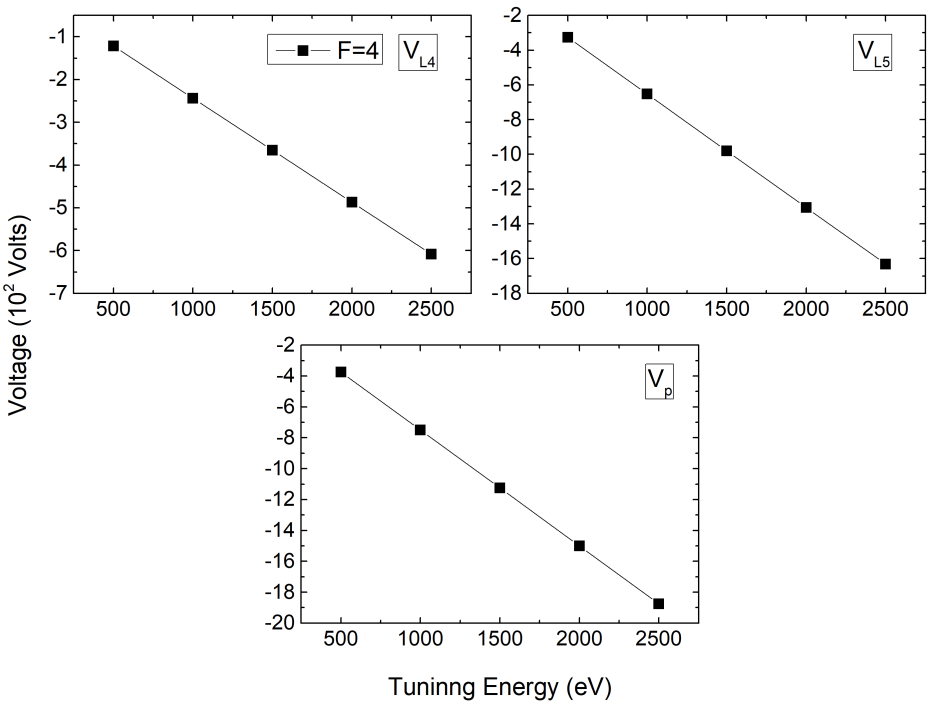

Figure 3.8: Lens voltages for F=4.

as electron multipliers. After the MCPs, there is a resistive anode encoder (RAE), which collects the events while encoding each location by distributing it to four outputs.

The MCP is a specially fabricated plate consisting of multiple micro-channels [1], set at $8° \pm 1°$ from the surface normal. When a single incident particle (electron in our case) enters a micro-channel, impact with the channel's walls causes the production of secondary electrons. An electric field developed by a voltage applied to the MCP plate accelerates these electrons until they strike again to the walls, thus producing even more secondary electrons. This process is repeated several times along the channel, leading to a cascade effect (see Fig. 3.9).

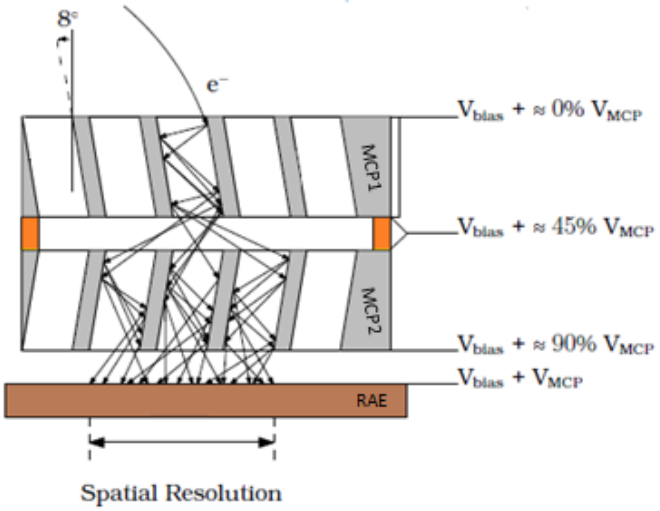

Figure 3.9: Schematic view of the PSD, showing the MCP's chevron-style arrangement. The illustration includes the cascade effect triggered from a charged particle incident onto a micro-channel. Voltages applied are also indicated.

Secondary electron production relies on the overall V_{MCP}. This voltage is divided into three fractions, as illustrated in Fig. 3.11. The first two fractions are equal, accounting for approximately 45% of the overall V_{MCP}, and they control the gain of the MCPs. The remaining 10% of the overall V_{MCP} is utilized as an extraction voltage to collect secondary electrons on the RAE surface. The optimal value for V_{MCP} depends on the MCPs' output and their condition. It is important to note that higher V_{MCP} values can lead to quicker degradation of the MCPs. Previous studies for our system have indicated that the optimum V_{MCP} value is +2050 Volts [9]. It should be mentioned that in addition to the V_{MCP} voltage, there is also the V_{bias}, which is applied to the MCP entry to ensure a constant impact energy of the electrons, and thus maintain a consistent MCP efficiency, necessary for our measurements.

The four signals produced from the PSD are decoupled, by 1 nF capacitors each, giving rise to small negative pulses ($\simeq$1 mV). Then, these pulses go to a DSP (Digital Signal Processor) unit, where they are digitized by an Analogue to Digital Converter (ADC) after passing first from a preamplifier, as shown in Fig. 3.11. There, the position of each event is decoded, according to Eq. 3.9. Thus, a two-dimensional

[1] very-small diameter (25 μm) glass capillaries

image is constructed, encoding the information of the electron position detection. The XY discretization of the 2D array was set to 256×256.

$$X = \frac{X_1 + Y_1}{X_1 + Y_1 + X_2 + Y_2}$$
$$Y = \frac{X_2 + Y_1}{X_1 + Y_1 + X_2 + Y_2} \tag{3.9}$$

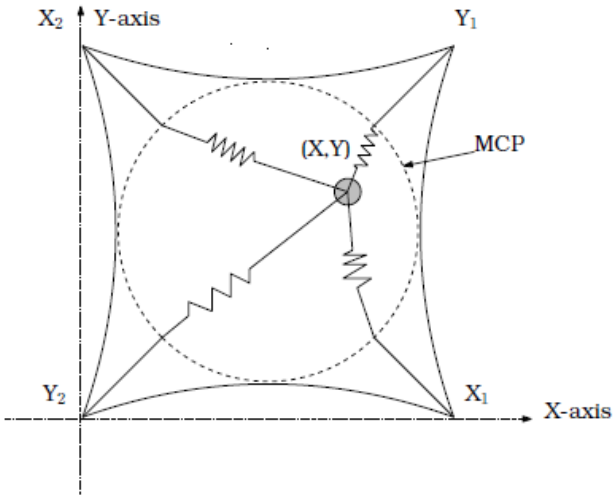

Figure 3.10: Diagram of the RAE. The signals originating from the four corners of the RAE are converted into XY coordinates through Eq. 3.9. Taken from [9].

3.2.5 Electronics

The electronics used for the setup are those controlling the voltages of the spectrograph and those controlling the data acquisition system (DAQ). The complete electronics arrangement is presented in Fig. 3.11 [10].

The high voltage power supplies (HVPS) used were the following types:

1. HMI: The HMI HVPSs, provided by the Hahn-Meitner-Institut [132], offer high precision with fixed predefined polarity and exhibit the lowest ripple, even at higher voltages, making them ideal for sensitive measurements.

2. Tennelec: The Tennelec HVPSs [133] are capable of inverting their polarity, but they require shutting down before any polarity change. While they may not match the precision of HMI HVPS, they still offer sufficient stability for high-resolution spectroscopy. These HVPS were connected to electrodes that rarely require polarity changes.

3. Applied Kilovolts: The Applied KiloVolts HVPSs [134, 135] have the ability to digitally reverse their polarity, but this comes at the cost of 1 bit, reducing their internal DAC's resolution to 15 bits.

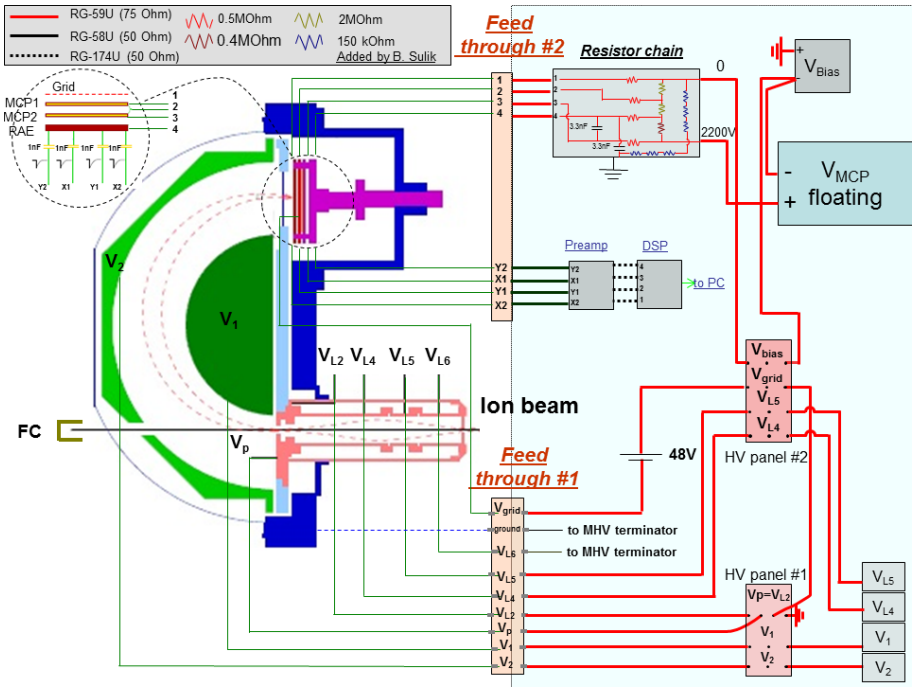

Figure 3.11: Schematic view of the electronics of the setup (from Ref. [10]).

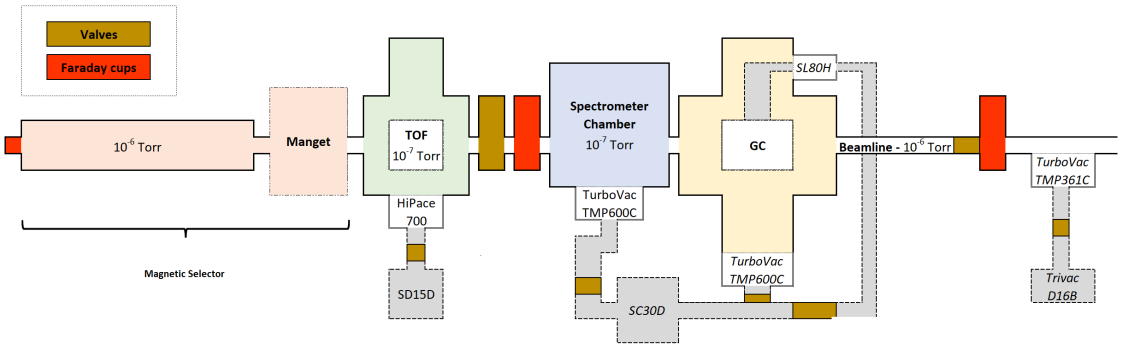

Figure 3.12: Schematic of the vacuum manifold of the atomic physics beamline. Typical pressures during gas cell operation are indicated.

3.2.6 Vacuum

In Fig. 3.12 we present a schematic of the vacuum manifold of the atomic physics beamline. Starting from the upstream point of the beamline, there is a turbomolecular pump (360 l/s) maintaining a vacuum pressure of 10^{-6} Torr. The gas cell 6-way cross and the HDA chamber are equipped with a turbomolecular pump each (600 l/s). The gas cell is doubly differentially pumped through a turbo molecular pump (80 l/s). This pumping scheme enables a maximum vacuum pressure of 10^{-6} Torr for the HDA chamber during gas operation. Furthermore, a turbomolecular pump (700 l/s) has been installed in the cross where the time-of-flight (TOF) spectrometer is hosted. The extension of the beamline setup (see Section 3.3) can be isolated through a valve. Thus, the ZAPS setup can operate independently. A typical vacuum pressure in the extension of the setup is 10^{-6} Torr. The gas cell and the spectrometer chamber turbomolecular pumps are backed by the same oil-free mechanical pump, as shown in Fig. 3.12. Similarly, the turbomolecular pump of the extended beamline is also backed by a second oil-free mechanical pump. Technical details about all the pumps used are given in Table 3.3.

Table 3.3: Details on the vacuum components used.

Position	Turbomolecular pump	Mechanical fore-pump
Beamline	TurboVac TMP361C [136]	Trivac D16B [137]
Gas cell's 6-way cross	TurboVac TMP600C [136]	
Gas cell	SL80H [139]	SC30D [138]
Spectrometer chamber	TurboVac TMP600C	
TOF's 6-way cross	HiPace 700 [140]	SC15D [138]

3.3 Upgrade of the Atomic Physics Installation

Recently the Atomic Physics installation has been upgraded to include the option of performing coincidence measurements. This project was supported by the IKYDA 2020 program, a program for the promotion of the exchange and scientific cooperation between Greece and Germany, and was focused around two main objectives: the development of (i) a TOF spectrometer and (ii) a projectile charge state magnetic selector. Also, the hardware electronics, and the DAQ software, have been upgraded, enabling electron-ion and ion-ion coincidence experiments. The upgraded Atomic Physics beamline is presented in Fig. 3.13. Details about the upgrade are discussed in the following subsections (see also Ref. [141]).

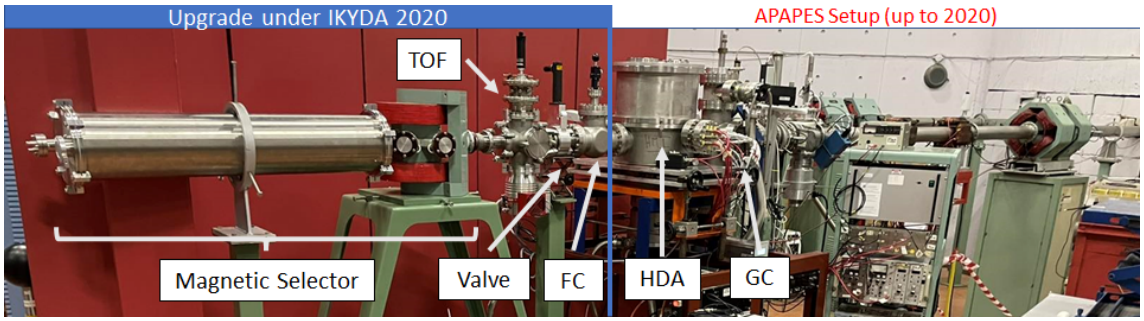

Figure 3.13: The upgraded Atomic Physics beamline of NCSR "Demokritos".

3.3.1 TOF spectrometer

The measurement of the time-of-flight of fragments is widely used in Atomic, Molecular and Optical Physics, mainly for measuring particle masses and energies of various processes such as ionization and molecular dissociation. Time-of-flight technique is also used in other sciences, i.e., in Biology and Chemistry, in applications such as the detection and characterization of chemical compositions, as well as the analysis of solid, liquid and even gaseous substances.

Here, we present the TOF spectrometer developed and installed in the Atomic Physics beamline, based on the typical arrangement of potential disks in series. In particular, the TOF spectrometer consisting of three metal discs separated by 2 cm distance each, namely the repeller, the extractor and the ground, is hosted in an ISO 100 6-way cross (see Fig. 3.14), which has been installed between the HDA spectrograph chamber and the charge-state selector. The TOF spectrometer is equipped with a gas jet target, a drift tube with an MCP detector on its one end for fragments detection, and a channeltron on the other side for electron detection, used as the start signal of the measurement. It should be noted that the optimal operation conditions of the TOF spectrometer have been studied using Monte Carlo simulations realized within the SIMION ion optics package.

3.3.2 Charge State Magnetic Selector

Our primary goal was to install a charge-state selector for distinguishing the projectile ion trajectories corresponding to different charge states. The required magnet for applying the necessary field (up to 0.5 T), was donated to the Atomic Physics group by the INPP institute of NCSR “Demokritos”. The corresponding magnet was part of a now decommissioned electron accelerator, and it can provide the required magnetic fields when driven by high current supplies and water cooling.

We studied the behavior of beam ion trajectories in homogeneous magnetic fields by performing analytical calculations. In parallel, these calculations were cross-checked with corresponding simulations using the SIMION ion optics package [142]. The results were used to determine the most suitable geometry and experimental parameters for the magnetic ion beam charge selector. As a result of these studies, we decided to place the magnet half a meter after the HDA chamber, to secure safe operation of the electron spectrometer without being affected by the fields of the magnet. After the magnet, an ISO-200 tube of 1 m length was installed off-centered, giving enough space for the projectile ion to bend (see Fig. 3.15) and be detected by the channeltron detector. It should be mentioned that the whole design allows

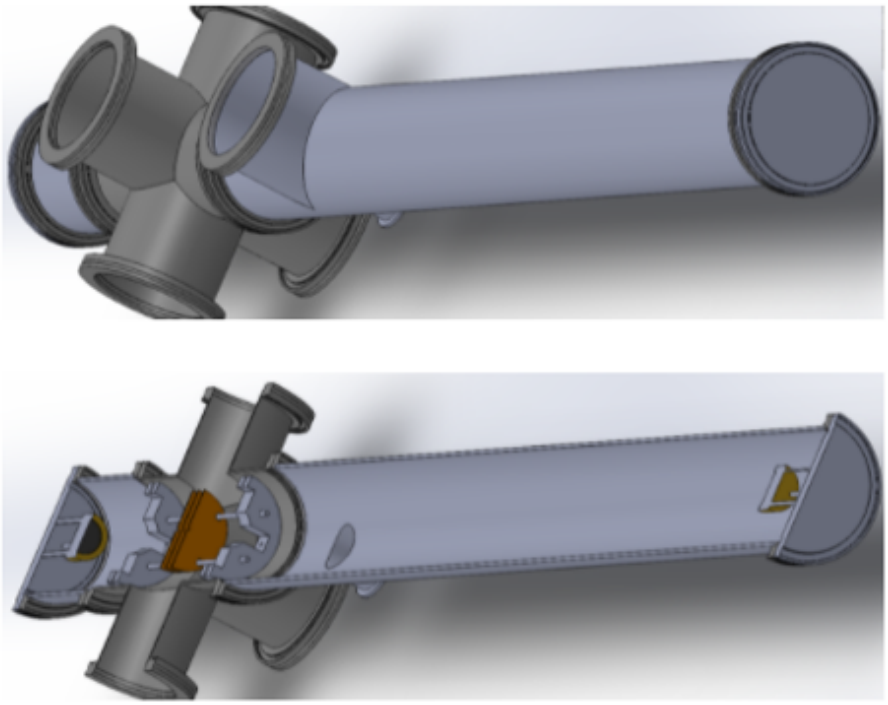

Figure 3.14: CAD drawing of the TOF spectrometer: [Top] Complete TOF arrangement; [Bottom] Horizontal cut, illustrating the three metal disks, their base, and the positions of the MCP and the Channeltron.

for the different charge states to be sufficiently separated at the end of the tube.

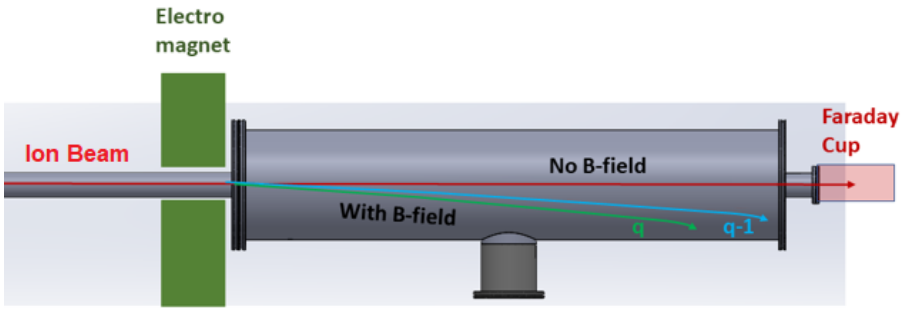

Figure 3.15: Drawing of the charge state magnetic selector. The ion trajectories are illustrated both with and without the magnet in operation.

3.3.3 Electronics and Data Acquisition System

The DSP unit, obtained from ATOMKI [143], has been also upgraded. An additional input was incorporated in the DSP which receives a TTL (Transistor-Transistor-Logic) signal from the channeltron source. This signal is used in an event mode acquisition to determine the zero time for ion-electron coincidences.

Chapter 4

Data Analysis

This chapter focuses on the analysis of the recorded data, which is essential for deriving the absolute double differential cross sections (DDCS). The analysis involves converting the measured electron spectra into single differential cross sections (SDCS) or total cross sections (TCS), depending on the specific requirements. The raw data obtained are the electron counts as a function of the channel number.

4.1 Raw Data

Raw data is the starting point for any analysis, forming the base on which all conclusions are built. It's crucial to closely examine the raw data throughout the analysis process, repeatedly reviewing it to ensure the accuracy of the findings. Here, we present a representative example that showcases the raw data spectrum in its original form, as recorded during a measurement. Specifically, Fig. 4.1 shows a typical 2D spectrum capturing the cusp electron peak observed in collisions of 1.5 MeV protons with Ne. The plot corresponds to the PSD image as it is recorded during the experiment. The spectrum includes projections along the x and y axes, providing valuable insights. The x-axis projection corresponds to the electron energy, while the y-axis projection offers an assessment of the overall quality of focusing conditions of the spectrometer.

4.2 Energy Calibration

In order to convert a spectrum recorded as a function of channel number into electron energy, an energy calibration process is required. This calibration process involves detecting electrons of known energies under the same experimental conditions as the measurement under study. There are two approaches to record electrons of well-known energies, i.e., using an electron-gun or utilizing well-known Auger lines produced by ion-atom collisions.

An electron-gun offers flexibility in providing electrons at various kinetic energies, controlled by its negative bias voltage with an accuracy of approximately 0.1%. While this method allows for precise energy calibration by recording multiple electrons at desired tuning energies, it can be time-consuming. Alternatively, well-known energies of recorded KLL Auger lines are used for energy calibration.

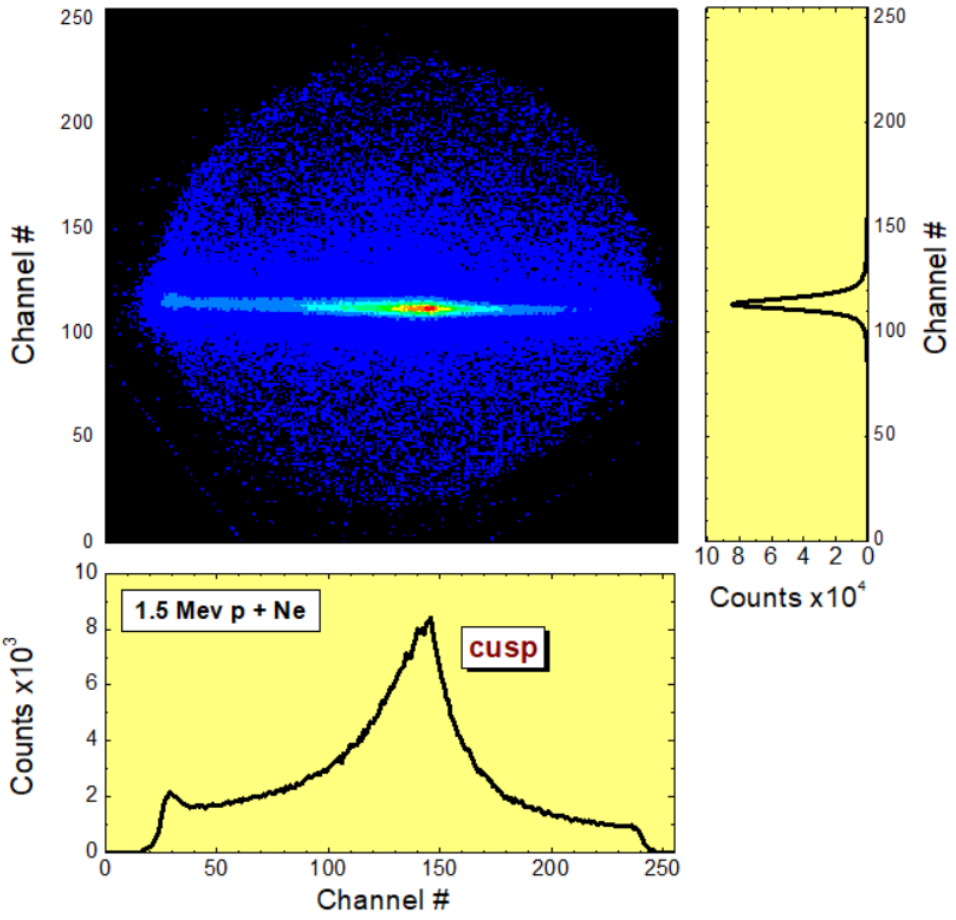

Figure 4.1: The 2D-PSD image showing the raw data recorded during the experiment. The spectrum showcases the cusp electron peak observed in collisions of 1.5 MeV protons with Ne. Accompanying the PSD image are the x (bottom) and y (right) projections, quantifying the information of the recorded data.

Although the measured electrons are emitted from a moving projectile and their detection energies depend on the projectile energy, which has an uncertainty of around 0.1%, this uncertainty leads to an acceptable uncertainty in the electron laboratory energy of less than 1 eV. It should be mentioned that auxiliary cusp electron measurements are performed to ensure that the nominal beam energy corresponds to the correct value, since the cusp peak energy is equal to the reduced energy of the ion beam t_p, already defined in Eq. 2.3 [144].

The energy calibration procedure involves a quadratic function, as in Eq. 4.1, that maps channel numbers to corresponding lab frame electron energies. The first step is to convert the known Auger energies (see for example typical Auger energies used in this thesis given in Table 4.1), from the rest frame to the lab frame. This is achieved by utilizing the reduced projectile energy, t_p, and Eqs. 2.7, 2.8 to calculate the expected laboratory energies. The center channel for each Auger calibration peak in the lab frame is measured directly from the raw data spectrum. The next step involves finding the optimal calibration constants (a, b, c) by applying the least squares fit method. It is important to emphasize that a minimum of three well-known Auger energy lines are required for the application of this method, due to the quadratic function of Eq. 4.1.

$$T(i) = a + b \cdot i + c \cdot i^2 \tag{4.1}$$

Table 4.1: KLL Auger lines of B^{2+}, C^{3+}, and O^{5+}, used for energy calibration.

	Auger Energy (eV)		
Auger line	B^{2+}[a]	C^{3+}[b]	O^{5+}[c]
$1s2s^2\ ^2S$	155.1	227.23	412.63
$1s2s2p\ ^4P$	157.0	229.64	416.02
$1s2s2p\ ^2P_-$	161.4	235.55	424.99
$1s2s2p\ ^2P_+$	164.3	238.86	429.71
$1s2p^2\ ^2D$	166.5	242.15	434.38

[a] Taken from Ref. [145]
[b] Taken from Ref. [146]
[c] Taken from Ref. [147]

Fig. 4.2 exemplifies the energy calibration process using Ne-KLL Auger lines, which originates from the target. In this case, the energies of the Ne-KLL Auger lines are in the laboratory frame. The depicted spectrum corresponds to collisions of 3.0 MeV p + Ne. The Ne-KLL Auger electron energies employed for calibration were taken from Ref. [11].

Certain spectral regions may contain fewer than three known Auger lines, and thus the aforementioned method for energy calibration cannot be applied. However, by repeating the energy calibration process for various Auger lines, elements, beam

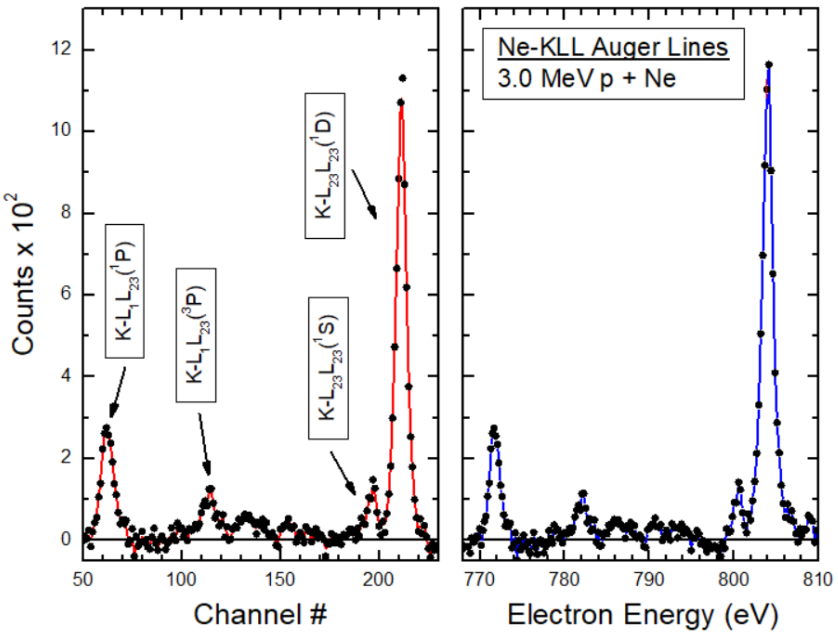

Figure 4.2: Neon-KLL Auger lines recorded for the collision of 3.0 MeV p + Ne. The image shows the energy calibration process, depicting the conversion of channel numbers (left) to electron energies (right). The Ne-KLL Auger electron energies utilized in this calibration were taken from Ref. [11].

energies, tuning energies W, and deceleration factors F, it is still feasible to calibrate any electron spectrum by determining the universal calibration factors A, B, C. Specifically, the initial calibration constants a, b, c can be transformed into their universal counterparts A, B, C through the following equations [8]:

$$A = \frac{a}{W}F - F + 1 \,, \tag{4.2}$$

$$B = \frac{b}{W}F \,, \tag{4.3}$$

$$C = \frac{c}{W}F \,. \tag{4.4}$$

Then, the calibration formula 4.1 results in:

$$T(i) = \frac{W}{F}\left[(A + F - 1) + Bi + Ci^2\right] \tag{4.5}$$

Fig. 4.3 shows the variation of the factors A, B, C for different tuning energies W, ranging from 1300 eV to 2500 eV, with a fixed deceleration factor $F = 4$. The plot includes not only the mean values determined in this study but also the mean values determined by I. Madesis [9] and E.P. Benis [8], who utilized the same experimental setup for their studies. The individual measurements demonstrate that A, B, C exhibit a predominantly linear dependence over the energy range. Consequently, by obtaining a diverse set of tuning energies W, the mean values of the universal calibration factors can be reliably determined and employed for the calibration of any spectrum. The mean values and corresponding uncertainties derived from this study are presented in Table 4.2.

The calibration factor values obtained in this study show a very good agreement with those determined in previous works. However, the mean values reported by I.

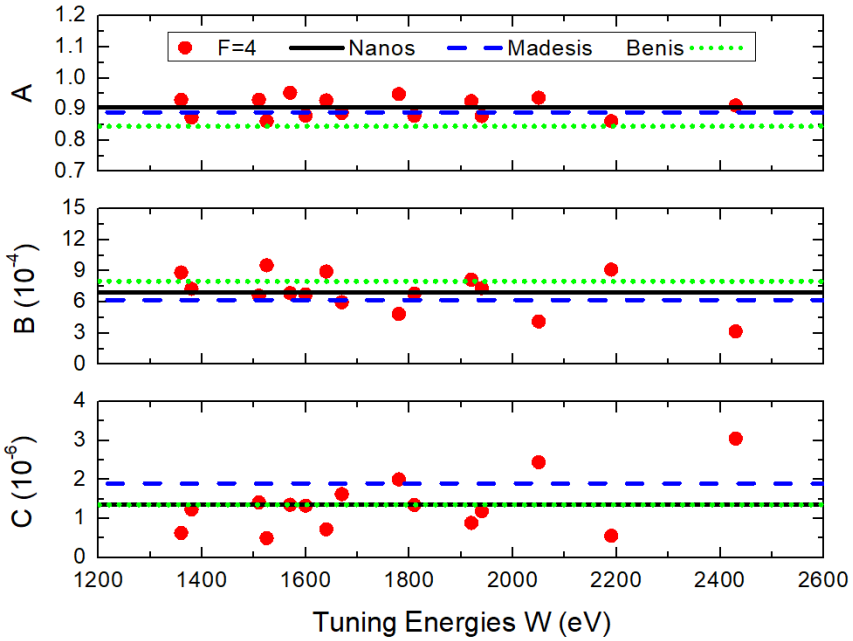

Figure 4.3: Plot of the universal factors A (up), B (middle), C (bottom) as a function of the tuning energy W, for a fixed deceleration factor $F = 4$. [Red dots] Experimental data determined in this work; [Black solid line] Mean values of the experimental data; [Blue dashed line] Mean values retrieved from [9]; [Green dotted line] Mean values retrieved from [8].

Table 4.2: Mean values and uncertainties of the A, B, C universal calibration factors, for a fixed deceleration factor $F = 4$. Numbers in parenthesis indicate powers of 10.

A	σ_A	B	σ_B	C	σ_C
0.905	0.8(-2)	6.96(-4)	0.48(-4)	1.35(-6)	0.18(-6)
0.890	0.69(-2)	6.2(-4)	0.61(-4)	1.9(-6)	0.24(-6)
0.845	0.2(-2)	8.00(-4)	0.17(-4)	1.35(-6)	0.06(-6)

First row: This work
Second row: Taken from Ref. [9]
Third row: Taken from Ref. [8]

Madesis were derived from a limited number of measurements, resulting in a relatively larger uncertainty. On the other hand, E.P. Benis conducted a comprehensive set of measurements utilizing an electron-gun, but it is noteworthy that these measurements were carried out when the setup was installed at the J.R. Macdonald laboratory at Kansas State University. Therefore, minor discrepancies between the calibration factors determined in this work and those reported by E.P. Benis can be attributed to the specific conditions and setup configurations during the respective experiments.

In Fig. 4.4 we show the energy calibration curves, which exhibit variations depending on the chosen universal calibration factors A, B, and C from different studies. The constant term (A) primarily affects the vertical position of the curve without altering its shape. Similarly, the linear term coefficient (B) maintains the curve's shape while introducing both vertical and horizontal shifts. The quadratic term coefficient (C) influences the slope of the curve.

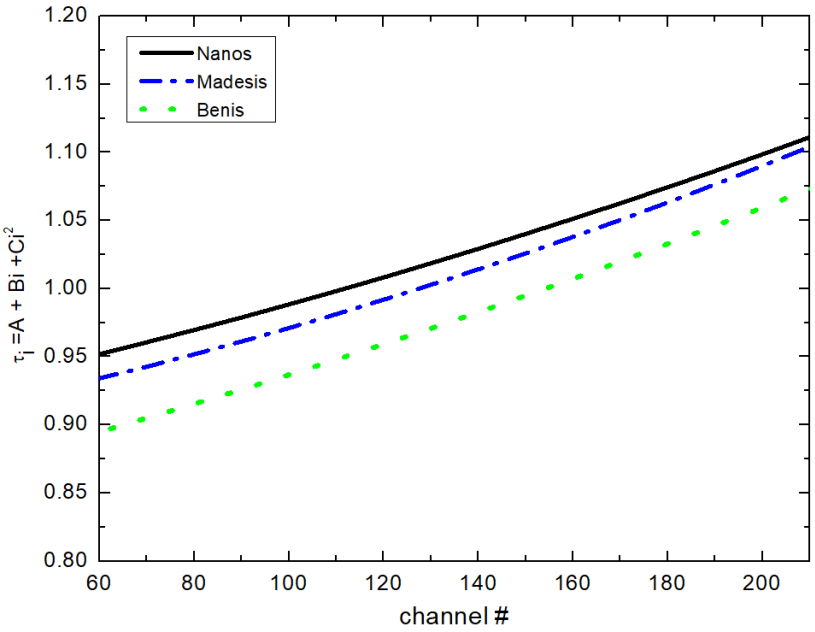

Figure 4.4: Plot of the universal calibration curves corresponding to the mean values of the universal calibration factors A, B, C from different studies. [Black solid line] Mean values determined from this work; [Blue dashed line] Mean values retrieved from [9]; [Green dotted line] Mean values retrieved from [8].

Notably, all three energy calibration curves in Fig. 4.4 exhibit a similar slope and are only vertically shifted within the range of interest (channels 60-210). This indicates that all three sets of universal calibration factors can be used to calibrate an energy spectrum, preserving the shape of the recorded peaks. However, a small energy shift may be experienced. Consequently, any set of universal calibration factors can be employed for energy calibration, with the requirement of having at least one known energy line in the spectrum to facilitate potential re-calibration and account for any slight energy shifts. Alternatively, in cases where a continuum electron spectrum is recorded, a reliable indication for the validity of the calibration process can be observed through the extent of overlapping between neighboring spectra. This serves as a useful criterion to assess the accuracy of the calibration, the details of which will be extensively discussed in Section 5.3.

4.3 The Double Differential Cross Section Formula

After completing the energy calibration process, the electron counts undergo a conversion to DDCS. This section elucidates the normalization required for transforming the measured electron spectra into laboratory DDCS. The laboratory DDCS is represented by the equation [8]:

$$DDCS_i \equiv \frac{d^2\sigma}{d\Omega dE_i} = \frac{N_{e_i}}{N_I\, L_c\, n\, \Delta\Omega\, \Delta E_i\, T\, \eta} \tag{4.6}$$

DDCS refers to a measure that characterizes the cross section for a specific collision process, taking into account both energy and solid angle. The index i in Eq. 4.6 corresponds to the channel number of the PSD x-projection.

It should be mentioned that Eq. 4.6 does not include a dead time correction (DTC) factor. The DTC factor is the ratio of the total counts recorded by a scaler to the total counts recorded by the ADC. It serves as an average correction when the count rate exceeds the capability of the DAQ. However, in our experiments, the recording frequency remains significantly below the maximum accepted frequency of our electronics, which is approximately 100 kHz. Therefore, there is no saturation of the recorded signal, and a relevant correction is not necessary.

Next, the symbols of Eq. 4.6 are detailed.

4.3.1 Number of Electrons Recorded in Channel i

N_{e_i} is the number of electron counts recorded at a specific channel i during the measurement. The process of electron counting involves random events that follow the Poisson distribution. Therefore, this parameter is accompanied by statistical uncertainty which is given by:

$$\delta N_{e_i} = \sqrt{N_{e_i}} \tag{4.7}$$

4.3.2 Number of Ions

The value of N_I is the number of ions collected at the last Faraday cup along the beamline during the measurement. It is determined by calculating the total collected charge Q and dividing it by the ion beam charge q, according to the following equation:

$$N_I = \frac{Q(nC)}{q\, 1.6 \times 10^{-10}}\ . \tag{4.8}$$

The total charge Q can be determined using the following formula:

$$Q(nC) = \frac{Q_{cnt} I_{FS}(nA)}{C_{nts}}\ , \tag{4.9}$$

where Q_{cnt} is the number of counts collected during a measurement and corresponds to the pulses generated by the Beam Current Integrator (BCI) fed to the DAQ. The value of Q_{cnt} determines the duration of the data acquisition, as the measurement process is concluded when a predetermined number of pulses is reached. I_{FS} denotes the maximum or full scale of the BCI, typically measured in nA. Additionally, C_{nts}

signifies the pulse rate generated by the BCI per second when the current integrator operates at its maximum reading for a certain scale. For the BCI used in all the conducted measurements thus far, this value remains fixed at 100 Hz.

The determination of N_I relies on the assumption that the beam current remains unaffected by collisions in the target. Soft and binary encounter electrons do not alter the charge of the projectile and, therefore, do not affect the beam current. However, the projectile electron loss processes increase the beam charge, while projectile electron capture processes decreases it. A rough estimation of beam charge variation can be made by considering an ion beam current, I_0, passing through a gas target of density n. In this scenario, the beam current, I, resulting from a path length, L, is given by

$$I = I_0 \sigma n L \ , \tag{4.10}$$

where σ is total cross section. Assuming a gas cell length of $L = 5$ cm, a typical target pressure of 20 mTorr, which corresponds to approximately 6×10^{14} molecules/cm^3, and a typical total cross section of 10^{-16} cm^2, we find that $I/I_0 = \delta N_I = 30\%$. Consequently, the beam current percentage variation amounts to $30/Z_p\%$, where Z_p denotes the initial beam charge. Assuming an average value of $Z_p = 6$, the uncertainty in the beam current and therefore in the number N_I is:

$$\frac{\delta N_I}{N_I} \leq 5\% \tag{4.11}$$

4.3.3 Effective Length of the Gas Cell

In general, for a gas cell with a length L_{gc} and aperture openings of diameter D_1 (entrance) and D_2 (exit), the effective length is calculated as

$$L_c = L_{gc} + \frac{D_1 + D_2}{2} \ . \tag{4.12}$$

In our case, where $D_1 = D_2 = 0.25$ cm, the effective length of the gas cell is determined to be $L_c = 5.25$ cm. The average of the entrance and exit aperture sizes can be considered as the uncertainty in the length determination, resulting in an uncertainty to the effective gas cell length of 5%, i.e.:

$$\frac{\delta L_c}{L} = 5\% \ . \tag{4.13}$$

4.3.4 Number of molecules per cm^3

Considering the gas pressures employed in these experiments, which were up to 80 mTorr, it is an accurate approximation to treat the gas target as an ideal gas. This ideal gas behavior can be described using the ideal gas law equation:

$$PV = \frac{N}{N_A} RT \ , \tag{4.14}$$

where P is the gas pressure, V is the volume, N denotes the number of molecules, $N_A = 6.022 \times 10^{23}$ mol^{-1} is the Avogadro number, R is the gas constant, and T is the temperature.

We first calculate the value of R under standard temperature and pressure (STP) conditions (see Table 4.3):

$$R = 1.0355^{-19}\ \frac{mol^{-1}\ mTorr\ L}{\#\,molecules\ K}\ . \tag{4.15}$$

Using the state equation once again, the gas density n can be expressed as a function of the gas pressure P at room temperature, $T = 300$ K, as follows:

$$\frac{N}{V} \equiv n\left(\frac{\#\ molecules}{cm^3}\right) = 3.22 \times 10^{13} P(mTorr)\ . \tag{4.16}$$

Table 4.3: Standard pressure and temperature (STP) conditions.

P	T	$V\ \left(n = \frac{V}{V_m}\right)$
1 atm $= 76 \times 10^4$ mTorr	273 K	22.4 L $= 22.4 \times 10^3$ cm^3

The molar volume V_m is 22.4 L/mol at STP conditions, thus V=22.4 L for n=1 mol.

The pressure P in Eq. 4.16 corresponds to the target gas pressure, which is measured using the MKS Baratron capacitive manometer. According to the manufacturer's specifications [148–151], the uncertainty of the pressure indication is less than 0.2%. Therefore, the uncertainty on the number of molecules per cm^3 is

$$\frac{\delta n}{n} \leq 0.2\%\ . \tag{4.17}$$

Before conducting the measurement, it is important to verify the assumption of single collision conditions by comparing the recorded yields at various target pressures. In Fig. 4.5, we show the yields of KLL Auger electrons obtained in collisions of 5.5 MeV B^{3+}+ He, and recorded at different target pressures. These yields have been normalized with respect to the target pressure and the number of ions, clearly showing a linear pressure dependence up to 80 mTorr for the specific spectrum. This linear relation indicates that single collision conditions are maintained within this range.

4.3.5 Solid Angle

The solid angle for point source emission can be calculated by considering the diameter of lens entry aperture, $d_{LE} = 4$ mm, and the distance between the lens entry and the center of the gas cell, $s_0 = 289.48$ mm. The solid angle in this configuration, as depicted in Fig. 4.6, can be determined using the following equation:

$$\Delta\Omega(s_0) = 2\pi(1 - \cos\theta) = 2\pi\left(1 - \frac{s_0}{\sqrt{\left(\frac{d_{LE}}{2}\right)^2 + s_0^2}}\right) = 1.50 \times 10^{-4}\ sr\ . \tag{4.18}$$

To accurately account for the decay of electrons emitted from prompt states, it is necessary to consider that they decay not only from the center of the gas cell but

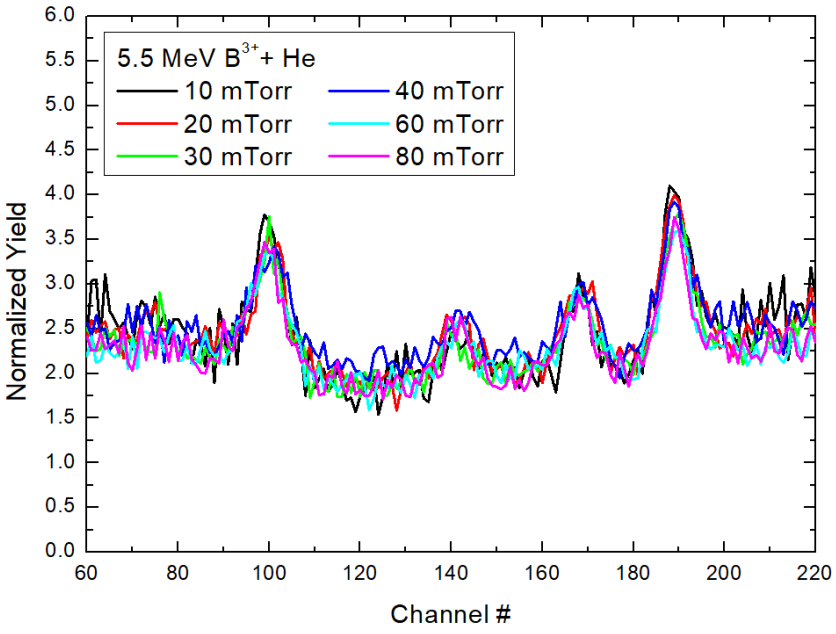

Figure 4.5: Typical pressure dependence study performed for collisions of 5.5 MeV B^{3+} + He.

from the entire gas cell area. Therefore, Eq. 4.18 needs to be integrated over the length of the gas cell ($L_c = 52.50$ mm) using the following form:

$$\Delta\Omega(s_0, L_c) = \frac{2\pi}{L_c} \int_{s_0-\frac{L_c}{2}}^{s_0+\frac{L_c}{2}} \left[1 - \frac{s}{\sqrt{\left(\frac{d_{LE}}{2}\right)^2 + s^2}} ds \right] = 1.51 \times 10^{-4}\ sr\ . \tag{4.19}$$

The difference is less than 1% and may be safely neglected.

The uncertainty in the solid angle is primarily attributed to the uncertainty in the measurement of s_0, which less than 2%. This results in an uncertainty in the determination of the solid angle of

$$\frac{\delta(\Delta\Omega)}{\Delta\Omega} \leq 2\%\ . \tag{4.20}$$

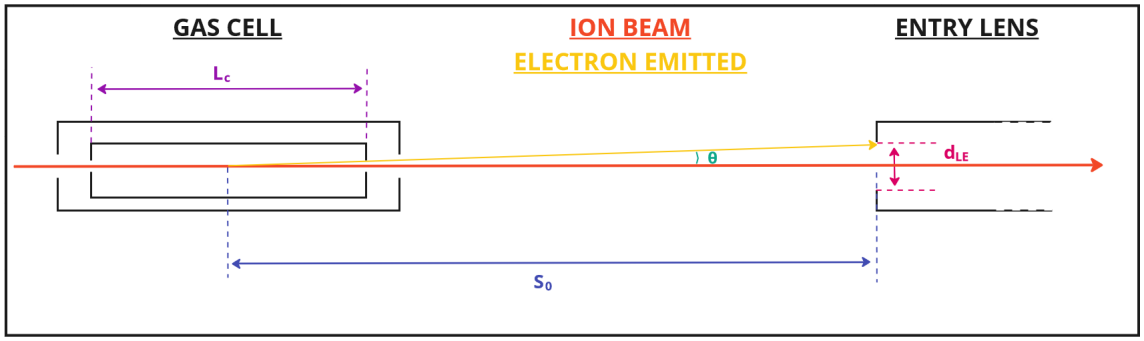

Figure 4.6: Illustration of the point source emission which corresponds to prompt decaying states.

4.3.6 Energy Step

The energy step of the spectrum per channel, ΔE_i, is determined by taking the first derivative of Eq. 4.1 with respect to the channel number. This calculation yields the following expression:

$$\Delta E_i = b + 2ci \ . \tag{4.21}$$

Alternatively, the energy step formula with respect to the universal calibration factors B and C can be obtained by taking the derivative of Eq. 4.5:

$$\Delta E_i = \frac{W}{F}(B + 2Ci) \ . \tag{4.22}$$

As we see, ΔE_i is not constant across the PSD area, with its magnitude increasing as the channel number i increases. In terms of sensitivity and importance, this correction stands out as it significantly influences the raw data analysis. Unlike other parameters, which act as multiplicative factors, ΔE introduces a tilt to the spectrum. This tilt ensures the accurate electron yield and proper matching of adjacent energy windows, thus playing a critical role in data analysis.

The uncertainty in ΔE can be calculated utilizing the uncertainty of the factors B and C. By assuming an average uncertainty for channel number $i = 130$ and referring to the values in Table 4.2, we determine the average uncertainty in ΔE as follows:

$$\frac{\delta(\Delta E)}{\Delta E} \leq 8\% \ . \tag{4.23}$$

4.3.7 Spectrograph Transmission

The transmission of the spectrograph, T, corresponds to the ratio of the number of particles reaching the PSD detector to the number of particles entering the spectrograph. The transmission value can depend on various factors, including the specific transmission characteristics of the lens, which, in turn, rely on the lens voltages and the retardation factor F [124].

Previous studies [8], have demonstrated that for our HDA system, the transmission remains nearly constant for F values up to 8, regardless of the lens voltages. Consequently, the transmission is primarily due to the three grids with 90% transmission each, located at the front of the PSD. Thus, the total transmission is determined as $T = (0.9)^3$, resulting in a transmission value of approximately 73%.

In the data analysis process, only the spectral range corresponding to the maximum transmission was considered, specifically within the channel interval of 60 to 210. This selection ensures the inclusion of the most reliable and accurate data for further analysis. The accuracy of the determined transmission value is expected to be better than 0.01, consequently:

$$\frac{\delta T}{T} = 1\% \ . \tag{4.24}$$

The electroformed meshes are used to mitigate the effects of fringe fields. However, an electroformed mesh consists of multiple small holes, which can act as miniature lenses, potentially affecting the trajectories of the outgoing electrons and compromising the PSD image. To address this issue, a second grid is introduced. The

arrangement of two grids creates a configuration where the small holes of both grids are not aligned, effectively compensating for the aforementioned problem. The third grid has been placed in front of the MCP and it was biased to $V_g = V_p - 9$ V to repel the spurious low energy electrons.

4.3.8 Overall Efficiency

The overall efficiency η corresponds primarily to the absolute efficiency of the MCP. The latter corresponds to the probability that an electron reaching the MCP surface will generate a detectable signal. Although η can be influenced by various factors such as the active area of the MCP, the voltages of the MCP, and the electron energy, it reaches its maximum efficiency at around 350 eV following a plateau for higher energies. However, to ensure a constant efficiency across the active area of the PSD for all detection energy windows, the entire MCP system is biased, ensuring that the central trajectory impinges on the MCP with an energy of 1000 eV [8].

The determination of the overall efficiency η can be performed through two methods: either from Binary Encounter electron (BEe) measurements, or from known cross sections for the production of target Auger electrons described below. Both techniques have been employed in our work, yielding consistent results, i.e.:

$$\eta = (50 \pm 5)\% \, . \tag{4.25}$$

Binary Encounter Electron Normalization

In the context of high-velocity, bare-ion projectiles interacting with atomic targets, the emission spectra of BEe serve as an important benchmark for the convergence of classical and quantum theories [152]. BEe are produced through direct and hard collisions, resulting in a broad peak structure in the spectra. The position of the peak's maximum can be predicted classically using energy and momentum conservation laws, leading to the well-known $k = 2\mathrm{v}\cos\theta$ result, where k and θ are the momentum and emission angle of the ejected electron, respectively.

The BEe peak is a characteristic feature of the zero-degree DDCS electron spectra, with the width of the peak attributed to the initial momentum distribution of the target electron. To analyze the BEe yield, we employed Eq. 4.6 with the exception of the overall efficiency η, and normalized it to the corresponding theoretical BEe DDCS calculation, as is commonly done in zero-degree projectile spectroscopy [76]. However, in this thesis, the CDW-EIS-numerical theory calculations (see Section 6.2 for more details) were preferred due to their better fit to the BEe peak [153].

Fig. 4.7 displays the measured electron DDCS spectra, which cover the energy range between the low-energy wing of the cusp peak and the high-energy wing of the BEe peak. The corresponding DDCS calculation is also presented for comparison.

Target Auger Electron Normalization

In order to utilize this technique, we employed the collision system 3.0 MeV p + Ne. After subtracting the background signal, the acquired spectrum shown in Fig. 4.2 was normalized using the factors of Eq. 4.6, with the exception of the efficiency

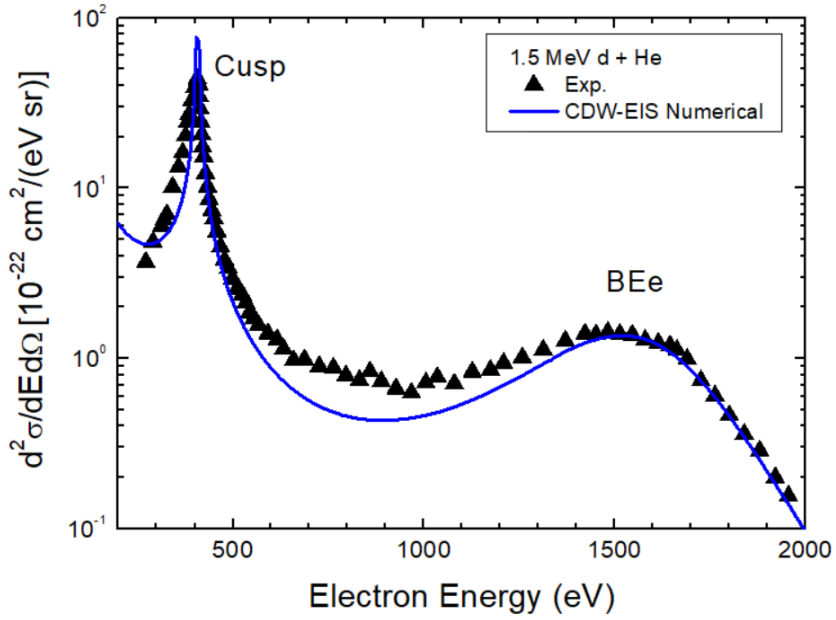

Figure 4.7: DDCS electron spectra measured at zero degrees with respect to the projectile velocity for collisions of 1.5 MeV deuterons with He. Symbols: experimental data. Line: CDW-EIS Numerical theoretical calculation. The spectral locations of the cusp and BEe peaks are indicated.

factor. Subsequently, the spectrum was integrated in energy and multiplied by a factor of 4π assuming isotropic angular distribution. Thus, we obtained the total experimental yield which was compared to the total cross section values reported in Ref. [154].

4.3.9 Overall DDCS Uncertainty

The determination of DDCS entails both statistical and systematic errors. Statistical uncertainties stem from the electron counts, i.e., $N_{e_i} \pm \sqrt{\delta N_{e_i}}$, while systematic uncertainties rely on accurately determining the other quantities involved in the DDCS equation. In Table 4.4 we present the experimental parameters discussed earlier, along with their maximum percentage uncertainties.

To estimate the average absolute uncertainty of the DDCS, $\delta\sigma/\sigma$, we can employ an error propagation analysis for uncorrelated variables. The following equation provides a means to calculate this uncertainty:

$$\frac{\delta\sigma}{\sigma} = \sqrt{\left(\frac{\delta N_I}{N_I}\right)^2 + \left(\frac{\delta L_c}{L}\right)^2 + \left(\frac{\delta n}{n}\right)^2 + \left(\frac{\delta(\Delta\Omega)}{\Delta\Omega}\right)^2 + \left(\frac{\delta(\Delta E)}{\Delta E}\right)^2 + \left(\frac{\delta T}{T}\right)^2 + \left(\frac{\delta\eta}{\eta}\right)^2}\,, \quad (4.26)$$

resulting in an overall systematic uncertainty of

$$\frac{\delta\sigma}{\sigma} \simeq 15\%\,. \quad (4.27)$$

Table 4.4: The maximum percentage uncertainties associated with the experimental quantities involved in the determination of the absolute DDCS, as described by Eq. 4.6.

Quantity	Symbol	Uncertainty
Number of ions	N_I	5%
Gas cell effective length	L_c	5%
Number of molecules per cm^3	n	0.2%
Solid angle	$\Delta\Omega$	2%
Energy step	ΔE	8%
Analyzer transmission	T	1%
Overall efficiency	η	10%

4.4 The Effective Solid Angle Correction Factor

In the ZAPS framework, prompt states refer to doubly excited projectile states satisfying the condition $V_p\tau/L_c << 1$, where V_p is the projectile velocity, τ is the total lifetime of the state, and L_c is the length of the target gas cell. In such cases, the emission of prompt Auger electrons occurs within the gas cell. For the HDA configuration used in this thesis, the solid detection angle $\Delta\Omega_0$ is described by Eq. 4.19.

However, when considering Auger electrons originating from long-lived projectile states, such as $1s2s2p\ ^4P_J$, their lifetimes can range from nanoseconds to milliseconds, depending on the atomic number Z_p and total angular momentum J of the state [104, 155], as shown in Fig 4.8. As a result, these long-lived projectile states can undergo Auger decay at various locations along the ion's path after exiting the gas cell, even inside and beyond the spectrometer. Moreover, the effective detection solid angle $\Delta\Omega$ increases as the emitting ion approaches the spectrometer entry. These factors necessitate a correction to the measured electron yield and subsequent cross section determination of long lived states. To account for the increase in solid angle due to emission as the projectile approaches the spectrometer, as well as the decrease due to the Auger state population decay, the G_τ correction factor was introduced. This correction factor involves a multiplicative term G_τ applied to $\Delta\Omega_0$, resulting in an effective solid angle [14, 77]:

$$\Delta\Omega = G_\tau \Delta\Omega_0 \ . \tag{4.28}$$

The experimental determination of the effective solid angle correction factor G_{τ_J} relies on collisions of Be-like projectile ions with light gas targets, i.e., hydrogen or helium. During the collision, the projectile ionizes the $1s$ electron of the metastable

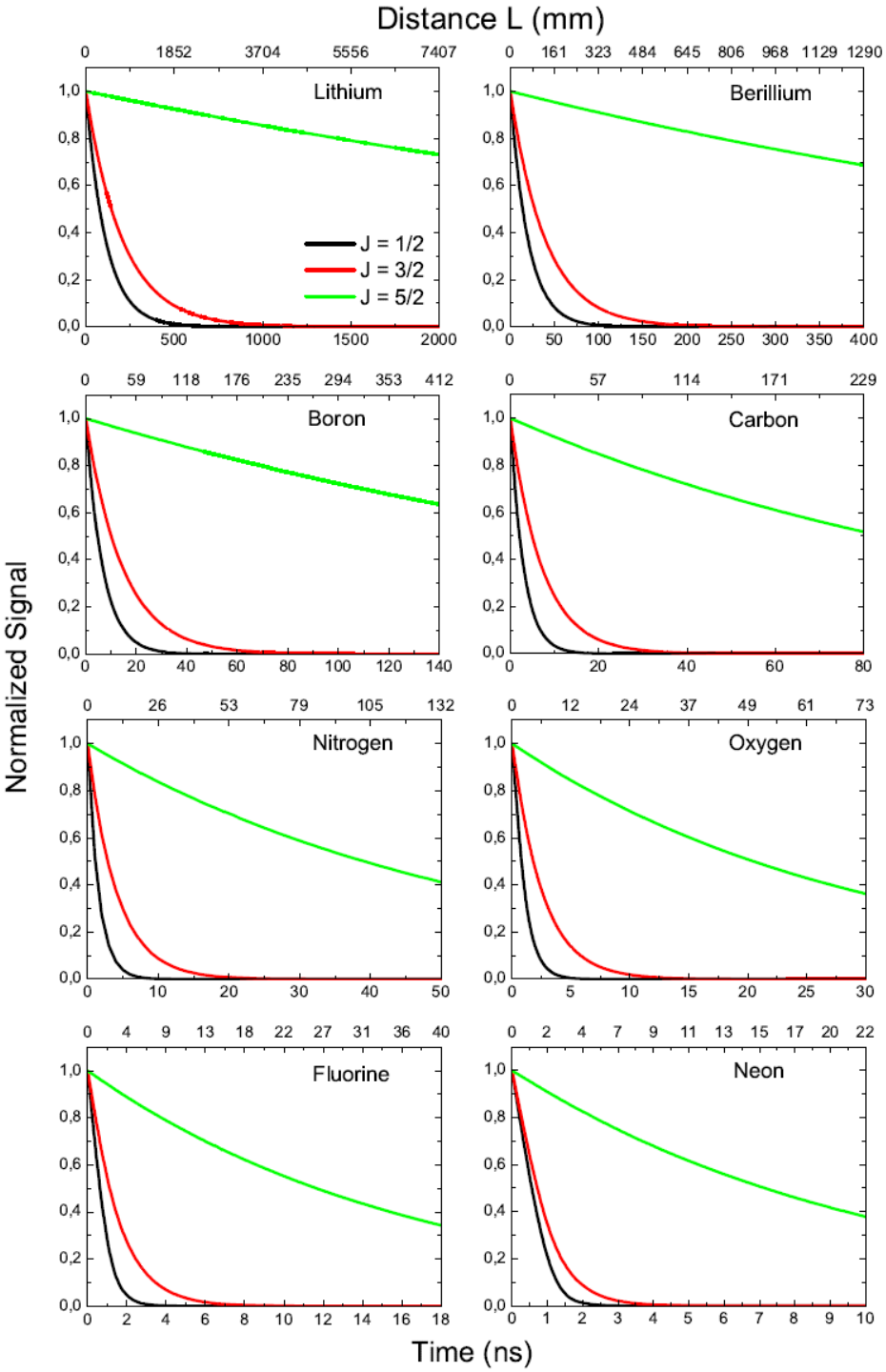

Figure 4.8: Theoretical exponential decay for the $1s2s2p\ ^4P_J$ levels of lithium, beryllium, boron, carbon, nitrogen, oxygen, fluorine, and neon. Time and corresponding distance are depicted in the bottom and top horizontal axes, respectively. Different J-levels are indicated by different colors, i.e., $J = 1/2$ (black), $J = 3/2$ (red), $J = 5/2$ (green).

beam component $1s^2 2s2p\ ^3P$, resulting in the formation of the $1s2s2p$ configuration and the related ^4P, $^2P_-$, and $^2P_+$ terms, according to LS coupling. This ionization process, known as *needle ionization*, has been described in the literature [74, 108].

In more detail, the sudden emission of the $1s$ electron leaves the ionic core in the $1s(2s2p\ ^3P)$ configuration, giving rise to the $1s(2s2p\ ^3P)^4P$ and $1s(2s2p\ ^3P)\ ^2P$ terms. The latter corresponds to the $1s2s2p\ ^2P_-$ term, while the $1s(2s2p\ ^1P)\ ^2P$ configuration, which corresponds to the $1s2s2p\ ^2P_+$ term, is highly unlikely to be formed due to the required spin-spin interaction. Therefore, after the $1s$ ionization, the internal ^3P coupling is maintained, resulting in the ^4P and $^2P_-$ peaks in the Auger spectra.

The ratio of the production cross section of the ^4P term to the $^2P_-$ term according to spin statistics should be 2, i.e.:

$$\frac{\sigma(^4P)}{\sigma(^2P_-)} = 2\ . \tag{4.29}$$

This ratio serves as the basis for the determination of the correction factor G_τ. This ratio is experimentally determined by comparing the areas of the ^4P and $^2P_-$ peaks, taking into account the Auger yields ξ and the correction factor G_τ:

$$\frac{\sigma(^4P)}{\sigma(^2P_-)} = \frac{Y(^4P)/(\xi_{^4P}G_\tau)}{Y(^2P_-)/\xi_{^2P_-}}\ , \tag{4.30}$$

where Y denotes the measured electron yield. Therefore, the experimental determination of G_τ can be obtained as:

$$G_\tau = \frac{1}{2}\frac{Y(^4P)}{Y(^2P_-)}\frac{\xi_{^2P_-}}{\xi_{^4P}}\ . \tag{4.31}$$

The use of Be-like projectiles is motivated by the absence of cascade effects [156], present in collision systems with He-like projectiles, that could influence the production of the ^4P and $^2P_-$ terms. In ion-atom collisions, various processes such as electron capture and ionization can lead to the generation of highly excited atomic states. These excited states then undergo de-excitation through radiative or Auger decays, often involving multiple steps and intermediate energy levels, a phenomenon known as cascade feeding.

To provide a visual representation of this cascade feeding mechanism, Fig. 4.9 illustrates a schematic diagram specifically for the single electron capture process occurring in the collision of $C^{4+}(1s2s\ ^3S)$ ions with He. As it is evident, the production of the $1s2s2p$ configuration in collisions of He-like ions, i.e., by single electron capture to the initial $1s2s\ ^3S$ state, favors the production of higher-lying $1s2snl\ ^{2,4}L$ states (with $n > 2$ and $L = l \leq n - 1$).

The doublet states experience efficient depletion through Auger decay to the ground state $1s^2$, which is much stronger compared to radiative decay. This efficient Auger decay limits the cascade feeding of lower-lying doublet levels. On the other hand, quartet states exhibit negligible Auger decay, allowing for significant cascade repopulation of lower-lying quartet states. As a result, a large portion of the population from higher-lying quartet states is effectively transferred to the $1s2s2p\ ^4P$ state, thus enhancing its electron yield in the corresponding electron spectra. Therefore, Be-like projectiles are the most suitable candidates to obtain accurate results for the

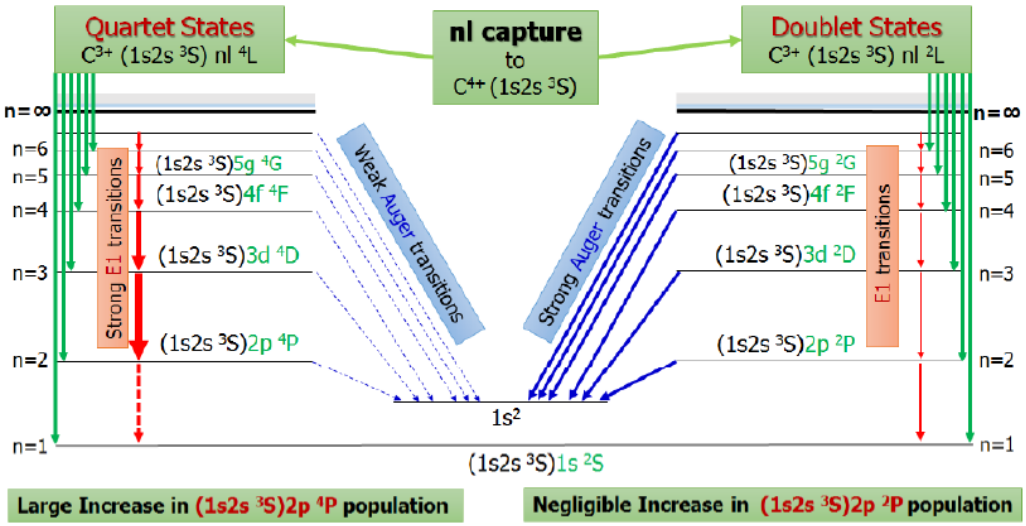

Figure 4.9: Schematic illustration of the $1s2s2p\ ^{2,4}P$ states selective cascade feeding mechanism. Taken from Ref. [12].

G_τ correction factor, which do not suffer from cascade effects, observed for example in collisions of He-like projectiles with gas targets.

In recent studies performed by our group [13], the O^{4+} + He collision system was utilized at various projectile energies for the determination of G_τ. A typical measurement, recorded utilizing 20 MeV Be-like oxygen ions, is shown in Fig. 4.10. Although the determination of G_τ is not influenced by the ion stripping method, we conducted experiments utilizing two different stripping methods as to include the determination of the beam content. In order to resolve the KLL Auger lines of interest, a deceleration factor of $F = 8$ was used. The normalized electron yields were determined through a fitting procedure utilizing the SIMION ion optics package. This method is detailed in Section 4.6.

To further validate our findings, Monte Carlo type simulations were conducted using the SIMION ion optics package. The experimental measurements and simulations show a very good agreement, strengthening the reliability of our investigation and confirming previous research results of our team [14, 15]. The corresponding experimental and simulated G_τ values are given in Table 4.5.

Table 4.5: The effective solid angle correction factor G_τ determined both experimentally and using the SIMION ion optics package. Taken from [13].

Beam Energy (MeV)	G_τ (Experiment)	G_τ (SIMION)
12	2.0 ± 0.2	2.28
16	1.9 ± 0.2	2.11
20	1.8 ± 0.2	2.03

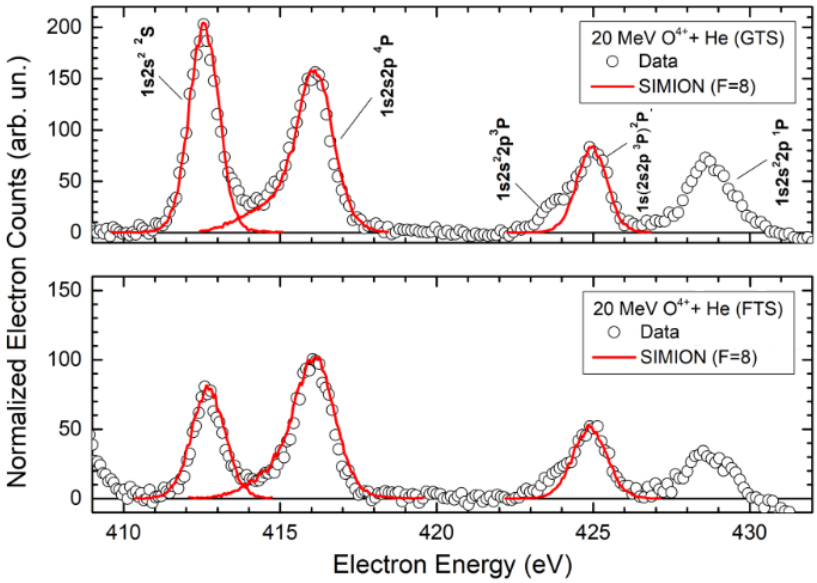

Figure 4.10: KLL Auger electron spectra obtain in collisions of 20 MeV O^{4+} + He with a deceleration factor $F = 8$ and two different stripping methods, i.e., GTS (top) and FTS (bottom). The figure shows both experiment (open circles) and SIMION normalized Auger distributions attained for fitting purposes (red lines). Taken from [13].

To facilitate a deeper understanding of the upcoming discussion, we refer to Eq. 4.32, which provides the expression for the effective solid angle averaged over the length of the gas cell for the metastable J-level,

$$\Delta\Omega_J(L, V_p\tau_J, L_c) = \frac{1}{L_c}\int_{z'=0}^{L_c} \Delta\Omega_0(L - z' - z)dz' \times \int_{z=0}^{L-z'} \frac{e^{-\frac{z}{V_p\tau_J}}}{V_p\tau_J}dz \ , \qquad (4.32)$$

where the first integral is termed as the geometrical term while the second integral is the temporal term. In Fig. 4.11, an illustration depicting the integration region is shown. Note that taking the limit $V_p\tau_J \to 0$ the effective solid angle is reduced to the prompt state solid angle, i.e.:

$$\Delta\Omega_0(s_0, L_c) = \frac{1}{L_c}\int_{z'=0}^{L_c} \Delta\Omega_0\left(\frac{L_c}{2} + s_0 - z'\right)dz' \ . \qquad (4.33)$$

Based on Eq, 4.32, 4.33, the solid angle correction factor G_{τ_J} is defined as:

$$G_{\tau_J} \equiv \frac{\Delta\Omega_J(L, V_p\tau_J, L_c)}{\Delta\Omega_0(s_0, L_c)} \ . \qquad (4.34)$$

In Fig. 4.12, we present the correction factor G_τ as a function of the universal variable $V_p\tau$, which has dimensions of length. Notably, the behavior of G_τ demonstrates distinct trends with respect to $V_p\tau$. Initially, as $V_p\tau$ values remain small, i.e., $V_p\tau << s_0$, corresponding to relatively short decay times τ, the majority of excited ions decay before reaching the entrance of the lens. Under these conditions, the temporal term can be considered constant, and the increase in the correction factor G_τ is primarily attributed to the expanding solid angle, or the geometrical term.

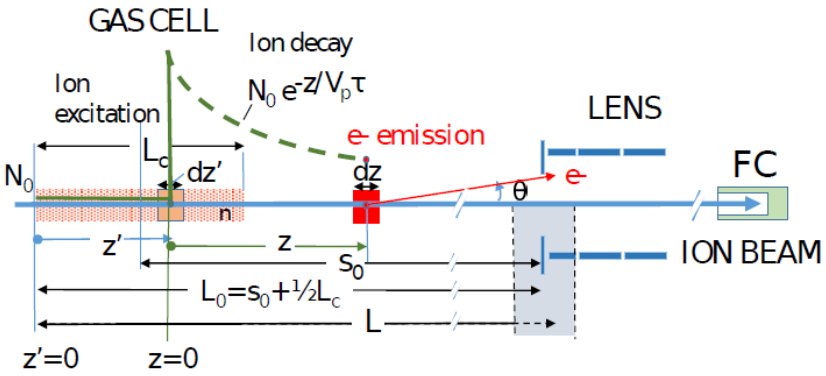

Figure 4.11: Illustration of the integration region. Initially, N_0 ions enter the gas cell with a velocity V_p. The gas cell has a length of L_c and is located at a distance s_0 from the lens entry. The ions undergo collisions and populate a long-lived excited state between z' and $z' + dz'$. Due to the long lifetimes of the excited state, it continues to travel beyond the gas cell before undergoing Auger decay. The emitted Auger electron is depicted at an angle θ, entering the lens and subsequently undergoing energy analysis by the HDA (not shown). The ions traverse the lens and a section of the HDA, exiting at the back of the HDA, and are finally collected in a Faraday cup (FC) used to measure the beam current for normalization purposes. The length L marks the part of the ion trajectory over which emitted electrons contribute to the excited state with non-negligible intensity as measured by the PSD. Taken from [14].

Conversely, as $V_p\tau$ surpasses s_0, i.e., $V_p\tau >> s_0$, a significant portion of ions undergo decay after entering the lens, traversing the spectrometer, and potentially even beyond its exit. In this case, the geometrical term remains largely constant, while the temporal term experiences an exponential decrease. As a consequence, the effective solid angle, and consequently the correction factor G_τ, follows an exponential decay pattern, as observed in our simulations. For intermediate decay times where $V_p\tau$ and s_0 are of comparable magnitudes, both the temporal and geometrical terms contribute significantly, leading to a peak at approximately 200 mm after the center of the gas cell.

It is important to point out that Fig. 4.12 is used for determining the correction factor G_{τ_J} for the effective solid angle corresponding to any J-level. The overall correction factor G_τ results from the statistical averaging of all the G_{τ_J} correction factors corresponding to the J-levels of a term, as [14]

$$G_\tau = \frac{\sum_J (2J+1)\xi_J G_{\tau_J}}{\sum_J (2J+1)\xi_J}. \tag{4.35}$$

4.5 Determination of the Metastable Beam Fraction

In ion accelerators, the magnetic selection of an extracted ion beam is typically based on a specific charge state and kinetic energy required for the experiment. However, magnetic selection alone is not sufficient to distinguish between different

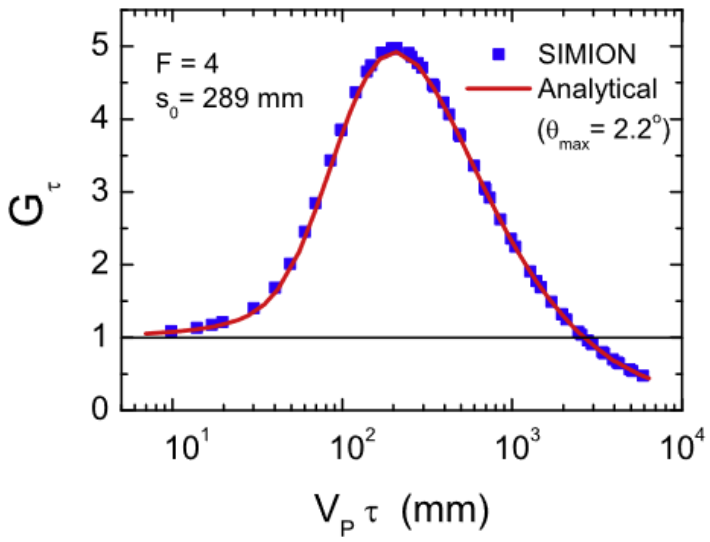

Figure 4.12: The effective solid angle correction factor G_τ is plotted as a function of the universal parameter $V_p\tau$ for deceleration factor $F = 4$. The solid lines represent analytical calculations based on Eq. 4.34 limited to a maximum angle $\theta_{\max} = 2.2°$ and the blue points to simulations performed within the SIMION optics package. Taken from [15].

electronic configurations of a specific ion charge state. This is due to the presence of mixed-state ion beams having long lifetimes surviving to the target area.

A prominent example of such mixed-state beams is the He-like ($1s^2\ ^1S$, $1s2s\ ^{1,3}S$) beam and Be-like beam ($1s^22s^2\ ^1S$, $1s2s^22p\ ^3P$). The additional $1s2s\ ^{1,3}S$ and $1s2s^22p\ ^3P$ metastable components of the He- and Be-like beams, respectively, opens up an opportunity to investigate dynamic collision processes in novel ionic environments that have an initial K-shell vacancy [77].

To effectively utilize such projectiles for related studies, it is important to determine the metastable fraction of the mixed-state beam. A recent technique has been proposed to obtain this information, based on the double measurement of the same collision system under identical conditions, with the only difference being the stripping method [157]. By using gas or foil as the stripping medium, the metastable fraction of the beam can be also varied [158].

4.5.1 He-like beams

For the collision energies used in this thesis, the $1s2s2p\ ^4P$ state is exclusively populated by single electron capture from the $1s2s\ ^3S$ component of the beam, while the $1s2p^2\ ^2D$ state is populated through transfer-excitation from the ground state $1s^2\ ^1S$ [26]. This assumption holds for collisions with light targets such as H_2 and He. Under these conditions, the metastable fractions of the beam can be determined using the following formula [157, 159]:

$$f^i_{1s2s\ ^3S} = Y_i[^4P]\frac{Y_2[^2D] - Y_1[^2D]}{Y_2[^2D]Y_1[^4P] - Y_1[^2D]Y_2[^4P]} \qquad (i = 1, 2)\ , \tag{4.36}$$

where Y_i is the normalized yield of the $^{(2S+1)}L$ Auger states for each of the two measurements with different fractions.

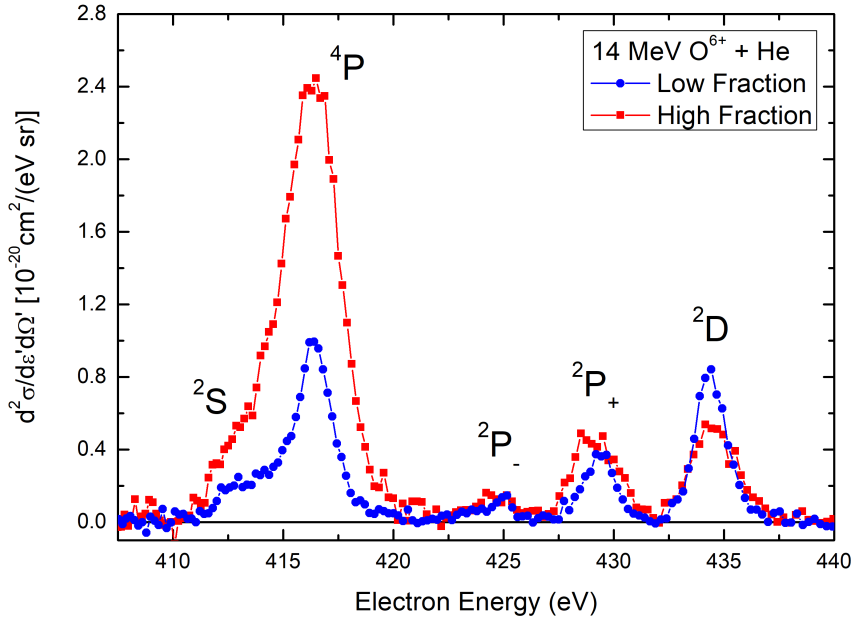

Figure 4.13: Typical KLL Auger spectra for collisions of 14 MeV O^{6+} + He indicating the differences on the metastable fraction $1s2s\ ^3S$. Red lines represent the results for the high metastable content spectra, while blue lines correspond to the low metastable content.

Note that the application of this technique requires the ability to control and vary the amount of the metastable beam component $f_{1s2s\ ^3S}$ in the two spectra. Earlier studies have demonstrated that the amount of metastable beam component primarily depends on the type of stripper employed, whether it is a foil stripper or a gas stripper. When using a foil stripper, the metastable fraction of the $1s2s\ ^3S$ state for He-like ions typically reaches a maximum of around 30% [157, 158, 160]. On the other hand, when a gas stripper is used, the metastable fraction can be significantly lower, around 5% or even less, thus delivering even pure ground state beams [16]. However, it is important to acknowledge that certain limitations exist in the determination of the metastable fraction, which require a meticulous analysis. These limitations, along with the methods employed to compensate for them, are discussed in Appendix E.

In Fig. 4.13, an example of the double measurement technique is presented for collisions of 14 MeV O^{6+} + He. The two spectra, corresponding to the $1s2s\ ^3S$ high and low fractions, clearly show differences in the yields of the ^4P and ^2D Auger peaks. The high fraction spectrum exhibits a higher yield for the ^4P Auger peak compared to the low fraction spectrum. Similarly, the high fraction spectrum exhibits a lower yield for the ^2D Auger peak compared to the low fraction spectrum. These differences in the ^4P and ^2D Auger yields indicate a variation in the percentage of the $1s2s\ ^3S$ beam content for the two measurements.

The double measurement technique provides a robust tool for studying various atomic physics processes involving pre-excited multi-open-shell ions. These processes include single electron capture, and excitation leading to the formation of doubly excited states (see Chapter 7), transfer-excitation [78], as well as cusp elec-

tron studies (see Chapter 6). In all of these studies, the reliable determination of the metastable fraction is necessary for accurately determining absolute cross sections and investigating the underlying physics involved.

Fig. 4.14 demonstrates the variation of the metastable fraction $1s2s\ ^3S$ for the He-like oxygen beams used in this study. The high fraction measurements consistently show a metastable fraction of approximately 19%, while the low fraction measurements exhibit a metastable fraction of around 5%. It should be mentioned that for collision energies up to 14 MeV, post stripping was employed due to insufficient beam current intensities with tandem terminal stripping alone. At 16 MeV collision energy, foil post stripping was used for the low fraction spectrum, while both foil terminal and foil post stripping were utilized for the high fraction measurement. As a result, the difference in the metastable fraction between the two measurements is less pronounced compared to the other cases. For the higher collision energies (20 and 24 MeV), only terminal stripping was employed. Notably, the low fraction spectra obtained with gas terminal stripping at these collision energies have a relatively small fraction, less than 2.5% for both cases. This value falls within the experimental error, suggesting a predominantly ground state beam in the target area. The statistical error bars depicted in Fig. 4.14 were individually estimated for each case, and the detailed analysis of the errors can be looked up in Appendix D.

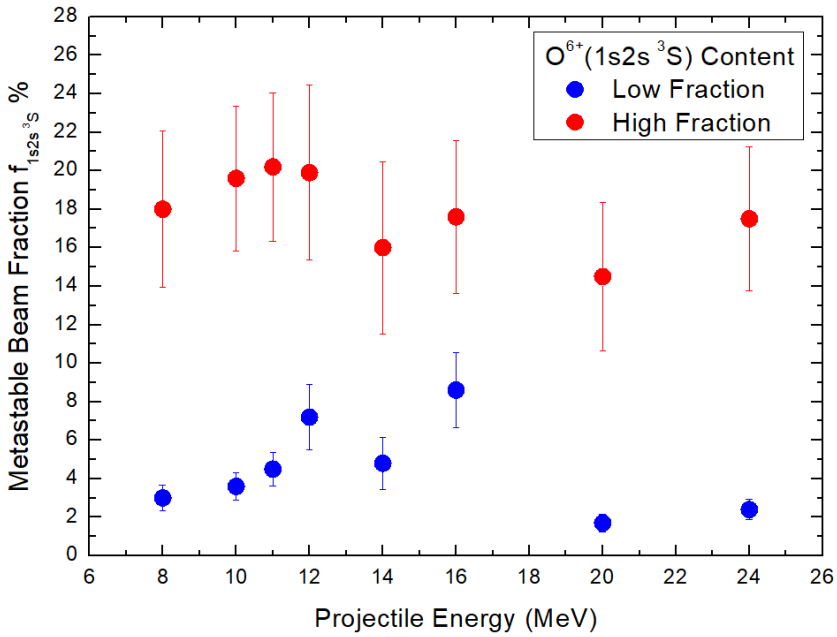

Figure 4.14: Metastable fraction of the $1s2s\ ^3S$ state in collisions of He-like oxygen projectiles with helium at various collision energies. Red dots correspond to the results for the high metastable content spectra, while blue dots correspond to the low metastable content. Statistical uncertainties are shown.

In the above discussion, it has been assumed that the $1s2s\ ^1S$ state has a negligible effect. This assumption is based on the statistical production of the states in a 3 : 1 ratio with a 30% content of $1s2s\ ^3S$ at the point of production. Due to its much longer lifetime, the $1s2s\ ^3S$ fraction remains practically intact across the entire range of $Z_p = 3 - 9$. On the other hand, the $1s2s\ ^1S$ fraction is considerably reduced as the ion beam approaches the target area, because of its much shorter

lifetime. Specifically, for the oxygen projectiles used in this work, it has been found that the surviving fraction of the $1s2s\ ^1S$ state is less than 1% for all collision energies. Therefore, a negligible effect of the $1s2s\ ^1S$ fraction in the analysis has been assumed [161].

4.5.2 Be-like beams

KLL Auger electron spectra obtained from collisions of Be-like projectiles with light gas targets are utilized for the determination of the G_τ correction factor, as described in Section 4.4. To an extent, the double measurement technique can be again employed to also determine the metastable fraction, for the $1s2s^22p\ ^3P$ component of the beam. The excited ^3P_J beam component exhibit varying lifetimes in the range of microseconds to seconds, depending on the atomic number Z_p and angular momentum J [162–164], thus reaching the target area without significant decay.

The needle ionization of the 1s electron of the ground state component, $1s^22s^2\ ^1S$, results in the intermediate state $1s2s^2\ ^2S$. This state Auger decays giving rise to a pronounced peak in the recorded Auger spectrum, as shown in Fig. 4.10. Also, during collisions with light gas targets, i.e., H_2 and He, the needle ionization of the $1s$ electron of the $1s^22s2p\ ^3P$ state gives rise to the $1s2s2p\ ^4P$ and $1s2s2p\ ^2P_-$ states, as mentioned in Section 4.4.

As the $1s$ ionization does not have a strong dependence on the L-shell configuration, the production cross sections from the ground and the metastable components should be equal, i.e., $\sigma_{1s}(1s^22s^2) = \sigma_{1s}(1s^22s2p)$ [108]. In addition, the production cross section ratios for the ^4P and $^2P_-$ states should result in the ratio $\sigma(^4P) : \sigma(^2P_-) = 2 : 1$, according to the multiplicity of the states. Thus, the production cross section ratios for the ^2S, ^4P and $^2P_-$ states should be $\sigma(^2S) : \sigma(^4P) : \sigma(^2P_-) = 3 : 2 : 1$. Then, the metastable fraction, $1s2s^22p\ ^3P$, of the beam can be obtained as [77]:

$$f_{1s2s^22p\ ^3P} \equiv \left[1 + \frac{Y(^2S)}{Y(^4P) + Y(^2P_-)}\right] = \left[1 + \frac{1}{3}\frac{Y(^2S)}{Y(^2P_-)}\right] . \tag{4.37}$$

In Fig. 4.15, we present the metastable fractions, $f_{1s2s^22p\ ^3P}$, as they were determined for collisions of 12, 16, and 20 MeV $O^{4+}(1s^22s^2\ ^1S,\ 1s^22s2p\ ^3P)$ with He. As observed in Fig. 4.15, the metastable fraction of the O^{4+} beam remains relatively constant for the energies considered. However, the differences in metastable fractions between the low and high fraction measurements are not as pronounced as those in He-like projectiles, as can be inferred from Fig. 4.14.

4.6 Determination of the Single Differential Cross Section

After determining the DDCS of KLL Auger spectra, we obtain the single differential cross section (SDCS) for each of the five Auger peaks: ^2S, ^4P, $^2P_-$, $^2P_+$, and ^2D. To derive SDCSs, we have to account for the content of the mixed-state beam by determining the metastable fraction.

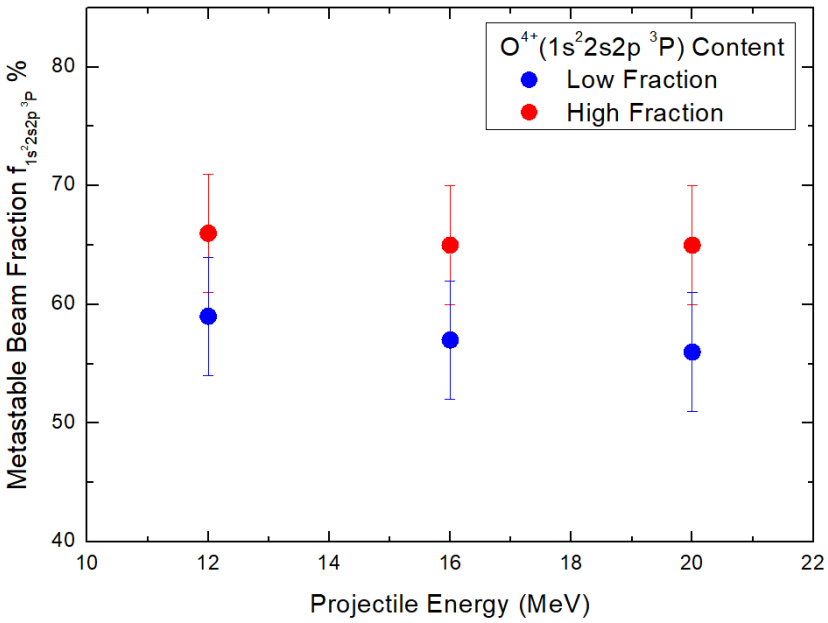

Figure 4.15: Metastable fractions of the $1s^2 2s2p\ ^3P$ state in collisions of Be-like oxygen projectiles with helium at various collision energies. Red dots correspond to the results for the high metastable content spectra, while blue dots correspond to the low metastable content. Statistical uncertainties are shown. Data retrieved from [13].

Early developments of the two-measurement technique assumed the low, yet non-zero, metastable fraction to be negligible, introducing minor errors. This led to the normalization of the two KLL spectra at the ^2D peak, followed by subtraction to isolate the $1s2s\ ^3S$ contributions [157, 165]. Recently, a method has been reported that does not necessitate the requirement of almost zero metastable fraction in the low fraction measurement, provided that the two fractions are appreciably different [159]. This is particularly advantageous when achieving an adequately low metastable fraction is not always feasible, as in our measurements [166].

Since we are interested in two separate measurements, $i = 1,\ 2$, each associated with a distinct metastable fraction f_i, the electron yield of each state can be written as [159]:

$$\frac{d\sigma_i[x]}{d\Omega'} = (1 - f_i)\frac{d\sigma_g[x]}{d\Omega'} + f_i\frac{d\sigma_m[x]}{d\Omega'}\ , \tag{4.38}$$

for x: ^4P, $^2P_\pm$, ^2D. Thus, Eq. 4.38 leads to two equations for each one of the four states. Therefore we arrive at a set of eight equations involving ten unknowns, i.e., the two metastable fractions as well as the four contributions from the ground and four contributions from the metastable beam components for each state. However, in collisions with He-like projectiles and under the assumptions that the ^4P state is populated predominantly from the metastable state by direct electron transfer and the ^2D state is populated predominantly from the ground state by transfer and excitation, we set $Y_g[^4P] \simeq 0$ and $Y_m[^2D] \simeq 0$. As a result, we eliminate two of the ten unknowns in the equation system, making it solvable and leading to the

following equations [159]:

$$\frac{d\sigma_g[x]}{d\Omega'} = \frac{Y_2[x]Y_1[^4P] - Y_1[x]Y_2[^4P]}{Y_1[^4P] - Y_2[^4P]} \tag{4.39}$$

$$\frac{d\sigma_m[x]}{d\Omega'} = \frac{Y_2[x]Y_1[^2D] - Y_1[x]Y_2[^2D]}{Y_1[^2D] - Y_2[^2D]} \ . \tag{4.40}$$

Alternatively, the above equations can also be written as [26]:

$$\frac{d\sigma_g[x]}{d\Omega'} = \frac{f_2 Y_1[x] - f_1 Y_2[x]}{f_2 - f_1} \tag{4.41}$$

$$\frac{d\sigma_m[x]}{d\Omega'} = \frac{(1-f_1)Y_2[x] - (1-f_2)Y_1[x]}{f_2 - f_1} \ . \tag{4.42}$$

Eqs. 4.41 and 4.42 are free of any assumptions and can be safely applied to any collision system to determine the SDCSs originating solely from the ground and the metastable part of the beam.

In this thesis, Eqs. 4.39 and 4.40 were used for the determination of SDCSs. However, in cases where the double measurement technique did not result in appreciable metastable fraction differences, we used Eqs. 4.41 and 4.42, after re-normalizing the metastable fractions according to the method described in Appendix E.

Chapter 5

SIMION Simulations

SIMION is a software package used to study electrostatic fields and orbits of charged particles within these fields [142]. SIMION uses electrodes in a certain configuration, voltages, and particles with defined initial conditions. The chosen configuration delimits the potential arrays and defines the geometry of the simulation.

In detail, the first step in solving a problem involves defining the geometry of a three-dimensional space. This is where all the required elements, such as electrodes, lenses, and detectors, will be positioned. The three-dimensional space is discretized into a three-dimensional grid, and the potential at each point is calculated for each element in the layout. The calculation is performed using the relaxation method, which approximates the solution of the Laplacian equation.

To calculate the potential at a specific point, SIMION considers the six closest points in the three-dimensional space and calculates their mean value. This process is repeated for every point in the grid. The solutions of the Laplacian equation are stored in separate files, and the final solution is obtained by combining the solutions of each element, multiplied by their respective potentials.

The resulting solution, representing the potential distribution, is saved in a separate file in the computer's RAM. This allows for faster calculation of ion trajectories based on the defined potentials within the simulated environment. For the ZAPS geometry, which has been integrated within the SIMION environment with a design accuracy of 0.254 mm per grid unit (see Fig. 5.1), a numerical code has been built in the Lua programming language to simulate the electron emission and the measurement process. There, a large number (typically $\sim 10^5 - 10^6$) electron trajectories are generated from random positions within the gas cell area with the required energies and random solid angles limited to the detection geometry. This way, the electron emission process following the interaction of the ion beam with the gas target is simulated in accordance to a Monte Carlo type approach. In a next step, the electrons that are detected on the PSD area are used to obtain the energy spectrum after considering the spectrograph operation voltages and the energy calibration process. Finally, the spectra are transformed to the projectile frame following the laboratory frame transformations discussed in Section 2.2, for a direct comparison with the corresponding DDCS measurements.

The Monte Carlo simulations performed in this study served multiple important purposes. Firstly, they were utilized for fitting the simulated results to the experimental DDCSs of Auger peaks. This fitting process enabled us to most-accurately determine the SDCSs of the Auger peaks. Furthermore, the simulations played a

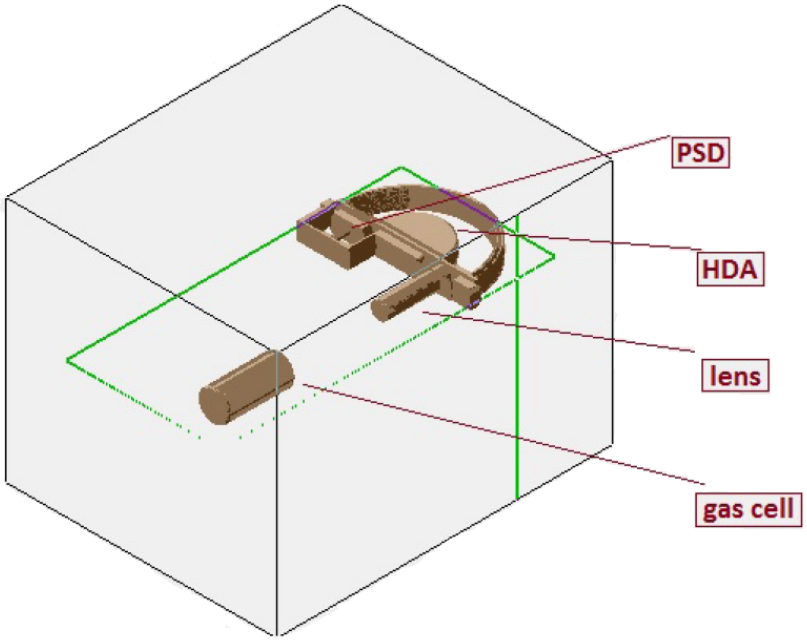

Figure 5.1: 3D illustration of the ZAPS setup integrated into the SIMION optics package environment. The key components, gas cell, entry lens, HDA, and PSD, are indicated.

crucial role in determining the effective solid angle correction factor of the spectrograph and compare with the corresponding experimental findings. Additionally, the Monte Carlo simulations were instrumental in investigating the parameters of the spectrograph, since they allowed us to validate the overlapping of adjacent energy windows, which is crucial for measuring the continuum electron spectra, such as the BEe and cusp peaks. Moreover, the simulations played a key role in determining the beam energy width by comparing the simulated peaks with high-resolution Auger spectra. Thus, they provided valuable insights and highlighted the usefulness of KLL Auger spectroscopy as a tool for beam diagnostics.

In summary, the Monte Carlo simulations performed within the SIMION environment for this study had a multifaceted impact on our research. In the following subsections, we will provide a detailed account of how these simulations were utilized for each case described above.

5.1 Determination of the Electron Yield

Traditionally, fitting software can be employed to determine the electron yields, which are then used to determine SDCSs, according to Eqs.4.39, 4.40. These programs, fit known distributions to the Auger peaks and integrate them with respect to energy. However, caution must be exercised as these fitting processes rely on a least square method and may yield multiple mathematically correct solutions, some of which may not be physically meaningful. Additionally, the ^4P Auger line does not conform well to any standard mathematical distribution, necessitating the convolution of two or three distributions for fitting.

While fitting tools can be useful for online analysis during experiments, they

can be cumbersome when accurate results are required. In contrast, our team has developed a Lua program that takes into account all experimental parameters and simulates the Auger energy distributions, except the ^2D, utilizing theoretical Auger energies and lifetimes of the Li-like doubly-excited states ($1s2s2l\ ^{2,4}L$) and pseudo-random Lorentzian distributions [16]. This program enables a comprehensive simulation of the Auger lines, which can then be normalized in height to match the experimental DDCS data. As shown in Fig. 5.2, the simulated peaks closely match the experimental peaks, with the simulated ^4P peak accurately capturing its unique shape. By directly integrating the simulated peaks, the SDCS can be determined. For the ^2D state, a straightforward integration is performed on the experimental data.

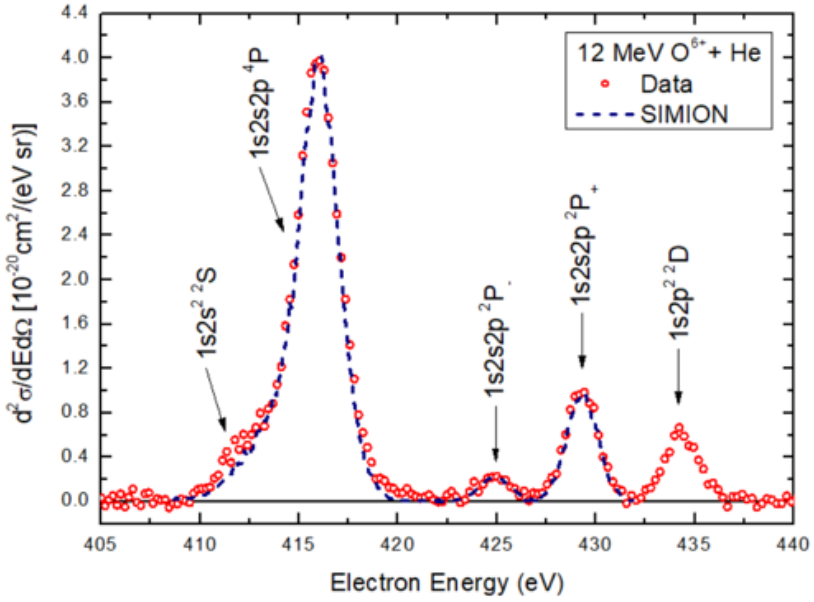

Figure 5.2: DDCS Auger electron spectrum for the collision system 12 MeV O^{6+} + He. Symbols: Data; Line: SIMION simulations.

It should be noted that the asymmetry observed in the $1s2s2p\ ^4P$ peak is attributed to the different lifetimes of its three J-levels [15]. Consequently, each J-level was simulated individually, and the final distribution $S(^4P)$ was obtained by statistically averaging over all three J-levels according to the formula

$$S(^4P) = \sum_J \frac{(2J+1)}{\sum_J (2J+1)} S(^4P_J)\ . \tag{5.1}$$

and shown in Fig. 5.3. It is noteworthy that our SIMION modeling accurately reproduces the asymmetry of the peak as can be clearly seen in Fig. 5.2.

5.2 Determination of the Effective Solid Angle Correction Factor G_{τ_J}

The determination of the G_{τ_J} correction factor was achieved through Monte Carlo simulations conducted in the SIMION package [13]. This process is based on a simple

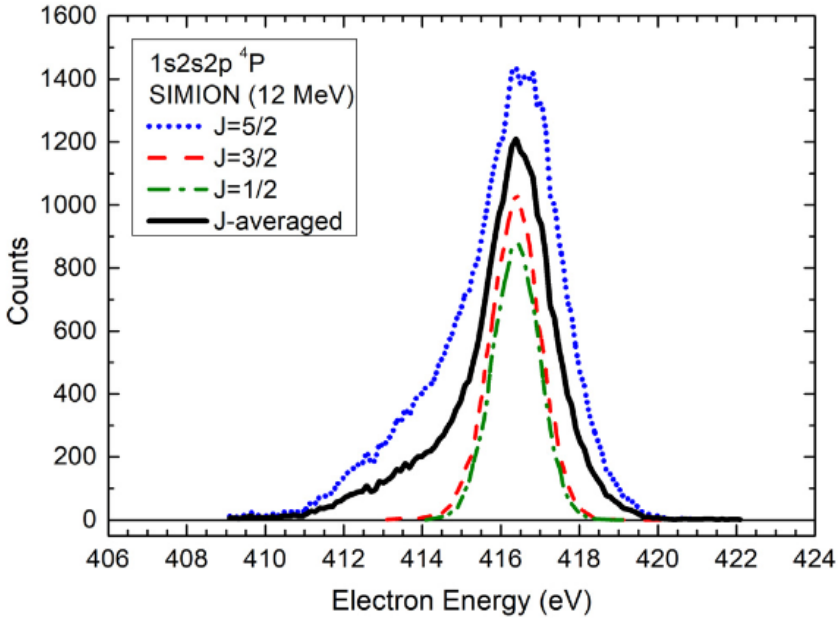

Figure 5.3: SIMION simulation of the $1s2s2p\ ^4P$ Auger peak distribution for a collision energy of 12 MeV and O^{6+} projectiles. The plot displays the contributions from the different J-levels as well as their statistical average. Blue dashed line: $J = 5/2$; Red dash-dotted line: $J = 3/2$; Green dotted line: $J = 1/2$; Black solid line: statistical sum. Taken from [16].

concept: By simulating the behavior of Auger electrons, we can calculate the ratio of observed electrons coming from a long-lived J-level to the number of the electrons coming from a prompt state with the same initial population. This ratio defines the effective solid angle correction factor G_{τ_J} for each J-level. By statistically averaging these correction factors over all J-levels, we obtain the J-averaged correction factor G_τ.

In detail, the number of observed Auger electrons, for a number of N_0 initially populated projectiles for each J-level is:

$$N^e_{obs_J} \simeq \xi_J N_0 \Delta\Omega_J(L, V_p\tau_J, L_c) \ . \tag{5.2}$$

However, the actual number of detected electrons should be calculated as:

$$N^e_{true_J} \simeq \xi_J N_0 \Delta\Omega_0(s_0, L_c) \ . \tag{5.3}$$

Dividing Eqs. 5.2, 5.3, results in:

$$\frac{N^e_{obs_J}}{N^e_{true_J}} = \frac{\Delta\Omega_J(L, V_p\tau_J, L_c)}{\Delta\Omega_0(s_0, L_c)} \equiv G_{\tau_J} \ , \tag{5.4}$$

and the J-averaged correction factor G_τ can be determined according to Eq. 4.35.

To gain a deeper understanding of the functional behavior of G_{τ_J}, we performed analytical calculations using the Mathematica package based on Eqs. 4.32, 4.33, 4.34, and 4.18. These calculations were independent of the deceleration factor and relied solely on geometrical and temporal parameters. In our approach, we introduced a restriction on the solid angle by setting a maximum value θ_{max}. We then varied

θ_{max} to match the analytical results with the value of G_τ obtained from SIMION simulations. In this way, we obtained the value of $\theta_{max} = 2.2°$ for the deceleration factor of $F = 4$[15]. Thus, the analytical solution presented in Fig. 4.12 serves as a chart for estimating any G_{τ_J} correction factor as well as the corresponding J-averaged correction factor G_τ of a long-lived state.

5.3 Overlapping of Consecutive Energy Spectra

Recently, we have initiated studies involving continuum electron spectra, specifically focusing on the cusp and BEe peaks. These peaks exhibit a wide energy range, which cannot be recorded in one energy window by our spectrograph. We Note that a ZAPS spectrum can be recorded in one energy window covering an energy range of about 20% of the tuning electron energy for deceleration factor of $F = 1$.

To overcome this limitation, we employ a technique where we record multiple overlapping electron spectra and subsequently stitch them together to obtain a larger spectrum. In Fig. 5.4, we present an example of a spectrum showcasing the cusp electron peak recorded from collisions of 1.5 MeV protons with helium. The figure demonstrates the combination of four adjacent energy windows with tuning energies W, 585, 685, 800, and 940 eV, along with a data averaging to enhance the visibility of the cusp peak.

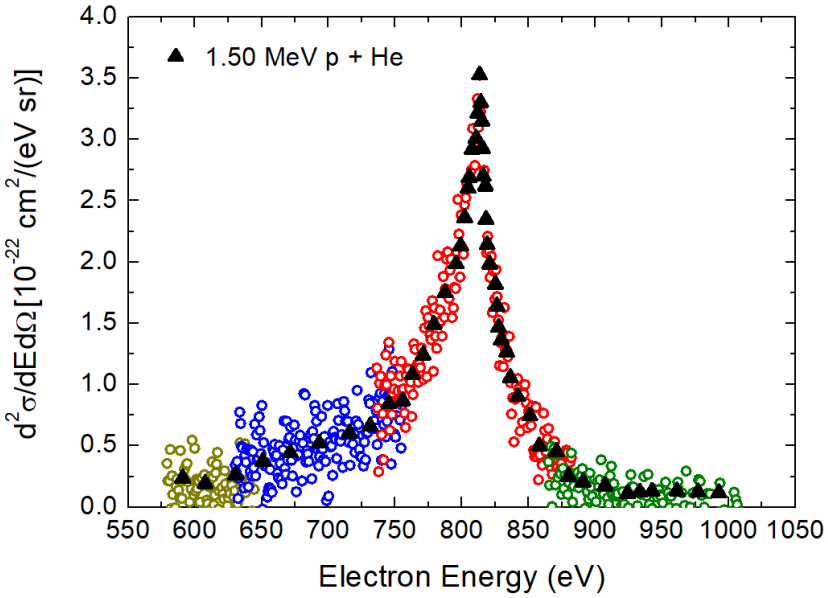

Figure 5.4: DDCS electron spectrum of cusp electron peak for the collision system 1.5 MeV p + He. Multi-coloured circles: Four overlapping energy windows; Black triangles: Averaging.

To validate the process of recording and combining overlapping spectra, we conducted SIMION studies in which we simulated ZAPS measurements using the Monte Carlo approach. The simulations involved generating electrons with initial kinetic energies described by a Gaussian distribution with FWHM greater than 200 eV. We simulated various broad Gaussian peaks centered at energies of 1000 eV and 2000 eV, each with different FWHM values.

In a next step, we energy calibrated the raw SIMION data by employing narrow Gaussian peaks with a FWHM of 2 eV at various energies to cover the entire area of the PSD. By determining the center of these peaks in terms of PSD-x dispersion, we obtained a calibration curve, which relates the energy of the electrons to their corresponding PSD positions. The calibration curves were fitted with a quadratic function, allowing us to determine the coefficients a, b, and c, as already described in Eq. 4.1.

It is worth noting that when simulating narrow Gaussian peaks for calibration purposes, a relatively small number of electrons (approximately 10k per run) was sufficient to obtain accurate calibration curves. However, for simulating broader peaks, a larger number of electrons ($\sim$ 250k) was required to ensure high statistical accuracy in the resulting spectra. This was achieved by performing a frequency count with a binning of 0.185 mm, effectively dividing the PSD area into 255 bins. By generating this larger number of electrons and employing appropriate binning, we were able to obtain simulated spectra that closely resemble the experimental ones, i.e. consisting of 255 bins (256 in the experiment).

Fig. 5.5 depicts the calibration curves recorded for this study at different tuning energies W. To determine the calibration factors a, b, and c, these curves were fitted with quadratic functions. Subsequently, the universal calibration factors A, B, and C for $F = 1$ were determined using Eqs. 4.2, 4.3, 4.4 and given in Fig. 5.6.

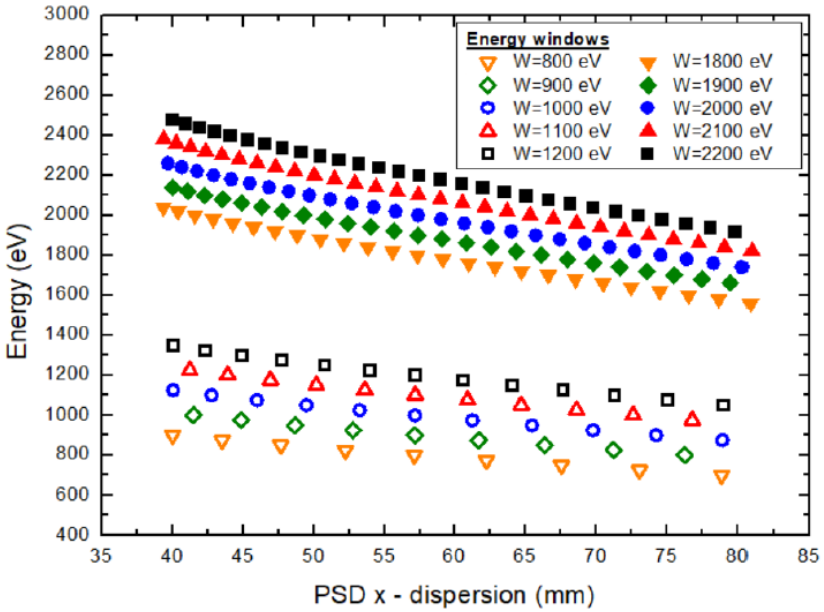

Figure 5.5: Simulated calibration curves determined with SIMION. Different symbols indicate different energy windows.

It should be noted that a direct comparison between the simulated calibration factors A, B, and C and those derived from experiment is not viable. This is because the simulation provides the exact position in millimeters of the simulated electron, while the experimental calibration curves are functions of the PSD channel number. The calibration curves are inherently different due to the different measurement systems used in simulation and experiment, thus a straightforward comparison is not feasible. Even though, such a comparison is not necessary for the purpose of this study, as the simulation only serves as a tool to understand and analyze the

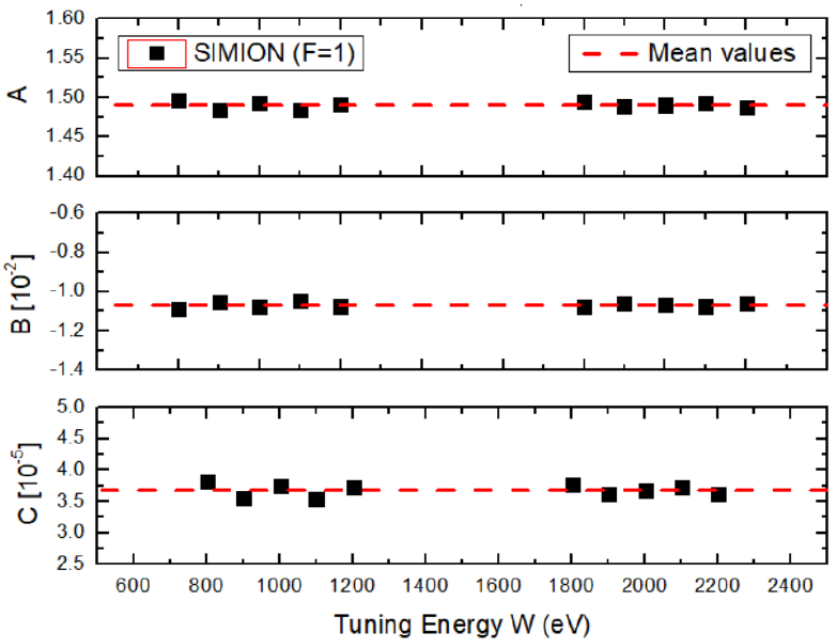

Figure 5.6: Universal factors A (up), B (middle), C (bottom) as a function of the PSD x - position, for deceleration factor $F = 1$ and various tuning energies W (black dots). Red dashed lines correspond to their mean values.

behavior of the system.

In Fig. 5.7, we present an example where we recorded a Gaussian distribution centered at 1000 eV with a FWHM of 200 eV. To capture the complete distribution, we employed the technique of recording overlapping energy windows. In this case, we measured five overlapping energy windows with tuning energies of $W = 880$, 900, 1000, 1100, and 1200 eV. Each of these energy windows was individually measured, energy calibrated, and then pieced together to obtain the complete spectrum. Finally, we compared the simulated spectrum with the initial Gaussian distribution used for the simulation. This comparison allowed us to assess the effectiveness of the recording and overlapping process and validate its agreement with the simulated distribution.

The results clearly demonstrate that the energy windows overlap perfectly, accurately reproducing the initial Gaussian distribution. It is important to note that although the convolution of the Gaussian peak with the response function of the spectrograph can be a concern, it is not an issue in this case. The response function is very narrow, typically around 2 eV, which is much smaller compared to the broader Gaussian distribution.

The successful implementation of the overlapping technique, as demonstrated in the SIMION simulations, provides strong evidence for the validity of the analysis performed to determine the experimentally measured DDCS of continuum spectra, such as the cusp and BEe peaks.

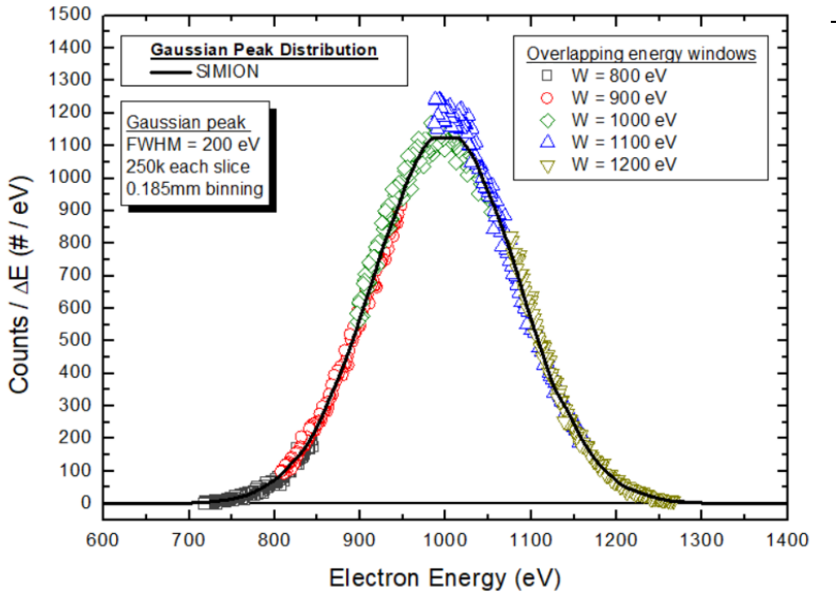

Figure 5.7: Simulated Gaussian distribution with a FWHM of 200 eV centered at 1000 eV. Multicoloured circles: Simulated data at different energy windows W; Black line: SIMION Gaussian distribution.

Chapter 6

Cusp electrons

6.1 Background and Motivation

The ionization of a target atom by a bare ion involves three primary processes, each giving rise to distinct peaks, as shown in Fig. 6.1: (a) the soft electron peak, (b) the cusp electron peak, and (c) the binary encounter electron (BEe) peak. The soft electron peak occurs during glancing collisions characterized by low energies and momentum transfers. In these collisions, the influence of the target atom on the active electron outweighs that of the projectile. The qualitative understanding of the soft electron peak has been developed since the early days of quantum mechanics, providing insights into the dynamics of ionization processes. On the other hand, in binary collisions, the active electron does not interact with the target atom but instead scatters off the projectile in a head-on collision. The target atom merely contributes to the initial velocity distribution of the electron. This type of ionization process is known as a binary encounter collision, and the corresponding peak is referred to as the binary encounter peak. The BEe emission spectra are crucial benchmarks where classical and quantum theories are expected to converge, especially for high-velocity ($v > V_p$) bare-ion projectiles colliding with atomic targets [152].

A third peak, namely the cusp electron peak, is observed when the velocity of the emitted electron matches that of the projectile ($\mathbf{V_p} \simeq \mathbf{v_e}$). This peak arises from electrons that become trapped in low-lying continuum states of the projectile. Depending on the collision system, the cusp electrons can stem from two competing processes. In the first process, the active electron is ionized from the target atom and subsequently captured into low-energy continuum states of the projectile. This ionization process may occur with or without the emission of a photon. The former is referred to as electron capture to the continuum (ECC) [83], while the latter is known as radiative electron capture to the continuum (RECC) [167]. In the second process, applicable only to non-bare projectiles, the emitted electron originates from the dressed ion and is ionized to the continuum of the projectile during the collision with a target atom. This process is termed electron loss to the continuum (ELC) [168]. It is important to note that in MeV/u collisions, the cusp peak is predominantly influenced by the ECC and ELC processes. Additionally, the identification of electrons originating from ELC requires the application of a coincidence condition between the observed electron and the up-charged projectile to ensure unambiguous identification.

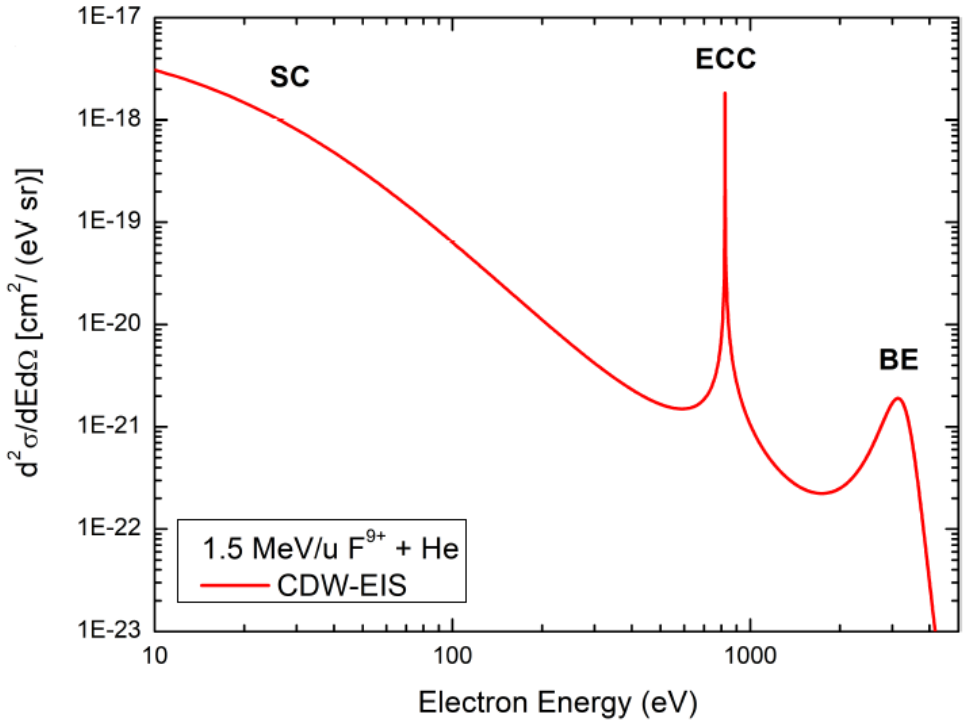

Figure 6.1: Example of DDCS electron spectrum demonstrating the different electron production processes, i.e., soft collisions (SC), electron capture to the continuum (ECC), and binary encounter (BE). The spectrum was determined through CDW-EIS calculations for collisions of 1.5 MeV F^{9+} + He. Taken from [5].

The observation of two-center effects dates back 50 years [169], marking an important milestone in the field. The pioneering investigation of the ECC peak can be credited to the experimental work conducted by Crooks and Rudd [83]. Theoretical interpretations by Salin [170] and Macek [171] further shed light on this phenomenon. Subsequently, a wealth of experimental data and theoretical treatments have significantly contributed to our understanding of the underlying physics behind cusp electrons. Noteworthy contributions in this area come from the pioneering theoretical efforts of Shakeshaft and Spruch [172–174], who have made significant strides in advancing our knowledge on the subject matter.

Observations of ECC and ELC processes contributing to the cusp peak have been made possible through experiments conducted at tandem Van de Graaff accelerators using low Z projectile ions and collision energies in the few MeV/u range [175–178]. Recent studies have expanded the understanding on ECC by investigating various factors: (a) the acceptance of electron solid angles [86], (b) the impact parameter [87], and (c) the recoil momentum of the target [88]. Surprisingly, experiments involving neutral He projectiles in target ionization studies have revealed the formation of a cusp-shaped peak [93, 179], while classical trajectory Monte Carlo calculations considering antiproton impacts have predicted the formation of a dip or anti-cusp at electron velocities close to the projectile velocity [180]. The advent of heavy-ion accelerators has further enabled investigations into the collision dynamics of these processes promoting the investigation of cusp electrons near the relativistic regime [89–92, 181, 182]. All these studies pushed the boundaries of existing theories and inspired the development of new ideas for further advancements in the field.

While there have been numerous experimental studies on electron emission that include the ECC cusp peak [3, 175, 176], only a limited number of investigations have focused on collisions of bare projectiles with heavy atomic targets [183]. Furthermore, most of these studies were conducted for collision energies ranging from 50 to 500 keV/u [86, 87, 184–188]. Notably, Biswas et al. performed a systematic study at 6 MeV/u collision energy using carbon bare ions in collisions with He and Ne targets to compare distorted wave (DW) theories [189] with experimental results. However, there were no measurements at zero degrees emission that could expose the features of the ECC process. Considering that Coulomb ionization dominates in the MeV collision energy range, ECC studies between bare ions and multielectron targets in energetic collisions offer stringent tests of theories, providing insights into the dynamics of the active electron and the role of passive electrons in the ionized atomic target.

Moreover, while collisions with pre-excited ions delivered by various types of accelerators have been used for studies on fundamental collision processes [190–195], the processes of ECC and ELC have not been thoroughly examined in such collisions. The dynamics of these processes depend on the combined long-range Coulombic fields of the projectile and the target, leading to a characteristic cusp-shaped peak in the DDCS electron spectra observed around zero degrees with respect to the projectile beam and with emission velocities close to the projectile velocity.

In light of these aspects, our study aims to address these challenges through a comprehensive experimental investigation of such collision systems. Our work is complemented by state-of-the-art DW theories, aiming for an in-depth analysis and understanding of the underlying physics in the fundamental processes of ECC and ELC.

6.2 The CDW and CDW-EIS Approximations

The cusp-shaped peak has been effectively described by continuum distorted wave (CDW) and continuum distorted wave-eikonal initial state (CDW-EIS) theories [84]. Over the last few decades, these distorted wave theories have been extensively developed to elucidate intriguing experimental findings concerning cusp electrons. Nonetheless, these models have found crucial practical applications, especially in collisions involving protons or highly charged ions (HCIs) with molecules of biological interest [196–198]. For instance, when HCIs interact with biological tissues, a substantial number of low-energy electrons is generated. Understanding the role of these secondary electrons in radiation damage is crucial for radiation therapy, and DW theories have played a pioneering role in related studies. Consequently, it is imperative to continue advancing DW theories to further address their application in these important areas, but also in understanding in detail the physical mechanisms behind fundamental processes. In this section, we will briefly discuss a few key aspects of the DW theories and highlight their advancements through the present studies.

6.2.1 CDW Theory

The CDW theory, initially developed for the study of single electron capture and ionization from monoelectronic targets by bare projectile impact [199–201], has been extended to include multielectronic targets [202, 203]. This extension is based on the concept that a multielectronic system can be effectively reduced to a monoelectronic one within the framework of the independent electron model. Within this model, the target potential, denoted as V_T, is expressed as a combination of the Coulomb interaction between the active electron, i.e., the one to be ionized, the target nuclear charge Z_T, and the electrostatic interaction between the active electron and the passive electrons, denoted as $V_{\alpha p}$, which remain in their initial subshells throughout the collision process [21]:

$$V_T(\mathbf{x}) = -\frac{Z_T}{x} + V_{\alpha p}(\mathbf{x}) \; . \tag{6.1}$$

The CDW approximation is a first-order approximation in a distorted-wave series, where the initial and final distorted waves are proposed as:

$$\begin{aligned} x_i^+(\mathbf{x},t) &= \Phi_i(\mathbf{x},t)\, \mathcal{L}_i^+(\mathbf{s}) && (6.2)\\ &= \phi_i(\mathbf{x}) \exp\left(-i\, \varepsilon_i t\right) \mathcal{L}_i^+(\mathbf{s}) \; , && (6.3) \end{aligned}$$

and

$$\begin{aligned} x_f^-(\mathbf{x},t) &= \Phi_f(\mathbf{x},t)\, \mathcal{L}_f^-(\mathbf{s}) && (6.4)\\ &= \phi_f(\mathbf{x}) \exp\left(-i\, \varepsilon_f t\right) \mathcal{L}_f^-(\mathbf{s}) \; , && (6.5) \end{aligned}$$

Here, s represents the active electron coordinate in the projectile reference frame. In Eqs. 6.2, 6.4, $\Phi_i(\mathbf{x},t)$ and $\Phi_f(\mathbf{x},t)$ represent the solutions of the time-dependent target Schrödinger equation for the initial bound and final continuum states, respectively. In Eq. 6.3, ε_i denotes the electron energy in the initial bound state, while in

Eq. 6.5, $\varepsilon_f = \frac{1}{2}k^2$ represents the electron energy in the final state, where k is the linear momentum of the ejected electron in the target reference frame.

The initial distortion is proposed as:

$$\mathcal{L}_i^+(\mathbf{s}) = N\left(\frac{Z_p}{\mathrm{v}}\right)\ {}_1F_1\left[i\,\frac{Z_p}{\mathrm{v}}; 1; i\ \ (\mathrm{v}s + \mathbf{v}\cdot\mathbf{s})\right]\ , \tag{6.6}$$

whereas the final distortion is chosen as:

$$\mathcal{L}_f^-(\mathbf{s}) = N^*\left(\frac{Z_p}{p}\right)\ {}_1F_1\left[-i\,\frac{Z_p}{p}; 1; -i\ \ (ps + \mathbf{p}\cdot\mathbf{s})\right]\ , \tag{6.7}$$

where $\mathbf{v}$ is the projectile velocity, $\mathbf{p} = \mathbf{k} - \mathbf{v}$ is the ejected electron momentum in the projectile reference frame, and $N(a) = \exp(\pi a/2)\Gamma(1+ia)$ (with Γ being the Euler Gamma function) is the normalization factor of the ${}_1F_1$ hypergeometric function.

The initial bound state of the target ϕ_i and its binding energy ε_i in Eq. 6.3 is calculated by means of Roothaan-Hartree-Fock atomic wavefunctions [31, 204]. On the other hand, the target final continuum state ϕ_f is chosen as an analytical hydrogen-like continuum function:

$$\begin{aligned}\phi_f(\mathbf{x}) =& \frac{1}{(2\pi)^{3/2}}\exp\left(i\ \mathbf{k}\cdot\mathbf{x}\right)\\ &\times N^*(\lambda)\ {}_1F_1\left[-i\ \lambda, 1, -i\ \ (kx + \mathbf{k}\cdot\mathbf{x})\right]\ ,\end{aligned} \tag{6.8}$$

with $\lambda = \tilde{Z}_T/k$, where $\tilde{Z}_T$ is an effective or net target charge to be chosen. This approximation has been previously used with success for electron capture [201]. It implies the replacement of the target potential by effective Coulombic ones for each target orbital in the final channel. However, this implies the loss of orthogonalization between initial and final states.

Finally, the double differential cross section in electron emission energy (E_k) and solid ejection angles is obtained as [205]:

$$\frac{d^2\sigma^\pm}{dE_k d\Omega_k} = k\int d\eta\left|\mathcal{R}_{if}^\pm(\eta)\right|^2\ , \tag{6.9}$$

$\mathcal{R}_{if}^\pm(\eta)$ being the scattering matrix element as a function of the transverse momentum transfer η, with the $-$ and $+$ sign denoting its *prior* and *post* form, respectively. The transition amplitude obtained with the *prior* version of the CDW theory is known to have intrinsic divergences that forbid its correct integration to obtain the differential cross sections [206].

The *post* CDW operator W^{CDW-} is given by

$$W_f^{CDW-}\chi_f^- = \Phi_f(\mathbf{x},t)\left[\nabla_\mathbf{x}\ln\phi_f(\mathbf{x})\cdot\nabla_\mathbf{s}\mathcal{L}_f^-(\mathbf{s})\right] + \tilde{V}_T(\mathbf{x})\chi_f^-\ , \tag{6.10}$$

where the first term is the well known *post* CDW perturbative operator and the second one is related to an additional potential left unsolved by the choice of ϕ_f

$$\tilde{V}_T(\mathbf{x}) = -(Z_T - \tilde{Z}_T)/x + V_{ap}(\mathbf{x})\ , \tag{6.11}$$

with $V_{ap}(\mathbf{x})$ being the interaction between the active electron and the passive ones [205].

The potential $\tilde{V}_T$ is typically not considered in the conventional *post* version of the CDW theory. In this version, we utilize an effective charge $\tilde{Z}_T = n_i\sqrt{-2\varepsilon_i}$ [201], where n_i represents the principal quantum number of the initial bound subshell. This effective charge accounts for the hydrogen-like continuum behavior of the residual target continuum final state. However, to incorporate the non-Coulombic interaction between the active and passive electrons, a more comprehensive CDW approximation includes the $\tilde{V}_T$ potential.

Following the work of [204] we consider $\tilde{V}_T$ in terms of a Green, Sellin, and Zachor (GSZ) analytical parametric potential [29], and re-write Eq. 6.11, giving:

$$\tilde{V}_T(\mathbf{x}) = -\frac{(q-\tilde{Z}_T)}{x} - \frac{(Z_T-q)}{x}\Omega(x)\,, \tag{6.12}$$

with

$$\Omega(x) = \left[H\left(e^{x/d}-1\right)+1\right]^{-1}\,, \tag{6.13}$$

$q = Z_T - N$ being the net charge of the target, with N the number of passive electrons, and d and $H(= d \times K)$ parameters dependent on Z_T and N [29]. The parameters used for each target in this work are shown in table 6.1.

Table 6.1: Parameters d (a.u.) and K (a.u.) of the GSZ potential for the different targets considered, extracted from [29].

Target	d	K
He	0.381	1.77
Ne	0.558	2.71
Ar	1.045	3.50

The transition amplitude for the *post* version of CDW is:

$$\mathcal{R}^+_{if}(\eta) = -i\,\frac{4\pi^2}{\mathrm{v}}\mathbf{F}^{a+}(\mathbf{K})\cdot\mathbf{G}^{a+}(\mathbf{K})\,, \tag{6.14}$$

where $\mathbf{K}$ is the momentum transfer in the center of mass of the system. Explicit expressions of $\mathbf{F}^{a+}$ and $\mathbf{G}^{a+}$ can be found in [206].

To address the issue of dynamic screening and overcome the inherent divergences encountered in the *post* version of the CDW theory, a comprehensive *hybrid* approach has been proposed [206]:

$$\mathcal{R}^+_{if}(\eta) = -i\,\frac{4\pi^2}{\mathrm{v}}\left[\mathbf{F}^{a+}(\mathbf{K})\cdot\mathbf{G}^{a+}(\mathbf{K}) + \; F^{b+}(\mathbf{K})G^{b+}(\mathbf{K})\right].$$

Explicit expressions of $\mathbf{F}^{a+}$, F^{b+}, $\mathbf{G}^{a+}$ and G^{b+} can be found in [206]. In G^{b+} of Eq. 6.15, $\mathcal{L}^+_i$ is considered as an Eikonal phase given by:

$$\lim_{\mathrm{v}s\to\infty}\mathcal{L}^+_i(\mathbf{s}) \equiv \mathcal{L}^{EIS+}_i(\mathbf{s}) = \exp\left[-i\,\frac{Z_P}{\mathrm{v}}\ln\left(\mathrm{v}s+\mathbf{v}\cdot\mathbf{s}\right)\right]. \tag{6.15}$$

6.2.2 CDW-EIS Theory

The CDW-EIS theory was initially introduced by Crothers and McCaan [207] to address the issue of the lack of normalization of the initial channel projectile distortion

in the study of electron ionization by bare ions. In this theory, the initial channel projectile distortion is proposed as:

$$\mathcal{L}_i^{EIS+}(\mathbf{s}) = \exp\left[-i\,\frac{Z_P}{\mathrm{v}}\ln\left(\mathrm{v}s + \mathbf{v}\cdot\mathbf{s}\right)\right]. \tag{6.16}$$

The final channel projectile distortion is considered as in Eq. 6.7.

The *prior* version of the CDW-EIS approximation is free of any divergences and the perturbative operator W^{EIS+} results as:

$$W_i^{EIS+}\,\chi_i^+ = \Phi_i(\mathbf{x},t)\left[\frac{1}{2}\nabla_{\mathbf{s}}^2\mathcal{L}_i^+(\mathbf{s}) + \nabla_{\mathbf{x}}\ln\phi_i(\mathbf{x})\cdot\nabla_{\mathbf{s}}\mathcal{L}_i^+(\mathbf{s})\right]. \tag{6.17}$$

The initial bound and final continuum target wavefunctions are considered as in the above mentioned CDW theory. Explicit expression for the *prior* CDW-EIS transition amplitude can be found elsewhere [205].

Instead of approximating the final target continuum with an effective Coulomb potential, the CDW-EIS theory employs numerical solutions of the target Schrödinger equation to obtain the initial bound and final continuum target wavefunctions. The procedure for calculating the transition amplitude within this theory was demonstrated by Gulyás et al. [208], resulting in the *numerical* version of CDW-EIS. Importantly, this approach maintains the orthogonality between the initial bound and final continuum target wavefunctions. It should be noted that in the calculation of the initial bound states in this *numerical* version of CDW-EIS, the binding energies ε_i for each subshell are taken from the values provided by Clementi and Roetti [31].

6.2.3 Distorted Wave Theories for Dressed Projectiles

The extension of distorted wave theories to electron emission in collision systems involving dressed projectiles has been studied in [209]. In such cases, the projectile potential is modeled as the combination of a long-range Coulombic potential and a screened short-range potential. The screening function, which governs the short-range interaction, depends on parameters that have been tabulated for a wide range of ground state ions [29]. However, for the specific case of the $O^{6+}(1s2s)$ excited state examined in this study, the necessary parameters were not available in existing tabulations. Therefore, we have performed calculations to determine the corresponding potential. The projectile potential is then determined by considering the interaction between the target's active electron and the projectile nucleus, as well as its interaction with the averaged electronic distribution of the projectile's electrons. Finally, the total potential, resulting from the combined effects of electronic repulsion and nuclear attraction, is expressed as a long-range term with an asymptotic net charge, along with a short-range screened potential.

The excited state $1s2s$ projectile orbitals were derived using the Hartree-Fock wavefunctions as described in [210]. This approach extends beyond the determination of ground states, as previously reported in [31], and enables the representation of lower excited states of atoms and ions with up to 18 electrons. The analytical form obtained through this method closely approximates the numerical solutions, allowing for a convenient description of each shell in terms of Slater orbitals.

Furthermore, in the context of the CDW-EIS framework for dressed projectiles, we also incorporate a dynamic effective charge for the final-channel projectile continuum factor, as proposed in the recent work [93]. This allows us to account for collision dynamics where the nuclear charge of the projectile is not completely shielded by its bound electrons, which is applicable in the current scenario. The dynamic effective charge is determined based on the projectile form factor, and as a result, it varies depending on the electronic configuration of the projectile. Consequently, excited state projectiles exhibit less screening, implying that their potential is more spatially extended.

According to the above considerations we have calculated the target ionization by ground or excited state projectile impact, particularly the ECC process. Then, for the ELC we reverse the collision system and then transform the DDCS from the projectile reference frame to the laboratory one [84]. Finally, the simultaneous ionization of both collision aggregates is estimated by means of their single-ionization DDCS and total cross sections, as done in [211].

6.2.4 Comparison of Distorted Wave Theories with Experimental Double Differential Cross Sections

We performed a detailed comparison of the DW theories with experimental DDCSs in our study. The experimental setup of the spectrograph allowed us to detect electrons emitted within a polar angle range of $\theta_{\max} = 0.4^{\circ}$ relative to the projectile velocity.

It is important to note that the peak position of the DDCS is determined by a mathematical pole, and as a result, its height is susceptible to variations depending on the integration process. In order to provide a meaningful comparison between our theoretical calculations and the experimental data, there are cases where we performed an averaging of our theoretical zero-degree DDCS calculations over the experimental polar angle θ. However, this averaging process mainly influences the height of the cusp peak in the pole region, while leaves the cusp wings essentially unaffected.

This phenomenon has been thoroughly demonstrated in [5], where an integration analysis has been carried out, as depicted in Fig 6.2. The results revealed that the net zero-degree calculation yields a cusp peak cross section that surpasses the integrated calculation, leading to a reduction in the overall magnitude of the cusp peak. Notably, the integration process primarily impacts the central region of the cusp peak, while the wings of the peak remain unaffected.

Additionally, we did not convolute our DDCS calculations with the experimental resolution, which was approximately $\Delta E/E \simeq 1\%$. This decision was made due to the fact that the energy step of our calculations was of the same order as the experimental resolution. Therefore, convoluting the calculations with the experimental resolution would not have provided any measurable additional information.

6.3 Preliminary Studies

Low energy resolution is sufficient for measuring the cusp continuum, eliminating the need for high resolution energy measurements. Consequently, our spectrograph was

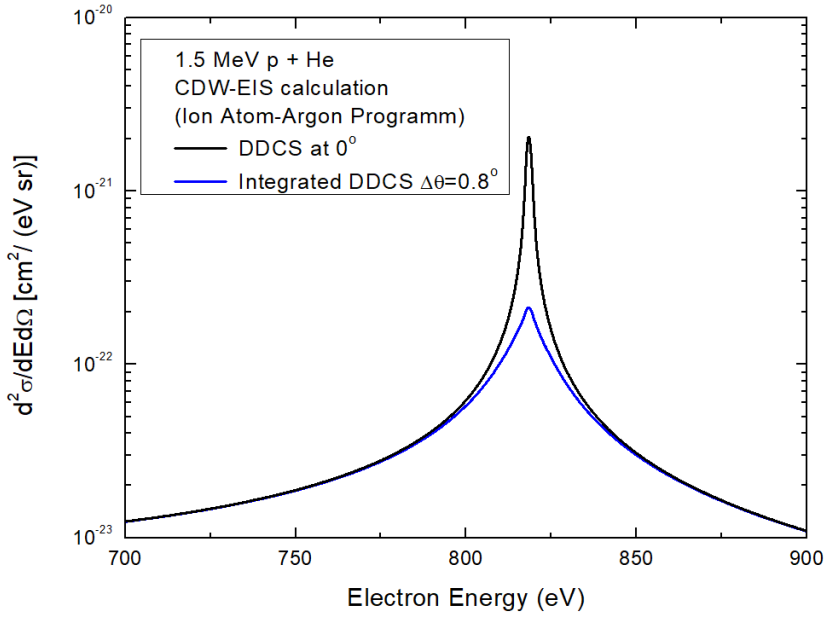

Figure 6.2: CDW-EIS DDCS calculations for the collision system 1.5 MeV p + He: (Black line) Calculation at zero degrees, (Blue Line) Angular integration of DDCS ($\Delta\theta = 0.8°$). The calculations were performed utilizing the Ion-Atom/Argon Program [17–20].

operated in low-resolution mode ($F = 1$). In this configuration, an electron spectrum covers approximately 20% of the tuning energy range. To capture the entire cusp peak, multiple energy windows were recorded at the corresponding tuning energies and subsequently combined [21].

An illustration of combining four overlapping energy windows for the collision system 1.50 MeV p + He is presented in Figure 6.3. The overlapping energy windows correspond to tuning energies of $W = 585,\ 685,\ 800$, and 940 eV. To account for background noise, spectra were also obtained without the target gas and subtracted from the spectra obtained with the gas target. The resulting spectra were then obtained calibrated using the established energy vs. channel calibration formulas, described in Section 4.2, followed by the DDCS determination using Eq. 4.6.

To ensure single collision conditions, the target gas pressure was appropriately adjusted. Due to the large number of detection channels in each energy window, a weighted averaging of the data was performed to enhance the visibility of the cusp peak. In Figure 6.3, the multicolored open circles represent the averaged data with statistical uncertainties within the size of the symbol. No statistical error bars are shown in the four overlapping energy windows for clarity. Overall, our measurements have an inherent absolute uncertainty of about 15%. The obtained DDCS spectrum is then compared to older measurements reported in [3], demonstrating a very good agreement. We mention that the data in [3] were obtained using a tandem parallel plate spectrometer with a smaller solid angle compared to our spectrograph, which explains the larger DDCS values at the cusp peak maximum.

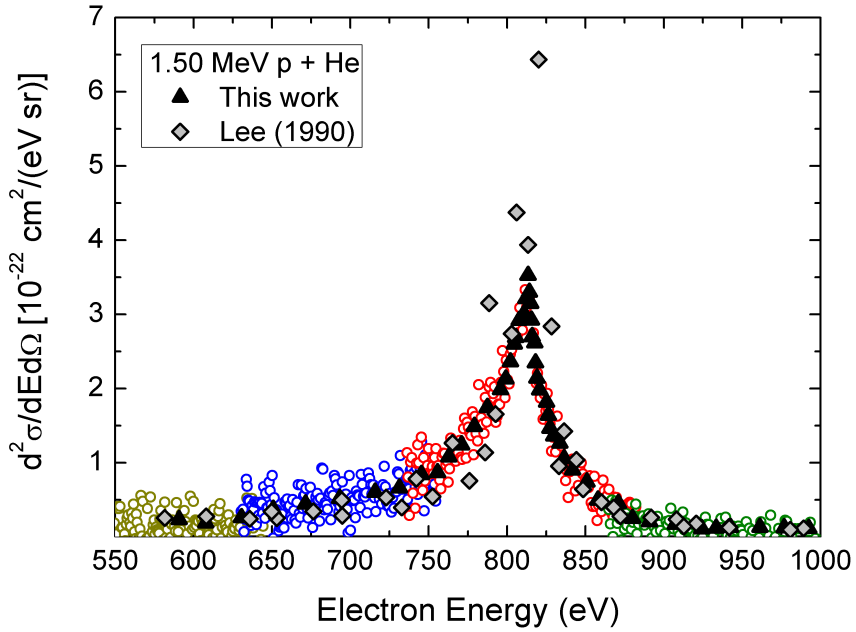

Figure 6.3: DDCS electron spectra measured at zero degrees with respect to the projectile velocity for collisions of 1.50 MeV protons with He. Triangles: Experimental data obtained in this work. Diamonds: Experimental data retrieved from [3]. Multicolored circles: The four overlapping energy windows covering the ECC cusp peak, the weighted average of which corresponds to the triangles (see text). Taken from [21].

6.4 Collisions with Bare Ions

This section focuses on a comparative study between the calculations of DW theories and the corresponding electron DDCS measurements at zero degrees emission angle for collisions of deuterons with multielectron Ne and Ar gas targets [21]. Ion-atom collision processes inherently involve complex many-body interactions, requiring the modeling of both target and projectile electrons. To establish benchmark calculations for collision models, He atoms are often considered due to their simpler two-electron ground state. In addition to the Ne and Ar gas targets, we also conducted measurements for the collision system of 1.50 MeV deuterons with He gas targets, spanning the energy range from the cusp peak to the BEe peak. The experimental DDCS electron spectra, along with the results from the examined DW theories, are presented in Fig. 6.4.

Fig. 6.4 demonstrates a generally similar behavior among the DW theories, with noticeable but significant differences, particularly in the low energy wing of the ECC cusp peak. At the high energy wing of the BEe peak, the theories converge. However, variations become more pronounced at the peak maximum. By comparing the absolute normalization of our measured electron yield to the BEe peak obtained from DW calculations, it is apparent that CDW-EIS-numerical calculations provide a better fit to the measurements.

It is worth noting that a recently developed four-body CDW-EIS theory demonstrates improved agreement with DDCS measurements involving proton collisions with He targets [212]. However, this approach is not included in this study as it is

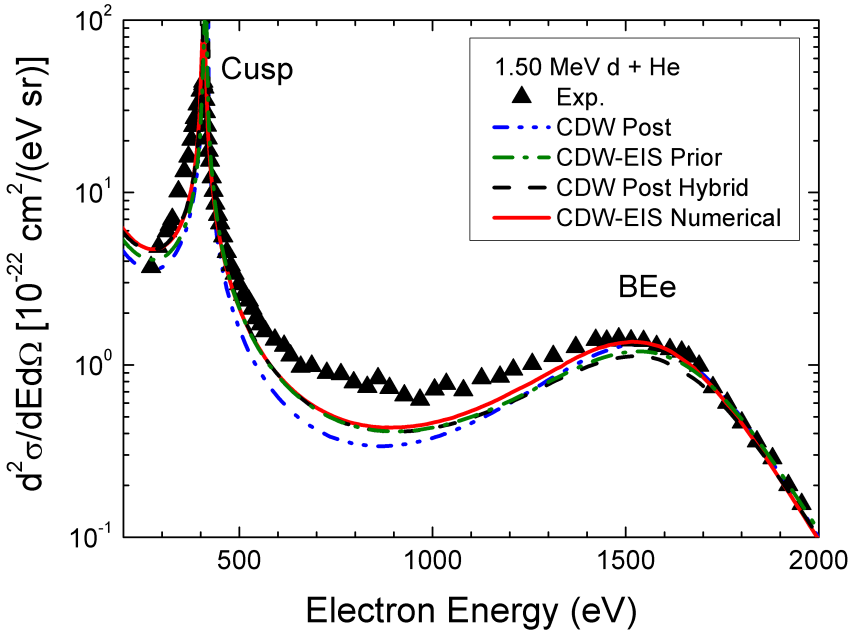

Figure 6.4: DDCS electron spectra measured at zero degrees with respect to the projectile velocity for collisions of 1.50 MeV deuterons with He. Symbols: experimental data. Lines: DW theories calculations (see Section 6.2). The spectral locations of the cusp and BEe peaks are depicted. Taken from [21].

only valid for two-electron targets. Regarding the electrons in the valley between the cusp and BEe peaks, all DW theories tend to underestimate the experimental DDCS.

Figure 6.5 displays the experimental DDCS obtained in collisions of deuterons with Ne and Ar gas targets at collision energies of 1.50, 3.00, and 6.00 MeV, along with the corresponding DDCS calculations from the DW theories. The experiments were conducted under identical conditions for each target, with the exception of the gas pressure, which was adjusted to ensure single collision conditions. To adequately capture the cusp peak, four overlapping energy windows were combined for the 1.50 and 3.00 MeV collision energies, while three energy windows were used for the 6.00 MeV collision energy.

At the 1.50 MeV collision energy with the Ne target, the CDW-post results deviate the most from the other theories, exhibiting the lowest DDCS value and lesser agreement with the experimental data. The remaining DW theories, CDW-EIS-numerical, CDW-EIS-prior, and CDW-post-hybrid, show a slight overestimation of the high energy wing of the ECC cusp peak and demonstrate close agreement with each other. However, at the low energy wing of the ECC peak, CDW-EIS-numerical exhibits better agreement with the experimental measurements, while CDW-EIS-prior and CDW-post-hybrid display similar behavior but with lower DDCS values. This qualitative behavior of the four considered theories remains consistent as the collision energy increases.

The behavior observed for the Ar target differs to some extent compared to the Ne target. At the 1.50 MeV collision energy, all the considered theories yield very similar results, showing good agreement with the low energy wing of the ECC cusp peak. However, there is an overestimation of the DDCS in the high energy wing by all theories. In contrast, at higher collision energies such as 3.00 MeV and particularly

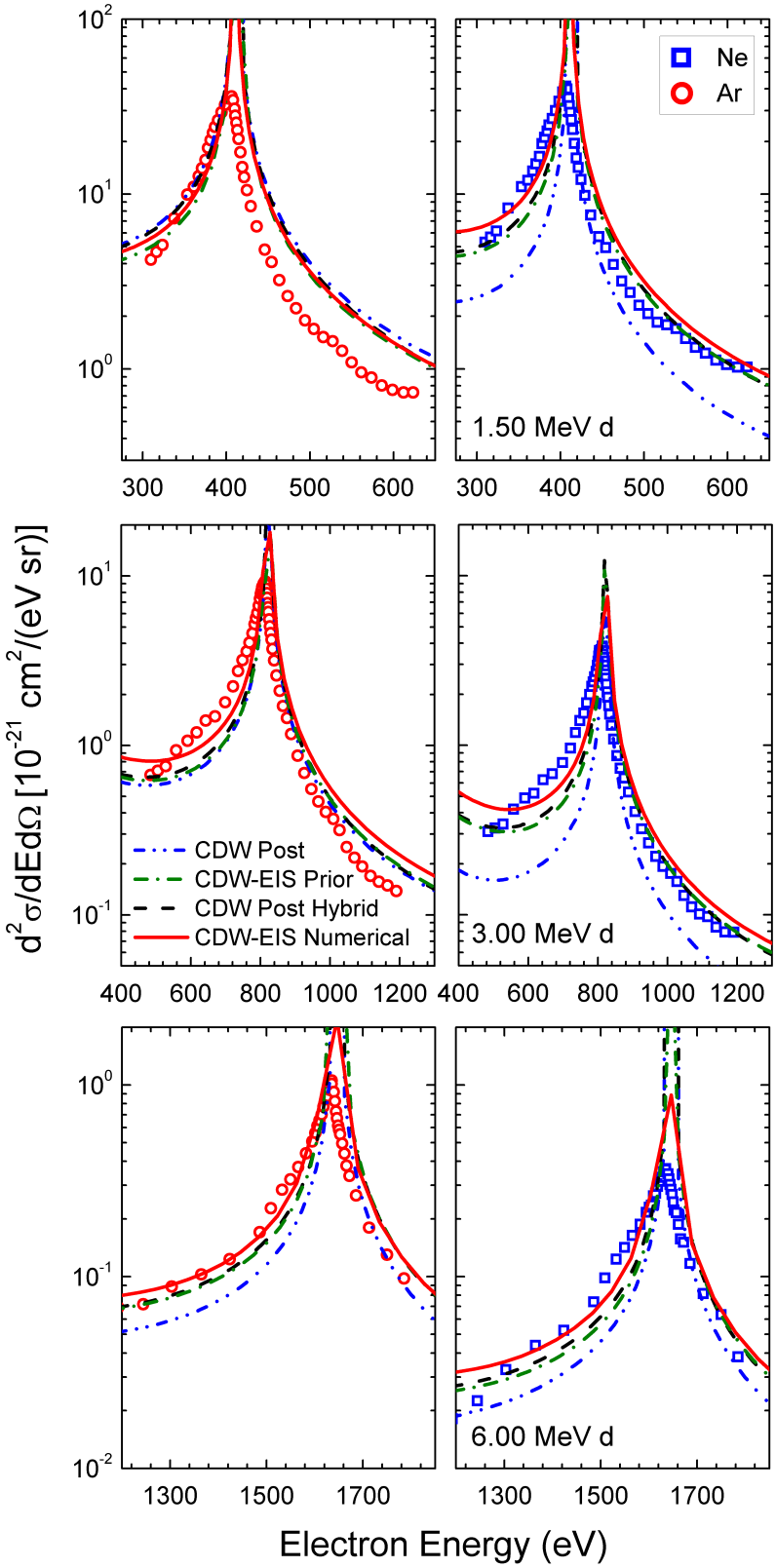

Figure 6.5: Electron DDCS measured at zero degrees with respect to the projectile velocity for collisions of: [top] 1.50 MeV; [middle] 3.00 MeV; [bottom] 6.00 MeV deuterons with [right] Ne and [left] Ar gas targets. The symbols correspond to the experimental data and the lines to the calculations of: (blue dash-dot-dotted line) CDW-post, (green dash-dotted line) CDW-EIS-prior, (black dashed line) CDW-post-hybrid, (red line) CDW-EIS-numerical. Taken from [21].

at 6.00 MeV, the theoretical results exhibit the qualitative behavior described earlier for the Ne target. These differences can be attributed to the contributions of different atomic subshells to the ECC process, which depend on the collision energy. Further details on these effects will be discussed below.

It is worth noting that the representation of the initial bound state has been shown to have a significant influence on the description of electron emission spectra [213]. An optimized potential model can be used instead of a Hartree-Fock-Slater model to calculate the initial state. It would be interesting to explore how the choice of initial bound state representation affects the asymmetry and height of the ECC cusp. This investigation could provide valuable insights into the sensitivity of the calculated results to the modeling of the initial state and help further refine our understanding of the electron emission process. While this subject remains an open question as it was beyond the scope of this study, and rather serves as an invitation for future research endeavors.

In our pursuit of a deeper understanding and a comprehensive analysis, we extended our investigation to explore the collision energies within the range of 1.25 to 2.00 MeV. Previous studies utilizing proton beams have reported the crossing of SDCSs for ECC as a function of collision energy in the range of 0.625 to 1.00 MeV for Ne and Ar targets [183]. For deuterons, this corresponds to the collision energy range of 1.25 to 2.00 MeV. Remarkably, this particular energy region has not been adequately detailed in the existing literature to the best of our knowledge, making it an unexplored domain that presents a rigorous challenge for the DW theories under examination.

In Fig.6.6(top), we present our experimental DDCS for the collision system of deuterons with Ne and Ar targets at collision energies of 1.25, 1.50, 1.75, and 2.00 MeV. It is evident that the DDCS for Ne is initially larger than that for Ar at the collision energy of 1.25 MeV, but it becomes smaller at the collision energy of 2.00 MeV. A subtle change in the magnitude of the DDCS for Ne and Ar is observed between the collision energies of 1.50 and 1.75 MeV, consistent with the findings reported in [183] for the corresponding SDCS results. This distinctive feature, revealed in the detailed level of the DDCS, can be unequivocally attributed to the contribution of the atomic subshells of the targets to the ionization process. Our theoretical results demonstrate that only the CDW-EIS-numerical theory can accurately reproduce this experimental result, whereas the other three CDW theories qualitatively capture the effect to some extent, but only at lower collision energies. In Fig.6.6(bottom), we present our DDCS calculations for the CDW-EIS-numerical theory, comparing them to the corresponding experimental measurements.

The successful reproduction of the change in the magnitude of the DDCS for Ne and Ar by the CDW-EIS-numerical theory highlights the importance of investigating the contributions of different atomic subshells to the ionization process. In Fig.6.7, we present CDW-EIS-numerical calculations that explore the contributions of the Ne and Ar atomic subshells to the formation of the ECC cusp peak in collisions with 1.25, 1.50, 1.75, 2.00, 3.00, and 6.00 MeV deuterons. The calculations consider the contributions of different magnetic quantum numbers of nl subshells by averaging over them. Generally, it can be argued that the relative contribution of each subshell to the ECC peak is primarily influenced by factors such as the relation between the electron linear velocity in the specific initial subshell and the projectile velocity, the subshell binding energy, and the number of electrons in that subshell. Detailed

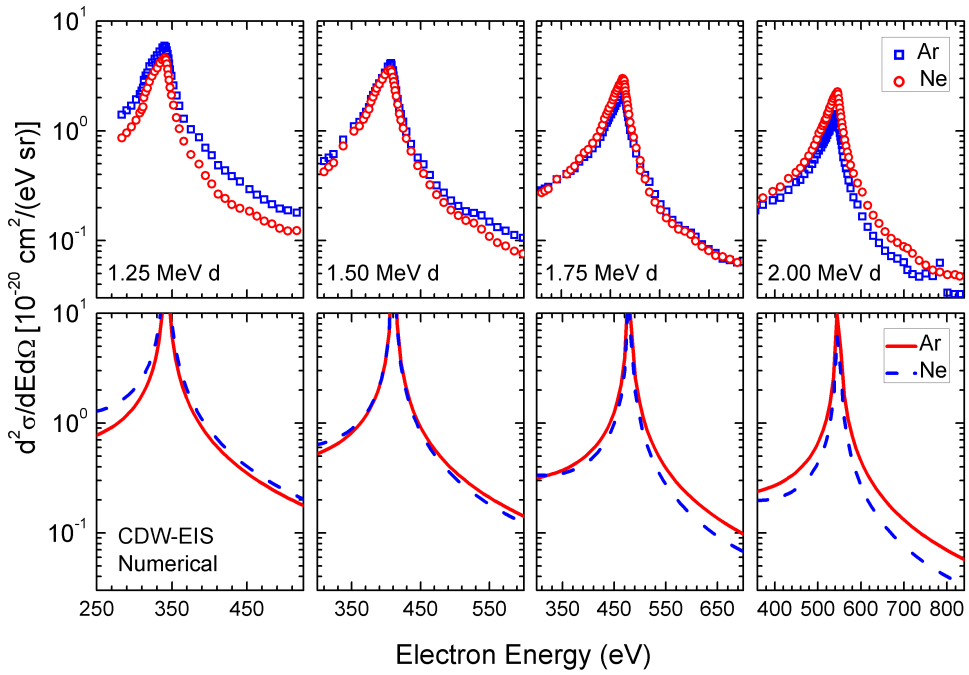

Figure 6.6: Electron DDCS measured at zero degrees with respect to the projectile velocity for collisions of 1.25-2.00 MeV deuterons with Ar (red) and Ne (blue) gas targets. The symbols correspond to the measurements and the lines to the calculations of the CDW-EIS-numerical theory. The small peak around 800 eV in the Ne spectrum of 2.00 MeV collision energy corresponds to the Ne-KLL Auger lines. Taken from [21].

information on subshell binding energies, velocities, as well as projectile energies and velocities, can be found in Table6.2. However, it is important to note that these relations serve as a general guide and cannot provide precise predictions.

From Fig.6.7 (top), we observe that in the case of Ne, the contributions from the $2p$ and $2s$ subshells decrease as the collision energy increases, with the $2p$ subshell exhibiting a faster decrease. The one-order-of-magnitude difference in contributions between the $2p$ and $2s$ subshells at a collision energy of 1.25 MeV becomes less significant at 6.00 MeV. Conversely, the contribution of the $1s$ subshell increases with increasing collision energy, eventually surpassing the contributions from the $2s$ and $2p$ subshells at 6.00 MeV. This can be attributed to the fact that the velocity of the ion beam is much closer to the linear velocity of the $1s$ subshell compared to the $2s$ and $2p$ subshells (see Table6.2), providing a partial explanation for this behavior. However, the most significant observation for the Ne case is that, in the collision energy range of 1.25 to 2.00 MeV, the $2p$ subshell makes the largest contribution to the ECC cusp peak.

From Fig.6.7 (bottom), we observe that for the Ar case, the contributions from the $3p$ and $3s$ subshells decrease as the collision energy increases, with the $3s$ subshell exhibiting a faster decrease. This behavior could be attributed to the higher binding energy of the $3s$ subshell compared to the $3p$ subshell (see Table6.2), as both subshells have relatively similar linear velocities. Interestingly, the contributions from the $2p$ and $2s$ subshells appear to be relatively insensitive to the collision energy in the range of 1.25 to 2.00 MeV, showing only a small decrease. The reduction in contributions becomes more noticeable at 3.00 MeV and even more pronounced at

Table 6.2: Subshell linear velocities, v_i (a.u.), [30], and binding energies, ε_i (a.u.), [31], for the Ne and Ar atoms, and deuteron projectile velocities, v (a.u.), for the different collision energies E_p (MeV) considered in Fig. 6.7.

Ne	1s	2s	2p			
$\lvert\varepsilon_i\rvert$	32.772	1.930	0.850			
v_i	8.113	1.299	2.500			
Ar	1s	2s	2p	3s	3p	
$\lvert\varepsilon_i\rvert$	118.610	12.322	9.572	1.277	0.591	
v_i	14.832	4.574	6.138	1.535	1.663	
E_p	1.25	1.50	1.75	2.00	3.00	6.00
v	7.074	7.749	8.370	8.948	10.959	15.498

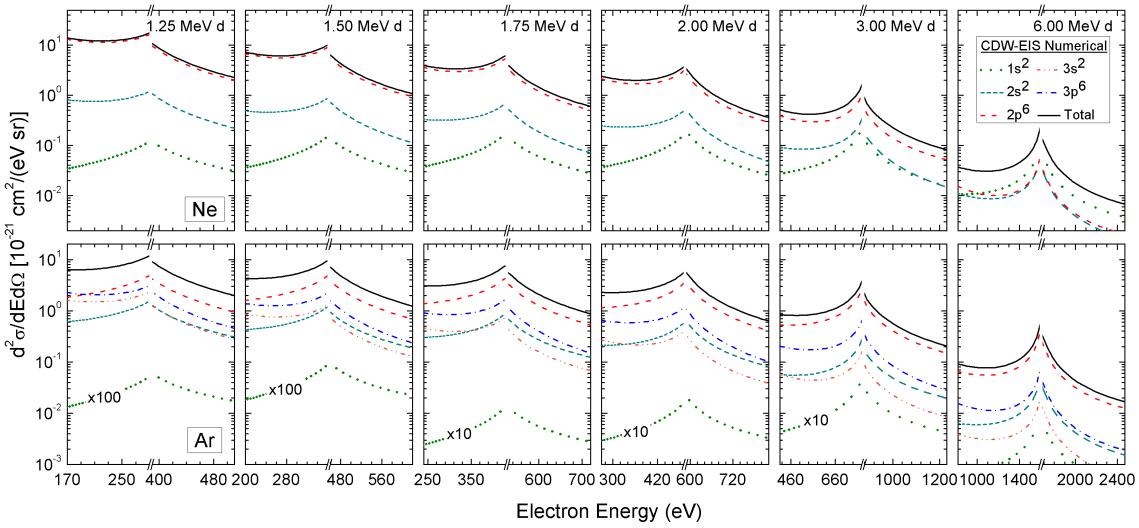

Figure 6.7: Contributions of the Ne [top] and Ar [bottom] atomic subshells to the formation of the ECC cusp peak in collisions with (from left to right) 1.25, 1.50, 1.75, 2.00, 3.00 and 6.00 MeV deuterons, corresponding to the CDW-EIS-numerical calculations. The break in the electron energy axes around the region of the pole of the cusp peak is to facilitate visibility. Note that the $1s$ contribution for Ar is multiplied by the factor of 100 for the collision energies of 1.25 and 1.50 MeV and by the factor of 10 for the collision energies of of 1.75, 2.00 and 3.00 MeV, respectively. Taken from [21].

6.00 MeV collision energies. The contribution from the $1s$ subshell is negligible and only becomes noticeable at the highest collision energy of 6.00 MeV. Similar to the case of Ne, the contribution from the $1s$ subshell increases with increasing collision energy, as expected from velocity matching arguments.

In the case of Ar, the most significant observation is that in the collision energy range of 1.25 to 2.00 MeV, the largest contribution to the ECC cusp peak comes from the $2p$ subshell, for which the CDW-EIS-numerical theory predicts an almost constant cross section. This subtle difference in the $2p$ contributions between the Ne and Ar cases seems to account for the crossing of their DDCS as shown in Fig. 6.6.

In our analysis, we also examined the subshell contributions for the other DW theories considered in this study. While similar general trends were observed, there were significant differences in their detailed behavior, leading to less accurate predictions compared to the CDW-EIS-numerical calculations within the range of collision energies considered.

To further investigate the source of the DDCS differences between the DW theories, we compared the initial radial wavefunctions used in CDW-EIS-prior (Clementi-Roetti wavefunction) and CDW-EIS-numerical (HF-numerical wavefunction). This comparison revealed only minor differences, which are unlikely to account for the observed differences in DDCS. This suggests that the discrepancies between CDW-EIS-prior and CDW-EIS-numerical can be attributed to differences in the final continuum functions.

In conclusion, we have presented experimental and theoretical results for the DDCSs for the ECC process in collisions of 1.25-6.00 MeV deuterons with He, Ne, and Ar targets. The comparison of the DDCS calculations obtained from four different DW theories showed that the CDW-EIS-numerical theory provided the best agreement with the experimental measurements. The differences among the DW theories were primarily attributed to the contributions of different atomic subshells to the ECC process. The analysis showed that the $2p$ subshell made the largest contribution to the ECC cusp peak for the collision energy range of 1.25 to 3.00 MeV for both Ne and Ar targets. Notably, the CDW-EIS-numerical theory accurately reproduced the observed subtle change in the magnitude of the DDCS for Ne and Ar in the collision energy range of 1.25 to 2.00 MeV. These findings lay the groundwork for future investigations that will encompass additional conditions (e.g. dressed projectiles) and wider energy ranges (e.g. soft electrons) to further assess the validity and applicability of different approximations.

6.5 Collisions with He-like Open-shell Excited State Projectiles

In this section, we present a combined experimental and theoretical study of cusp electrons generated in collisions of 24 MeV open-shell $O^{6+}(1s2s)$ projectiles and He targets [22]. Experimental cusp DDCS electron spectra were obtained using our double measurement technique, described in Section 4.5. In Fig. 6.8, we showcase the double measurement technique employed in the cusp study, specifically for the measurement of $1s2s2l$ KLL Auger spectra in collisions of 24 MeV O^{6+} beams with He. The technique involves using two O^{6+} beams with significantly different fractions of the ($1s^2$, $1s2s$) configuration.

The fraction f_{1s2s}, which is essential for our cusp studies, is determined by calculating the fraction $f_{1s2s\,^3S}$ and considering the statistical production ratio and the survival percentages of the $1s2s\ ^1S$ and $1s2s\ ^3S$ states. Assuming a statistical production ratio of 1/3 between the two states, and taking into account their lifetimes of 4.3×10^{-7} s and 9.6×10^{-4} s [77], respectively, the distance between the production area at the accelerator tank and the target area (25 m), and the velocity of the 24 MeV O^{6+} beam which is 1.7×10^7 m/s, we safely conclude that the fraction $f_{1s2s\,^3S}$ remains unaffected. However, the initial population of the $1s2s\ ^1S$ state is reduced by a factor of approximately 10. This reduction corresponds to about 1/30 of the population of the $1s2s\ ^3S$ state and can be safely neglected. Thus, under these experimental conditions, we can obtain the f_{1s2s} fraction using Eq.4.36, where $f_{1s2s} \simeq f_{1s2s\,^3S}$. For the spectra presented in Fig.6.8, the high and low f_{1s2s} fractions were determined as $f_{1s2s} = (23 \pm 4)\%$ and $f_{1s2s} < 2\%$, respectively. The latter value falls within the experimental uncertainty, allowing us to consider it as a nearly pure ground state beam.

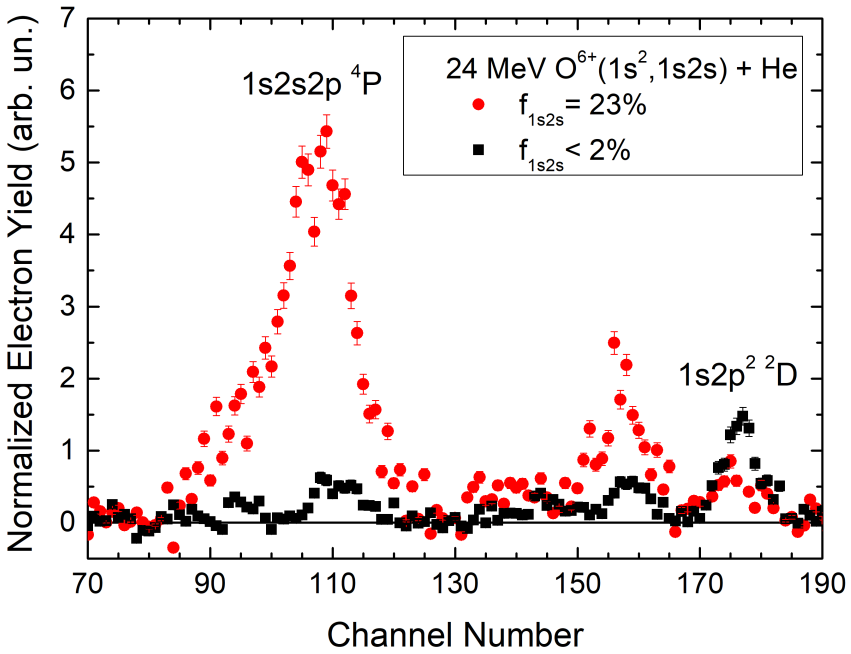

Figure 6.8: KLL Auger spectra measured at zero degrees with respect to the projectile velocity for collisions of 24 MeV $O^{6+}(1s^2,\ 1s2s)$ with He. The red-filled circles correspond to a mixed-state beam (high fraction measurement), while the black-filled squares correspond to an almost pure ground state beam as evidenced by the absence of the $1s2s2p\ ^4P$ peak (low fraction measurement). Taken from [22].

In Fig.6.9, we present the DDCS cusp measurements obtained for collisions of He-like O^{6+} beams with He, corresponding to the KLL Auger spectra shown in Fig.6.8. The cusp peak was observed for two different beams: the $O^{6+}(1s^2,\ 1s2s)$ mixed-state beam with a fraction of $f_{1s2s} = (23 \pm 4)\%$, and the nearly pure ground state beam $O^{6+}(1s^2)$. The maximum of the cusp peak is determined by the reduced projectile energy t_p, given by Eq. 2.3. The difference in magnitude and shape between the two cusp peaks is clearly visible in the experimental data.

In Fig.6.10, we show the contributions of the ECC and ELC processes to the DDCS cusp peak, as obtained from CDW-EIS calculations for collisions of 24 MeV

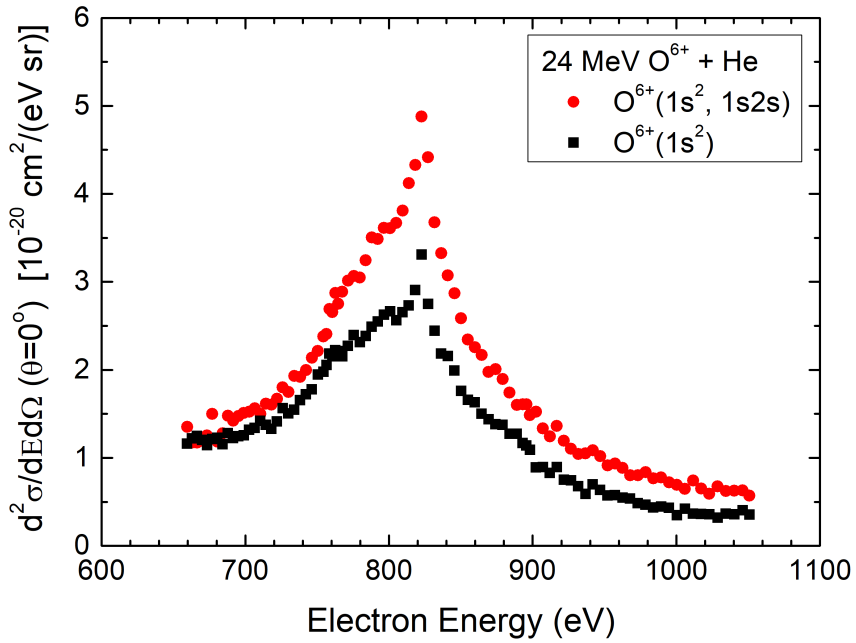

Figure 6.9: Zero-degree DDCS of cusp electrons measured in collisions of 24 MeV O^{6+} with He. Red filled circles: Mixed-state $O^{6+}(1s^2,\ 1s2s)$ beam with $f_{1s2s} = 23\%$. Black filled squares: Ground state $O^{6+}(1s^2)$ beam. Taken from [22].

$O^{6+}(1s^2)$ and 24 MeV $O^{6+}(1s2s)$ with He targets. The results clearly demonstrate that the ELC cross section from the $2s$ electron (ELC($2s$)) is approximately one order of magnitude larger compared to the ELC cross section for the $1s$ electron (ELC($1s$)) or the ECC cross section for both projectile configurations. Furthermore, the CDW-EIS calculations include the contribution of ELC from both $1s$ and $2s$ electrons with the simultaneous single ionization of the He target (ELC-I), which is found to be almost equally significant as the ELC($1s$) and ELC($2s$) for the ground and excited projectile cases, respectively.

A notable observation is that the ELC($1s$) cross section for the $O^{6+}(1s2s)$ configuration is smaller in comparison to the $O^{6+}(1s^2)$ configuration, despite the latter involving two electrons that need to be divided by two for a fair comparison. This discrepancy can be attributed to the reduced screening effect for the $1s$ electron in the $O^{6+}(1s2s)$ configuration, resulting in a different binding energy, as discussed earlier. Furthermore, although not significantly, the ECC process is influenced by the electronic configuration of the projectile through the projectile potential. It is noteworthy that the ECC cross section for the $O^{6+}(1s2s)$ configuration appears larger and exhibits more asymmetry compared to that of the $O^{6+}(1s^2)$ configuration. This behavior could be associated with the larger spatial extent of the electrons in the $O^{6+}(1s2s)$ configuration, favoring the capture process. A similar enhancement of the cusp peak due to metastable projectiles has been reported in a previous study [214].

The higher magnitude of the measured DDCS for the mixed-state beam can be primarily attributed to the larger contribution of the ELC($2s$) cross section. This enhanced contribution of the ELC process is also evident from the qualitative shape of the low-energy cusp wing. The ECC process exhibits a more pronounced asymmetry in its distribution compared to the ELC process [84]. As a result, in

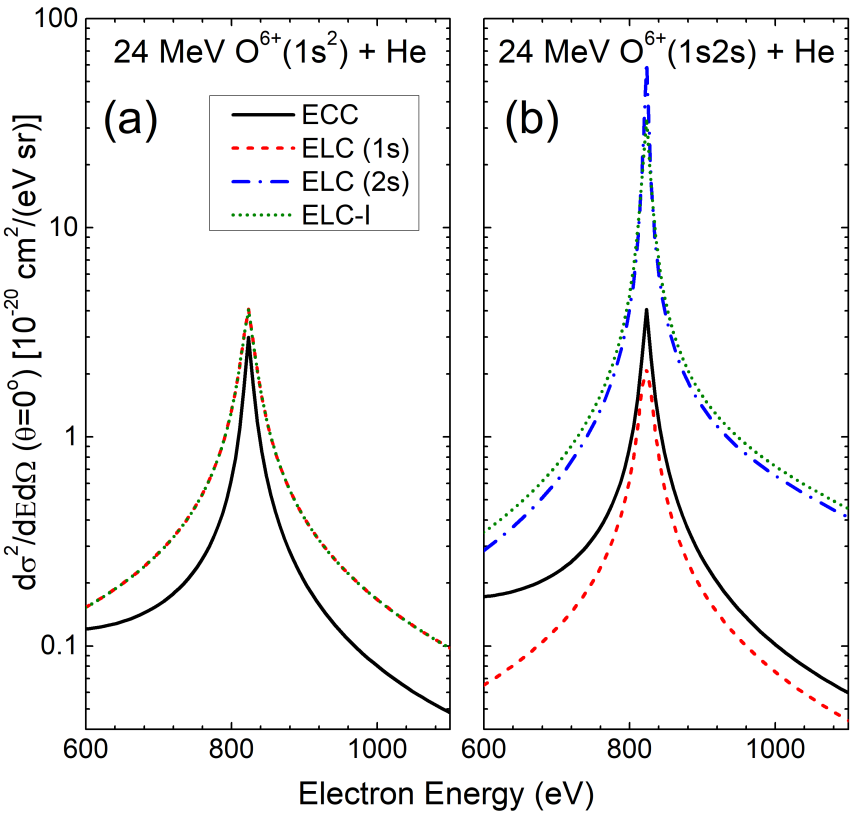

Figure 6.10: CDW-EIS calculations for zero-degree DDCS of cusp electrons for collisions of (a) 24 MeV $O^{6+}(1s^2)$ and (b) 24 MeV $O^{6+}(1s2s)$ with He. Black solid line: ECC contribution. Red short dashed line: ELC from the $1s$ electron. Blue dash-dotted line: ELC from the $2s$ electron. Green short-dotted line: Total ELC with simultaneous He target single ionization. Taken from [22].

the case of the ground state beam where ECC is dominant, the cusp peak displays a larger degree of asymmetry compared to the mixed-state beam where ELC($2s$) plays a predominant role.

In the double measurement technique, when one of the measurements corresponds to a pure $1s^2$ ground state beam, the electron DDCS spectra exclusively associated with the open-shell $1s2s$ configuration can be obtained straightforwardly using the following formula (see Appendix F):

$$\frac{d^2\sigma[1s2s]}{d\Omega dE} = \frac{\frac{d^2\sigma[1s^2,1s2s]}{d\Omega dE} - (1-f_{1s2s})\frac{d^2\sigma[1s^2]}{d\Omega dE}}{f_{1s2s}} \,. \tag{6.18}$$

In this study, significant efforts were made to fulfill the necessary conditions for the double measurement technique, as evident from the DDCS cusp spectra presented in Fig.6.9. By applying Eq.6.18 to the data shown in Fig.6.9, we successfully obtained the DDCS cusp spectra corresponding exclusively to the open-shell $O^{6+}(1s2s)$ configuration. These experimental results are presented in Fig.6.11, alongside the CDW-EIS theory calculations already shown in Fig. 6.10(b) for each individual process contribution. The uncertainties in the experimental data primarily arise from the determination of the f_{1s2s} fraction, which carries inherent uncertainties.

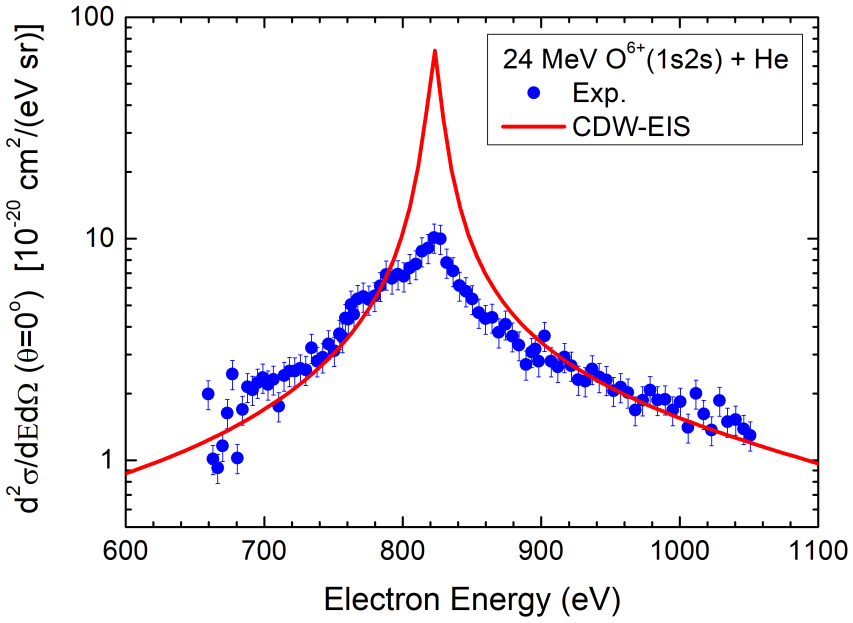

Figure 6.11: Zero-degree DDCS of cusp electrons for collisions of 24 MeV $O^{6+}(1s2s)$ with He. Blue-filled circles: Experimental data obtained from the double measurement cusp data shown in Fig. 6.9. Red line: Calculations based on the CDW-EIS theory. Taken from [22].

The CDW-EIS calculations demonstrate a remarkable agreement with the experimental data, particularly in reproducing the wings of the cusp peak. The position of the peak in energy is determined by a mathematical pole, which can introduce some variations in its height depending on the integration process (see Section 6.2.4). However, the excellent agreement observed in the wings of the cusp peak strongly

indicates that well-established and sophisticated collision theories like CDW-EIS can be further advanced and refined when tested against non-trivial collision systems.

In our specific case, the inclusion of appropriate projectile screened potentials, as well as the use of high-quality projectile wavefunctions for the $1s2s$ excited state, have proven to be instrumental in achieving a very good agreement with the experimental cusp data. These advancements in the CDW-EIS framework have shed light on the intricate interplay between the ECC and ELC processes in the production of cusp electrons, as discussed earlier. Overall, these improvements validate the effectiveness and accuracy of the CDW-EIS approach and highlight its ability to capture the essential features of complex dynamics in collision processes involving dressed projectiles.

6.6 Collisions with Be-like Projectiles

Our study on cusp electrons with multielectronic projectiles was extended to include Be-like oxygen ions, which are delivered in a mixture of a ground state $1s^22s^2\ ^1S$ and an excited state $1s^22s2p\ ^3P$, as detailed in Subsection 4.5.2. The inclusion of the $2p$ electron provides an exceptional laboratory for investigating cusp electrons, facilitating an expansion of our understanding about the ECC and ELC processes.

In detail, we recorded cusp electron peaks utilizing O^{4+} projectiles. In these studies, we incorporated the double measurement technique as to record cusp electron peaks originating from a projectile ion having either a $1s^22s2p\ ^3P$ high or low metastable fraction. The corresponding cusp electron peaks are shown in Fig. 6.12.

Interestingly, in the cusp electron peaks shown in Fig. 6.12, we observe the presence of secondary peaks that symmetrically emerge on both sides of the maximum of the cusp peak. These secondary peaks correspond to inelastic resonantly scattered Auger electrons and they are symmetrically located in the low and high energy wings of the cusp peak due to the doubling effect, described in Subsection 2.3.1. While the presence of these additional features in the spectra offers valuable insights into the underlying scattering processes, a comprehensive investigation of these peaks was beyond the scope of the present research. Future studies could utilize the high-resolution capabilities of our spectrometer to explore these features in various collision systems and further enhance our understanding of the involved dynamics.

It is noteworthy that the yield difference observed in the cusp electron peaks recorded with a low fraction content is not significantly different from those recorded with a high fraction content. This is attributed to the relatively small difference in the metastable beam fraction between the two measurements. However, it is evident that the cusp peaks originating from a projectile with a higher percentage of ions in the $1s^22s2p$ configuration are more prominent in all cases. This observation emphasizes the significance of the $2p$ electron in the collision process. The enhanced contribution may be attributed to the ELC process, as the $2p$ electron is more easily ionized during the collision. This argument is further supported by the symmetric shape of the cusp electron peaks observed in all cases. This symmetry suggests that the ELC process dominates over the ECC process for the collision systems at hand. Finally, the observed decrease in the cusp electron yield with increasing collision energy is consistent with expectations, as both the ECC and ELC DDCSs decrease with increasing collision velocity [176, 215].

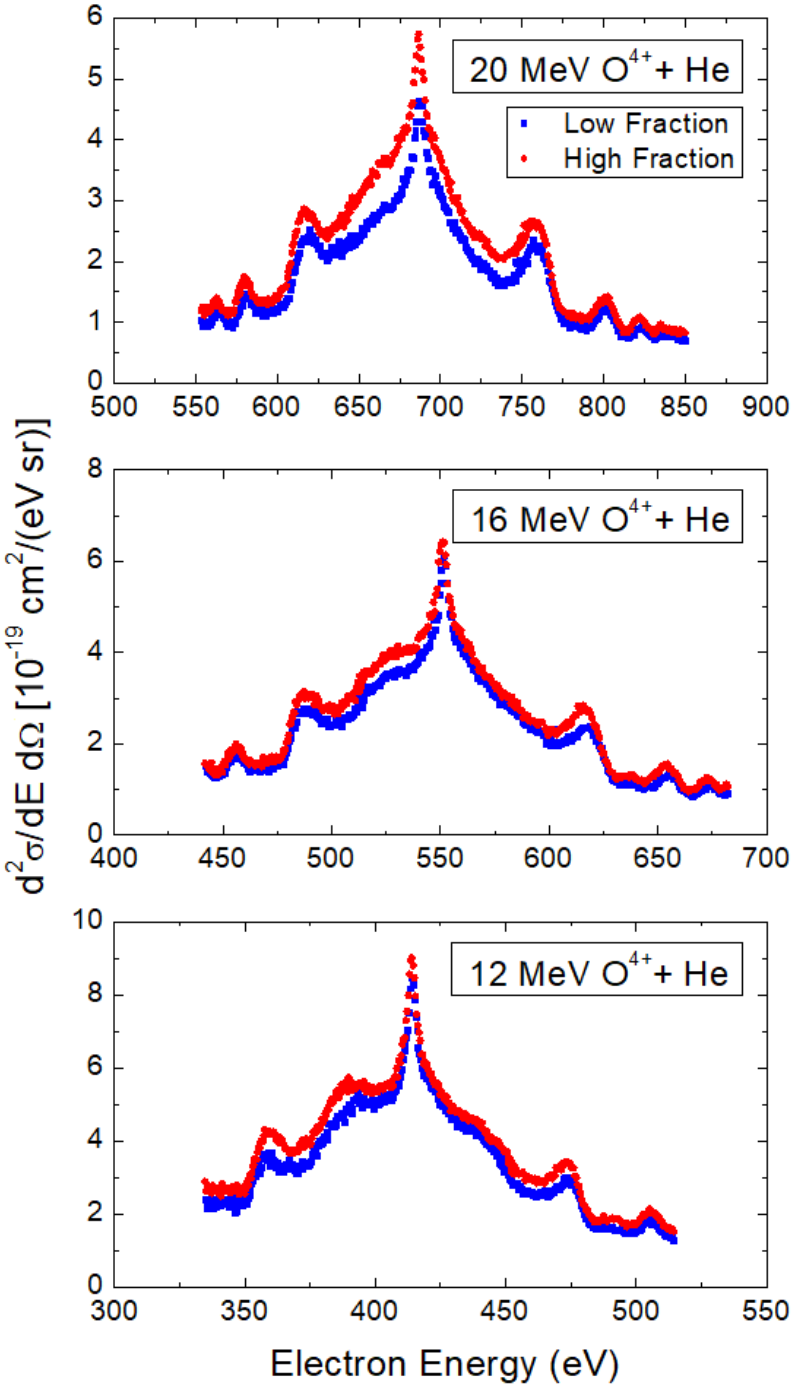

Figure 6.12: Zero-degree DDCS of cusp electrons for collisions of 20 MeV O^{4+} (top), 16 MeV O^{4+} (middle), and 12 MeV O^{4+} (bottom) with He; Blue-filled circles: Data corresponding to the low fraction measurement; Red-filled circles: Data corresponding to the high fraction measurement.

It should be mentioned that preliminary theoretical calculations for the above results are under way by our collaborating theoretical team in Rosario, Argentina. The complexity of the problem, involving four projectile electrons in open-shell configuration necessitates copious work before reaching safe results.

6.7 Evidence of ELC with simultaneous target ionization

During our cusp electron studies with He-like beams, we observed a small peak present in the low energy wing of the cusp peak, as evident in Fig. 6.9. This feature, never reported in the literature to the best of our knowledge, drew our attention and interest to systematically investigate it and determine its nature and origin.

First of all, it is important to mention that this observed peak cannot be attributed to any artifacts or analysis-related procedures. The peak is clearly evident in the central window of the spectra, ruling out any influence from the technique of overlapping spectra. Additionally, the peak cannot be explained by field ionization, as electrons undergoing ionization inside the spectrometer would gain energy, resulting in a peak located in the high energy wing of the cusp peak. Furthermore, we have excluded the possibility of this peak being an artifact caused by the optics of our setup or the fields of the HDA entry lens, as it is not consistently observed in all of our cusp measurements.

We started our systematic investigation by looking for the presence of the small peak using simpler configuration H-like projectiles. In Fig. 6.13, we present the cusp electron peak recorded in collisions of 24 MeV O^{7+} with He. An indication of a small peak in the low energy wing of the cusp peak can be argued. However, this indication is marginally above the range of experimental error, making it difficult to draw definitive conclusions.

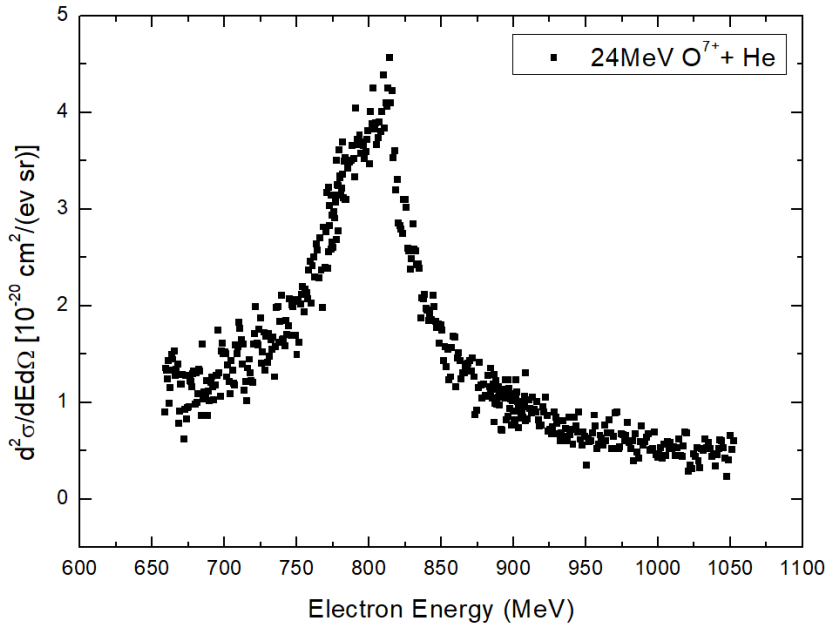

Figure 6.13: Zero-degree DDCS of cusp electrons for collisions of 24 MeV O^{7+} with He.

Since the peak is evident in collisions with He-like projectiles, as can be inferred from Fig. 6.9, we continued our investigations by utilizing Li-like projectiles. As it is clearly shown in Fig. 6.14, a peak is clearly seen in the low energy wing of the cusp peak for collisions of 24 MeV MeV O^{5+} + He. Interestingly, the location of the peak is approximately 25 eV lower than the maximum of the cusp electron peak, similarly to the case of He-like projectiles.

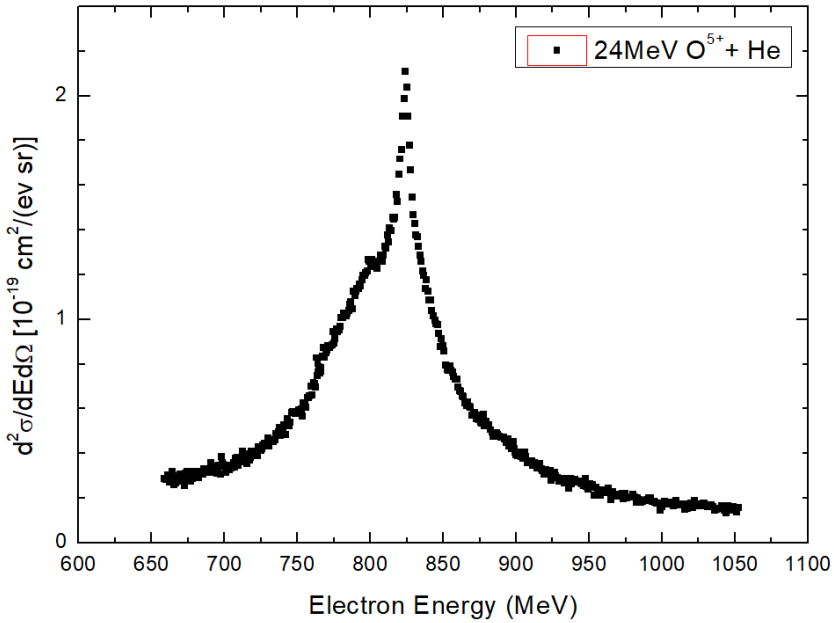

Figure 6.14: Zero-degree DDCS of cusp electrons for collisions of 24 MeV O^{5+} with He. A peak is evident on the low energy wing of the cusp peak, located around 25 eV lower than the cusp peak maximum.

To further validate our results we conducted experiments using He-like carbon beams. In Fig. 6.15, we present the cusp electron peak obtained from collisions of 12 MeV C^{4+} with He. Remarkably, the peak is again clearly observed in the low energy wing of the cusp peak, with its location being approximately 25 eV lower than the maximum of the cusp electron peak, as in the cases of oxygen ions.

In a next step, we extended our cusp electron studies to include multielectron targets and boron projectiles. In this set of experiments, we employed He-like boron projectiles and investigated their collisions with various gas targets, namely H_2, He, Ne, and Ar. The results of these experiments are presented in Fig. 6.16, showcasing the cusp electron spectra obtained from the different collision systems.

The presence of the peak is clearly evident in all the cusp electron spectra shown in Fig. 6.16. Consistently with our previous findings, we observe that the peak is located approximately 25 eV lower than the cusp peak maximum for collisions with He. Similar results corresponding to the peak location can be seen for collisions with Ne. Surprisingly, for collisions with H_2 and Ar targets, the peak is seen to be located approximately 16 eV lower than the cusp peak maximum.

It is noteworthy that He and Ne have similar ionization potentials (24.6 and 21.7 eV, respectively), while H_2 and Ar have also similar ionization potentials (15.5 and 15.75 eV, respectively). This observation suggests a relation between the location of the peak and the gas target. Furthermore, the shape of the shoulders

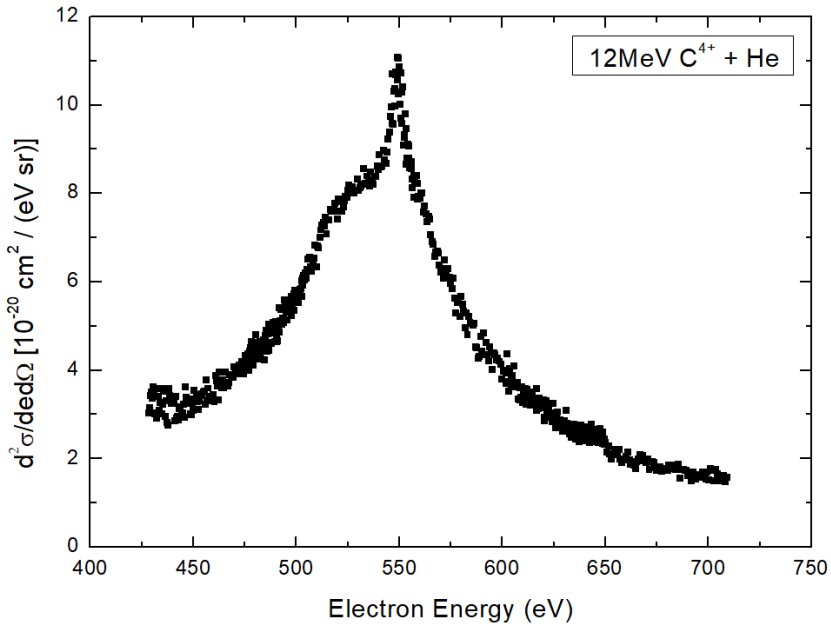

Figure 6.15: Zero-degree DDCS of cusp electrons for collisions of 12 MeV C^{4+} with He. A peak is evident on the low energy wing of the cusp peak, located around 25 eV lower than the cusp peak maximum.

observed in the cusp electron spectra for the pairs of (He, Ne) and (H_2, Ar) differ, possibly reflecting the underlying Compton profiles of the respective targets.

Based on these observations, we propose that the existence of the peak can be understood within a collision picture where the electron loss to the continuum occurs simultaneously with the ionization of the target electron through the projectile-electron–target-electron interaction process. As a result, the energy of the projectile cusp electron is lowered by an amount corresponding to the ionization energy of the target electron, leading to the observed shift in energy.

In our continued investigation, we extended our studies to include Li-like boron projectiles in collisions with H_2, He, Ne, and Ar. The cusp electron spectra obtained for these collision systems, as shown in Fig. 6.17. It is seen that the location and shape of the peak exhibit similarities for the pairs (He, Ne) and (H_2, Ar), as previously discussed for He-like boron projectiles. These consistent findings points toward a new electron loss to the continuum process that involves correlated electron-electron interactions (ELCee). This process is distinct from the typical ELC process and represents a novel contribution to the cusp electron formation in ion-atom collisions.

A noteworthy observation is that the intensity of the peak appears to decrease with increasing atomic number Z of the projectile. This behavior could be attributed to the fact that the ELC process becomes more dominant as Z increases [216], potentially overshadowing the ELCee process. These findings highlight the need for further adjustments and refinements in the distorted wave models to accurately account for this cusp electron shoulder and gain deeper insights into its underlying dynamics. Ongoing theoretical developments aim to shed light on these experimental findings and provide a comprehensive understanding of the observed phenomenon.

As a last comment, we would like to point that the absence of this small peak in

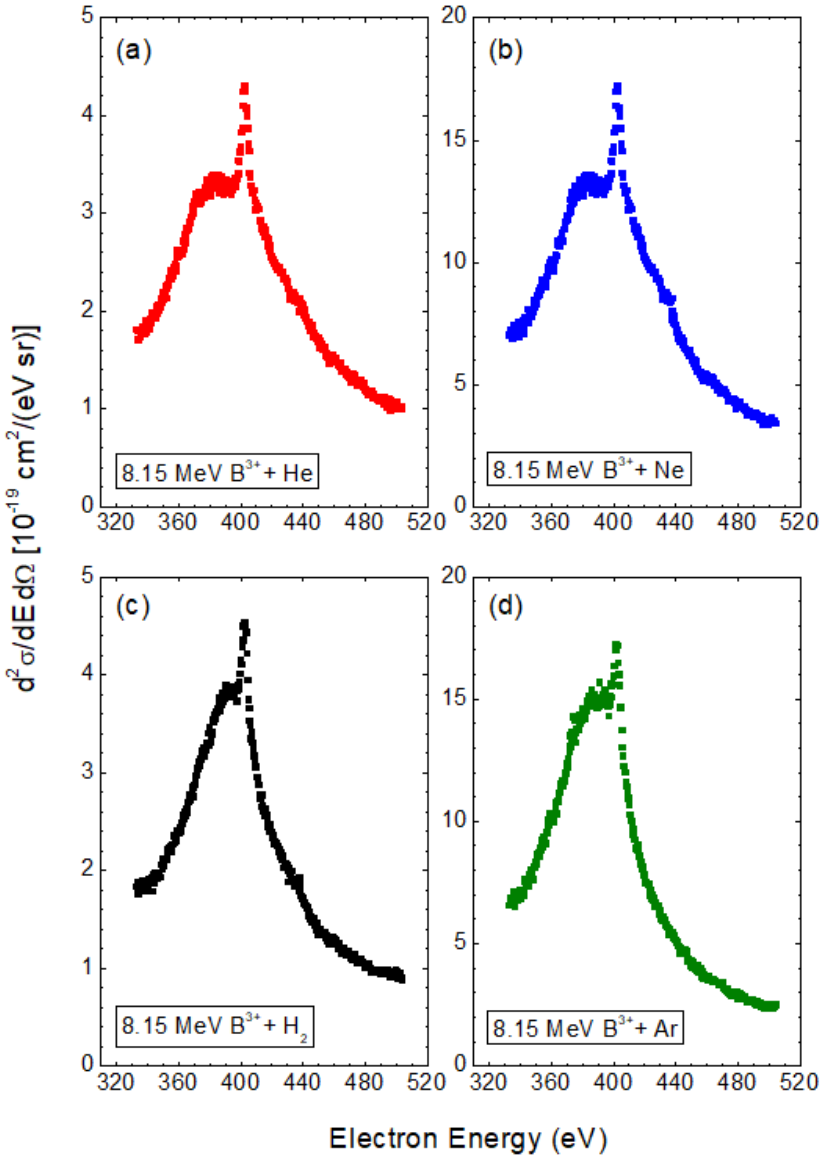

Figure 6.16: Zero-degree DDCS of cusp electrons for collisions of 8.15 MeV B^{3+} with (a) He, (b) Ne, (c) H_2, and (d) Ar. A peak is evident on the low energy wing of the cusp peak, located around 25 eV and 15 eV lower than the cusp peak maximum for the pairs of (He, Ne) and (H_2, Ar), respectively.

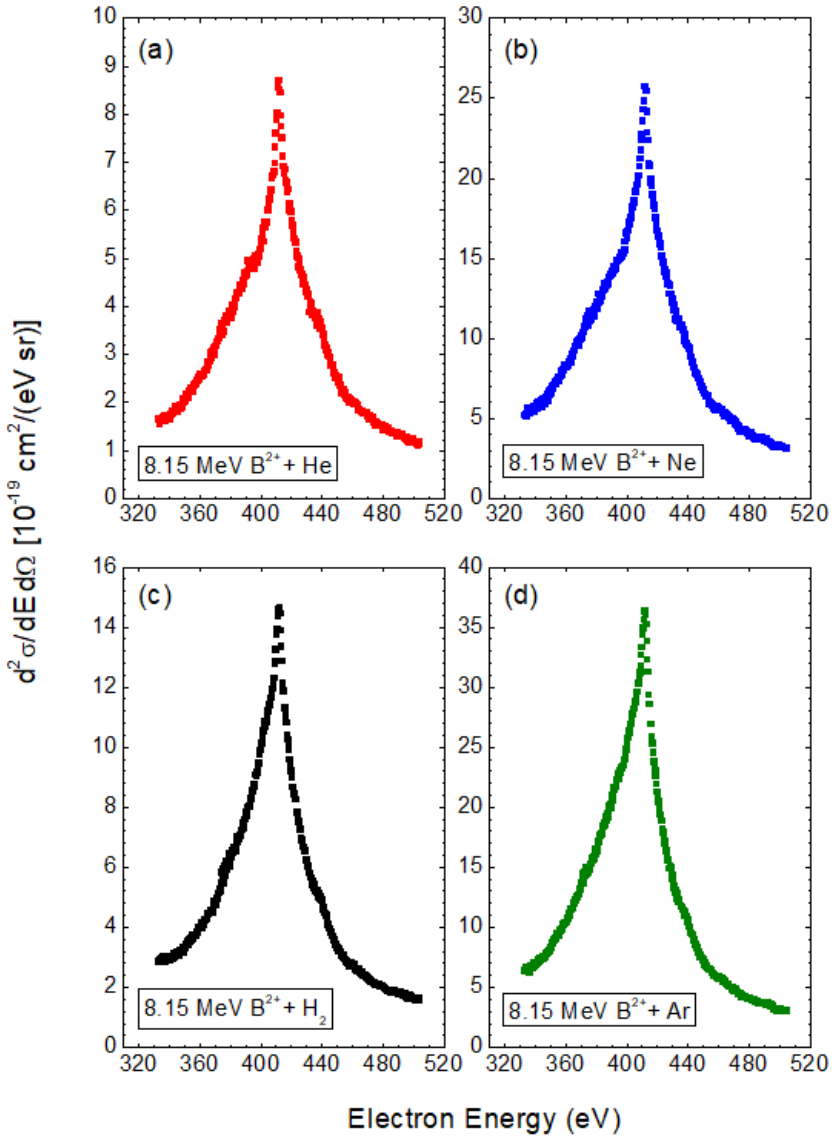

Figure 6.17: Same as Fig. 6.16 for for collisions of 8.15 MeV B^{2+} with (a) He, (b) Ne, (c) H_2, and (d) Ar.

previous studies can be attributed to several factors. Firstly, electron spectrometers used in those studies were often tuned to large energy resolutions, as the cusp peak is a continuous peak where high resolution is not necessary. Consequently, this feature would be smeared out in low-resolution measurements. For instance, in [211] the setup used allowed for an energy resolution of $\Delta E/E = 6\%$, i.e., 12 eV for a cusp of 200 eV. Secondly, the larger acceptance solid angles typically employed in previous measurements may have contributed to the lack of observation. In contrast, our measurements utilized a smaller solid angle of 0.4 degrees, allowing for a more precise characterization of the cusp electron spectra. Lastly, previous cusp electron studies often focused on lower collision energies where the cusp peak is more pronounced, potentially overshadowing the presence of the ELCee shoulder. Thus, the combination of our relatively high-resolution measurements and the specific collision conditions probably account for the appropriate conditions to expose the small peak and the related proposed process.

In conclusion, our experimental results have unequivocally confirmed the existence of a distinct peak in the DDCS cusp electron spectra. Remarkably, this peak is observed for various low-Z projectile ion species, while its location and shape are seen to be largely determined by the gas target. To explain this behavior, we proposed a new process that involves an electron loss to the continuum process accompanied by an electron-electron ionization of the target electron, termed ELCee. The emergence of this previously unreported feature presents new challenges and opportunities for advancing collision theories, and further theoretical investigations are warranted to unravel the underlying dynamics and provide deeper insights into the intriguing physics of this dynamic collision process.

Chapter 7

Single Electron Capture

7.1 Background and Motivation

Understanding the dynamics of excited atomic structures with multiple unpaired electrons presents a challenging task in theoretical modeling, primarily due to the intricate interplay of fundamental quantum aspects such as multiple spin symmetries, electronic correlation, and strong coupling among various open reaction channels. To delve into this level of complexity and gain deeper insights, high-energy collisions involving few-electron ions and atomic targets offer an ideal quantum system for probing the underlying physics at its most fundamental level. State-selective Auger electron spectra provide invaluable information about the atomic structure of the observed states and their fundamental production proceses, thus serving as rigorous tests for theoretical models [74, 217, 218]. Beyond fundamental research, such experimental and theoretical studies find practical applications in diverse areas, including astrophysical and laboratory plasmas [219, 220].

In a recent breakthrough study [23], a long-standing puzzle concerning the behavior of multi-unpaired-electron ion cores during fast ion-atom collisions was successfully addressed, particularly focusing on the process of single electron capture (SEC). In detail, experimental measurements were combined with state-of-the-art calculations to thoroughly describe the SEC process involving multi-open-shell excited ions, thus providing conclusive answers to two crucial questions:

1. Whether similarly configured final states corresponding to different spins are populated according to spin statistics.

2. Whether the initial electronic configuration undergoes changes during the collision process, known as the frozen core approximation.

To address these questions, we focused on the $2p$ SEC channel in MeV collisions of He-like carbon projectiles with He targets:

$$\mathrm{C}^{4+}(1s2s\ ^3S) + \mathrm{He} \rightarrow \mathrm{C}^{3+}(1s2s2p\ ^4P,\ ^2P_{\pm}) + \mathrm{He}^{+} \tag{7.1}$$

In this study, the ratio R_m of the $1s2s2p\ ^4P$ and ^2P SEC cross sections was investigated. The ratio R_m, given by

$$R_m \equiv \frac{\sigma_m(^4P)}{\sigma_m(^2P_+) + \sigma_m(^2P_-)} \tag{7.2}$$

provides valuable information about the spin population and the underlying dynamics [156, 159, 165, 221, 222]. The study involved intensive close coupling calculations, incorporating the dynamics of three active electrons, considered for the first time in such problems (see Section 7.2). Interestingly, the obtained ratio R_m was found to fall between 0.9 and 1.5 for collision energies ranging from 6 to 18 MeV, as shown in Fig. 7.1).

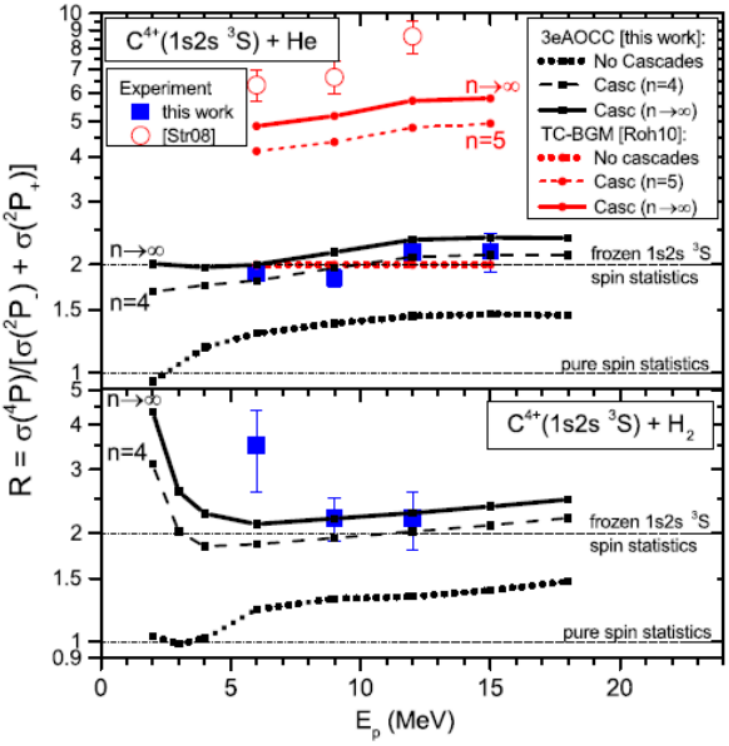

Figure 7.1: Ratio R_m for $C^{4+}(1s2s\ ^3S)$ colliding with He (top) and H_2 (bottom). Older work by other groups is shown in red, while recent works performed in [23] is shown in black (theory) and in blue (experiment). Taken from [23].

In earlier studies conducted by Tanis et al. [221], a larger value of $R_m \simeq 2.9$ was reported for collisions at 20.9 MeV between mixed-state F^{7+} ($1s^2$, $1s2s\ ^3S$) ions He. This observation prompted the introduction of a new mechanism, the dynamic Pauli exchange interaction, as an explanation for the dominance of the $1s2s2p\ ^4P$ state over the $1s2s2p\ ^2P_\pm$ states populations. Zouros et al. [222] proposed that a similar enhancement of R_m could be qualitatively accounted for by a selective cascade feeding mechanism that favors the production of the ^4P state. In both scenarios, the measured R_m ratio does not reflect the statistics of final state spins, which corresponds to the value of $R_m = 1$.

A more comprehensive follow-up study of the process described by Eq. 7.1 reported even larger experimental ratios, $R \simeq 6 - 9$ [165]. This investigation incorporated calculations based on a frozen core single-active electron approach using the non-perturbative two-center basis generator method (TC-BGM) [223, 224]. It also included a thorough radiative cascade analysis [165] along with supplementary Auger corrections [156]. The outcomes of this research unambiguously showcased a selective cascade-induced enhancement of the ^4P state, resulting in $R \simeq 4.9 - 5.8$. However, for cases involving only $2p$ capture (absence of cascades), computed values

led to $R_m \simeq 2$ [156], aligning with the spin statistics prediction within the frozen core approximation.

Recent studies by Madesis et al. [23] clearly demonstrated that the ratio R_m is neither $R_m = 1$, which corresponds to only spin multiplicity, nor $R_m = 2$, which corresponds to the frozen core approximation. In this study special care was taken for the accurate determination of the effective solid angle correction factor G_τ for the long-lived ^4P state, using both simulations within the SIMION ion-optics package [14, 15], as well as additional measurements using Be-like ions [225], as explained in Section 4.4. Thus, earlier miscalculated G_τ values, leading to erroneous determination of the value of R_m [165], were properly addressed.

Furthermore, Madesis et al. [23] included radiative cascade contributions within the quartet series, which substantially increase the population of the $1s2s2p\ ^4P$ state, as discussed in Section 4.4. The cascade contributions were evaluated using radiative branching ratios calculated with the COWAN code [226] and SEC cross sections to higher-lying $1s2snl\ ^4L$ states provided by AOCC calculations [12]. Thus, experimental and theoretical values of R_m were for the first time in agreement, highlighting the inappropriateness of the frozen core approximation as well as pure spin statistics in highly correlated dynamic atomic systems.

Additionally, the study proposed an elegant Pauli shielding mechanism, previously unreported, related to strong exchange effects. This mechanism selectively and counter-intuitively obstructs specific reaction channels. The population of the $1s2s2p\ ^2P_-$ state, for instance, was strongly suppressed by Pauli shielding and could only be populated through much weaker spin exchange interactions. To gain more insight into this intriguing phenomenon, a simplified representation of the three $1s2s2p\ ^4P$, $^2P_\pm$ states using the $1s$, $2s$, and $2p$ atomic orbitals can be adopted. For simplicity, we represent them solely by their spins as [23]:

$$|^4P> \equiv |\uparrow\uparrow\uparrow| \tag{7.3}$$

$$|^2P_-> \equiv \frac{1}{\sqrt{2}}(|\uparrow\downarrow\uparrow| - |\downarrow\uparrow\uparrow|) \tag{7.4}$$

$$|^2P_+> \equiv \frac{1}{\sqrt{6}}(|\uparrow\downarrow\uparrow| + |\downarrow\uparrow\uparrow| - 2|\uparrow\uparrow\downarrow|) \tag{7.5}$$

where these wave functions are eigenfunctions of the total spin operator, $\mathbf{S^2}$, and correspond to the largest M_S components. Despite their simplicity, these determinental wave functions correctly represent the energy ordering of the states, mainly driven by the dominant exchange integral between the 2s and 2p orbitals. Starting from the initial $1s2s\ ^3S$ state ($\equiv |\uparrow\uparrow|$), a spin-up or spin-down target electron can be directly transferred to the projectile, leading to the creation of the ^4P state [Eq. 7.3] or the $^2P_+$ state [through the third term in Eq. 7.5]. However, the formation of the $^2P_-$ state requires an additional spin exchange between the active target electron and one of the projectile electrons. This process involves a second-order mechanism and is less likely compared to the direct capture processes that populate the ^4P and $^2P_+$ states. These findings shed light on the intricate quantum dynamics occurring during fast ion-atom collisions and underscore the significance of electron correlations in determining final atomic state populations.

Here, our primary objective is to conduct a systematic investigation of the intricate quantum details and underlying mechanisms involved in the fundamental SEC

process during fast ion-atom collisions. Building upon the methods and approaches utilized in the recent work on carbon He-like ions [23], we aim to perform a part of an isoelectronic study with low Z (Z<10) ionic projectiles. By doing so, we intend to expand and validate the initial findings across a wider range of elements and conditions, thereby assessing their broader applicability.

The SEC process, along with the corresponding spin statistical population schemes, is often employed to simplify complex problems concerning the computation of relative populations, such as in high-energy plasmas. Thus, extending the SEC study from carbon ions (Z=6) to a systematic isoelectronic sequence holds significant promise and presents a challenge for current theories and approaches. It is anticipated that elements with Z<6 might exhibit more pronounced correlation effects, while those with Z>6 might display less pronounced effects, although this hypothesis requires empirical verification and quantification, as proposed in this study. By systematically exploring these isoelectronic elements, we aspire to gain deeper insights into the SEC process and advance our understanding of the role of electron correlations in different atomic systems.

7.2 3eAOCC Theory

During the past decades, the realm of atomic and molecular physics has been marked by extensive theoretical explorations into collision phenomena. In parallel with the utilization of simplified models to offer approximate depictions of scattering events, quantum theory has flourished in addressing potential scattering. Methods such as solving the time-independent Schrödinger equation, often through partial wave expansion techniques, have found application. However, at elevated energies where partial wave expansions falter, approximations must be introduced to capture temporal dynamics [25].

When investigating processes unfolding in collisions with impact energies of a few MeV, a semiclassical approach can be adopted. In this scheme, the relative motion between the projectile and target is described through classical trajectories, while the behavior of the electrons within the system is treated quantum mechanically. In this section, we will provide an overview of such a theory, e.g., the 3eAOCC (3-electron atomic orbital close-coupling) theory, that has been employed to describe the SEC process.

The 3eAOCC theory is based on a semiclassical atomic orbital close-coupling treatment, with asymptotic (atomic) descriptions of the neutral and charged collision partners. This approach exhibits remarkable versatility, accommodating the inclusion of three active electrons within the calculations. This adeptly characterizes the behavior of He-like / Li-like ions, and He with precision. Specifically, in the case of He, the computational framework encompasses a single electron attached to He^+ through the utilization of a model potential, expressed as:

$$V(r) = \sum_{i=1}^{13} -\frac{c_i}{r} e^{-a_i r^2} \tag{7.6}$$

where the coefficients and exponents are optimized to ensure the ground state attains a binding energy closely aligned with the first ionization energy (24.6 eV), while

also satisfying accurate representation of the first excitation energies and proper Coulombic limits as r approaches both 0 and $+\infty$.

The atomic states centered on He (represented by the potential of Eq. 7.6), He-like and Li-like ions are formulated through collections of optimized Gaussian-Type orbitals (GTOs), expressed as

$$\mathcal{G}(r) = \mathcal{N} r^l e^{-ar^2} \tag{7.7}$$

where $\mathcal{N}$ is a normalization factor. These states are then combined using antisymmetrized products of these GTOs. This methodology aims to yield both ground and excited states for the considered neutral and ionized species, with a specific focus on key energy levels, i.e., $1s2s2p\ ^4P,\ ^2P_\pm$.

The 3-electron time-dependent Schrödinger equation (TDSE) is written as [24]:

$$\left[H_e - i\frac{\partial}{\partial t}\Big|_{\mathbf{r_1},\mathbf{r_2},\mathbf{r_3}}\right] \Psi\left(\mathbf{r_1},\mathbf{r_2},\mathbf{r_3},\mathbf{R}(t)\right) = 0\ , \tag{7.8}$$

where H_e is the electronic Hamiltonian:

$$H_e = \sum_{i=1}^{3}\left(-\frac{1}{2}\nabla_i^2 + V_T(r_i) + V_P(r_i^P) + \sum_{i<j}\frac{1}{|\mathbf{r_i}-\mathbf{r_j}|}\right)\ , \tag{7.9}$$

where $\mathbf{r_i}$, $\mathbf{r_i^P} = \mathbf{r_i} - \mathbf{R}(t)$ are the position vectors of the electrons with respect to the target and the projectile, respectively. The relative projectile-target position $\mathbf{R}(t)$ defines the trajectory, with $\mathbf{R}(t) = \mathbf{b} + \mathbf{v}t$ in the usual straight-line, constant-velocity approximation. The terms $\mathbf{b}$ and $\mathbf{v}$ correspond to the impact parameter and velocity, respectively (see Fig. 7.2). Finally, V_T and V_P are the electron-target and electron-projectile nucleus potentials, respectively.

The Schrödinger equation is solved by expanding the wave function onto a basis set composed of states of the isolated collision partners [24, 227], i.e.:

$$\begin{aligned}\Psi(\mathbf{r_1},\mathbf{r_2},\mathbf{r_3},\mathbf{R}(t) = \sum_{n_T,n_P}\sum_{J=1}^{N_{(n_T,n_P)}}\Big[a_j^{(n_T,n_P)}(t)\\ \times\,\Phi_J^{(n_T,n_P)}\left(\mathbf{r_1},\mathbf{r_2},\mathbf{r_3},\mathbf{R}(t)\right)e^{-iE_J^{(n_T,n_P)}}\Big]\ ,\end{aligned} \tag{7.10}$$

with

$$\Phi^{(n_T,n_P)}_{J\equiv j_T,j_P}\left(\mathbf{r_1},\mathbf{r_2},\mathbf{r_3},\mathbf{R}(t)\right) = \widehat{\mathbb{P}}\Big[\phi_{j_T}^{T_{n_T}}\left(\mathbf{r_1}\right)\times\phi_{j_P}^{P_{n_P}}\left(\mathbf{r_2^P},\mathbf{r_3^P}\right)\Big]\ , \tag{7.11}$$

Here, $N_{(n_T,n_P)}$ represents the number of states and their associated energies where n_T and n_P electrons reside on the target and projectile, respectively, with the constraint $n_T + n_P = 3$. The multielectron states $\Phi^{(n_T,n_P)}$ are formulated through linear combinations of spin-adapted products of GTOs centered on individual collision partners. The permutation operator $\widehat{\mathbb{P}}$ ensures the full antisymmetry of the wave functions with respect to the interchange of two electrons. Note that, for all electrons, these projectile states contain plane-wave electron translation factors ensuring Galilean invariance of the results.

Substituting Eqs. 7.10 and 7.11 into Eq. 7.9 gives rise to a set of first-order coupled differential equations, which can be expressed in matrix form as

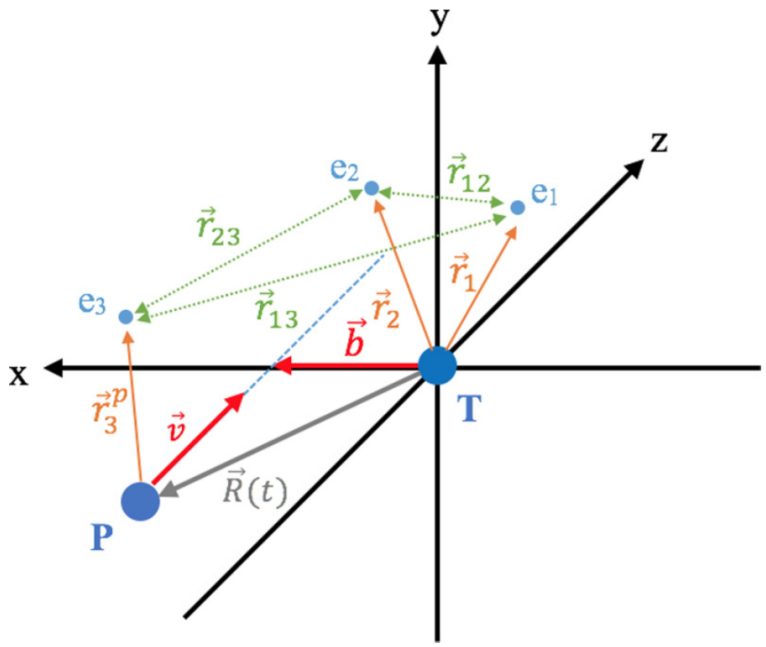

Figure 7.2: Schematic illustration of the collision geometry. The collision plane (xz) is defined by the impact parameter **b** and velocity **v**, while the projectile trajectory $\mathbf{R}(t)$ is indicated with respect to the target (T). The positions of the initial two electrons relative to the target center are labeled as $\mathbf{r_1}$ and $\mathbf{r_2}$, while the third electron relative to the projectile center is represented as $\mathbf{r_3^p}$. The $\mathbf{r_{12}}$, $\mathbf{r_{13}}$, and $\mathbf{r_{23}}$ signify the relative vectors between each pair of electrons. Taken from [24].

$$i\frac{d}{dt}\mathbf{a}(t) = \mathbf{S^{-1}}(\mathbf{b},\mathbf{v},t)\mathbf{M}(\mathbf{b},\mathbf{v},t)\mathbf{a}(t)\ , \tag{7.12}$$

where $\mathbf{a}(t)$ is the column vector of the time-dependent expansion coefficients and $\mathbf{S}$, $\mathbf{M}$ are the overlap and coupling matrices, respectively.

The probability of a transition $i \to f$ is given by the coefficients a_f as

$$P_{fi}(b,\mathrm{v}) = \lim_{t\to\infty} |a_f(t)|^2\,, \tag{7.13}$$

where $a_f \equiv a_J^{(n_T,n_P)}$. The corresponding total cross sections for the considered transition are given as

$$\sigma_{fi}(\mathrm{v}) = 2\pi \int_0^\infty bP_{fi}(b,\mathrm{v})db\ . \tag{7.14}$$

7.3 Auger Electron Angular Distributions

The 3eAOCC calculations yield probability amplitudes dependent on the impact parameter b, enabling the straightforward evaluation of production cross sections for any of the treated $1s2l2l'\ ^{2S+1}L$ channels. After an Auger decay of the ^{2S+1}L state to a final ionic state with $L_f = 0$, the SDCS only relies on the cross sections of the magnetic states, $\sigma(L,\ M_L)$, of the autoionizing levels [228]. Hence, the Auger electron SDCSs can be determined at any observation angle θ' for the generated ^2L

states. This computation employs the well-known Auger electron angular distribution LS-coupling formula [228], which is expressed as an expansion of even-order Legendre polynomials, $P_k(\cos\theta')$ [26]:

$$\frac{d\sigma[^2L]}{d\Omega'}(\theta) = \overline{\xi}[^2L]\frac{\sigma_{tot}[^2L]}{4\pi}\sum_{k=0,\,even}^{2L} A_k(L)P_k(\cos\theta') \ . \tag{7.15}$$

where the total LS-multiplet production doublet cross section, $\sigma_{tot}[^2L]$, is computed as

$$\sigma_{tot}[^2L] = \sum_{M_L=-L}^{L} \sigma(L,\ |M_L|) \ . \tag{7.16}$$

The symbol $\overline{\xi}$ of Eq. 7.15 is the mean Auger yield of the LS-multiplet given in general by

$$\overline{\xi}[^{2S+1}L] \equiv \frac{\sum_{J=|L-S|}^{J+L+S}(2J+1)\xi_J}{(2S+1)(2L+1)} \ . \tag{7.17}$$

Finally, the angular distribution parameters A_k are, in general, complicated functions involving partial cross sections $\sigma(SLJ)$, the interfering phases of the emitted l, j partial Auger waves, and the reduced Auger matrix elements of the $SLJ \rightarrow S_fL_fJ_f$ Auger transition. However, in cases where just a single Auger partial wave is emitted, these coefficients are much simplified. This is the case for our study in which the final state is $1s^2$ having $S_f = L_f = J_f = 0$. Thus, it has been proved that for the SDCS at $\theta = 0^\circ$, as in our ZAPS measurements, the following equation holds [26]:

$$\frac{d\sigma[^2P_\pm]}{d\Omega'}(\theta = 0^\circ) = 3\overline{\xi}[^2P_\pm]\frac{\sigma[^2P_\pm](L=1, M_L=0)}{4\pi} \ . \tag{7.18}$$

Therefore, the $\theta = 0^\circ$ SDCSs are seen to be sensitive only to the $M_L = 0$ component of the partial cross section. We also mention that since the spin-orbit interaction is negligible for low-Z_p ions, the spin has a negligible effect on the production of the resonances. Thus, Eq. 7.18 is assumed to be a good approximation for the $1s2s2p\ ^4P$ state, as well [26].

Eq. 7.18 has been utilized for the determination of theoretical SDCSs of ^4P and $^2P_\pm$ states, for a straightforward comparison with the measurements. We should also mention that the theoretical SDCSs, resulted form Eq. 7.18 and the 3eAOCC calculations, were multiplied by 2 to account for the two electrons of the He target.

7.4 SEC in Collisions with $O^{6+}(1s2s\ ^3S)$ Projectiles

We initiated the isoelectronic study of the SEC process using He-like mixed-state oxygen projectiles. For these experiments we employed our double measurement technique over a wide range of collision energies spanning 8-24 MeV. The necessary $1s2s\,^3S$ metastable fractions in each set of measurements were tailored according to the stripping schemes described in Section 4.5. The thus determined metastable

beam fractions, $f_{1s2s\,^3S}$, are presented in Fig. 4.14. The DDCSs Auger spectra corresponding to low and high $1s2s\,^3S$ fractions for all the measured collision energies are shown in Fig. 7.3.

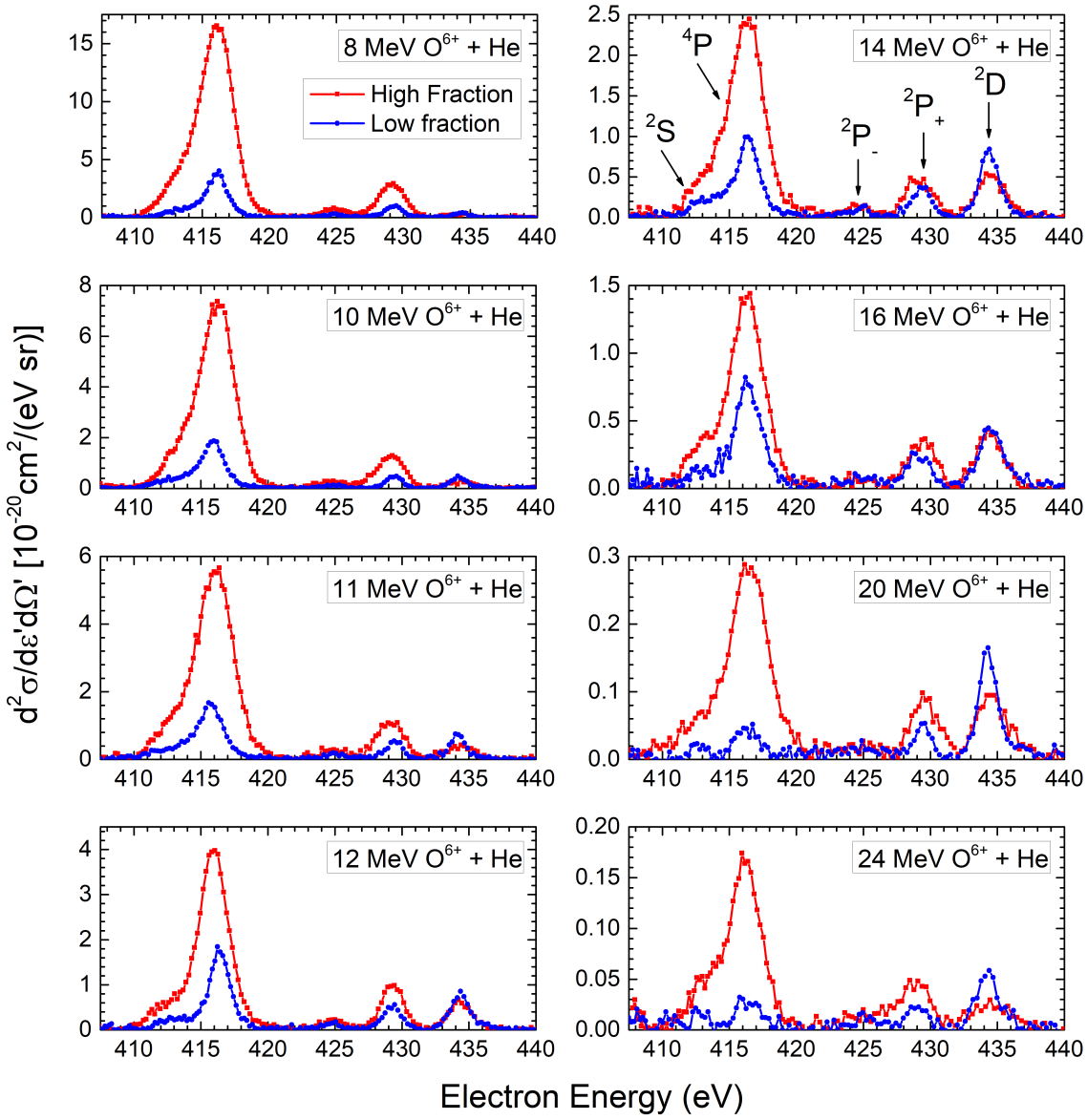

Figure 7.3: Projectile rest frame 0° DDCSs for collisions of 8-24 MeV $O^{6+}(1s^2\ ^1S,\ 1s2s\ ^3S)$ mixed-state beams with He. The red and blue lines correspond to the high and low $f_{1s2s\,^3S}$ beam fractions, respectively. The stripping schemes for all high and low fraction spectra are given in Fig. 8.2

7.4.1 Single Differential Cross Sections

In Fig. 7.4, we present the SDCS experimental and theoretical results for the $1s2s2p$ ^4P and $^2P_\pm$ states, obtained in collisions of $O^{6+}(1s2s\ ^3S)$ with He. The experimental SDCSs were obtained according to the method outlined in Section 4.6. Special care was taken for the proper background fit and subtraction, since our double-measurement technique is sensitive to electron yield differences. The SDCSs were obtained after fitting the peaks with distributions generated by SIMION simulations,

as described in Section 5.1. It should be reminded that in the case of the $1s2s2p\ ^4P$ peak, the yield was corrected considering the solid angle correction factor G_τ, as discussed in Section 4.4.

The corresponding theoretical 3eAOCC calculations are also shown in Fig. 7.4. It is mentioned that theory has been multiplied by 2 to account for the two electrons of the target [26]. It is clearly seen that the theoretical SDCSs follow the same energy dependence as the measurements, i.e., a rapid decrease with the collision energy. However, theory systematically overestimates the absolute values of the measurements. At this point it should be emphasized that the 3eAOCC calculations are not in their final stage, since rigorous evaluations for the convergence of the calculations are still carried out. Since our 3eAOCC calculations are not yet finalized, we did not include the cascade feeding contributions for the $1s2s2p\ ^4P$ state, as it was done in the previous studies with carbon projectiles [23, 26]. However, for the sake of completeness, we outline below the basic steps for including the cascades in the analysis, once our theoretical results are finalized.

The SEC process results in both doublet and quartet $1s2snl\ ^{2,4}L$, $n \geq 2$, states. Those configurations with $n > 2$ might decay radiatively to the $1s2s2p$ configuration through E1 transitions, which could amplify its initial population. However, the $1s2snl\ ^2L$ doublets experience rapid Auger decay rates towards the $1s^2\ ^1S$ ground state, depleting them quickly and thereby having negligible effect on the initial population of $1s2s2p\ ^2P_\pm$ states. On the contrary, the $1s2snl\ ^4L$ quartet states have weak Auger decay rates to the $1s^2$ ground state and then decay radiatively to the lowest quartet state, namely, the $1s2s2p\ ^4P$, functioning somewhat as an *excited ground state* for the radiative cascades of these higher-lying $nl\ ^4L$ quartet states, as discussed in Section 4.4. In a recent study of our team, the selective cascade feeding mechanism in carbon was addressed, resulting in a notable increase in the population of the $1s2s2p\ ^4P$ state [12]. The cascade feeding included contributions from the $n = 3$ and $n = 3 + n = 4$ shells, as well as the extrapolation to include all $n \to \infty$, adhering to the well-established n^{-3} rule for SEC [156, 229]. Consequently, the complete contribution to the ^4P state, including cascade repopulation (SEC+C), is described as [26]:

$$\frac{d\sigma[^4P]}{d\Omega'}(0^\circ) = 3\bar{\xi}[^4P]\frac{\sigma[^4P](L=1, M_L=0) + \sigma_0^C[n\to\infty]}{4\pi} \tag{7.19}$$

with $\sigma_0^C[n \to \infty]$ being the cascade contribution to the $M_L = 0$ magnetic state of the ^4P. The SDCSs according to Eq. 7.19 led to an overall increase of approximately 55% for the collision systems studied in [26].

7.4.2 The Production Ratio $\mathbf{R_m}$

In Fig. 7.5 we present the experimental and theoretical findings for the production ratio R_m, defined in Eq. 7.2, which experimentally can be determined from the corresponding measured SDCSs as [26]:

$$R_m = \frac{\frac{1}{\bar{\xi}[^4P]}\frac{d\sigma[^4P](0^\circ)}{d\Omega'}}{\frac{1}{\bar{\xi}[^2P_-]}\frac{d\sigma[^2P_-](0^\circ)}{d\Omega'} + \frac{1}{\bar{\xi}[^2P_+]}\frac{d\sigma[^2P_+](0^\circ)}{d\Omega'}}\ , \tag{7.20}$$

with ξ being the Auger yields of the states. It should be pointed out that after applying the Auger angular distributions discussed in Section 7.3, the theoretical

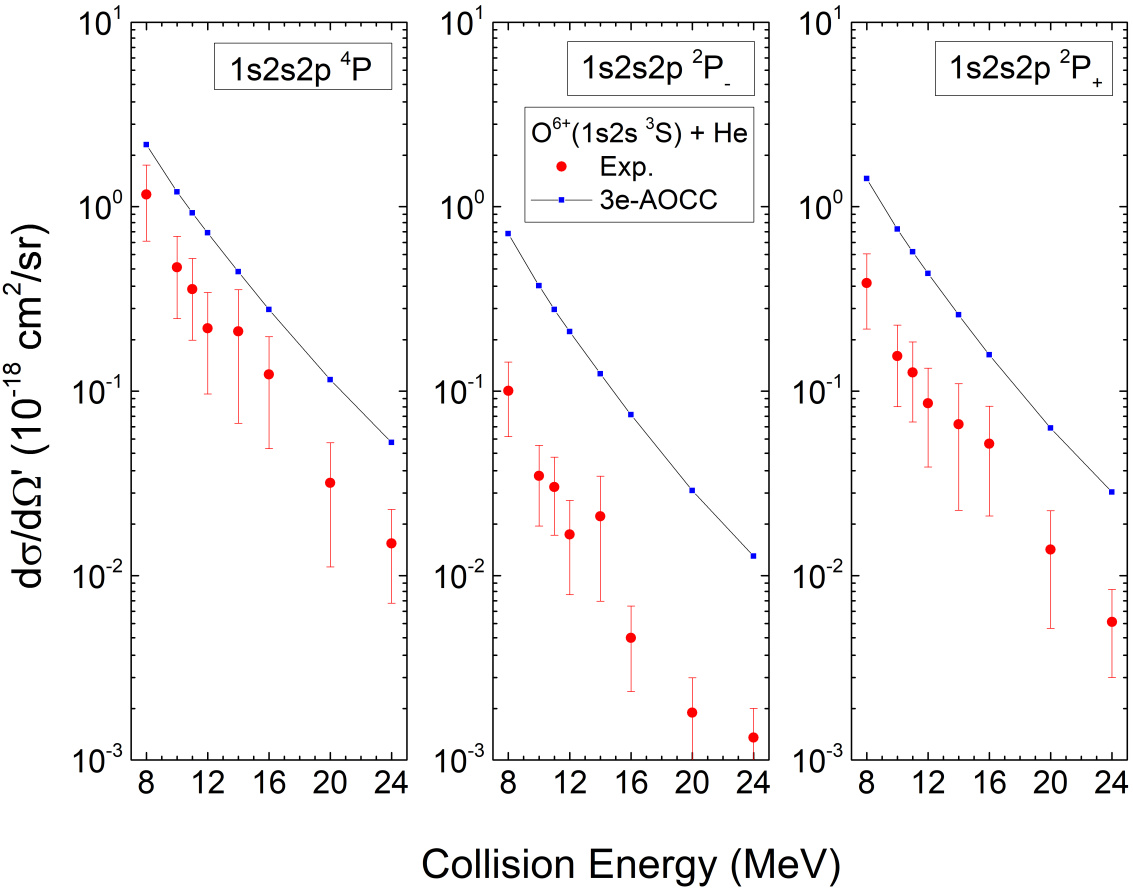

Figure 7.4: Zero-degree Auger electron SDCSs for the $1s2s2p\ ^4P$, $1s2s2p\ ^2P_-$, and $1s2s2p\ ^2P_+$ states obtained in collisions of $O^{6+}(1s2s\ ^3S)$ with He. Red circles correspond to the measurements and blue squares to the 3eAOCC preliminary calculations [25]. Theory has been multiplied by 2 to account for the two electrons of the target as in [26]. Only statistical uncertainties are shown. The lines between the theoretical points are used to guide the eye.

expression for R_m is equivalently written as:

$$R_m = \frac{\sigma[^4P](L=1, M_L=0)}{\sigma[^2P_-](L=1, M_L=0) + \sigma[^2P_+](L=1, M_L=0)} \ . \tag{7.21}$$

It is clearly seen that the experimentally determined R_m shows a relatively constant value of $R_m \simeq 2.3$ for all the collision energies. This result is in agreement with the behaviour of R_m in similar measurements with carbon ions [26, 161]. The main difference is that in our case of oxygen the average value of R_m is higher than the value of $R_m \simeq 2.0$ for carbon ions. This behaviour will be discussed below in the text after considering similar results from boron ions. Here, we may only comment that the experimental R_m values deviate from both the pure statistical spin value of $R_m = 1$ and the frozen core $1s2s\ ^3S$ spin statistic value of $R_m = 2$.

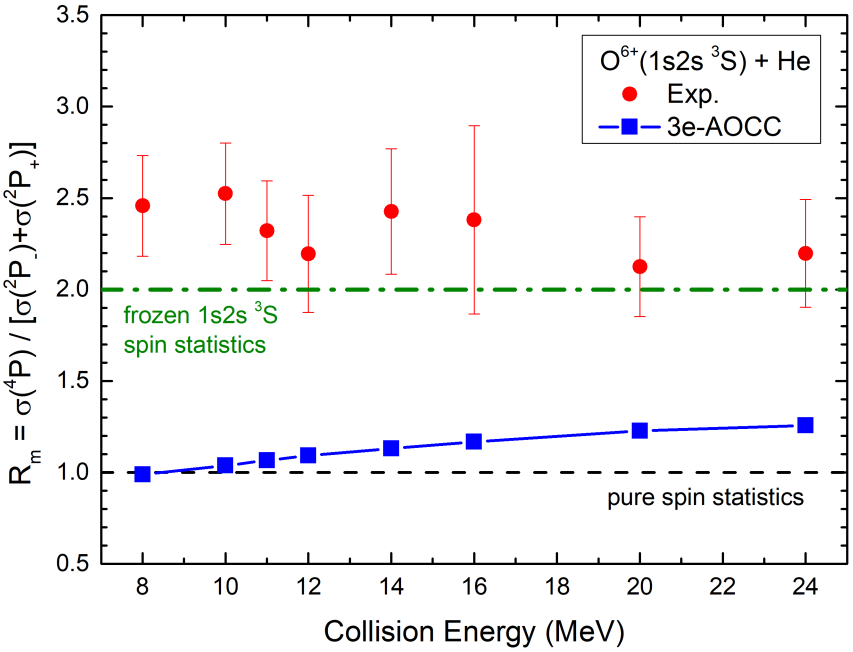

Figure 7.5: Experimental and 3eAOCC preliminary results on the R_m ratio for collisions with He-like oxygen projectiles. The frozen core $1s2s\ ^3S$ spin statistics and the pure spin statistics values are also indicated.

The disagreement between pure statistical or frozen core concepts and experiment have also been shown in previous studies using carbon projectiles. In detail, the 3eAOCC calculations resulted in $R_m \simeq 1.4$ for carbon projectiles and collisions velocities higher than 0.50 MeV/u. Similarly, in the case of oxygen, the 3eAOCC calculations predict slightly lower R_m values than those reported for carbon, i.e., $R_m \simeq 1.2$. It should be noted, that these theoretical R_m values do not include the cascade repopulation mechanism of the ^4P state, discussed previously in the text. It is expected that cascade contributions will appreciably enhance the R_m value, similar to the case of carbon.

It should be mentioned here that in an energetic ion-atom collision the SEC process depends primarily on the parameters of projectile charge, target ionization potential, and the collision velocity. Based on these parameters, a SEC probability distribution around the central value of a principal quantum number n_{max} is formed, known as the *reaction window* [80, 230]. Higher Z_P/Z_T ratios correspond to larger

n_{max} numbers. In our case, the O^{6+} + He collision system exhibits a higher Z_P/Z_T ratio compared to C^{4+} + He collision system, and thus a larger n_{max} is expected for oxygen. This in turn supports larger cascade feeding for oxygen, which could explain the higher R_m values for oxygen compared to that of carbon [9, 161].

7.4.3 Additional results from the $1s^2\ ^1S$ ground state beam component

Our double-measurement technique allows for the determination of the SDCSs of $1s2s2p\ ^4P$ and $^2P_\pm$ states resulting either from the $1s2s\ ^3S$ metastable state through the SEC process or the $1s^2\ ^1S$ ground state through the process of transfer and excitation. However, even though the contributions from the ground state are not in the main focus in this study, we include it here for completeness purposes. Thus, in Fig. 7.6, we present the obtained SDCS, and corresponding 3eAOCC calculations, obtained in collisions of $O^{6+}(1s^2\ ^1S)$ with He. There, it is clearly seen that the 3eAOCC theory reproduces the energy dependence of the SDCSs, as in the case of the results for the $1s2s\ ^3S$ metastable beam.

7.5 SEC in Collisions with B^{3+}(1s2s ^{3}S) Projectiles

Our isoelectronic study on SEC was extended to include boron projectiles that have lower atomic number than carbon, where electron correlations are expected to be enhanced compared to both carbon and oxygen.

Before we proceed to the data presentation, we should emphasize that the boron measurements coincided with a massive upgrade of the tandem Van de Graaff accelerator. Given the machine's frequent use for nuclear physics experiments and a substantial backlog of scheduled experiments, the facility's staff decided not to introduce foil strippers into the tandem terminal at this stage of operation. Consequently, our plan for boron experiments faced a challenge due to the absence of terminal foil strippers.

Under these circumstances, we proceeded conducting measurements with only GTS and/or GTS-FPS stripping schemes. In addition, we observed negligible differences in the metastable fractions obtained with GTS and GTS-FPS for collision energies beyond 0.75 MeV/u projectile velocities. This is a vital requirement for our double measurement technique makes it obsolete for these conditions. Although these stripping approaches may not have been optimal for our experimental objectives, they proved adequate for the collision systems 5.5 MeV and 8.25 MeV B^{3+} + He. The resulted DDCS electron spectra are shown in Fig. 7.7. It is worth mentioning that this is the first time that boron beams were delivered by the tandem accelerator of "Demokritos".

The value of R_m was derived from the spectra of Fig. 7.7, similarly to that for oxygen, for both collision energies. The result is shown in Fig. 7.8. It is surprising that the R_m value for He-like boron projectiles is substantially lower compared to the corresponding R_m values determined in previous studies for carbon (see Fig. 7.1) and here for oxygen (see Fig. 7.5). The experimental R_m values clearly deviate from the frozen core value of 2, once again demonstrating that this approximation cannot be employed to describe the SEC process in highly correlated atomic systems.

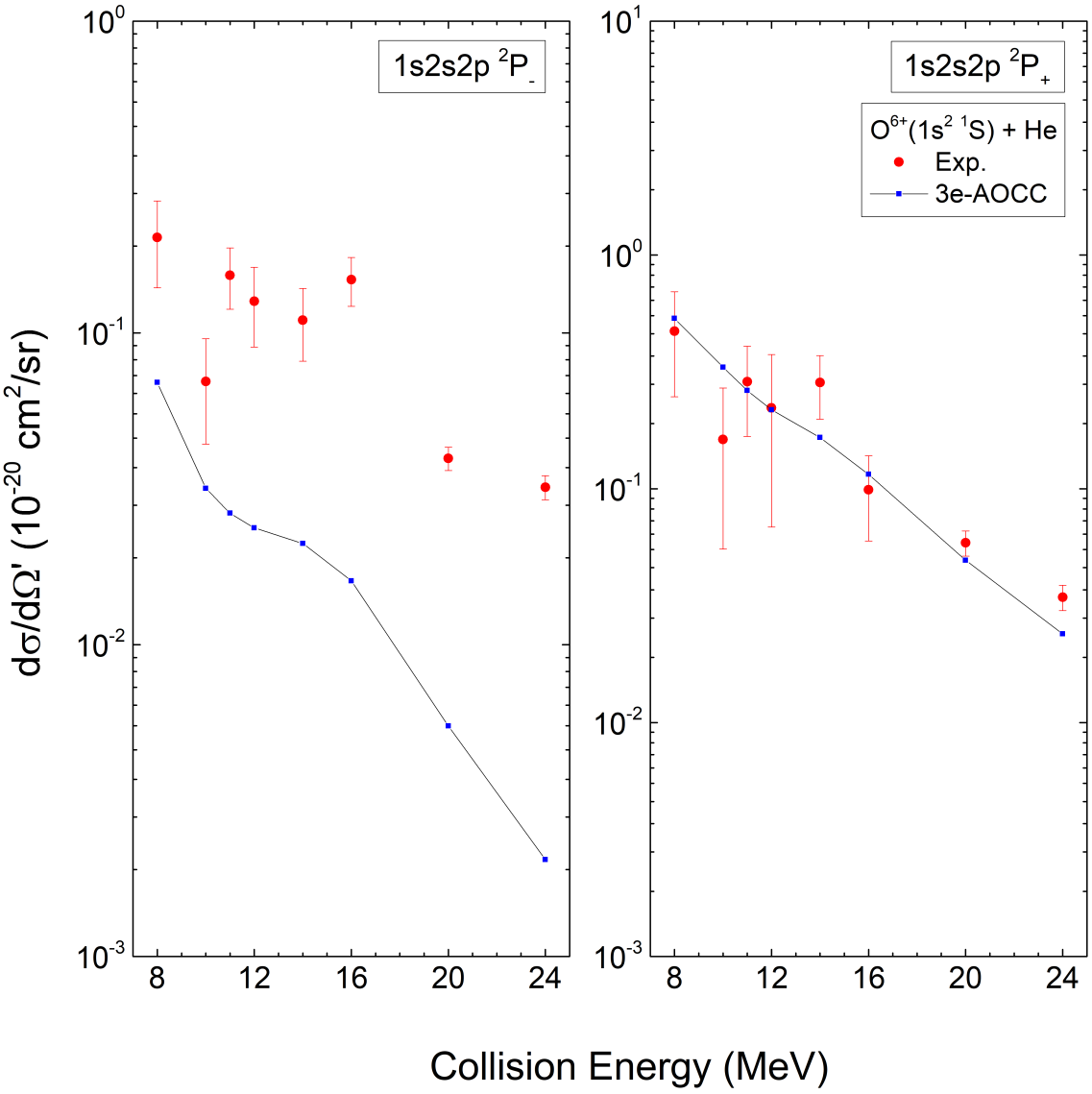

Figure 7.6: Same as in Fig. 7.4, but for collisions of $O^{6+}(1s^2\ ^1S)$ with He.

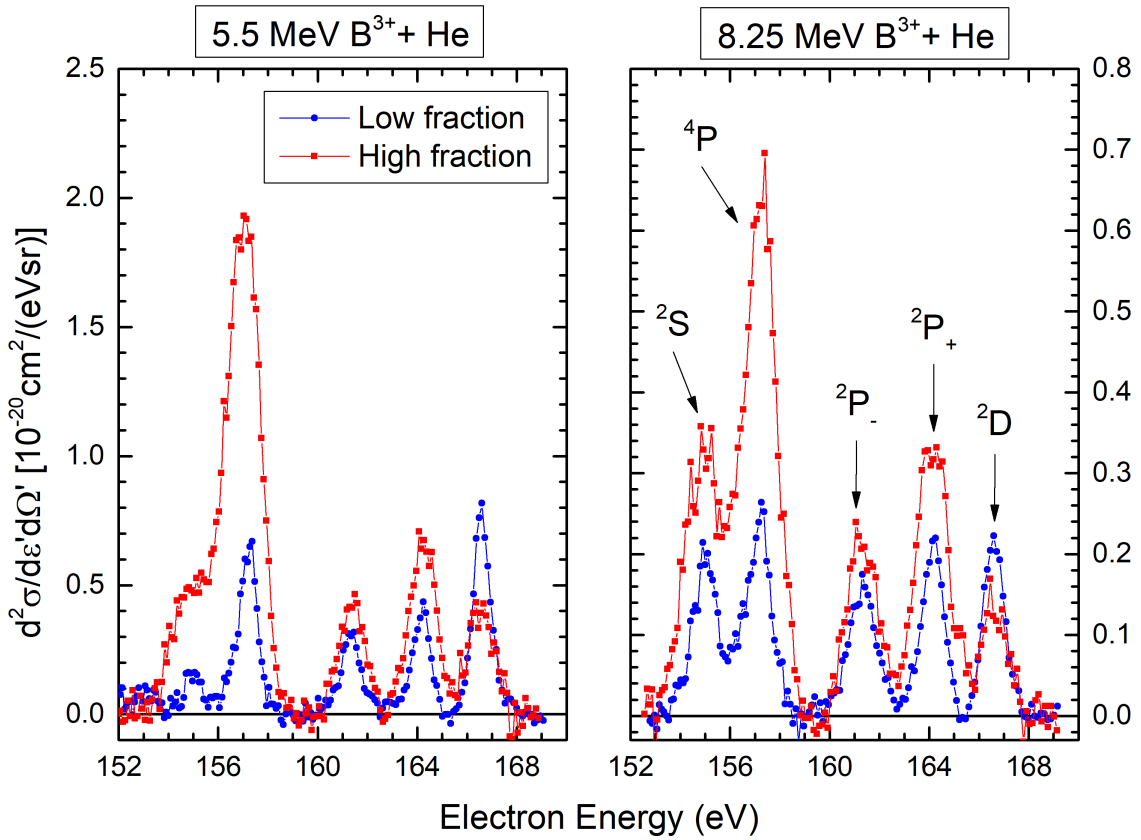

Figure 7.7: Projectile rest frame 0° DDCSs for collisions of 5.5 and 8.25 MeV $B^{3+}(1s^2\ {}^1S,\ 1s2s\ {}^3S)$ mixed-state beams with He. The red and blue colours correspond to the high and low $f_{1s2s\,{}^3S}$ beam fractions, respectively.

On the other hand, the experimental value agrees with the pure spin statistics prediction. However, this result has to be treated with caution, as the systematic studies performed with carbon and oxygen projectiles, clearly demonstrate that this model cannot be adopted for the description of the SEC process.

Following the discussion of Subsection 7.4.1, collision systems involving boron projectiles and He targets have a lower Z_P/Z_T ratio, thus favoring electron capture to lower n_{max} values. Therefore, it is expected that cascade repopulation of the ^4P state will be lower compared to collision systems involving carbon or oxygen projectiles. This alone justifies a lower R_m value for boron. However, a more thorough discussion considering all the aspects of our isoelectronic study is presented below.

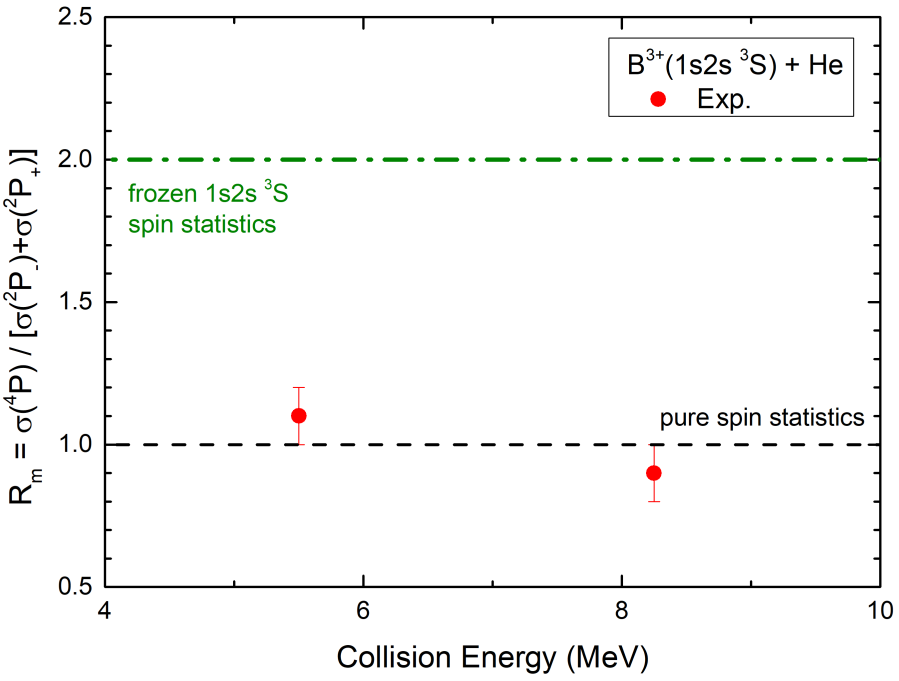

Figure 7.8: Experimental results on the R_m ratio for collisions with He-like boron projectiles. The frozen core $1s2s\ ^3S$ spin statistics and the pure spin statistics values are also indicated.

7.6 Isoelectronic study

In the following we present the main findings of the so far isoelectronic study for the ions of B^{3+}, C^{4+}, and O^{6+} in collisions with He.

In Fig. 7.9 we summarize the experimental SDCSs obtained for the ^4P, $^2P_-$, and $^2P_+$ states as a function of Z_p, for the collision energy of 0.50 MeV/u. It is clearly seen that for all the state the SEC SDCS experience a rapid increase with the atomic number Z_p. This increase in the SDCSs is consistent with the SEC process probability, which is favoured for heavier projectiles due to their increased Coulomb potential.

It should be stressed that the SDCS values for the ^4P state exhibit a steep increase with increasing Z_p, amounting to approximately two orders of magnitude from boron to oxygen. In contrast, the corresponding increase in the SDCS values for the $^2P_\pm$ states is only within one order of magnitude. This behaviour provides a clear indication of the cascade repopulation mechanism affecting the cross section of the ^4P state, a phenomenon that becomes more pronounced for higher values of Z_p, as previously discussed.

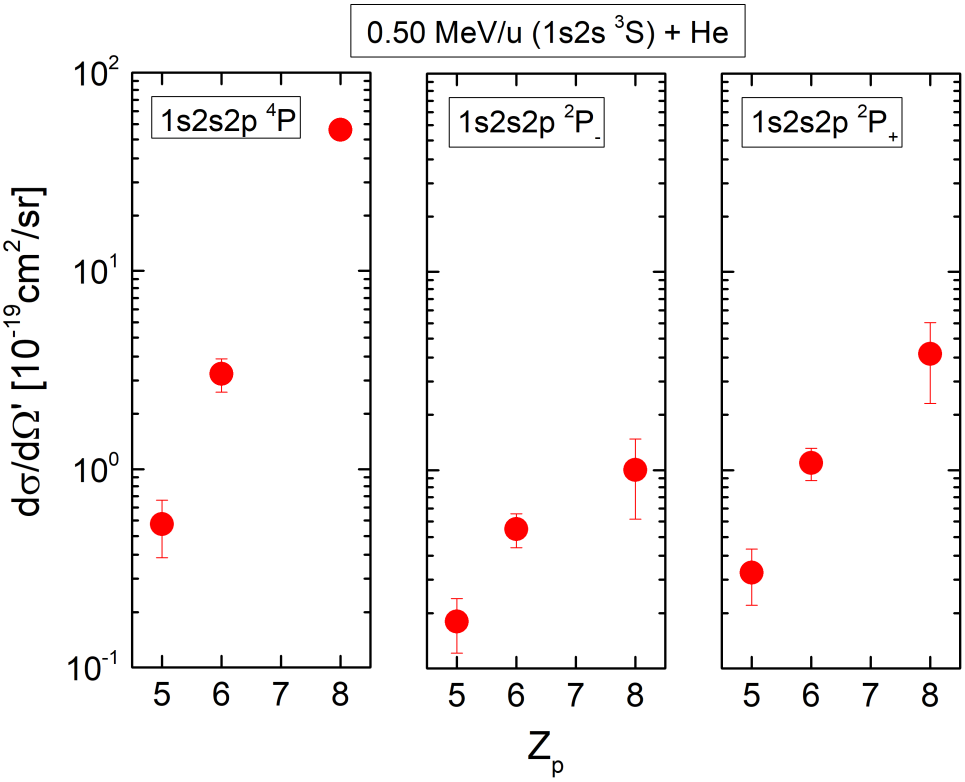

Figure 7.9: Experimental results on the SDCSs of ^4P (left), $^2P_-$ (middle), and $^2P_+$ (right) for collisions of 0.5 MeV/u B^{3+}, C^{4+}, and O^{6+} with He.

Furthermore, the differences in the SDCS values between the ^4P state and the $^2P_\pm$ states decrease as the projectile atomic number Z_p decreases. To better visualize this, we present in Fig. 7.10 the DDCS spectra for collisions of mixed-state B^{3+}, C^{4+}, and O^{6+} with He for 0.50 MeV/u collision energy. Additionally, the DDCS spectrum for similar collisions of mixed-state F^{7+} ions with He, at a collision energy of 0.63 MeV/u (the closest possible to compare with the 0.50 MeV/u), taken from [27], is also included. While the collision energy for the fluorine case is slightly different, it is sufficiently close to allow for a meaningful comparison and a broader discussion. The decrease in the sequence of the DDCS value for the ^4P state for the fluorine case is partially justified by the higher projectile energy. In addition, the fluorine measurement was done with a parallel plate analyser that has a correction factor close to $G_\tau \simeq 1$ [225], a factor that also contributes to a smaller DDCS for the ^4P state.

The data shown, in Fig. 7.10, for boron and oxygen correspond to the high fraction measurements displayed in Figs. 7.7 and 7.3, respectively. The data for carbon, retrieved from [9], also correspond to a high fraction measurement. In all three cases, the data collection took place with our ZAPS setup, and the metastable

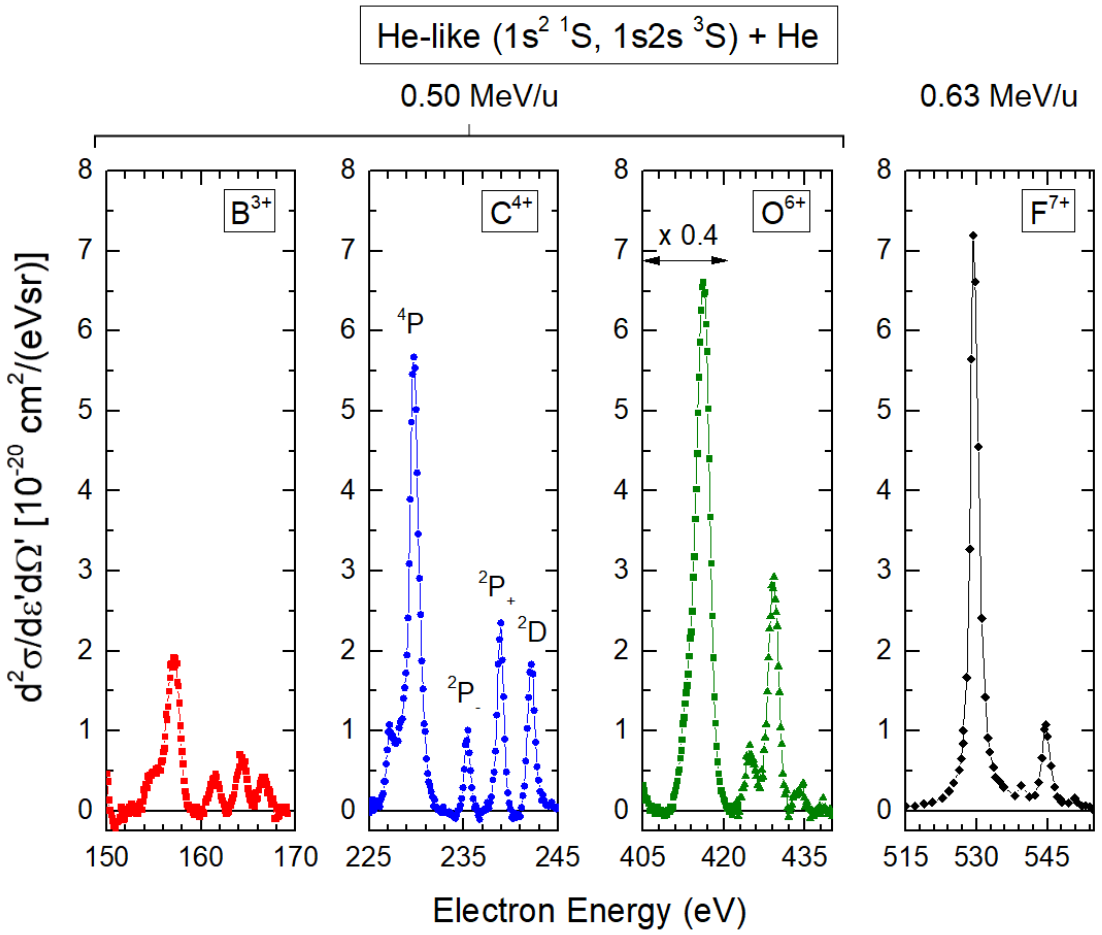

Figure 7.10: DDCS electron spectra for collisions of 0.50 B^{3+} (red squares), C^{4+} (blue circles), and O^{6+} (green triangles) with He. The DDCS spectrum for collisions of 0.63 MeV/u F^{7+} (black diamonds) with He, taken from [27], is also displayed. The ^4P peak in the oxygen case has been multiplied by a factor of 0.4 for better visibility.

fraction, $f_{1s2s\,^3S}$, was determined using our double measurement technique. For the boron case we obtained $f_{1s2s\,^3S} = 28 \pm 5\%$, while for carbon and oxygen cases, where the measurements were performed for a wide set of collision energies, an average value of $f_{1s2s\,^3S} = 18 \pm 4\%$ was determined. However, for the fluorine case, there is no information given for the metastable fraction, although based on the stripping method applied (i.e., foil stripping) it has a relatively high value.

Fig. 7.10 clearly depicts the relative strength between the $^2P_\pm$ peaks as a function of the atomic number Z_p. For the fluorine case, the $^2P_-$ peak is barely visible and substantially in lower intensity compared to the $^2P_+$ peak. For oxygen, where the atomic number Z_p is decreased by one, the $^2P_\pm$ peak is appreciably enhanced compared to the fluorine case, as also its intensity with respect to the to the $^2P_+$ peak. Continuing to the lighter targets of carbon and boron, the intensities of the $^2P_-$ peaks are further enhanced and become comparable to the $^2P_+$ peak.

The role of the $^2P_-$ state as part of the denominator of the ratio R_m is essential. Even though it has a smaller SDCS value than the $^2P_+$ state, this value increases relative to that of the $^2P_+$ state with decreasing Z_p values. Thus, a direct effect on the ratio R_m is expected, i.e., a decrease of R_m with decreasing the projectile atomic number Z_p. This behaviour is clearly shown in Fig. 7.11(a). However, it should be cleared that the a decrease of R_m with decreasing the projectile atomic number Z_p should only partially be attributed to the relative increase of the SDCS of the $^2P_-$ state. The other vital factor is the cascade feeding of the ^4P state, for which a lesser contribution is expected for lower Z_p elements, as commented earlier in the text. Thus, a further reduction of the R_m factor is justified.

To further examine the role of the $^2P_\pm$ states on the SEC process, we extended our study employing the ratio r_m between the cross section of the $^2P_+$ and $^2P_-$ states, defined as:

$$r_m \equiv \frac{\sigma_m(^2P_+)}{\sigma_m(^2P_-)} \,, \tag{7.22}$$

which, for ZAPS, is equivalently determined as

$$r_m = \frac{\sigma[^2P_+](L=1, M_L=0)}{\sigma[^2P_-](L=1, M_L=0)} \,. \tag{7.23}$$

The ratio r_m is experimentally determined by the corresponding measured SDCSs, similarly to the ratio R_m, as [26]:

$$r_m = \frac{\frac{1}{\bar{\xi}[^2P_+]} \frac{d\sigma[^2P_+](0^\circ)}{d\Omega'}}{\frac{1}{\bar{\xi}[^2P_-]} \frac{d\sigma[^2P_-](0^\circ)}{d\Omega'}} \,. \tag{7.24}$$

It is worth mentioning that the ratio r_m although sensitive in its determination due to the small SDCS values, it has the advantage of being free of cascade effects, as well as from solid angle correction schemes. The obtained ratio r_m for boron, carbon and oxygen is presented in Fig. 7.11(b). A decrease of r_m with decreasing the projectile atomic number Z_p, similarly to that of the ratio R_m, is evident. This is primarily due to the relative increase of the cross section of the $^2P_-$ state compared to that of the $^2P_+$ state with lowering the atomic number, as shown in Fig. 7.10.

The above results, that the population of the $^2P_-$ state considerably affects the dependence of both the ratios r_m and R_m, is a clear signature of the strong electron-electron interaction effects in the SEC process in fast ion-atom collisions. This effect

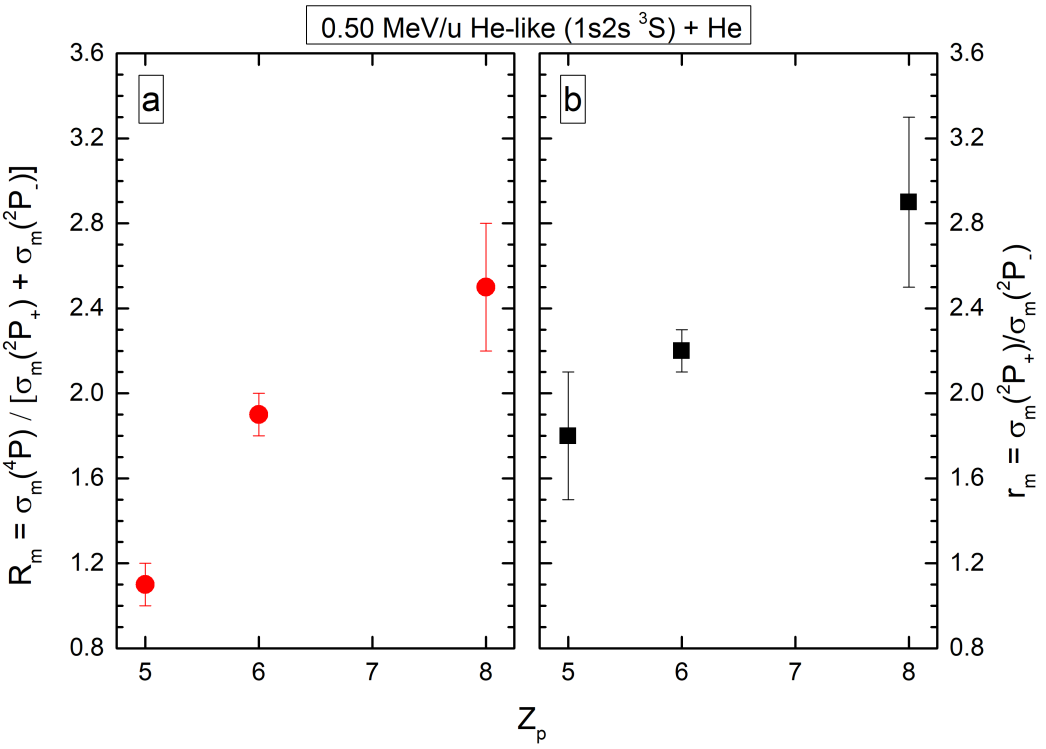

Figure 7.11: Isoelectronic study of the R_m (a) and r_m (b) ratios for collisions of 0.50 MeV/u B^{3+}, C^{4+}, and O^{6+} with He.

was clearly demonstrated in Ref. [161] and actually was termed as Pauli shielding mechanism, detailed here in Section 7.1. According to this, the population of the $1s2s2p\ ^2P_-$ state is not allowed by pure Coulombic interaction but rather by a weaker higher-order spin exchange process. Here, our isolectronic study strongly supports these arguments, showing enhanced electron-electron interaction vs electron nucleus interaction effects for the $^2P_-$ state with decreasing the atomic number Z_p.

Chapter 8

Determination of the Ion Beam Energy Width

8.1 Background and Motivation

As we mentioned in Chapter 3, in tandem Van de Graaff accelerators, the production of the desired charge state, is accomplished through a stripping process. Software packages based on semiempirical models allow estimation of the ion beam intensity by varying parameters like the incoming charge state, stripping energy, medium, and stripping location [231–234]. However, these models do not provide information about the inherent energy width of the ion beam, which is an important parameter affecting the energy resolution of the measurements. Generally, gas stripping results in narrower energy widths compared to foil stripping due to energy straggling effects in thin foils. While gas stripping is often preferred, foil stripping may be suitable for higher currents or to avoid complex pumping schemes.

Several techniques have been proposed for determining the energy width of a beam. Beam current measurement is such a method, where Faraday cups are employed to measure the beam current at different energies, allowing for the inference of the beam's energy width [235]. Beam profile monitors provide information about the spatial distribution of the beam, which can then be used to determine the energy width [236]. Nuclear resonances offer another approach, involving the measurement of γ-ray yield in specific reactions such as (p, γ) or $(p, p'\gamma)$. By deconvoluting the measured yield and considering the intrinsic resonance width, the energy width of the beam can be determined [237, 238].

While these techniques have been widely utilized, here we propose an alternative, *in situ* method for determining the energy width of ion beams in tandem Van de Graaff accelerators. Our approach relies on the analysis of state-selective projectile Auger electron spectra using Monte Carlo simulations in the SIMION ion optics package [16]. In the following discussion we detail the specifics of this method.

8.2 SIMION Simulations

In the proposed method, we determine the energy width of the ion beam by comparing the measured KLL Auger peak width to those obtained from Monte Carlo type simulations performed using the SIMION ion optics package, as described in

Chapter 5. Precise values for all experimental and theoretical parameters were considered in our numerical code utilized in the simulations. Geometric dimensions were considered with the highest level of detail, and the spectrometer voltages were measured with a precision better than 0.1%.

The Auger energies and the lifetimes of the Li-like, $1s2s2l\ ^{2,4}L$, doubly-excited states, were taken from Refs. [15, 239]. The Auger energy distributions, with widths derived from their lifetimes, were simulated using pseudo-random Lorentzian distributions. Thus, the only parameter treated as a variable within the code was the beam energy width, $\Delta E_P/E_P$. A Gaussian pseudo-random distribution was employed to model the energy width for the ion beam energy.

8.3 KLL Auger Projectile Spectroscopy as a Beam Diagnostics Tool

In Fig. 8.1, we present an example showing the comparison of a measured KLL Auger electron spectrum with the corresponding SIMION simulations for collisions of 12 MeV O^{6+} + He. It is evident that when we used a zero energy width for the ion beam, the simulated Auger spectra exhibited an energy resolution approximately half of that of the experimental Auger spectra. This corresponds to the convolution of the natural widths of the Auger states and the kinematic broadening [76] with the response function of the spectrometer. However, when we set the energy width to $\Delta E_P/E_P = 0.18\%$, the simulated and experimental spectra showed the best agreement, judged by minimizing the sum of the residuals between the two spectra.

In Fig. 8.2, we present the results of our analysis regarding the O^{6+} beam energy widths, $\Delta E_P/E_P$, obtained using the method described earlier. These measurements were performed for collision energies ranging from 8 to 24 MeV. For higher energies, i.e., above 18 MeV, we employed single-step terminal stripping, as the ion beam currents delivered to our experimental setup was in the order of a few nA, suitable for our KLL Auger measurements. On the other hand, for lower collision energies, the ion beam currents were lower, and thus we utilized two-step stripping processes.

To estimate the uncertainty of our method, we obtained the lower and upper limits of $\Delta E_P/E_P$ from the corresponding SIMION-generated distributions that marginally encompassed the experimental distribution. We found that the average uncertainty value was approximately 10% for all the measurements. It is worth noting that high statistics were ensured for all KLL Auger spectra recorded, which was essential for the reliable application of our method.

From Fig. 8.2, it is apparent that the ion beam energy width exhibits a general decreasing trend with increasing collision energy, regardless of the stripping method employed. Additionally, the energy width of the ion beam is higher when foil strippers are used, which aligns with our expectations based on energy straggling considerations.

Indeed, as it is demonstrated in Fig. 8.3, the stripping process affects the Auger line widths, as it is evident by the comparison of two KLL Auger spectra resulting from different post-stripping method. For both cases, the O^{4+} beams resulted from stripping the O^- ions in the gas terminal stripper. The final O^{6+} resulted from post-stripping the O^{4+} beam onto either gas or thin carbon foils. Note that the different Auger peak widths, evident in Fig. 8.3, originate from the different configurations

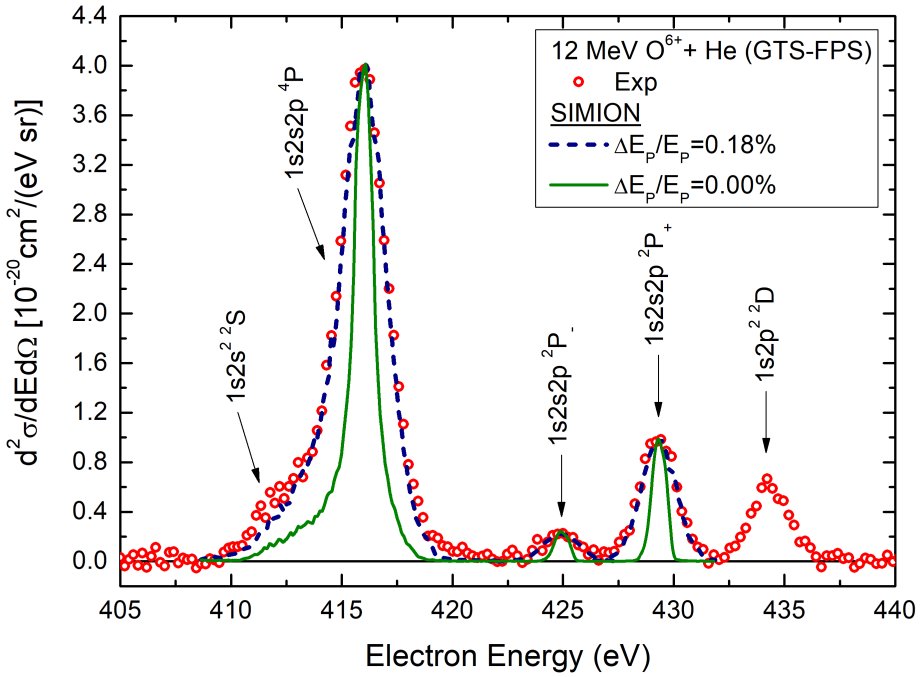

Figure 8.1: Projectile rest frame zero-degree DDCS obtained for collisions of 12 MeV O^{6+} with He. Symbols: Experiment; Lines: SIMION simulations for $\Delta E_P/E_P = 0.18\%$ (dashed blue line) and for $\Delta E_P/E_P = 0.00\%$ (full green line). Simulations were normalized to the measurements. Taken from [16].

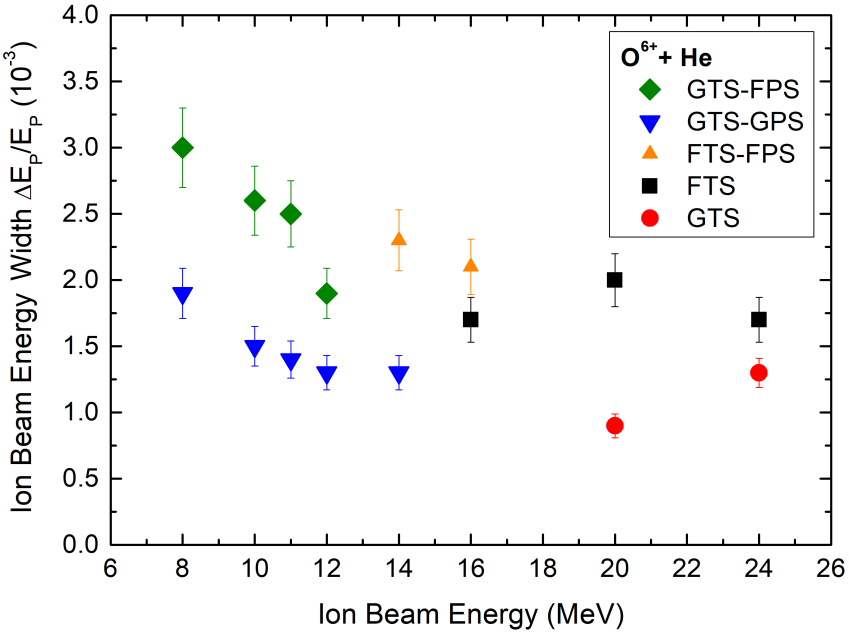

Figure 8.2: O^{6+} ion beam energy width, $\Delta E_P/E_P$, obtained for collisions of 8-24 MeV O^{6+} + He. Different symbols refer to different beam stripping processes: Green diamonds, GTS-FPS; Blue down-pointing triangles, GTS-GPS; Orange up-pointing triangles, FTS-FPS; Black squares, FTS; Red circles, GTS. Taken from [16].

fractions of the ions delivered in the $O^{6+}(1s^2\ {}^1S, 1s2s\ {}^3S)$ mixed-state, as resulting from the different stripping methods [157].

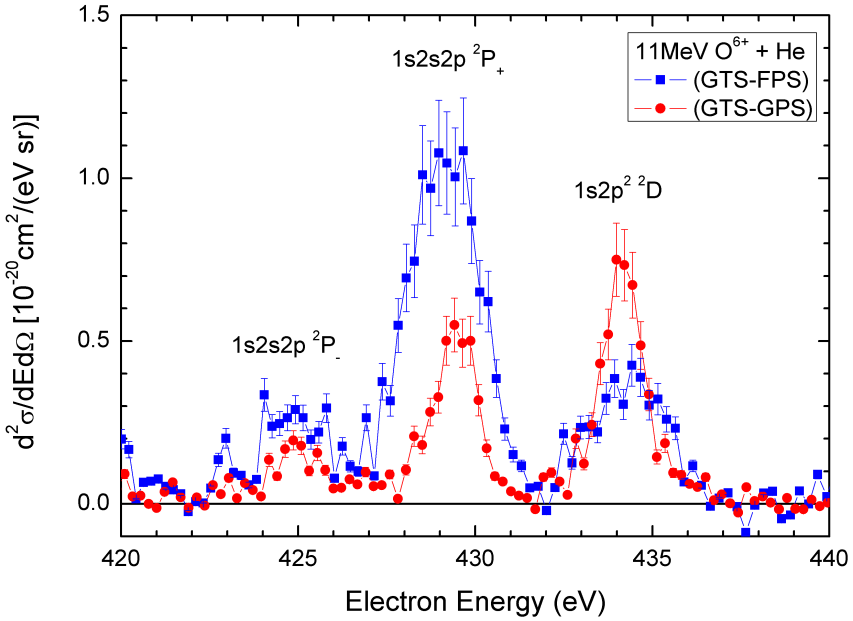

Figure 8.3: DDCS electron spectra for the collisions of 11 MeV O^{6+} ions with He, showing the effect of the stripping method on the Auger line widths. Blue filled squares: GTS-FPS; Red filled circles: GTS-GPS. Taken from [16].

Our study was expanded to include O^{4+} beams. We measured the same KLL Auger peaks for the collisions of 12-20 MeV O^{4+} + He. In these measurements, we used only the single-step stripping inside the tandem accelerator, specifically the gas terminal stripper and the foil terminal stripper. The results are presented in Fig. 8.4. It is evident that the ion beam energy width exhibits an overall decrease with increasing collision energy, regardless of the stripping method employed, which is consistent with the findings for O^{6+} beams. However, the values of $\Delta E_P/E_P$ are generally smaller for the O^{4+} beams compared to the O^{6+} beams. This can be attributed to the higher terminal voltages used for the production of the O^{4+} beams, resulting in higher stripping collision energies, as can be seen from Eq. 3.1.

Our results show good agreement with the corresponding results obtained using the nuclear resonances technique, which is commonly employed in nuclear experiments at the NCSR "Demokritos" Tandem Van de Graaff accelerator facility [237]. However, a direct comparison between the two sets of results is not feasible due to the differences in experimental setups and beam transportation conditions.

It is important to highlight that our technique incorporates all the parameters responsible for the broadening of the Auger peaks within the simulation, eliminating the need for independent determinations. One significant advantage of the proposed approach is the minimization of line broadening effects in the ZAPS technique, as discussed in Section 2.4. Moreover, the natural widths of the Auger peaks, calculated based on theoretical lifetimes, are typically on the order of meV or smaller, as shown in Table 8.1. Consequently, the primary factor contributing to the broadening of Auger peaks is the response function of the spectrometer. As a result, in the high-resolution ZAPS technique, the impact of solid angle line broadening and natural width is negligible, enabling the measurement of broadening effects originating from

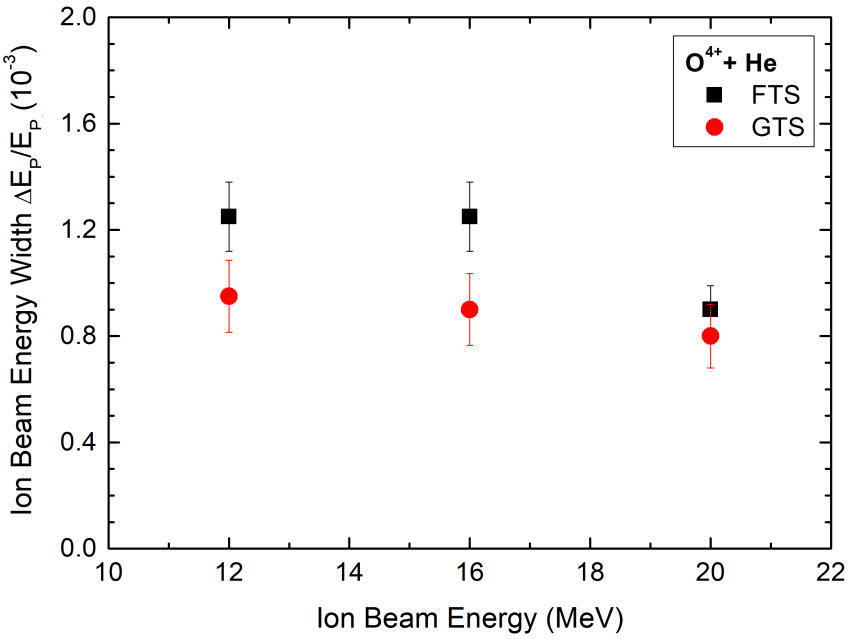

Figure 8.4: O^{4+} ion beam energy width, $\Delta E_P/E_P$, obtained for collisions of 12-20 MeV O^{4+} + He. Different symbols refer to different beam stripping processes: Black squares, FTS; Red circles, GTS. Taken from [16].

the energy width of the ion beam.

Table 8.1: Lifetimes and natural widths for the $1s2s2p\ ^{2,4}P_J$ states of O^{5+}. Numbers in parentheses stand for powers of 10. Taken from [16].

State	Lifetimes (ns)	Natural width (eV)
$^4P_{1/2}$	0.900	7.31(−7)
$^4P_{3/2}$	2.500	2.63(−7)
$^4P_{5/2}$	29.57	2.23(−8)
$^2P_-$	9.44(−5)	6.97(−3)
$^2P_+$	1.36(−5)	4.84(−2)

In conclusion, this *in situ* method for the determination of the ion beam energy width, $\Delta E_P/E_P$ allows for the convolution of the ion beam's energy width within the Auger electron spectra, eliminating the need for additional measurements. Furthermore, it offers the flexibility to vary parameters such as the stripping location and accelerator settings for each experiment, enabling accurate determination of the energy width under specific conditions.

Chapter 9

Summary and Conclusions

In this dissertation we studied the intricate atomic mechanisms governing electron capture and ionization in fast (a few MeV/u) ion-atom collisions, with a specific focus on collision systems with multi-electron open-shell ions, including He-like ($1s2s\ ^3S$) and Be-like ($1s2s^22p\ ^3P$) ions. These pre-excited ions, initially having a K-shell vacancy, provide a unique view into the dynamic collision processes in ionic environments, deviating from the ground state. Our research has shed light on the complex phenomena of electron capture/loss to the projectile continuum and single electron capture, serving as a ground for testing advanced collision theories and unraveling the underlying fundamental physics.

Our cusp electron investigations encompassed collision systems featuring both bare and dressed projectiles of diverse ion species. The primary objectives were to decipher the contributions of multielectronic target subshells and open-shell projectiles in generating cusp electrons. Accompanied by state-of-the-art distorted wave theories, our studies have unveiled intriguing insights into electron capture and loss processes, notably the pivotal role of the target $2p$ electron in collisions involving bare projectiles and multielectronic Ne and Ar targets. Furthermore, we investigated for the first time, both experimentally and theoretically, the cusp electron peak originating exclusively from collisions of pre-excited ions with He targets, at the DDCS level. A notable discovery was the identification of a small peak on the low-energy wing of the cusp peak, with an energy offset from the cusp maximum equal to the target's ionization potential. This signifies a novel electron loss to the continuum process involving correlated electron-electron interaction.

In addition to cusp electron studies, our research focused on the investigation of the single electron capture process in collisions of fast He-like mixed-state projectiles ($1s^2\ ^1S$, $1s2s\ ^3S$) with He. Building upon previous work with He-like carbon projectiles, our investigations extended to He-like oxygen and boron projectiles, supporting evidence of strong electron correlations, showcased by the values of the ratio R_m between the yields of the ^4P and $^2P_\pm$ peaks. In detail, our isoelectronic SEC study highlighted the population of the $^2P_-$ state, showing enhanced electron correlation effects with decreasing the projectile's atomic number Z_p. Furthermore, we determined the SDCSs of $1s2s2p\ ^4P$, $^2P_\pm$ states originating from both ground, $1s^2$, and metastable, $1s2s\ ^3S$, configurations of the incident oxygen beam across a wide range of collision energies. These findings hold significant value as benchmarks for refining and validating advanced three-active electron theories, such as the 3eAOCC theory, which we critically compared against our measurements.

It is worth noting that the SDCSs associated with the $1s2s2p\ ^2P_-$ state, for collisions of O^{6+}+He, exhibit the lowest values, i.e., of the order of 10^{-22} cm^2/sr. Nevertheless, our double-measurement ZAPS technique, has enabled the precise determination of absolute SDCSs even under such challenging conditions. This outcome underscores the capabilities of our atomic physics setup, signaling opportunities for similarly demanding experiments in the foreseeable future. Such an example is the investigation of double electron capture in collisions of H-like projectiles with He, that holds immense potential, as this three-electron collision system could serve as an exceptional laboratory for the scrutiny of advanced 3-electron theories, such as the 3eAOCC.

Lastly, we introduced a new method for determining the energy width of ion beams in tandem Van de Graaff accelerators, an important parameter influencing experimental resolution. Our approach relied on measurements of KLL Auger spectra, complemented by Monte Carlo simulations within the SIMION ion optics package. This novel technique enables the in-situ determination of ion beam energy width directly from the KLL Auger spectra, eliminating the need for additional measurements and enhancing the precision of experimental outcomes.

The goal of this dissertation was to make significant contributions to the understanding of electron capture and ionization processes in fast ion-atom collisions, advancing our knowledge of atomic physics phenomena and providing valuable insights for future research in this field. In this spirit, we have upgraded our experimental setup so as to enable experiments including coincidences techniques. This upgrade has substantially increased the arsenal of the Atomic Physics beamline operating at the INPP of NCSR "Demokritos", paving the way for continued exploration of fundamental collision processes in the field of atomic physics.

Appendices

Appendix A

Supplemental Material of Chapter 2

Derivation of Eq. 2.1.

Proof. Starting from the velocity diagram depicted in Fig. 2.2, the velocity of the electron in the laboratory frame can be determined using the vector addition rule as:

$$\mathbf{v} = \mathbf{v}' + \mathbf{V_p} \ .$$

By squaring both sides we have:

$$\mathrm{v}^2 = \mathrm{v}'^2 + V_p^2 + 2\mathbf{v}' \cdot \mathbf{V_p} \Rightarrow \mathrm{v}^2 = \mathrm{v}'^2 + V_p^2 + 2\mathrm{v}' V_p \cos\theta' \ .$$

Multiplying all terms by $\frac{1}{2}m$ yields:

$$\frac{1}{2}m\mathrm{v}^2 = \frac{1}{2}m\mathrm{v}'^2 + \frac{1}{2}mV_p^2 + 2\frac{1}{2}m\mathrm{v}'V_p\cos\theta' \Rightarrow \epsilon = \epsilon' + t_p + 2\sqrt{\epsilon t_p}\cos\theta'$$

since

$$\frac{1}{2}m\mathrm{v}'V_p = \sqrt{\frac{1}{4}m^2\mathrm{v}'^2V_p^2} = \sqrt{\epsilon t_p} \ .$$

■

Derivation of Eq. 2.2.

Proof. To establish Eq. 2.2, we begin with the relation:

$$\mathbf{v}' = \mathbf{v} - \mathbf{V_p} \ .$$

The steps to prove this equation are analogous to those followed in the previous derivation.

■

Derivation of Eqs. 2.5, 2.6.

Proof. By substituting $\sqrt{\epsilon} \equiv x$ into Eq. 2.2, we can rewrite it as follows:

$$x^2 - 2x\sqrt{t_p}\cos\theta + t_p - \epsilon' = 0 \ .$$

Solving this quadratic equation yields two possible solutions:

$$x_\pm = \sqrt{\epsilon_\pm} = \sqrt{t_p}\cos\theta \pm \sqrt{t_p\cos^2\theta - t_p + \epsilon'} \ .$$

Taking the square root of both sides, we obtain the solution:

$$\epsilon_{\pm}(\theta) = \epsilon'(\zeta\cos\theta \pm \sqrt{1-\zeta^2\sin^2\theta})^2\,,$$

where we have introduced the dimensionless parameter ζ (see Eq. 2.4).

It is important to note that the expression under the square root must be larger than or equal to zero. In the case of slow emitters ($\zeta < 1$), this mathematical requirement is satisfied for any emission angle θ. However, for fast emitters ($\zeta > 1$), the maximum attainable observation angle θ is limited as follows:

$$1-\zeta^2\sin^2\theta \geq 0 \Rightarrow \theta_{max} = \arcsin\left(\frac{1}{\zeta}\right)\,.$$

■

Derivation of Eqs. 2.7, 2.8.

Proof. The derivation of both equations can be easily obtained from Eq. 2.5 by considering $\theta = 0°$. The plus (+) sign corresponds to the higher laboratory electron energy, associated with a projectile rest frame ejection angle $\theta' = 0°$, while the minus (−) sign corresponds to the lower laboratory electron energy, associated with a projectile rest frame ejection angle $\theta' = 180°$. These relations hold for fast emitters ($\zeta > 1$). For slow emitters ($\zeta < 1$), there is only one solution, which corresponds to the plus (+) sign.

■

Derivation of Eq. 2.9.

Proof. The expressions for line stretching (or compression) can be obtained by taking the derivatives of Eqs. 2.7:

$$\begin{cases} \left.\frac{d\epsilon}{d\epsilon'}\right|_{+} = \frac{d(\sqrt{\epsilon'}+\sqrt{t_p})^2}{d\epsilon'} = \frac{\sqrt{\epsilon'}+\sqrt{t_p}}{\sqrt{\epsilon'}} = 1+\zeta & (\text{All } \zeta,\ \theta' = 0°, \theta = 0°) \\ \left.\frac{d\epsilon}{d\epsilon'}\right|_{-} = \frac{d(\sqrt{\epsilon'}-\sqrt{t_p})^2}{d\epsilon'} = \left|\frac{\sqrt{\epsilon'}-\sqrt{t_p}}{\sqrt{\epsilon'}}\right| = |1-\zeta| & (\zeta > 1,\ \theta' = 180°, \theta = 0°)\,, \end{cases}$$

where the absolute value is taken into consideration for the case of fast emitters in order to avoid negative values that do not have any physical meaning.

■

Derivation of Eq. 2.10.

Proof. Starting from Eq. 2.9 we have:

$$\frac{\Delta\epsilon}{\Delta\epsilon'} = |1\pm\zeta| = \sqrt{(1\pm\zeta)^2} = \frac{\sqrt{\epsilon'(1\pm\zeta)^2}}{\epsilon'}\,.$$

Combining the last equation with Eqs. 2.7, 2.8 we obtain:

$$\frac{\Delta\epsilon}{\Delta\epsilon'} = \sqrt{\frac{\epsilon}{\epsilon'}} \Rightarrow \Delta\epsilon = \sqrt{\frac{\epsilon}{\epsilon'}}\Delta\epsilon' = \sqrt{\frac{\epsilon'}{\epsilon}\frac{\epsilon}{\epsilon'}}\Delta\epsilon' \Rightarrow \frac{\Delta\epsilon}{\epsilon} = \sqrt{\frac{\epsilon'}{\epsilon}}\frac{\Delta\epsilon'}{\epsilon'}\,.$$

■

Derivation of Eq. 2.11.

Proof. According to the geometric representation shown in Fig. 2.3, the angle transformation can be calculated as follows:

$$\sin\theta = \frac{v'\sin\theta'}{v} \Rightarrow \sin\theta = \sqrt{\frac{\epsilon'}{\epsilon}}\sin\theta' .$$

By squaring both sides of the above equation and multiplying both parts with 4π we obtain:

$$4\pi\sin^2\theta = \frac{\epsilon'}{\epsilon}4\pi\sin^2\theta' .$$

The solid angle of a cone, with its apex at the same point as the solid angle and an apex angle of 2θ, can be represented by the area of a spherical cap on a unit sphere, i.e.:

$$\Omega = 2\pi(1-\cos\theta) = 4\pi\sin^2\left(\frac{\theta}{2}\right) .$$

By combining the last two equations we obtain the following expression:

$$\Delta\Omega = \frac{\epsilon'}{\epsilon}\Delta\Omega' .$$

Finally, by utilizing Eqs. 2.7, 2.8 we obtain the final equation:

$$\frac{\Delta\Omega}{\Delta\Omega'} \Rightarrow \begin{cases} \frac{\Delta\Omega}{\Delta\Omega}\Big|_+ = \frac{1}{(1+\zeta)^2} & (\text{All } \zeta,\ \theta' = 0°, \theta = 0°) \\ \\ \frac{\Delta\Omega}{\Delta\Omega}\Big|_- = \frac{1}{(1-\zeta)^2} & (\zeta > 1,\ \theta' = 180°, \theta = 0°) . \end{cases}$$

■

Derivation of Eq. 2.12.

Proof. The derivation of the equation can be easily obtained by combining Eqs. 2.10 and 2.3, resulting in:

$$\frac{d^2\sigma}{d\Omega d\epsilon} = \frac{d^2\sigma}{\frac{1}{(1\pm\zeta)^2}d\Omega'|1\pm\zeta|d\epsilon'} = |1\pm\zeta|\frac{d^2\sigma}{d\Omega' d\epsilon'} .$$

■

Appendix B

The TARDIS program

The TARDIS (Transmitted charge Distribution) code for charge state analysis was developed in C# programming language to calculate the expected charge state distributions and corresponding probabilities after ion beam stripping [240]. The code is based on the older FORTRAN program CHARGE used in the 7 MV Tandem accelerator laboratory of J.R. Macdonald at Kansas State University [241].

The program utilizes four semiempirical formulae [231–234], which provide beam and stripper characteristics. Regarding the beam, the energy E (in MeV), corresponding velocity u (in mm/ns), atomic number of ions Z_p, mass of the introduced element m (in amu), and incoming charge value can be specified. A multiplication factor can also be introduced to scale the outgoing current values. As for the stripping medium, both solid (thin foil) and gas options are available, with the corresponding atomic number selection. Results based on the calculations of the four models are presented together for comparison.

Charge state distributions can be represented by Gaussian distributions characterized by an average charge $\bar{q}$ and corresponding width d. The four formulae predict these parameters based on the beam interaction with the solid or gas stripper, considering electronic loss and capture processes taking place during the collision. The equations implemented in the TARDIS program for each semiempirical formula are given in Fig. B.1. Each formula has a different range of values for Z_p, around which it exhibits optimal use, and these regions are incorporated into the program. The interface of the TARDIS program is shown in Fig. B.2. The program allows the retrieval of the four distributions in a consolidated table and the exportation of results in graphical representations. For a comprehensive understanding of the TARDIS code and the four semiempirical formulae employed, a detailed description can be found in [28].

For example, according to the formulae, the dominant charge state produced after the collision of a 1.2 MeV C^- ion beam (corresponding to 1.2 MV tandem voltage) is $q = 3$, i.e., C^{3+} for this specific collision scheme. Additionally, C^{2+} and C^{4+} ions have considerable production fractions. It is worth noting that the final energy of each charge state differs depending on its final charge (see Eq. 3.1). For instance, the C^{4+} ion beam will have a final energy of 6 MeV, while the C^{3+} ion beam will have a final energy of 4.8 MeV, for a tandem voltage of 1.2 MV.

While a single stripping process (tandem stripping) is adequate to produce a 6 MeV C^{4+} ion beam, there are cases where a higher charge state at adequate intensity is required. In such scenarios, a second stripping process (post-stripping) must be

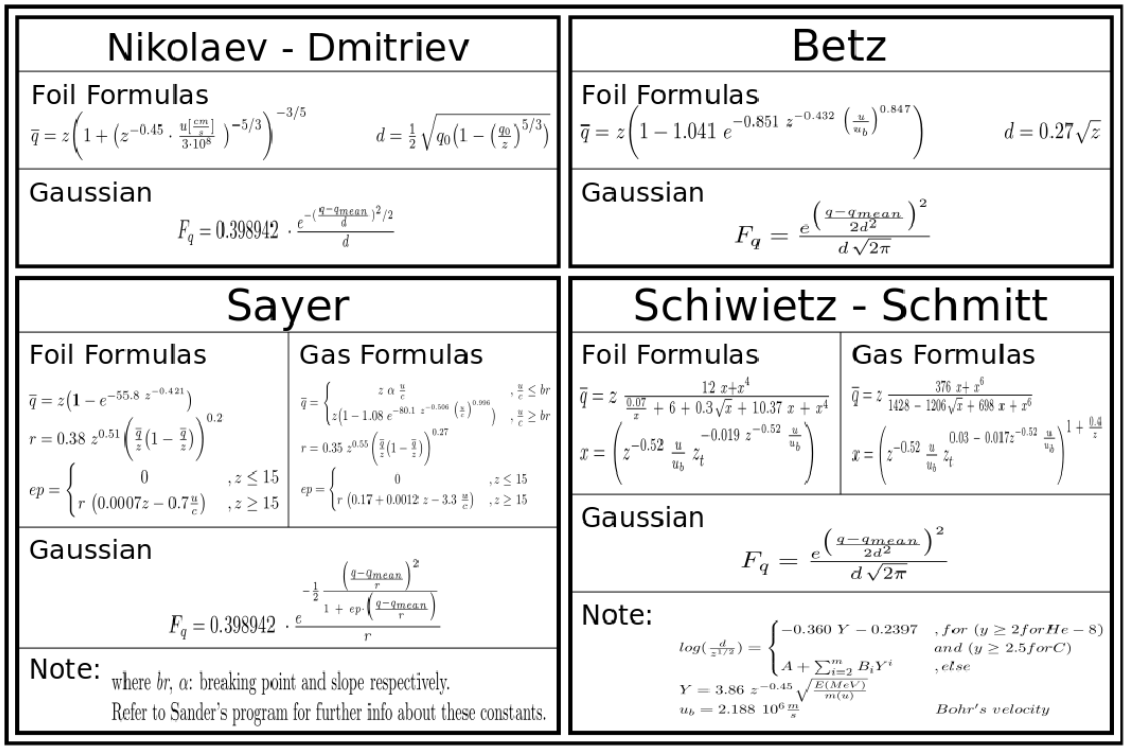

Figure B.1: The four semiempirical formulae utilized by the TARDIS code. Taken from [28].

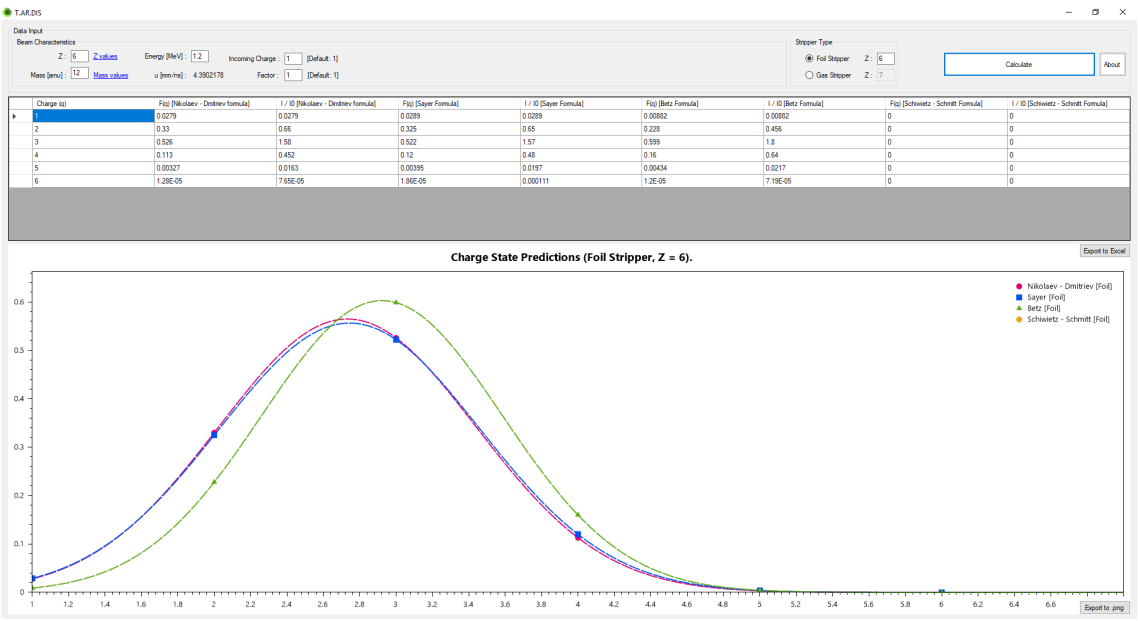

Figure B.2: The TARDIS code interface displays the charge state distributions resulting from the collision of 1.2 MeV C^- ions with a carbon thin foil.

employed. Thus, a 6 MeV C^{2+} or C^{3+} ion can be further stripped after exiting the accelerator in the post-stripper (foil of gas), resulting in charge state distributions centered around $\bar{q} = 4$, with an increased intensity for the C^{5+} ion beam, compared to the single stage tandem stripping case. This scenario is depicted in Fig. B.3.

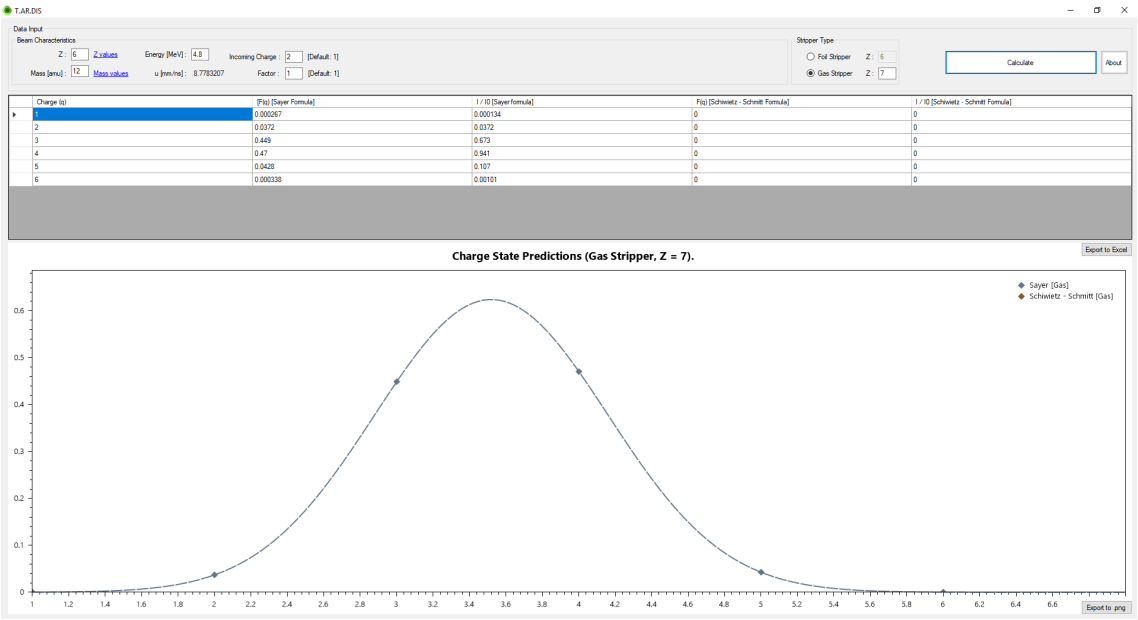

Figure B.3: Same as Fig. B.2 for the collision of 6 MeV C^{2+} ions with a N_2 gas medium.

Appendix C

Beamtime: Beamline Preparation and Data Acquisition

C.1 Introduction

In this appendix, we provide a guide on how to prepare the Atomic Physics beamline for experiments. We will cover the alignment procedure, electrical connections, and essential power supply requirements. Additionally, we will explain how to record spectra step-by-step during the experiment.

C.2 Alignment

The first step in preparing for beamtime is the geometrical alignment of the beamline. To achieve optimal alignment, we calibrate the telescope using the farthest set of slits, which is SL1. The goal is to align the telescope with the beamline's optical axis, and this involves identifying two stable points in space. The base of the telescope serves as the first point, while the second one is found along the beamline. For the L45 line, this stable point is defined twice using SL1 and SL2. Each set of slits has central settings, where the slits align precisely with the optical axis. SL1 is preferred for telescope alignment, as it is the furthest stable point on the beamline. Both SL1 and SL2 are equipped with LED lights powered by the current outputs of the slits, along with an external power supply of 9 V. The alignment process involves setting only two perpendicular slits to the centered position, aligning the telescope's cross-hair with their edges, and then repeating the process with the other two slits. Once the telescope is aligned, it serves as a guide to align everything else in the beamline.

Typically, the alignment of the HDA chamber is necessary, especially after extended periods of time or heavy-duty activities within the chamber. However, the support table allows for corrections in case of slight misalignment. The alignment process is conducted from the outside to the inside and from upstream to downstream. If both the chamber and the HDA are misaligned, the chamber is aligned first, and then the HDA is adjusted accordingly. Similarly, if both the chamber and the gas cell are misaligned, the gas cell is corrected first. During the alignment process, the gas cell apertures should appear as circles. An improperly aligned gas cell will appear as an ellipsoid shape.

C.3 Vacuum

After aligning the beamline, the next step is to pump it down before testing any power supplies. The process begins by opening the fore-pumps until a pre-vacuum of 10^{-2} Torr is achieved. At this point, the turbo pumps are activated, but it's important to be cautious until they reach their full speed. Fig. C.1 illustrates the HDA chamber vacuum as a function of time during the pump down process.

It is essential to start pumping the beamline at least one week before the beamtime to allow enough time for identifying and correcting any possible sealing problems. This early start also helps to ensure that the desired pressures can be reached in case out-gassing occurs due to previous work in the beamline.

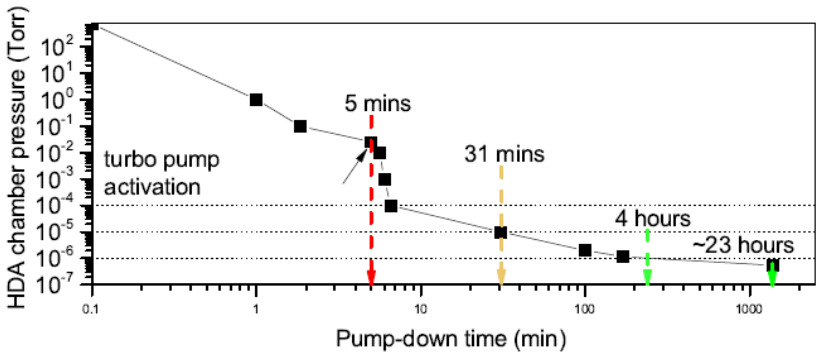

Figure C.1: HDA chamber vacuum as a function of time during pump down. Taken from [9].

C.4 Power supplies

C.4.1 Steerers

The Steerers PSU (Power supply units) provide current to the double pair of steerers that control the ion beam's trajectory. Before each experiment, a thorough test is conducted to ensure their proper operation. Ideally, each of the four current supplies should be capable of providing up to 2.5 to 3 Amperes in both polarities. To test the Steerers PSU, a simple multimeter can be used, but it is crucial to exercise caution during the high current measurement. These power supplies should be turned on a few days before the experiment to stabilize their performance. Throughout the experimental period, they are kept operational to prevent any hysteresis effects on the currents. This ensures the stability and reliability of the steerers during the experiment.

C.4.2 Suppressor

The Suppressor is an electrode positioned on the final Faraday cup for suppressing electrons emitted from the cup. This suppression is crucial for the accurate beam current measurement, since it suppresses all the secondary electrons not to leave the

FC volume and wrongly measured as excessive current. The power supply unit provides a voltage of -300 VDC (Volts direct current). To ensure its proper operation, a simple voltage check should be performed on both ends of the connections.

C.4.3 Master Valve Switch

The Master Valve Switch is a transformer that converts 240 VAC (Volts altering current) to 24 VAC, providing the necessary power for the valves. Each isolation valve has its dedicated switch, which is connected in series with the Master Valve Switch. This setup ensures proper control and operation of the valves during the experiment.

C.4.4 MCP

The MCP HVPS can be checked by setting its voltage (V_{MCP}) to a value lower than 1 kV, which allows us to verify the performance of the voltage divider. Additionally, we can check the floating voltage by setting $V_{bias} + V_{MCP}$ to a value lower than 1 kV. V_{bias} can be independently checked as well.

C.4.5 HDA

To verify the HDA HVPS, the rack-mounted voltage divider is utilized, offering a division factor of 10.900608. For instance, if the set voltage is 2000 Volts, the measured value of the accurate multimeter should be 2000/10.900608 = 183.476 VDS.

C.5 MCP image

Proper testing of the DAQ system involves checking for signals on the MCP surface. After applying a high voltage on the MCP (less than 2300 Volts), small sparks, also known as dark current, may be detected all over the MCP image. These sparks are considered random noise, and after a few minutes, a uniform round picture should be detected on the MCP, indicating proper operation.

C.6 Counter

To test the counter, a pulse generator and a custom-made *.vi (a LabVIEW virtual instrument file) in the laboratory computer can be used. The pulse generator generates electrical pulses that simulate particle signals, and the custom-made *.vi helps in monitoring and analyzing the response of the counter to these pulses.

C.7 Gas Delivery System

The gas delivery system must be thoroughly checked and properly purged before the experiment. During the experiment, the pressure in the pre-valve should be kept higher than atmospheric pressure to prevent any contamination of the gas target. This ensures the integrity of the gas target and maintains the purity of the gas used in the experiment.

C.8 Baratron

The Baratron unit should be warmed up for a minimum of 24 hours before the experiment, allowing it to reach its operating temperature. It is recommended to perform the zeroing just before the experiment to ensure accurate gas pressure readings during the experiment.

C.9 The HV Fasmatech program

The Fasmatech Company [242] has developed a LabView program designed for the APAPES apparatus. The main purpose of this program is to control the voltages applied by the power supplies to the various elements of the HDA. Additionally, it works in conjunction with a second program known as the MCP program, which is responsible for controlling the initiation and termination of the data recording process. The HV Fasmatech program's interface is shown in Fig. C.2

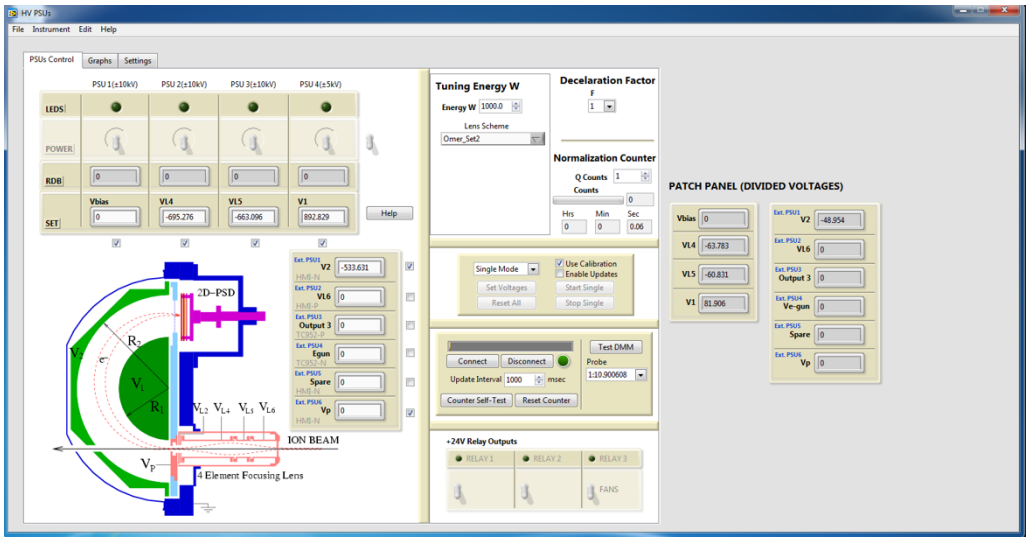

Figure C.2: Interface of the HV Fasmatech program.

To begin using the program, start by clicking the Connect button to establish the connection. Once connected, you will notice that the program's colors become more vibrant. Next, turn on the virtual power supply switch, located above the Help button, and check the Enable Updates box. From this point onwards, the program is ready to set the desired voltages.

The HDA requires different sets of voltages according to the desired measurement, which can be selected through the Lens Scheme option. Additionally, you can modify the deceleration factor by choosing the appropriate value from the Deceleration Factor option. To complete the configuration, set the desired tuning energy in the Tuning Energy W option.

After selecting all the necessary parameters, press the Set Voltages button to apply the settings. With these steps completed, the desired voltages have been applied to the HDA.

Before commencing the measurement, it is essential to determine the number of counts to be recorded, which can be configured using the Normalization Counter

option. The count number is influenced by several factors, primarily by the ion beam current and the desired process cross section to be measured. To ensure reliability and consistency throughout the experiment, it is generally recommended to record multiple spectra with a few thousand counts each.

Depending on the specific circumstances of each experiment, it is advisable to set the recording time for a single spectrum to be equal to or less than 5 minutes. This approach facilitates efficient data acquisition until the desired statistics is reached.

C.10 The MCP program

The MCP program is the data acquisition program. It was developed by the electronics laboratory of the ATOMKI Institute in Hungary [143] When launched, the interface shown in Fig. C.3 will appear. If the preamplifier and DAQ are powered on, an IP address ending in "112" will be displayed in the "Connect to hardware" window. To ensure proper functionality and avoid image freezing, it is crucial that the IP address ends with "112".

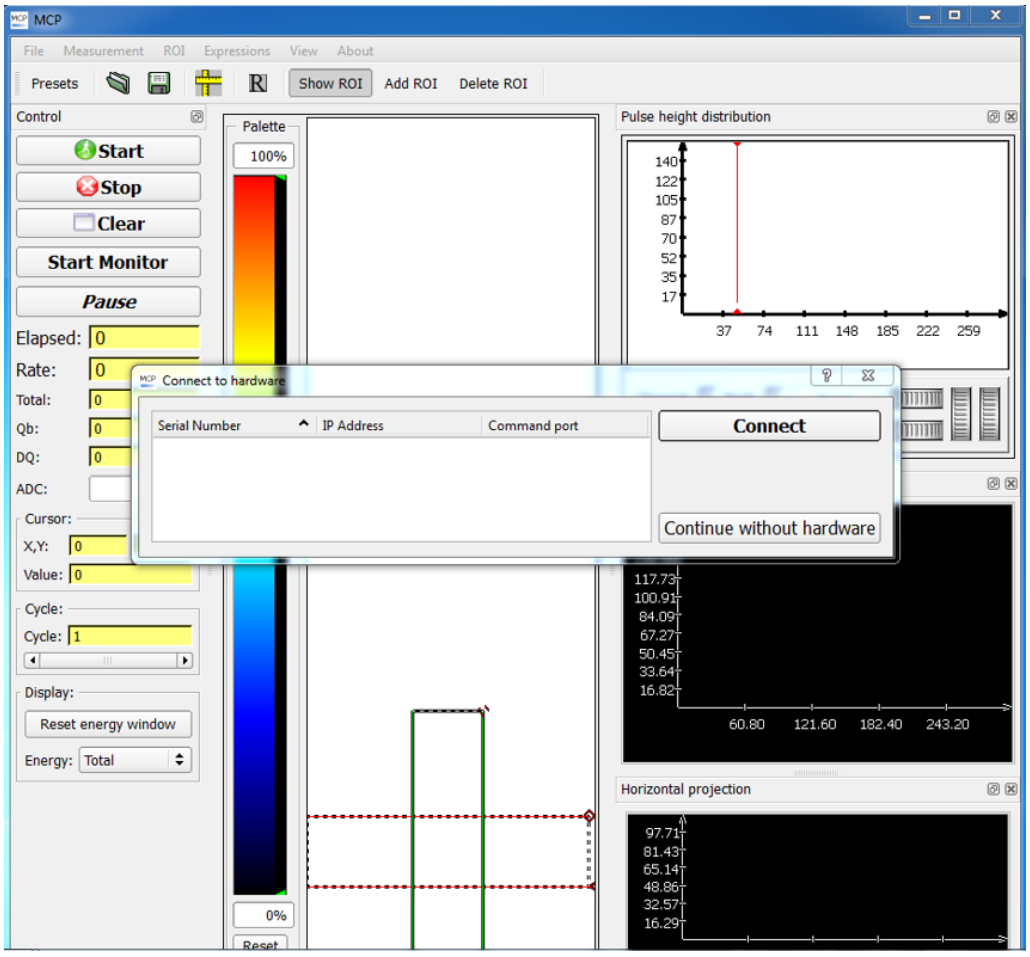

Figure C.3: Interface of the MCP program upon initialization.

The "Start Monitor" button enables the acquisition system to display the electron signal on the screen without recording and saving the corresponding data. This option is useful for adjusting the following parameters before starting the data acquisition process:

1. To fix the projection windows, one can adjust the projection by hand using the mouse or input exact values by going to "View → Show projection position ...". The rotation angle of the image can also be selected through "View → Show image transformation". Properly adjusting these parameters should result in the Horizontal Projections forming a square containing the entire PSD image, while the Vertical Projections should form a rectangle containing the energy-analyzed electrons.

2. Set the range of the "Pulse Height Distribution - PHD": This parameter controls the number of channels in the pulse's amplitude distribution. This corresponds to a smooth function of a fast increase followed by a much slower decrease. Usually, a cut-off by a small number is necessary to avoid noise in the PHD, judged by a sharp peak present at small number channels. The acquisition program calculates the sum signal of the MCP for each incoming event and displays the amplitude distribution in the software. It is important to note that the product of the number of image pixels and the energy spectrum channels should not exceed 1.4×10^8.

3. Finally, select "Window" in the "Energy' option. Now, the program is capable of applying a window on the raw data, displaying only those events with amplitudes between the two red lines set on the Pulse Height Distribution.

Now that all the settings have been configured, data acquisition can begin. To initiate the recording, click on the "Start" button. A pop-up window will appear, prompting to choose the location and filename for the saved files. Once these parameters are set, click "OK" and return to the HV PSUs program. By clicking on the "Start Single" button, the measurement begins. A typical screenshot in recording conditions of the MCP program corresponding to the measurement of 5.5 MeV B^{3+} + He is shown in Fig. C.4. As it is evident from the peak present at the pulse height distribution (upper right window), the spectrum is quite noisy, and thus a cut-off was necessary, as described above.

In Fig. C.5 a more detailed picture of the MCP area is shown identifying the peaks of the spectrum in the raw data.

C.11 Gas loading

When loading gas into the target gas cell, it is essential to close the beamline valve to prevent any contamination of the accelerator upstream beamline. Additionally, the MCP voltage should be set to zero during this process. Before introducing a new gas, a purging procedure must be performed to ensure the purity of the gas. This involves loading and flushing the gas cell three to four times to remove any residual contaminants.

C.12 End of the experiment

At the end of the experiment, several steps need to be followed for the proper shutdown. First, the switching valve should be closed to isolate the APAPES beamline

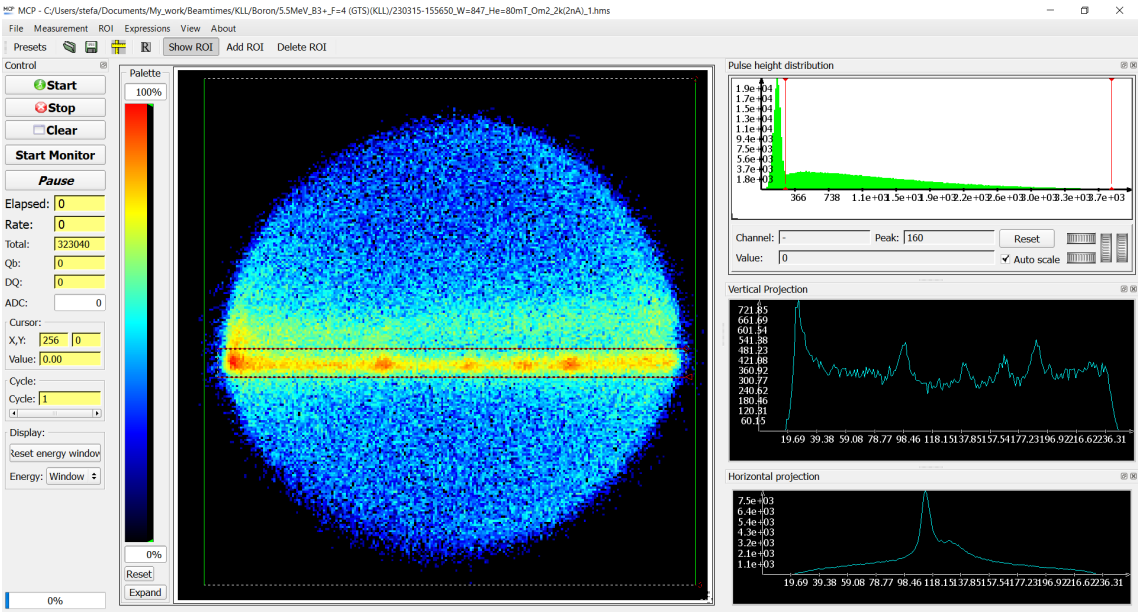

Figure C.4: Screenshot of the MCP program corresponding to the measurement of 5.5 MeV B^{3+} + He.

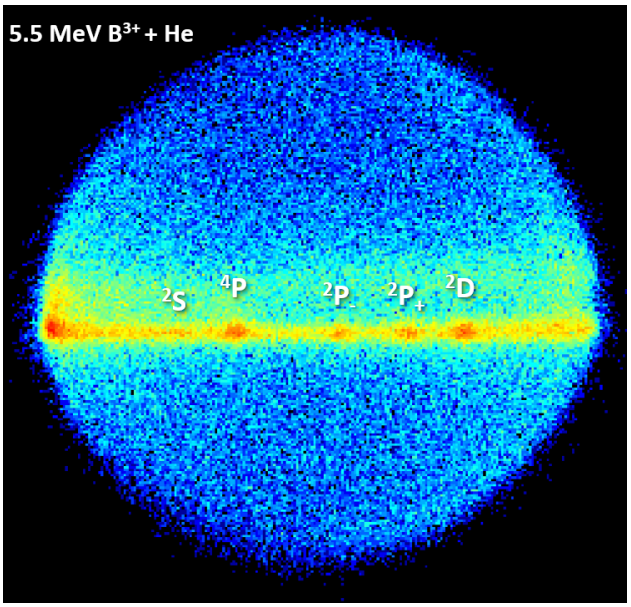

Figure C.5: Detail of the MCP area of Fig. C.4 identifying the peaks of the spectrum in the raw data.

from the accelerator beamline. Next, the power supplies should be turned off, followed by closing the gas bottles. Once these steps are completed, the pumping system can be shut down.

There are two options for handling the beamline after shutdown. The first option is to leave the beamline as is, maintaining a pre-vacuum. This option is preferred when the next beamtime is scheduled soon enough. Alternatively, the spectrometer chamber can be loaded with N_2 gas slightly above the atmospheric pressure to ensure the MCPs are safe, preventing them from being exposed to air humidity.

Appendix D

Metastable Beam Fraction Error Estimation via Monte Carlo Approach

The calculation of the error associated with the value of the fraction f is based on the uncertainties of the four individual parameters ${}^4P_{(1)}$, ${}^4P_{(2)}$, ${}^2D_{(1)}$, and ${}^2D_{(2)}$, corresponding to the SDCS values for the two measurements, (1) and (2). One way to approach this problem is to use the propagation of uncertainty formula and calculate the error as:

$$\sigma_f = \sqrt{\left(\frac{\partial f}{\partial P_1}\sigma_{P_1}\right)^2 + \left(\frac{\partial f}{\partial P_2}\sigma_{P_2}\right)^2 + \left(\frac{\partial f}{\partial D_1}\sigma_{D_1}\right)^2 + \left(\frac{\partial f}{\partial D_2}\sigma_{D_2}\right)^2}, \tag{D.1}$$

where we have used the notation P_i and D_i instead of ${}^4P_{(i)}$ and ${}^2D_{(i)}$ $(i = 1, 2)$ for brevity. Here, σ_{P_1}, σ_{P_2}, σ_{D_1}, and σ_{D_2} are the uncertainties associated with the measurements of P_1, P_2, D_1, and D_2, respectively. Note that all four parameters are estimated to have the same uncertainty since they are affected by the background choice and the accuracy of the simulations used to fit the experimental data. More specifically, we estimated the uncertainty of the parameters due to the background selection to be $\sigma_{BKG} = 5\%$. After the background subtraction, determination of the SDCSs was performed via Monte Carlo simulations utilizing the SIMION optics package. The error of the integration due to this analysis is estimated to be $\sigma_{SIM} = 5\%$. Finally, the overall uncertainty of the SDCSs is:

$$\sigma_{SDCS} = \sqrt{\sigma_{BKG}^2 + \sigma_{SIM}^2} \simeq 7\%. \tag{D.2}$$

Eq. D.1 can occasionally lead to excessively large error estimates. This may occur because the formula assumes that the uncertainties of each parameter are independent and uncorrelated, but in reality, the values of P_1 and D_1 are correlated, as are P_2 and D_2, since they pertain to the same electronic spectrum.

To address this issue, we performed a Monte Carlo simulation approach, where we randomly sampled values for each of the four parameters, i.e., the P_1, P_2, D_1, and D_2, based on their uncertainty distribution, and then calculated the resulting value of fraction f for each set of the sampled parameters. By repeating this process

we obtained a distribution of f values, which gave us a more accurate estimation for the uncertainty associated with f.

In detail, we developed a code written in the Python programming language using PySimpleGUI, a Graphical User Interface (GUI) framework [243]. The GUI layout is divided into five sections, i.e., "Values Info", "Errors Info", "Number of Iterations", "Experimental Results", and "Monte Carlo Results", as shown in Fig. D.1. Users can insert values for the four parameters of interest, their uncertainties, and the number of iterations N.

Figure D.1: GUI layout corresponding to the Python script utilized to optimize the fractions error estimation.

The "Run" button triggers the calculation process, where the program first calculates the experimental fractions and displays them in the "Experimental Results" section. Then, the program proceeds to execute the Monte Carlo simulation, where random values are generated using triangular distributions. The random values are centered around the inputs which are the experimentally determined values, with the limits of the generated values determined from the corresponding uncertainties σ_{P_i} and σ_{D_i} $(i = 1, 2)$ as:

$$\begin{aligned} X_{i,min} &= X_i - \sigma_{X_i} X_i, \\ X_{i,max} &= X_i + \sigma_{X_i} X_i, \end{aligned} \tag{D.3}$$

where X stands for P and D parameters. Note that the choice of a triangular distribution for sampling the random numbers was made due to the lack of knowledge about the distribution of the individual parameters, X_i. In Monte Carlo simulations, the triangular distribution, also known as a *lack of knowledge distribution*, is commonly used in such situations where the true distribution of a variable is unknown or difficult to determine [244, 245].

During the sampling process, it is important to ensure that the generated values meet certain conditions. In this particular simulation, there are two such conditions that must be met, i.e., $P_1 > P_2$ and $D_1 < D_2$. These conditions are a direct result of the physical system under investigation and must be taken into account in order to obtain meaningful results.

As a final step, the sampled values are stored in two different lists, corresponding to the fractions of the two electronic spectra at hand. The average and standard deviation of these lists are then calculated and displayed in the "Monte Carlo Results" section. Additionally, the program exports the sampled values and the corresponding

fractions for each set of data in a text file, allowing the user to further analyze the results or use them for subsequent calculations. This feature provides the user with flexibility in analyzing the results beyond the program's built-in functionality. In Fig. D.2 we present a flowchart showcasing the script's reasoning.

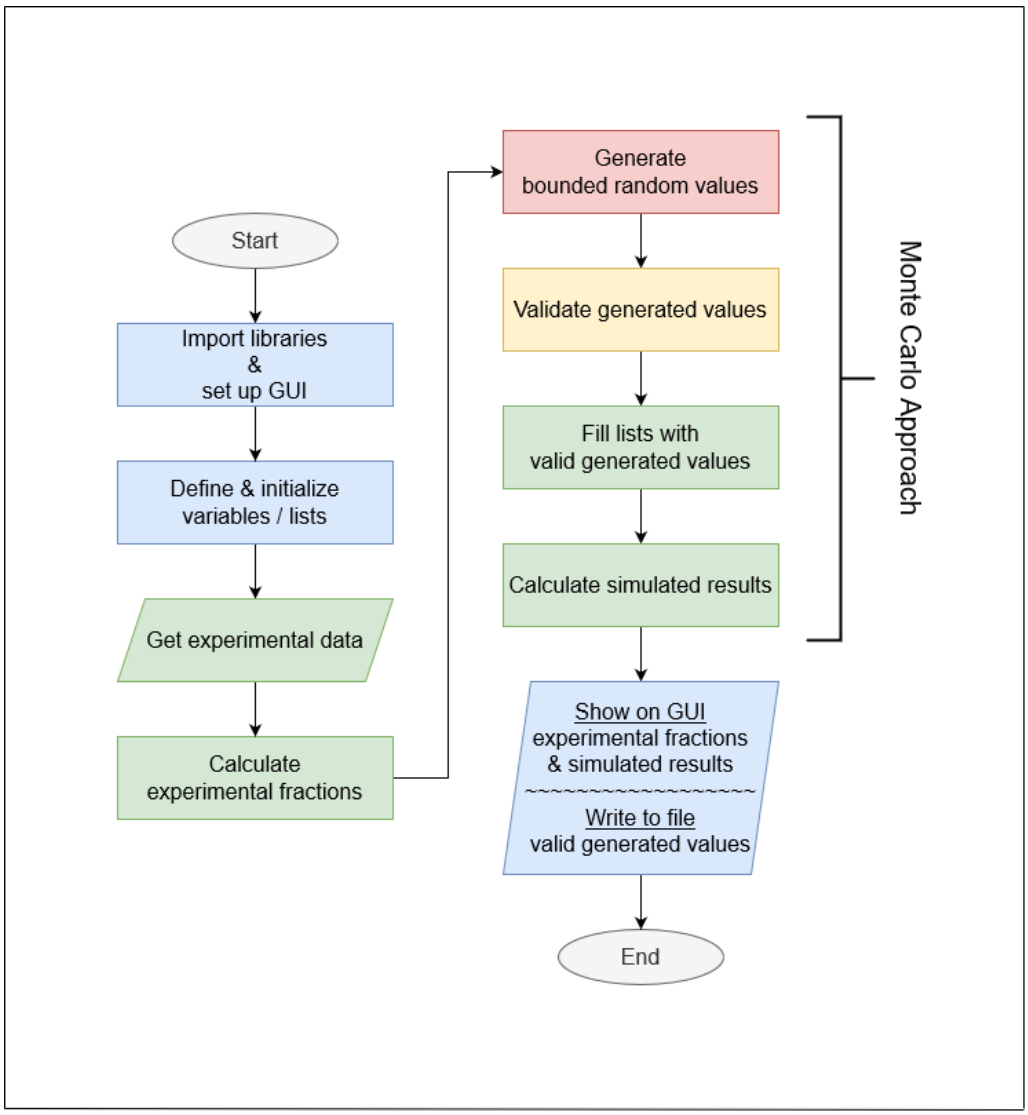

Figure D.2: Flowchart of the Python script using a Monte Carlo approach to calculate metastable fraction errors. Different colours have been used for sake of readability: [Gray] Start / stop; [Blue] Data manipulation is not involved; [Green] Data involved are considered to be valid; [Yellow] Data involved are undergoing checks; [Red] Data involved are considered to be potentially invalid.

To ensure the validity of the simulation, it is important to first verify that the sampled values follow the distribution that was requested. One way to do this is by varying the number of iterations used in the simulation and observing the resulting distribution of sampled values. For instance, in the case of 10 MeV O^{6+}+He, the initial choice of $N = 100$ did not produce a triangular distribution that was satisfactory, as shown in Fig. D.3.

By increasing the number of iterations, it was observed that the distribution of sampled values began to better follow the desired triangular distribution. This ap-

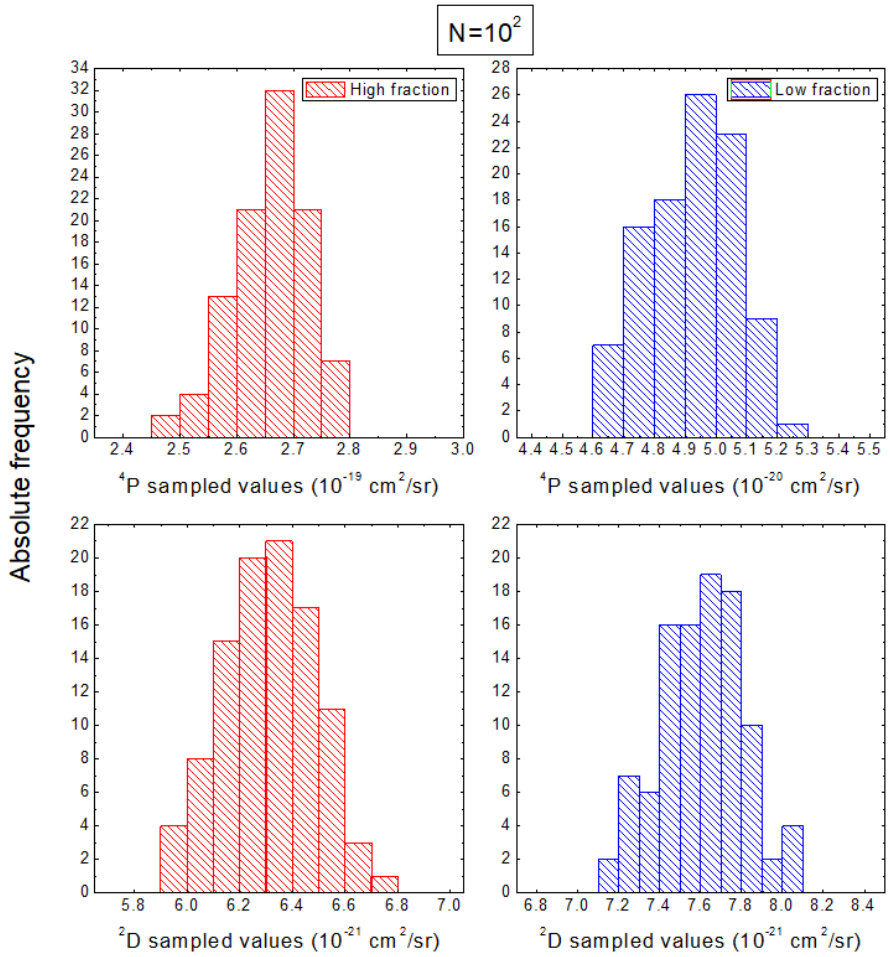

Figure D.3: Histogram diagrams showing the distributions of the sampled values of the ^4P and ^2D, obtained through the Monte Carlo approach with $N = 100$ number of iterations for the case of 10 MeV O^{6+}+He collisions. Red colors refer to the values corresponding to the high fraction measurement while blue colors to the low fraction measurement.

proach of varying the number of iterations and examining the resulting distribution can help to identify the optimal number of iterations needed to produce accurate simulation results, which in our case is $N = 10^4$. However, given the computational resources available, we decided to increase the number of iterations by an order of magnitude, bringing it to $N = 10^5$. The results obtained with this larger N value are qualitatively similar to those obtained with $N = 10^4$, indicating that the simulation has converged and the results are reliable. Therefore, we can conclude that $N = 10^5$ is an appropriate choice for generating accurate results for this particular simulation.

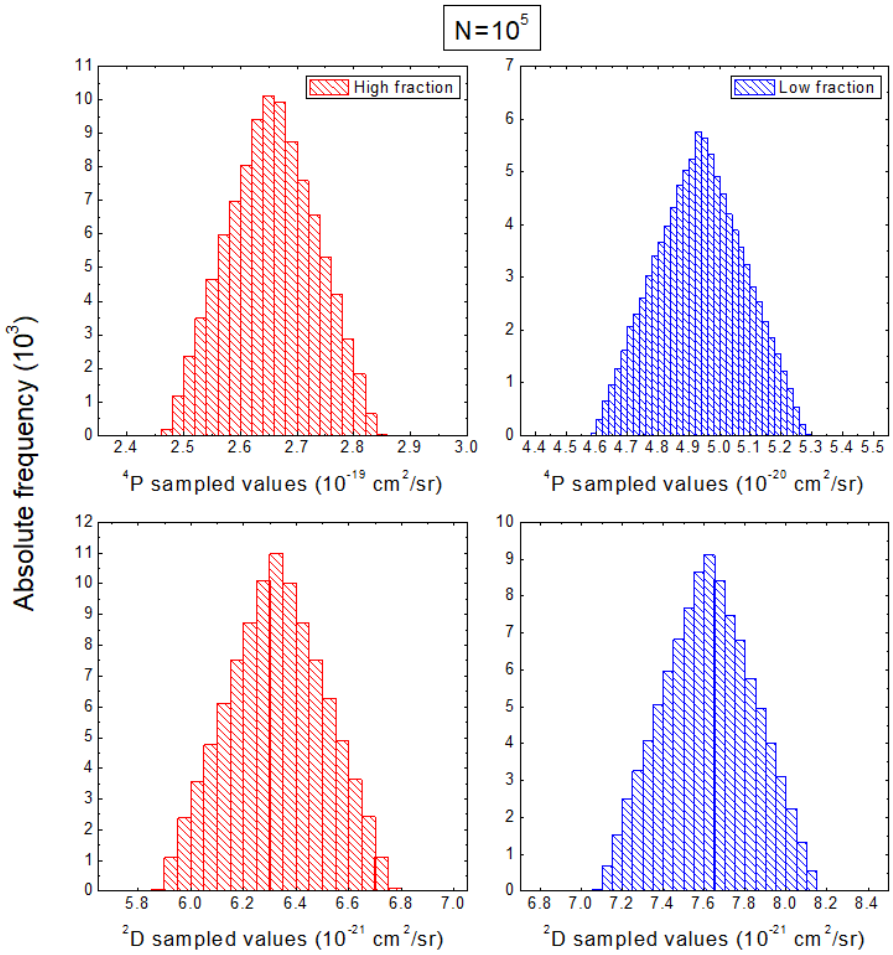

Figure D.4: Same as Fig. D.3 for $N = 10^5$.

After finding the N value to be used throughout the simulations, we plotted the distribution of the f values as they were calculated for each set of the sampled values. The related graphs are shown in Fig. D.5. The f values follow a normal distribution around the mean, in agreement with the Central Limit Theorem (CLT). According to the CLT, the distribution of sample means of any random variable will be approximately normal, provided that the sample size is sufficiently large [246].

As we see in the histogram diagrams of Fig. D.5, the mean values of f determined from the simulation agrees with the experimental determined values. In addition, the standard deviations of the sample, taken from the simulation, are used as an estimate of the error of the experiment. This is because the error of the mean value decreases with increasing sample size, thus leading to an underestimate of the true

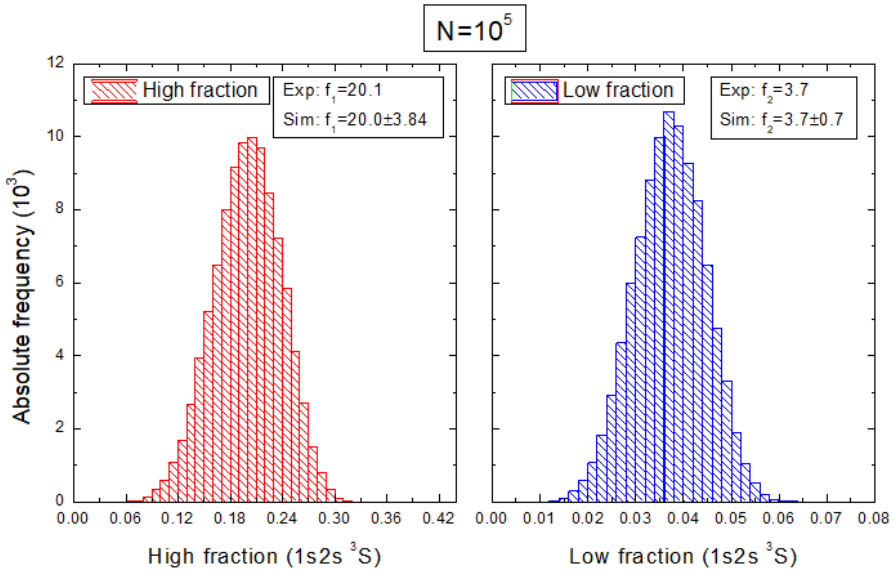

Figure D.5: Histogram diagrams showing the distributions of the f values obtained through the Monte Carlo approach with $N = 10^5$ number of iterations for the case of 10 MeV O^{6+}+He collisions. Red colors refer to the values corresponding to the high fraction measurement while blue colors to the low fraction measurement. The experimentally determined f values along with the mean values of the simulation and the corresponding standard deviations are also indicated.

error. Therefore, we use the standard deviation of the sample as a more reliable estimate of the error, as it is not affected from the sample size after convergence of the simulated mean values. This process ensures that our simulation results are not only in agreement with the experimental values, but also have a valid error estimate.

Appendix E

Limitations of the Metastable Beam Fraction Determination and Compensation Methods

The method outlined in Section 4.5 requires the measurement of a KLL Auger spectrum under identical collision conditions, but with different metastable beam components. The crucial question is how much the $1s2s\ ^3S$ fraction should differ between the two measurements.

It should be emphasized that seemingly small differences in the metastable fraction leads to substantial differences in the ^4P yield, since it is exclusively populated by the $1s2s\ ^3S$ state through single electron capture. The magnitude of this difference corresponds to the ratio of the metastable fractions for the two measurements, as evident from Eq. 4.36. Conversely, the ^2D state is populated via transfer-excitation from the ground state $1s^2$. Considering that the ground state content is dominant for He-like beams at all collision energies (e.g., at least 70% or more for oxygen projectiles), a seemingly small difference in the metastable fraction only slightly affects the percentage of the ground state in the beam, and thus the difference in the ^2D yield for the two measurements.

For the cases where the small differences in the metastable fraction do not provide reliable differences for the ^2D yields, Eq. 4.36 cannot determine the metastable fraction values, rendering the double measurement technique inapplicable. Fig. E.1 illustrates such a scenario for collisions of 16 MeV O^{6+} + He, where noticeable differences are observed in the ^4P peak yields between the two measurements, whereas the ^2D Auger peaks show negligible differences.

Compensating for the limitations of the double measurement technique in situations where it cannot be applied is possible by incorporating additional measurements at different collision energies. Foil strippers have been found to consistently produce a He-like beam with a constant metastable fraction across various collision systems, regardless of the stripping point used (tandem or post stripping), as discussed in Section 4.5. Thus, by averaging the fractions obtained from the high fraction spectra across different collision energies, the fraction of the high fraction spectrum can be determined at the specific collision energy where the double measurement technique is not applicable. Subsequently, by taking the ratio of the ^4P peaks between the two measurements in this collision energy, the ratio of the fractions can be obtained as discussed earlier. Knowing the $1s2s\ ^3S$ percentage in

one spectrum and the ratio of the fractions between the two measurements, the metastable fraction of the low fraction spectrum can be indirectly determined. This approach provides a means to compensate for the limitations of the double measurement technique and derive the metastable fraction even in cases where direct application of the technique is not feasible, as in the case presented in Fig. E.1.

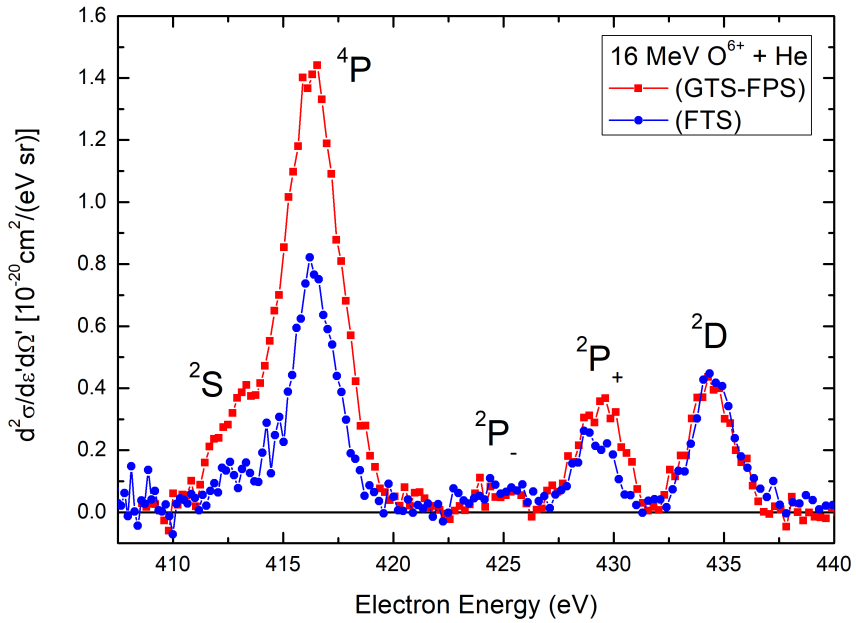

Figure E.1: KLL Auger spectra for collisions of 16 MeV O^{6+} + He showing the limitations of the double measurement technique for determining the metastable fraction $1s2s\ ^3S$ due to insufficient differences in the ^2D yields. Red lines correspond to the results for the high fraction metastable content spectra, while blue lines correspond to the low fraction metastable content.

Through the utilization of a comprehensive dataset consisting of experimental KLL Auger spectra for collisions of O^{6+} + He at various collision energies, we conducted a thorough investigation into the feasibility of employing the double measurement technique. Fig. E.2 illustrates the percentage difference in the ^2D Auger lines between the low fraction and high fraction measurements obtained at each collision energy. Based on careful analysis, we identified three distinct regions.

- In cases where the ^2D differences were less than 10%, it was determined that the double measurement technique could not be reliably applied. The uncertainties associated with such small differences prevented accurate determination of the metastable fractions using this technique.

- For ^2D differences falling within the range of 10% to 16%, the double measurement technique proved to be applicable, allowing for the accurate determination of metastable fractions.

- Finally, in instances where the ^2D differences exceeded 16%, the double measurement technique demonstrated its robustness, providing accurate results for the metastable fractions. The significant differences in the ^2D yield between the two measurements allowed for the accurate determination of the metastable fraction with high confidence.

This analysis of the percentage differences in the ^2D Auger lines across different collision energies provided valuable insights into the reliability and effectiveness of the double measurement technique, enabling the determination of appropriate conditions for its safe application in determining the metastable fractions.

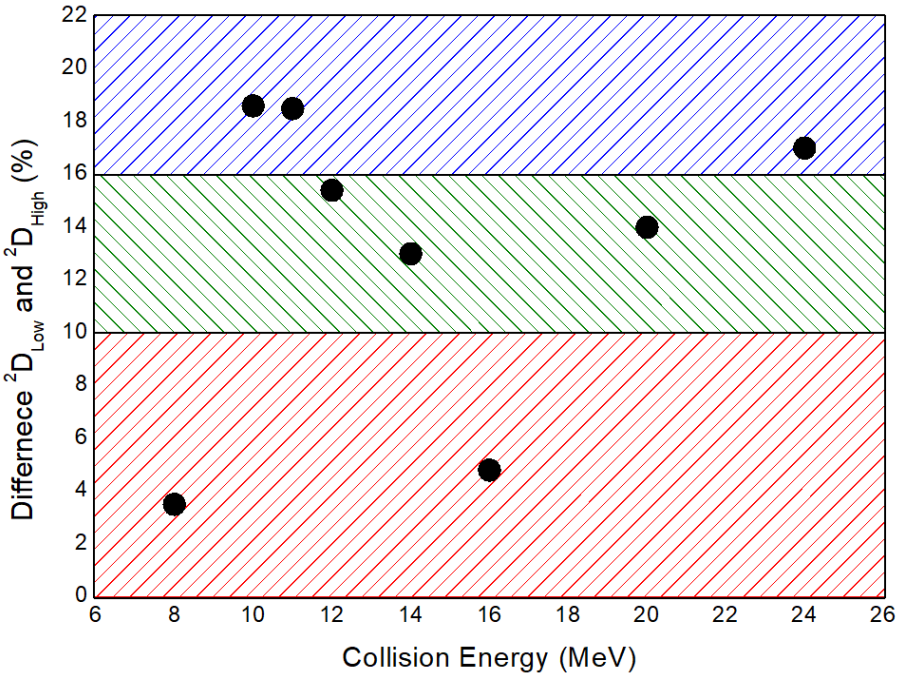

Figure E.2: Percentage difference in the ^2D Auger lines between the low fraction and the high fraction measurements for O^{6+} + He collisions at different collision energies. The figure highlights the applicability of the double measurement technique, indicating three distinct regions based on color: (red) the technique cannot be reliably applied, (green) the technique can be safely applied, and (blue) the technique can be utilized with high accuracy.

Appendix F

DDCS Determination of the Cusp Electron Peak from the 1s2s Configuration

Cusp electron studies involving mixed-state He-like beams encompass both the ELC and ECC processes. Both the ground state, $1s^2$, and the excited $1s2s$ configurations need to be considered for the cusp peak formation. To separate the contributions of the ground and excited states, the double measurement technique is utilized. In cases where the double measurement involves one measurement with pure ground state, the analysis results in Eq. 6.18. Here, we present the derivation of this equation.

For the pure ground state beam, the DDCS of the cusp peak results from both ECC process and the ELC of a K-shell electron. In order to account for the two $1s$ electrons, the ELC part has to be multiplied by a factor of 2. Thus,

$$\frac{d^2\sigma[1s^2]}{d\Omega dE} = \left.\frac{d^2\sigma[1s^2]}{d\Omega dE}\right|_{ECC} + 2\left.\frac{d^2\sigma[1s^2]}{d\Omega dE}\right|_{K-ELC}. \tag{F.1}$$

For the mixed-state beam, the equation describing the DDCS of the cusp peak is more complicated due to the presence of two configurations as well as the L-shell electron of the $1s2s$ configuration. Considering the metastable fraction f, the corresponding equation reads as:

$$\begin{aligned}\frac{d^2\sigma[1s^2,\ 1s2s]}{d\Omega dE} =& (1-f)\left.\frac{d^2\sigma[1s^2]}{d\Omega dE}\right|_{ECC} + 2(1-f)\left.\frac{d^2\sigma[1s^2]}{d\Omega dE}\right|_{K-ELC} \\ &+ f\left.\frac{d^2\sigma[1s2s]}{d\Omega dE}\right|_{ECC} + f\left.\frac{d^2\sigma[1s2s]}{d\Omega dE}\right|_{K-ELC} \\ &+ f\left.\frac{d^2\sigma[1s2s]}{d\Omega dE}\right|_{L-ELC}.\end{aligned} \tag{F.2}$$

Finally, by combining Eqs. F.1 and F.2 as

$$\frac{\frac{d^2\sigma[1s^2,\ 1s2s]}{d\Omega dE} - (1-f)\frac{d^2\sigma[1s^2]}{d\Omega dE}}{f}$$

we can readily extract the contribution to the cusp electron peak from the excited state component, $1s2s$, as given by Eq. 6.18, since

$$\frac{d^2\sigma[1s2s]}{d\Omega dE} \equiv \left.\frac{d^2\sigma[1s2s]}{d\Omega dE}\right|_{ECC} + \left.\frac{d^2\sigma[1s2s]}{d\Omega dE}\right|_{K-ELC} + \left.\frac{d^2\sigma[1s2s]}{d\Omega dE}\right|_{L-ELC} \tag{F.3}$$

Εκτεταμένη Σύνοψη
Extended Greek Summary

Σε αυτό το σημείο παρατίθεται μία εκτενής ελληνική σύνοψη της διατριβής με τίτλο "Μηχανισμοί ηλεκτρονικής σύλληψης και απώλειας σε ταχείες κρούσεις ιόντων-ατόμων". Ακολούθως, θα γίνει μία σύντομη περιγραφή της πειραματικής διάταξης που χρησιμοποιήθηκε και θα παρουσιαστούν τα αποτελέσματα των μελετών που έγιναν στα πλαίσια της παρούσας διατριβής.

9.1 Η Πειραματική Διάταξη

Τα πειράματα πραγματοποιήθηκαν στο εργαστήριο του επιταχυντή tandem Van de Graaff του Ινστιτούτου Πυρηνικής και Σωματιδιακής Φυσικής του Εθνικού Κέντρου Φυσικών Επιστημών "Δημόκριτος". Συγκεκριμένα, για τις ανάγκες της παρούσας διατριβής αξιοποιήθηκε η πειραματική διάταξη του σχήματος 9.1, η οποία είναι αφιερωμένη σε πειράματα κρούσεων ιόντων-ατόμων για μελέτες που άπτονται του πεδίου της Ατομικής Φυσικής.

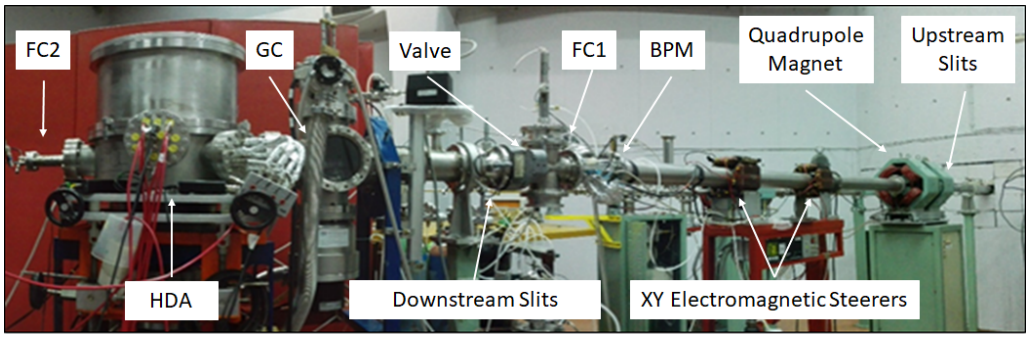

Figure 9.1: Η πειραματική διάταξη Ατομικής Φυσικής που λειτουργεί στο εργαστήριο του επιταχυντή tandem Van de Graaff του «Δημόκριτου».

Τα κύρια μέρη της εν λόγω διάταξης είναι το κελί αέριου στόχου και ο φασματογράφος (HDA). Κατά τη διαδικασία της κρούσης, όταν η δέσμη ιόντων αλληλεπιδρά με τα άτομα του αέριου στόχου, παράγονται ηλεκτρόνια είτε από τον στόχο είτε από την επιταχυνόμενη δέσμη. Τα ηλεκτρόνια που εκπέμπονται σε μηδέν μοίρες σε σχέση με τη δέσμη ιόντων εστιάζονται από τον φακό στην είσοδο του φασματογράφου, αναλύονται ενεργειακά και καταλήγουν στον δισδιάστατο ανιχνευτή θέσης (PSD). Η δέσμη ιόντων διασχίζει το φασματογράφο, καταλήγοντας σε ένα κελί Faraday όπου το ρεύμα της μετράται για λόγους κανονικοποίησης των καταγεγραμμένων φασμάτων.

Η διατήρηση σταθερά χαμηλής πίεσης της πειραματική γραμμής, $\sim 10^{-6}$–10^{-7} Torr, είναι ζωτικής σημασίας για την ασφαλή λειτουργία του φασματογράφου και για τη λήψη φασμάτων ηλεκτρονίων υψηλής ποιότητας με χαμηλό θόρυβο. Για τον λόγο αυτό, το κελί αερίου αποτελείται από δύο ομόκεντρες κυψέλες: μια εσωτερική κυψέλη, όπου εισάγεται ο στόχος αερίου και μια εξωτερική κυψέλη που περιλαμβάνει την εσωτερική και συνδέεται άμεσα με μια στροβιλομοριακή αντλία 80 l/s, όπως φαίνεται στο σχήμα 9.2. Η μέθοδος αυτή είναι γνωστή ως διπλά διαφορική άντληση (double differential pumping).

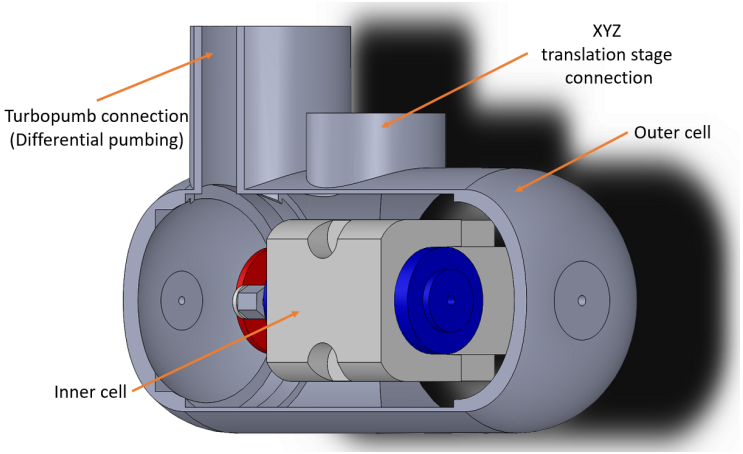

Figure 9.2: Σχέδιο CAD του κελιού αερίου.

Ο δισδιάστατος ανιχνευτής θέσης PSD αποτελείται από ένα ζεύγος ανιχνευτών τύπου MCP, καθώς και ένα κωδικοποιητή αντίστασης ανόδου (RAE), ο οποίος συλλέγει τα συμβάντα ενώ κωδικοποιεί κάθε θέση διανέμοντάς τη σε τέσσερις εξόδους, όπως φαίνεται στο σχήμα 9.3. Εν συνεχεία, τα τέσσερα σήματα ενισχύονται μέσω ενός

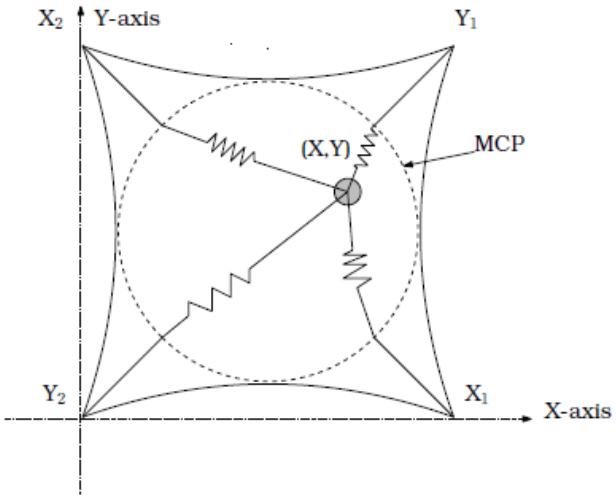

Figure 9.3: Διάγραμμα του συστήματος RAE.

προ-ενισχυτή και οδηγούνται σε μία μονάδα επεξεργασίας ψηφιακού σήματος (DSP) όπου το αναλογικό σήμα μετατρέπεται σε ψηφιακό (ADC). Εκεί, η τελική δισδιάστατη εικόνα του φάσματος ηλεκτρονίων σχηματίζεται σύμφωνα με τις εξισώσεις 9.4.

$$X = \frac{X_1 + Y_1}{X_1 + Y_1 + X_2 + Y_2}$$
$$Y = \frac{X_2 + Y_1}{X_1 + Y_1 + X_2 + Y_2} \tag{9.4}$$

Η καταγραφή των φασμάτων ηλεκτρονίων βασίζεται στην τεχνική φασματοσκοπίας Auger ηλεκτρονίων δέσμης στις μηδέν μοίρες, ευρέως γνωστή ως ZAPS. Η τεχνική ZAPS προσφέρει μια αποτελεσματική λύση για τον μετριασμό των κινηματικών φαινομένων διεύρυνσης των φασματικών γραμμών, μέσω της ανίχνευσης των ηλεκτρονίων Auger που εκπέμπονται σε μηδέν μοίρες σε σχέση με την τροχιά της ιοντικής δέσμης. Αυτή η τεχνική έχει αναδειχθεί ως πολύτιμο εργαλείο καθώς παρουσιάζει τη μέγιστη δυνατή διακριτική ικανότητα, καθιστώντας την εξαιρετική για μελέτες διπλά διαφορικής ενεργού διατομής (DDCS) σε επίπεδο ατομικών καταστάσεων (state-selective). Ως εκ τούτου, η τεχνική ZAPS μας δίνει τη δυνατότητα να αποκτήσουμε ακριβείς και λεπτομερείς πληροφορίες για την ηλεκτρονική δομή των ατόμων, αλλά και να αποκτήσουμε πολύτιμες γνώσεις σχετικά με τους μηχανισμούς κρούσεων ιόντων με άτομα.

Πέρα από την εφαρμογή της στη φασματοσκοπία Auger ηλεκτρονίων δέσμης, η τεχνική ZAPS βρίσκει πρόσθετη χρησιμότητα σε μελέτες cusp ηλεκτρονίων, των οποίων οι κορυφές εμφανίζονται ιδιαίτερα έντονες για γωνία εκπομπής ίση με μηδέν μοίρες. Έτσι, μέσω της τεχνικής ZAPS μπορούν να μελετηθούν τα πιο ευαίσθητα χαρακτηριστικά των cusp ηλεκτρονίων εκτίθοντας, μεταξύ άλλων, την περίπλοκη αλληλεπίδραση μεταξύ των πεδίων των ατόμων του στόχου και των ιόντων δέσμης.

9.2 Ανάλυση δεδομένων

Κατά την καταγραφή των φασμάτων, η πληροφορία αποθηκεύεται ουσιαστικά σε αριθμό ηλεκτρονίων ανά αριθμό καναλιού. Κατά την ανάλυση, ο αριθμός καναλιών μετατρέπεται σε ενέργεια και εν συνεχεία ο αριθμός ηλεκτρονίων σε DDCS. Η διαδικασία ενεργειακής βαθμονόμησης των φασμάτων γίνεται μέσω της σχέσης 9.5, όπου ο προσδιορισμός των σταθερών a, b, και c γίνεται μέσω καλά καθορισμένης ενέργειας KLL Auger κορυφών.

$$T(i) = a + bi + ci^2 \tag{9.5}$$

Η διαδικασία προσδιορισμού της DDCS πληροφορίας γίνεται μέσω της σχέσης 9.6, όπου N_{e_i} είναι ο αριθμός ηλεκτρονίων που καταγράφηκε στο i-κανάλι, N_I ο αριθμός των ιόντων που μετράται στο κελί Faraday, L_{eff} το μήκος του κελιού αερίου, n η πίεση του αερίου, $\Delta\Omega$ η στερεά γωνία ανίχνευσης, ΔE_i το βήμα ενέργειας ανά κανάλι που προσδιορίζεται μέσω της παραγώγου της σχέσης 9.5, T η μετάδοση του φασματογράφου, και η η συνολική απόδοση.

$$DDCS_i \equiv \frac{d^2\sigma}{d\Omega dE_i} = \frac{N_{e_i}}{N_I\, L_{eff}\, n\, \Delta\Omega\, \Delta E_i\, T\, \eta} \tag{9.6}$$

Σημειώνεται πως η στερεά γωνία ανίχνευσης είναι γνωστή από τα γεωμετρικά χαρακτηριστικά της διάταξης, ωστόσο όσο αφορά τη μεταστατή κατάσταση $1s2s2p\ ^4P$, η οποία αποδιεγείρεται σε όλο το μήκος της διαδρομής μεταξύ κελιού αερίου φασματογράφου, η στερεά γωνία ανίχνευσης μεταβάλλεται. Για τον προσδιορισμό της αξιοποιούνται φάσματα KLL Auger ηλεκτρονίων παραγόμενα σε πειράματα κρούσεων

βυρηλλιοειδών ιοντικών δεσμών με αέριο στόχο ήλιο που δεν παρουσιάζουν φαινόμενα τροφοδοσίας αλληλουχίας. Εναλλακτικά, ο προσδιορισμός της γίνεται με χρήση προσομοιώσεις στο πακέτο οπτικής ιόντων SIMION.

Σε ιοντικούς επιταχυντές οι δέσμες ιόντων δεν αποτελούνται από μία μόνο κατάσταση, τη βασική, αλλά πολλές φορές και από διεγερμένες μετασταθείς καταστάστεις. Χαρακτηριστικό παράδειγμα αποτελούν οι ηλιοειδείς δέσμες ιόντων που παράγονται σε μία μίξη καταστάσεων, αυτή της βασικής $1s^2\ ^1S$ και της διεγερμένης $1s2s\ ^3S$. Η ομάδα μας αξιοποιεί το γεγονός αυτό βασιζόμενη σε μία τεχνική διπλής καταγραφής των KLL Auger φασμάτων μέσω του οποίου μπορεί να γίνει προσδιορισμός του ποσοστού ιόντων που βρίσκονται στη διεγερμένη κατάσταση ($f_{1s2s\ ^3S}$). Ένα τέτοιο παράδειγμα φαίνεται στο σχήμα 9.4. Η τεχνική βασίζεται στις σχετικές διαφορές των κορυφών ^4P και ^2D, και οφείλονται στο γεγονός ότι η πρώτη προκύπτει από τα ιόντα δέσμης που βρίσκονται στη κατάσταση $1s2s\ ^3S$ μέσω ηλεκτρονικής σύλληψης, ενώ η δεύτερη από διεργασία μεταφοράς και διέγερσης από τη βασική κατάσταση $1s^2$. Συγκεκριμένα, για

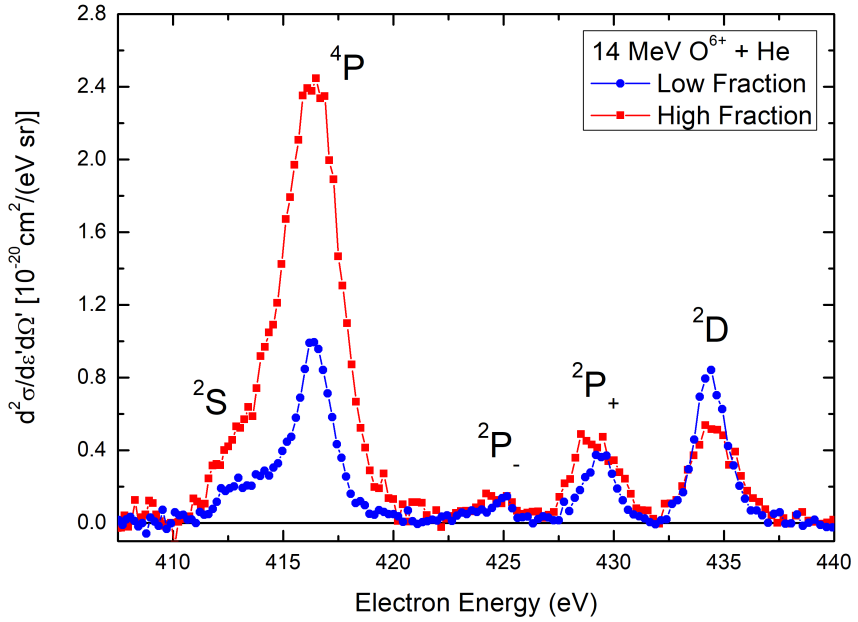

Figure 9.4: KLL Auger φάσματα με διαφορετικά ποσοστά διεγερμένης κατάστασης $1s2s\ ^3S$ για κρούσεις 14 MeV $O^{6+}(1s^2, 1s2s\ ^3S)$ + He.

τον προσδιορισμό του ποσοστού $f_{1s2s\ ^3S}$ αξιοποιείται η σχέση 9.7:

$$f^i_{1s2s\ ^3S} = Y_i[^4P]\frac{Y_2[^2D] - Y_1[^2D]}{Y_2[^2D]Y_1[^4P] - Y_1[^2D]Y_2[^4P]} \qquad (i = 1, 2)\ , \tag{9.7}$$

όπου Y_i είναι το κανονικοποιημένο σήμα των $^{(2S+1)}L$ Auger καταστάσεων για κάθε μία από τις δύο μετρήσεις.

Τέλος, η τεχνική διπλής μέτρησης μπορεί να προσφέρει περεταίρω πλεονεκτήματα, καθώς αποτελεί εξαιρετικό εργαλείο για τον προσδιορισμό απλών διαφορικά ενεργών διατομών (SDCS). Σημειώνεται πως η διαδικασία απαιτεί την ολοκλήρωση των Auger κορυφών σε ενέργεια, μία διαδικασία μη τετριμμένη για την οποία μπορούν να χρησιμοποιηθούν διάφορα προγράμματα ανάλυσης. Στην περίπτωσή μας, προτείνουμε ένα νέο τρόπο ανάλυσης ο οποίος προϋποθέτει προσομοιώσεις στο πακέτο προσομοίωσης SIMION και αποτελεί ασφαλέστερη μέθοδο καθώς εξαρτάται μόνο από τις πειρα-

ματικές συνθήκες του εκάστοτε πειράματος και παραμένει ανεξάρτητη της επιλογής μαθηματικών συναρτήσεων για την αναπαράσταση των υπό μελέτη κορυφών.

9.3 Αποτελέσματα

Στην παρούσα διατριβή μελετήθηκαν οι μηχανισμοί ηλεκτρονικής σύλληψης στο συνεχές (ECC) καθώς και ηλεκτρονικής απώλειας στο συνεχές (ELC) της δέσμης ιόντων μέσω καταγραφής φασμάτων cusp ηλεκτρονίων, καθώς και ο μηχανισμός απλής ηλεκτρονικής σύλληψης (SEC) μέσω της φασματοσκοπίας Auger ηλεκτρονίων. Επιπροσθέτως, προτάθηκε ένας νέος τρόπος για τον προσδιορισμό του ενεργειακού εύρους δεσμών ιόντων που παράγονται σε επιταχυντές tandem Van de Graaff. Ακολούθως, παρουσιάζονται οι εν λόγω μελέτες καθώς και τα αποτελέσματά μας.

Cusp Ηλεκτρόνια: Κρούσεις με Πλήρως Απογυμνωμένες Δέσμες Ιόντων

Ενώ έχουν υπάρξει πολυάριθμες πειραματικές μελέτες για του μηχανισμό της ECC, μόνο ένας περιορισμένος αριθμός ερευνών έχει επικεντρωθεί σε κρούσεις πλήρως απογυμνομένων ιόντων δέσμης με πολυηλεκτρονικούς ατομικούς στόχους. Στα πλαίσια της παρούσας διατριβής, πραγματοποιήθηκαν σχετικές μελέτες, για την καταγραφή των cusp κορυφών σε επίπεδο DDCS. Τα εν λόγω αποτελέσματα προσφέρουν σημαντικές πληροφορίες για τη δυναμική του ενεργού ηλεκτρονίου και τον ρόλο των παθητικών ηλεκτρονίων στον ιονισμένο ατομικό στόχο. Κατ'επέκταση, βοηθούν στην περαιτέρω ανάπτυξη θεωριών γνωστές ως distorted wave (DW) που αξιοποιούνται για την περιγραφή των cusp ηλεκτρονίων.

Συγκεκριμένα, πραγματοποιήθηκαν πειράματα κρούσεων στο εύρος ενέργειας 1.25-6.00 MeV αξιοποιώντας δέσμες ιόντων δευτερίου και αέριους στόχους ηλίου, νέου και αργού. Οι μετρήσεις συγκρίθηκαν με τέσσερις διαφορετικές DW θεωρίες, δείχνοντας πως η αριθμητική θεωρία CDW-EIS παρείχε την καλύτερη συμφωνία με τις πειραματικές μετρήσεις. Οι διαφορές μεταξύ των θεωριών του DW αποδόθηκαν κυρίως στη συνεισφορά διαφορετικών ατομικών τροχιακών στη διαδικασία ECC. Η ανάλυση έδειξε ότι το τροχιακό $2p$ είχε τη μέγιστη συνεισφορά στην κορυφή ECC για το εύρος ενέργειας κρούσεων από 1.25 έως 3.00 MeV για τους στόχους Ne και Ar. Συγκεκριμένα, η αριθμητική θεωρία CDW-EIS αναπαρήγαγε με ακρίβεια την παρατηρούμενη λεπτή αλλαγή της cusp κορυφής σε επίπεδο DDCS για τους στόχους Ne και Ar στο εύρος ενέργειας κρούσης από 1.25 έως 2.00 MeV, όπως φαίνεται στο σχήμα 9.5.

Cusp Ηλεκτρόνια: Κρούσεις με Μερικώς Απογυμνωμένες Δέσμες Ιόντων

Ενώ οι κρούσεις με προ-διεγερμένα ιόντα έχουν χρησιμοποιηθεί για μελέτες βασικών ατομικών διεργασιών, οι διαδικασίες ECC και ELC δεν έχουν εξεταστεί διεξοδικά σε τέτοιες συνθήκες. Στα πλαίσια της παρούσας διατριβής πραγματοποιήθηκαν σχετικές μελέτες, αξιοποιώντας την τεχνική διπλής καταγραφής KLL Auger φασμάτων. Με αυτόν τον τρόπο, επιτεύχθηκε, για πρώτη φορά, η καταγραφή της cusp κορυφής σε επίπεδο DDCS προερχόμενη από κρούσεις μεταξύ προ-διεγερμένων δεσμών ιόντων οξυγόνου, $O^{6+}(1s2s)$, με αέριους στόχους ηλίου. Η εν λόγω μέτρηση, καθώς και ο αντίστοιχος CDW-EIS θεωρητικός υπολογισμός, φαίνονται στο σχήμα 9.6.

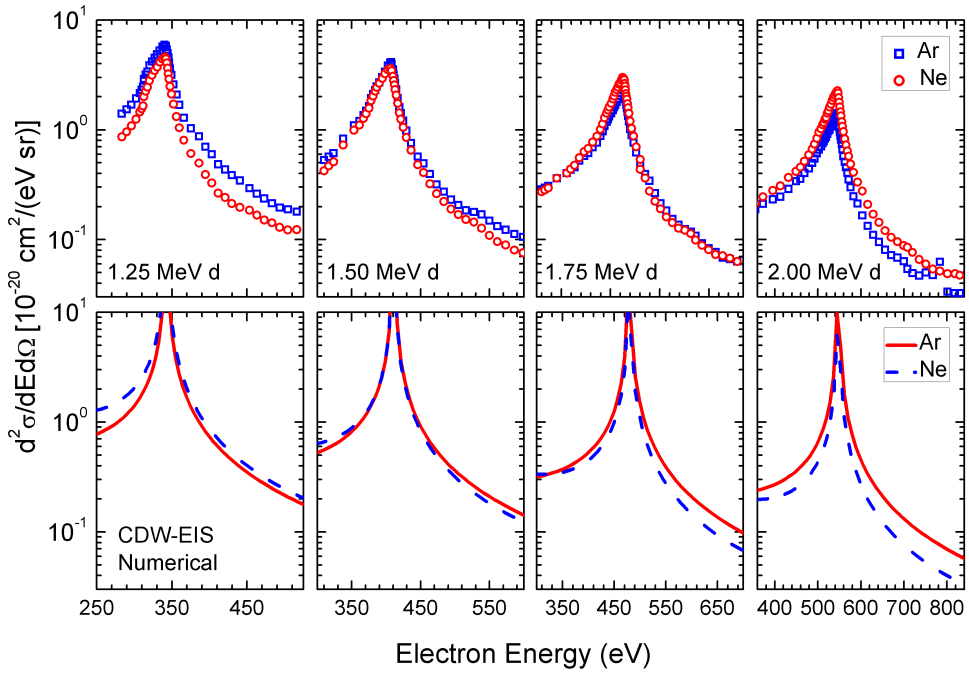

Figure 9.5: DDCS cusp κορυφές σε μηδέν μοίρες σε σχέση με την ταχύτητα της δέσμης ιόντων για κρούσεις ιόντων δευτέριων ενέργειας 1.25-2.00 MeV με στόχους Ar (κόκκινο) και Ne (μπλε). Τα σύμβολα αντιστοιχούν στις μετρήσεις και οι γραμμές στους υπολογισμούς της αριθμητικής θεωρίας CDW-EIS. Λήψη από [21].

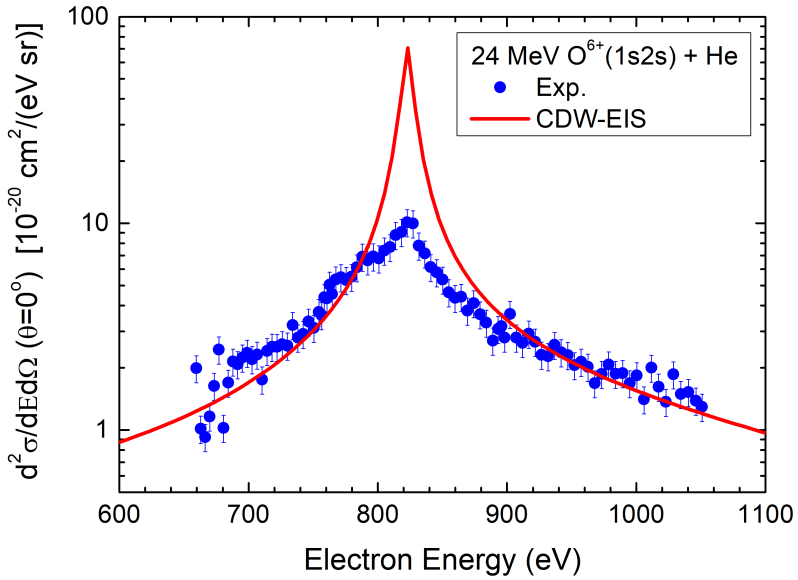

Figure 9.6: DDCS της cusp κορυφής για κρούσεις 24 MeV $O^{6+}(1s2s)$ με He. Μπλε κύκλοι: Πειραματικά δεδομένα. Κόκκινη γραμμή: CDW-EIS θεωρία. Λήψη από [22].

Οι υπολογισμοί CDW-EIS καταδεικνύουν μια αξιοσημείωτη συμφωνία με τα πειραματικά δεδομένα, ιδιαίτερα στην αναπαραγωγή των πτερυγίων της κορυφής. Αξίζει να σημειωθεί πως το θεωρητικό μέγιστο της κορυφής καθορίζεται από έναν μαθηματικό πόλο, ο οποίος μπορεί να εισάγει ορισμένες διακυμάνσεις στο ύψος του ανάλογα με τη διαδικασία ολοκλήρωσης. Ωστόσο, η εξαιρετική συμφωνία που παρατηρείται εκατέρωθεν του μεγίστου υποδεικνύει ότι οι καθιερωμένες και εξελιγμένες θεωρίες κρούσης, όπως η CDW-EIS, μπορούν να προωθηθούν περαιτέρω και να βελτιωθούν όταν δοκιμάζονται έναντι μη τετριμμένων συστημάτων κρούσεων.

Σε αυτήν την κατεύθυνση, αξιοποιήσαμε βηρυλλιοειδείς δέσμες ιόντων οξυγόνου για την καταγραφή cusp ηλεκτρονίων. Για τα πειράματα αυτά αξιοποιήσαμε και πάλι την τεχνική διπλής καταγραφής, μεταβάλλοντας το ποσοστά των ατομικών δομών των ιόντων δέσμης, δηλαδή τα ποσοστά της βασικής κατάστασης, $1s^2 2s^2\ ^1S$, και της διεγερμένης κατάστασης, $1s^2 2s2p\ ^3P$. Να αναφέρουμε ότι οι προκαταρκτικοί θεωρητικοί υπολογισμοί βρίσκονται σε εξέλιξη από τη συνεργαζόμενη θεωρητική μας ομάδα στο Πανεπιστήμιο του Rosario της Αργεντινής.

Τέλος, σημειώνεται πως σε αρκετά ηλεκτρονικά φάσματα παρατηρήθηκε η ύπαρξη μιας μικρής κορυφής σε χαμηλότερες ενέργειες σε σχέση με το μέγιστο της cusp κορυφής. Μετά από πολλαπλές μελέτες που διασφάλισαν την ύπαρξη της κορυφής αυτής σε διαφορετικά συστήματα κρούσεων, καταλήξαμε πως η εν λόγω κορυφή πιθανώς να αποδίδεται σε ένα νέο μηχανισμό ηλεκτρονικής απώλειας στο συνεχές με ταυτόχρονο ιονισμού του στόχου. Η εκτίμηση αυτή στηρίζεται στις πειραματικές μας μελέτες, ιδιαίτερα από τα αποτελέσματα που εξίχθησαν σε κρούσεις μεταξύ ηλιοειδών δεσμών βορίου με αέριους στόχους H_2, He, Ne, και Ar, όπου η μικρή κορυφή φαίνεται να μετακινείται αναλόγως του αέριου στόχου που χρησιμοποιείται. Συγκεκριμένα, η ενεργειακή απόσταση της κορυφής από το μέγιστο της cusp κορυφής φαίνεται να ισούται κάθε φορά με το δυναμικό ιονισμού του στόχου. Τα εν λόγω αποτελέσματα παρουσιάζονται στο σχήμα 9.7.

Απλή Ηλεκτρονική Σύλληψη

Πρόσφατα, μία καινοτόμα μελέτη έδωσε απάντηση σε ένα μακροχρόνιο ερώτημα σχετικά με τη διαδικασία της απλής σύλληψης ηλεκτρονίου σε συστήματα κρούσεων με προδιεγερμένες δέσμες ιόντων. Οι πειραματικές μετρήσεις συνδυάστηκαν με κβαντομηχανικούς υπολογισμούς από πρώτες αρχές τριών ενεργών ηλεκτρονίων (3eAOCC) για να περιγράψουν διεξοδικά τη διαδικασία SEC, μελετώντας τον τρόπο εποίκισης των καταστάσεων $1s2s2p\ ^4P$ και $^2P_\pm$, μέσω του λόγου:

$$R_m \equiv \frac{\sigma_m(^4P)}{\sigma_m(^2P_+) + \sigma_m(^2P_-)} \tag{9.8}$$

Οι μελέτες πραγματοποιήθηκαν με ηλιοειδή δέσμες ιόντων άνθρακα και απέδειξαν πως οι απλοποιημένες θεωρίες ενός ενεργού ηλεκτρονίου δεν μπορούν να περιγράψουν τη διαδικασία SEC. Στα πλαίσια της παρούσας διατριβής, θέλοντας να ελέγξουμε τα πρόσφατα αυτά ευρήματα αλλά και να βοηθήσουμε στην περεταίρω ανάπτυξη της 3eAOCC θεωρίας, πραγματοποιήσαμε μία ισοηλεκτρονική μελέτη χρησιμοποιώντας ηλιεοδείς δέσμες ιόντων οξυγόνου και βορίου.

Στις εν λόγω μελέτες, εκτός από το λόγο R_m μελετήθηκε και ο λόγος r_m, ο οποίος ορίζεται ως:

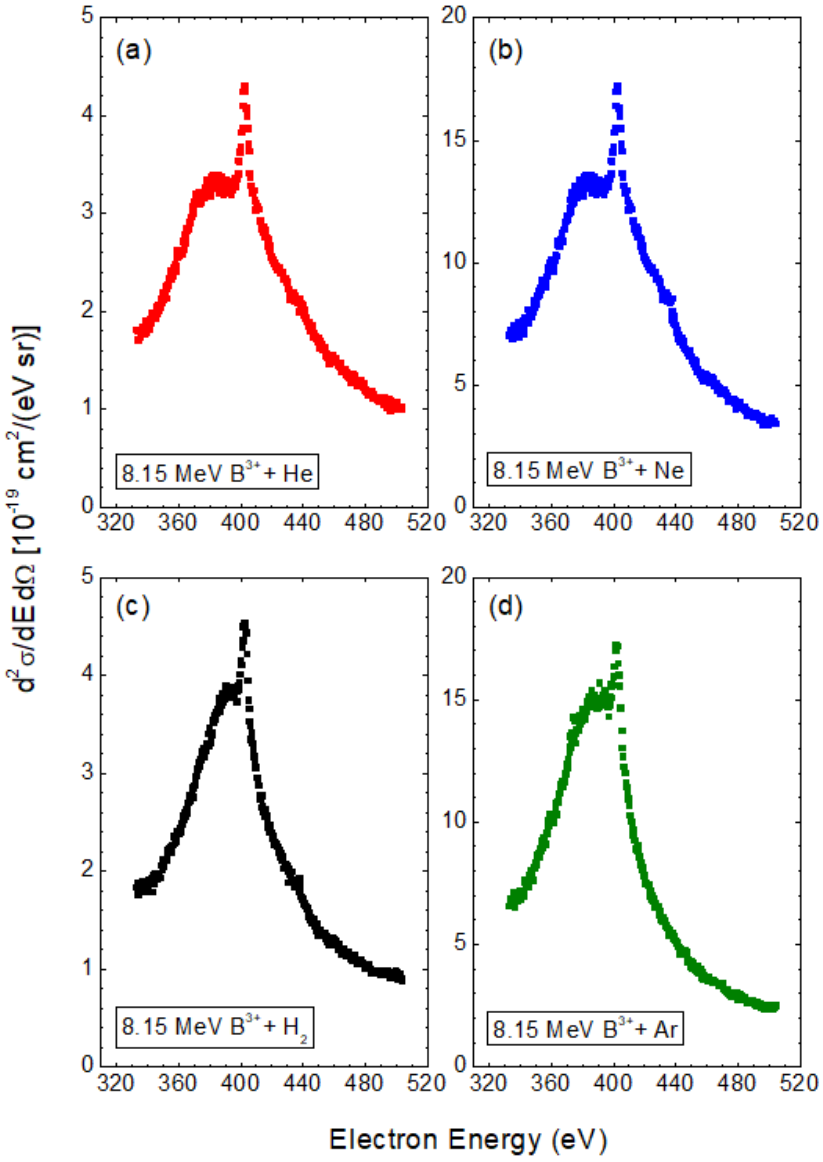

Figure 9.7: DDCS cusp ηλεκτρονίων για κρούσεις 8.15 MeV B^{3+} με (a) He, (b) Ne, (c) H_2, και (d) Ar.

$$r_m \equiv \frac{\sigma_m(^2P_+)}{\sigma_m(^2P_-)} \,. \tag{9.9}$$

Αξίζει να σημειωθεί ότι ο λόγος r_m είναι ανεξάρτητος από φαινόμενα τροφοδοσίας αλληλουχίας καθώς και από διορθώσεις της στερεάς γωνίας ανίχνευσης. Οι τιμές των λόγων R_m και r_m για το βόριο, τον άνθρακα και το οξυγόνο που εξήχθησαν από τα πειραματικά δεδομένα παρουσιάζονται στο σχήμα 9.8.

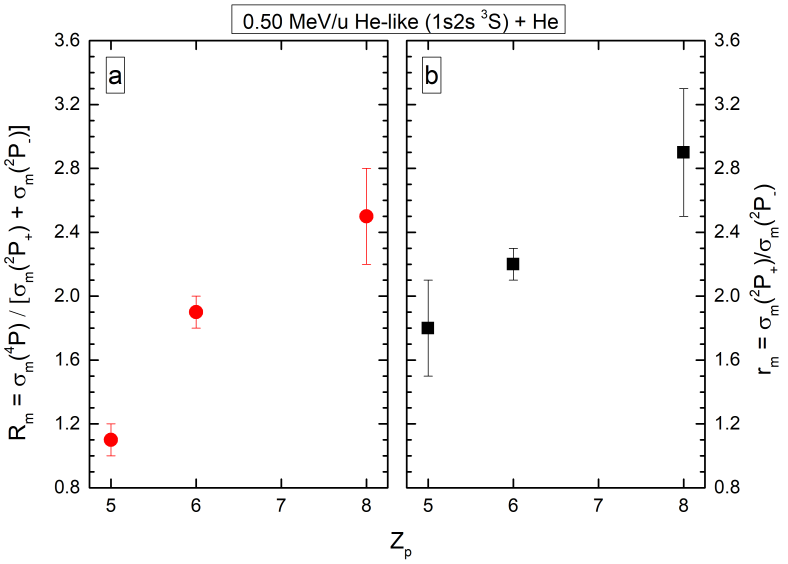

Figure 9.8: Ισο-ηλεκτρονική μελέτη των λόγων R_m (a) και r_m (b) για κρούσεις 0.50 MeV/u B^{3+}, C^{4+}, και O^{6+} με He.

Όπως είναι εμφανές, οι λόγοι R_m και r_m μειώνονται με τη μείωση του ατομικού αριθμού του ιόντος δέσμης Z_p. Αυτό οφείλεται κυρίως στη σχετική αύξηση της ενεργού διατομής για το σχηματισμό της κατάστασης $^2P_-$ σε σύγκριση με αυτήν για το σχηματισμό της κατάστασης $^2P_+$, με τη μείωση του ατομικού αριθμού Z_P. Το αποτέλεσμα αυτό, καταδεικνύει τον ρόλο της φύσης της αλληλεπίδρασης ηλεκτρονίου-ηλεκτρονίου στη διαδικασία SEC σε γρήγορες κρούσεις ιόντων-ατόμων. Αξίζει να σημειωθεί πως το αποτέλεσμα έχει καταδειχθεί ήδη σε πρόσφατες μελέτες της ομάδας μας και ονομάστηκε ως μηχανισμός θωράκισης Pauli (Pauli shielding). Σύμφωνα με τον μηχανισμό αυτόν, ο πληθυσμός της κατάστασης $1s2s2p\ ^2P_-$ δεν προάγεται από την Κουλομπική αλληλεπίδραση, αλλά από τον ασθενέστερο μηχανισμό μαγνητικής αλληλεπίδρασης της ανταλλαγής ιδιοστροφορμής. Εδώ, η ισο-ηλεκτρονική μας μελέτη υποστηρίζει σθεναρά αυτά τα επιχειρήματα, δείχνοντας ενισχυμένη αλληλεπίδραση ηλεκτρονίου-ηλεκτρονίου έναντι αλληλεπιδράσεων ηλεκτρονίου-πυρήνα για την κατάσταση $^2P_-$ με τη μείωση του ατομικού αριθμού Z_p. Στο σχήμα 9.9 παρουσιάζονται ξεκάθαρα οι σχετικές διαφορές των κορυφών $^2P_\pm$ για τα διαφορετικά συστήματα κρούσεων.

Τέλος, αξίζει να αναφερθεί πως η συστηματική μελέτη που πραγματοποιήθηκε με ιόντα οξυγόνου σε συστήματα κρούσεων πολλών ενεργειών, επέτρεψε τη μελέτη των SDCS για τις καταστάσεις $1s2s2p\ ^4P$ και $^2P_\pm$ που προκύπτουν από κρούσεις προδιεγερμένων ιοντικών δεσμών, $1s2s\ ^3S$ με He. Στο σχήμα 9.10 παρουσιάζονται τα SDCS πειραματικά αποτελέσματα, τα οποία συγκρίνονται με προκαταρκτικούς 3eAOCC υπολογισμούς. Όπως φαίνεται ξεκάθαρα, οι θεωρητικές SDCS τιμές ακολουθούν την

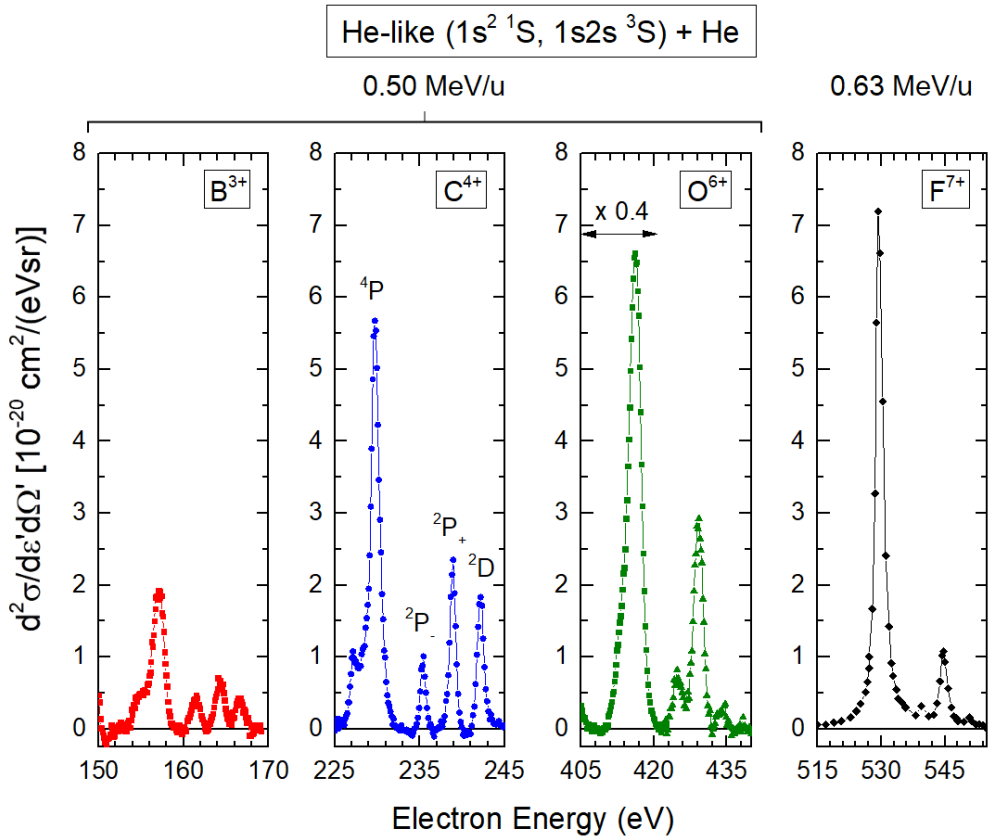

Figure 9.9: DDCS ηλεκτρονικά φάσματα για κρούσεις 0.50 B^{3+} (κόκκινα τετράγωνα), C^{4+} (μπλε κύκλοι), και O^{6+} (πράσινα τρίγωνα) με He. Το DDCS φάσμα για κρούσεις 0.63 MeV/u F^{7+} (μαύρα διαμάντια) με He, λύφθηκε από [27].

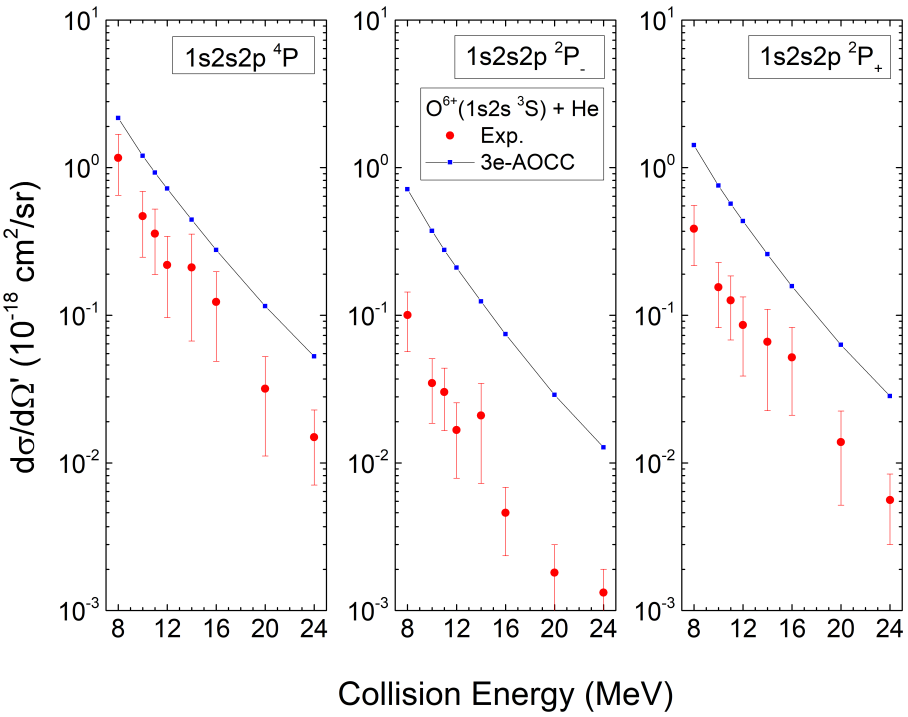

Figure 9.10: SDCS των καταστάσεων $1s2s2p\ ^4P$, $1s2s2p\ ^2P_-$, και $1s2s2p\ ^2P_+$ για κρούσεις $O^{6+}(1s2s\ ^3S)$ με He. Οι κόκκινοι κύκλοι αντιστοιχούν στις μετρήσεις και τα μπλε τετράγωνα σε 3eAOCC προκαταρκτικούς υπολογισμούς [25].

ίδια ενεργειακή εξάρτηση με τις μετρήσεις, δηλαδή μια ταχεία μείωση με την αύξηση της ενέργειας κρούσης.

Προσδιορισμός του Ενεργειακού Εύρους της Δέσμης Ιόντων

Στο παρελθόν έχουν προταθεί αρκετές τεχνικές για τον προσδιορισμό του ενεργειακού εύρους $\Delta E_P/E_P$ μιας ιοντικής δέσμης. Ενώ αυτές οι τεχνικές έχουν χρησιμοποιηθεί ευρέως, στην παρούσα διατριβή προτείνουμε μια εναλλακτική μέθοδο, η οποία βασίζεται στην ανάλυση των φασμάτων Auger ηλεκτρονίων δέσμης και προσομοιώσεις τύπου Monte Carlo που πραγματοποιούνται με τη βοήθεια του πακέτου οπτικής ιόντων SIMION.

Συγκεκριμένα, για την εν λόγω μέθοδο χρησιμοποιείται ένας αριθμητικός κώδικας προσομοίωσης των KLL Auger κορυφών, του οποίου οι παράμετροι είναι όλοι γνωστοί, εκτός από το ενεργειακό εύρος της δέσμης. Μεταβάλλοντας την παράμετρο $\Delta E_P/E_P$ έως ότου οι προσομοιωμένες κορυφές να ταιράζουν με τις πειραματικές είναι δυνατός ο προσδιορισμός του ενεργειακού εύρους της δέσμης. Ένα τέτοιο παράδειγμα φαίνεται στο σχήμα 9.11.

Η μέθοδος δοκιμάστηκε για ένα πλήθος συστημάτων κρούσεων, και τα αποτελέσματά μας βρέθηκαν σε καλή συμφωνία με αντίστοιχα αποτελέσματα που εξήχθησαν με τη χρήση της τεχνικής πυρηνικών συντονισμών, η οποία χρησιμοποιείται συνήθως σε πειράματα πυρηνικής φυσικής στην εγκατάσταση του επιταχυντή tandem Van de Graaff του Ε.Κ.Ε.Φ.Ε. «Δημόκριτος». Ωστόσο, μια άμεση σύγκριση μεταξύ των δύο συνόλων αποτελεσμάτων δεν είναι εφικτή λόγω των διαφορών στις πειραματικές δι-

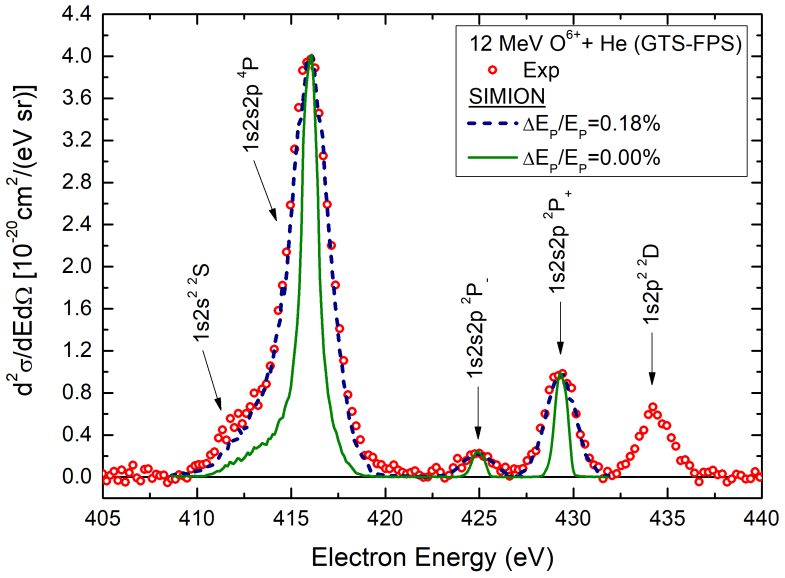

Figure 9.11: DDCS φάσμα ηλεκτρονίων για κρούσεις 12 MeV O^{6+} με He. Σύμβολα: Πείραμα; Γραμμές: SIMION προσομοιώσεις για $\Delta E_P/E_P = 0.18\%$ (μπλε διακεκομμένη γραμμή) και για $\Delta E_P/E_P = 0.00\%$ (πράσινη γραμμή). Λήφθηκε από [16].

ατάξεις και στις συνθήκες μεταφοράς της δέσμης ιόντων.

Bibliography

[1] National Museums Scotland. *Cockcroft-Walton generator*, Accessed: 14-09-2023. URL https://www.nms.ac.uk/explore-our-collections/stories/science-and-technology/cockcroft-walton-generator/.

[2] A. Grigoriadis. *Acceleration of electrons to relativistic velocities using an ultra-intense laser, Anastasios Grigoriadis*. PhD thesis, Dept. of Physics, University of Ioannina, 2023. URL https://doi.org/10.12681/eadd/54068.

[3] D.H. Lee and P. Richard and T.J.M. Zouros and J.M. Sanders and J.L. Shinpaugh and H. Hidmi. *Binary-encounter electrons observed at 0° in collisions of 1–2-MeV/amu* H^+, C^{6+}, N^{7+}, O^{8+}, *and* F^{9+} *ions with* H_2 *and* He *targets*. *Phys. Rev. A*, 41:4816, 1990. URL https://doi.org/10.1103/PhysRevA.41.4816.

[4] M. Brauner and J.H. Macek. *Ion-impact ionization of* He *targets*. *Phys. Rev. A*, 46:2519, 1992. URL https://doi.org/10.1103/PhysRevA.46.2519.

[5] S. Nanos. *Electron capture to the continuum in fast collisions of protons with gas targets*. Master's thesis, Dept. of Physics, University of Ioannina, 2019 (unpublished). URL https://drive.google.com/file/d/1-XMHKErQkfZ5wbM6rjF6DEXqkFrC6vOX/view.

[6] F. Fremont and K. Sommer and D. Lecler and S. Hicham and P. Boduch and X. Husson and N. Stolterfoht. *Angular distribution of Auger-electron emission following double-electron capture in* C^{6+} *+*He *collisions*. *Phys. Rev. A*, 46:222–229, 1992. URL https://doi.org/10.1103/PhysRevA.46.222.

[7] S. Harissopulos and M. Andrianis and M. Axiotis and A. Lagoyannis and A.G. Karydas and Z. Kotsina and A. Laoutaris and G. Apostolopoulos and A. Theodorou and T.J.M. Zouros and I. Madesis and E.P. Benis. *The Tandem Accelerator Laboratory of NCSR Demokritos: Current status and perspectives*. *Eur. Phys. J Plus*, 136:617, 2021. URL https://doi.org/10.1140/epjp/s13360-021-01596-5.

[8] E.P. Benis. *A novel high-efficiency paracentric hemispherical spectrograph for zero-degree Auger projectile spectroscopy*. PhD thesis, Dept. of Physics, University of Crete, 2001 (unpublished). URL https://drive.google.com/file/d/19IIS7fhecX9-x9FKnMhMLPVsQ_8NsK8k/view.

[9] I. Madesis. *Investigation of electron capture in swift* $C^{4+}(1s2s\ ^3S)$ *collisions with gas targets using a zero-degree Auger projectile spectroscopy*

apparatus built with the L45 beam line at the "Demokritos" 5.5MV tandem accelerator. PhD thesis, Dept. of Physics, University of Crete, 2021 (unpublished). URL https://apapes.physics.uoc.gr/thesis/Madesis_PhDThesis-v.d2.4-11pt.pdf.

[10] T.J.M. Zouros and others. *APAPES: Atomic Physics with Accelerators - Projectile Electron Spectroscopy*, Accessed: 30-06-2023. URL https://apapes.physics.uoc.gr/.

[11] N. Stolterfoht and H. Gabler and U. Leithäuser. *High Resolution Ne-Auger Spectrum Produced in 4.2 MeV* $H^+ - Ne$ *Collisions*. *Phys. Lett.*, 45A:351, 1973. URL https://apapes.physics.uoc.gr/references/Stolterfoht_PL45A_351_1973.pdf.

[12] T.J.M. Zouros and S. Nikolaou and I. Madesis and A. Laoutaris and S. Nanos and A. Dubois and E.P. Benis. *Radiative Cascade Repopulation of* $1s2s2p\,^4P$ *States Formed by Single Electron Capture in 2-18 MeV Collisions of* $C^{4+}(1s2s\ ^3S)$ *with* He. *Atoms*, 8(3), 2020. URL https://doi.org/10.3390/atoms8030061.

[13] A. Biniskos. *Experimental determination of the effective detection solid angle of a hemispherical spectrograph for metastable Auger projectile states*. Master's thesis, Dept. of Physics, University of Ioannina, 2022 (unpublished). URL https://drive.google.com/file/d/1yWbDb55pAqZhKfmX1WHR-rvSffEy7rO4/view.

[14] S. Doukas and I. Madesis and A. Dimitriou and A. Laoutaris and T.J.M. Zouros and E.P. Benis. *Determination of the solid angle and response function of a hemispherical spectrograph with injection lens for Auger electrons emitted from long lived projectile states*. *Rev. Sci. Instr.*, 86(4), 2015. URL https://doi.org/10.1063/1.4917274.

[15] E.P. Benis and S. Doukas and T.J.M. Zouros and P. Indelicato and F. Parente and C. Martins and J.P. Santos and J.P. Marques. *Evaluation of the effective solid angle of a hemispherical deflector analyser with injection lens for metastable Auger projectile states*. *Nucl. Instrum. Meth. Phys. Res. B*, 365: 457–461, 2015. URL https://doi.org/10.1016/j.nimb.2015.07.006.

[16] S. Nanos and A. Biniskos and A. Laoutaris and M. Andrianis and T.J.M. Zouros and A. Lagoyannis and E.P. Benis. *Determination of the ion beam energy width in tandem Van de Graaff accelerators via Auger projectile spectroscopy*. *Nucl. Instrum. Meth. Phys. Res. B*, 541:93, 2023. URL https://doi.org/10.1016/j.nimb.2023.05.027.

[17] D.M. McSherry and S.F.C. O'Rourke and D.S.F. Crothers. *Ion–Atom/Argon—Calculation of ionization cross sections by fast ion impact for neutral target atoms ranging from hydrogen to argon*. *Comp. Phys. Com.*, 155(2):144, 2003. URL https://doi.org/10.1016/S0010-4655(03)00342-4.

[18] D.S.F. Crothers and M. McCartney. *ION — a program to evaluate cross-sections for ionisation in ion-atom collisions*. *Comp. Phys. Com.*, 72(2):288, 1992. URL https://doi.org/10.1016/0010-4655(92)90155-R.

[19] B.S. Nesbitt and S.F.C. O'Rourke and D.S.F. Crothers. *Ion-Atom-Wave — Calculation of single ionization cross sections in ion—atom collisions*. *Comp. Phys. Com.*, 114(1):385, 1998. URL https://doi.org/10.1016/S0010-4655(98)00072-1.

[20] S.F.C. O'Rourke and D.M. McSherry and D.S.F. Crothers. *ION-ATOM/NEON - Calculation of ionization cross sections by fast ion impact for neutral target atoms ranging from lithium to neon*. *Comp. Phys. Com.*, 131 (1):129, 2000. URL https://doi.org/10.1016/S0010-4655(00)00075-8.

[21] S. Nanos and M.A. Quinto and I. Madesis and A. Laoutaris and T.J.M. Zouros and R.D. Rivarola and J.M. Monti and E.P. Benis. *Subshell contributions to electron capture into the continuum in MeV/u collisions of deuterons with multielectron targets*. *Phys. Rev. A*, 105:022806, 2022. URL https://doi.org/10.1103/PhysRevA.105.022806.

[22] S. Nanos and N.J. Esponda and P.-M. Hillenbrand and A. Biniskos and A. Laoutaris and M.A. Quinto and N. Petridis and E. Menz and T.J.M. Zouros and Th. Stöhlker and R.D. Rivarola and J.M. Monti and E.P. Benis. *Cusp-electron production in collisions of open-shell He-like oxygen ions with atomic targets*. *Phys. Rev. A*, 107:062815, 2023. URL https://doi.org/10.1103/PhysRevA.107.062815.

[23] I. Madesis and A. Laoutaris and T.J.M. Zouros and E.P. Benis and J.W. Gao and A. Dubois. *Pauli Shielding and Breakdown of Spin Statistics in Multi-electron Multi-Open-Shell Dynamical Atomic Systems*. *Phys. Rev. Lett.*, 124: 113401, 2020. URL https://doi.org/10.1103/PhysRevLett.124.113401.

[24] J.W. Gao and Y. Wu and J.G. Wang and N. Sisourat and A. Dubois. *State-selective electron transfer in* $He^+ + He$ *collisions at intermediate energies*. *Phys. Rev. A*, 97:052709, 2018. URL https://link.aps.org/doi/10.1103/PhysRevA.97.052709.

[25] S. Passalidis. *Modelling of multi-electronic processes occurring during atomic collisions*. PhD thesis, Laboratoire de Chimie Physique-Matière et Rayonnement, 2022 (unpublished). URL https://theses.hal.science/tel-03622169/document.

[26] I. Madesis and A. Laoutaris and S. Nanos and S. Passalidis and A. Dubois and T.J.M. Zouros and E.P. Benis. *State-resolved differential cross sections of single-electron capture in swift collisions of* $C^{4+}(1s2s\ ^3S)$ *ions with gas targets*. *Phys. Rev. A*, 105:062810, 2022. URL https://doi.org/10.1103/PhysRevA.105.062810.

[27] D.H. Lee. *Electron-electron interaction in ion-atom collisions studied by projectile state-resolved electron spectroscopy*. PhD thesis, Kansas State University, Manhattan, 1990 (unpublished). URL https://www.proquest.com/docview/303878409.

[28] S. Voikopoulos. *Production of fast highly charged ion beams through stripping techniques*. Master's thesis, Dept. of Physics, University of Ioannina, 2021 (unpublished). URL https://drive.google.com/file/d/1wcNWksEHVMhzDGZ30lCQLT_gsX0pBuoc/view.

[29] P.P. Szydlik and A.E. Green. *Independent-particle-model potentials for ions and neutral atoms with $Z \leq 18$*. *Phys. Rev. A*, 9:1885, 1974. URL https://doi.org/10.1103/PhysRevA.9.1885.

[30] V.H. Ponce. *Velocity Parameters of Atomic Wavefunctions*. *At. Data Nucl. Data Tables*, 19:63, 1977. URL https://doi.org/10.1016/0092-640X(77)90009-2.

[31] E. Clementi and C. Roetti. *Roothaan-Hartree-Fock atomic wavefunctions: Basis functions and their coefficients for ground and certain excited states of neutral and ionized atoms, $Z \leq 54$*. *At. Data Nucl. Data Tables*, 14:177, 1974. URL https://doi.org/10.1016/S0092-640X(74)80016-1.

[32] J.D. Cockcroft and E.T.S. Walton. *Experiments with high velocity positive ions.—(I) Further developments in the method of obtaining high velocity positive ions*. *Proc. Roy. Soc. A*, 136, 1932. URL https://doi.org/10.1098/rspa.1932.0107.

[33] The Nobel prize. *Ernest Lawrence - Facts*, Accessed: 14-09-2023. URL https://www.nobelprize.org/prizes/physics/1939/lawrence/facts/.

[34] National Institute of Standards and Technology. *Positive-Ion Van de Graaff Accelerator*, Accessed: 14-09-2023. URL https://www.nist.gov/history/radiation-physics-building/facilities/positive-ion-van-de-graaff-accelerator.

[35] Letournel, M. *Brief review of the development of electrostatic accelerators and continuing work at Strasbourg*. In *Proceedings of the 1989 IEEE Particle Accelerator Conference, Accelerator Science and Technology*, page 1103, 1989. URL https://doi.org/10.1109/PAC.1989.73366.

[36] Brookhaven National Laboratory. *A History of Leadership in Particle Accelerator Design*, Accessed: 14-09-2023. URL https://www.bnl.gov/about/history/accelerators.php.

[37] Berkeley Lab. *Bevatron Site Recognized for Historical Contributions to Physics*, Accessed: 14-09-2023. URL https://newscenter.lbl.gov/2021/06/25/bevatron-contributions-to-physics/.

[38] CERN Accelerating science. *The Proton Synchrotron*, Accessed: 14-09-2023. URL https://home.cern/science/accelerators/proton-synchrotron.

[39] L.D. Lella and C. Rubbia. *The Discovery of the W and Z Particles*. *Adv. Ser. Direct. High Energy Phys.*, 23:137, 2015. URL https://doi.org/10.1142/9789814644150_0006.

[40] SLAC National Accelerator Laboratory. *SLAC at a glance*, Accessed: 23-09-2023. URL https://www6.slac.stanford.edu/about/lab-overview/at-a-glance.

[41] Argonne National Laboratory. *The Advanced Photon Source*, Accessed: 14-09-2023. URL https://www.aps.anl.gov/.

[42] DESY. *Free-Electron Laser FLASH*, Accessed: 14-09-2023. URL https://flash.desy.de/.

[43] The European Synchrotron. *ESRF: The European Synchrotron*, Accessed: 14-09-2023. URL https://www.esrf.fr/.

[44] Helmholtz. *GSI Helmholtz Centre for Heavy Ion Research*, Accessed: 14-09-2023. URL https://www.helmholtz.de/en/about-us/helmholtz-centers/centers-a-z/centre/gsi-helmholtz-centre-for-heavy-ion-research/.

[45] G. Zschornack and M. Kreller and V.P. Ovsyannikov and F. Grossman and U. Kentsch and M. Schmidt and F. Ullmann and R. Heller. *Compact electron beam ion sources/traps: Review and prospects (invited)*). *Rev. Sci. Instr.*, 79 (2):02A703, 2008. URL https://doi.org/10.1063/1.2804901.

[46] R. Geller. *Electron cyclotron resonance sources: Historical review and future prospects*. *Review of Scientific Instruments*, 69(2):613, 1998. URL https://doi.org/10.1063/1.1148724.

[47] Dž. Belkić. *Review of theories on ionization in fast ion-atom collisions with prospects for applications to hadron therapy*. *J. Math. Chem.*, 47:1366, 2010. URL https://doi.org/10.1007/s10910-010-9662-x.

[48] N. Aide and C. Lasnon and A. Kesner and C.S. Levin and I. Buvat and A. Iagaru and K. Hermann and R.D. Badawi and S.R. Cherry and K.M. Bradley and D.R. McGowan. *New PET technologies – embracing progress and pushing the limits*. *Eur. J. Nucl. Med. Mol. Imag.*, 48:2711, 2021. URL https://doi.org/10.1007/s00259-021-05390-4.

[49] J. Trotter and A.R. Pantel and B.-K.K. Teo and F.E. Escorcia and T. Li and D.A. Pryma and N.K. Taunk. *Positron Emission Tomography (PET)/Computed Tomography (CT) Imaging in Radiation Therapy Treatment Planning: A Review of PET Imaging Tracers and Methods to Incorporate PET/CT*. *Adv. Rad. Onc.*, 8(5):101212, 2023. URL https://www.sciencedirect.com/science/article/pii/S2452109423000416.

[50] P.S. Rahimabadiand M. Khodaei and K.R. Koswattage. *Review on applications of synchrotron-based X-ray techniques in materials characterization*. *X-Ray Spec.*, 49(3):348, 2020. URL https://doi.org/10.1002/xrs.3141.

[51] G. Dearnaley. *Ion implantation*. *Nature*, 256:701, 1975. URL https://doi.org/10.1038/256701a0.

[52] L.A. Larson and J.M. Williams and M.I. Current. Ion Implantation for Semiconductor Doping and Materials Modification. *Rev. Accel. Sci. Tech.*, 04(01): 11, 2011. URL https://doi.org/10.1142/S1793626811000616.

[53] S.E. Chatoutsidou and S. Papagiannis and D.F. Anagnostopoulos and K. Eleftheriadis and M. Lazaridis and A.G. Karydas. *Application of a handheld X-ray fluorescence analyzer for the quantification of air particulate matter on Teflon filters*. *Spec. Acta Part B At. Spec.*, 196:106517, 2022. URL https://www.sciencedirect.com/science/article/pii/S0584854722001616.

[54] F. Lucarelli and G. Calzolai and M. Chiari and S. Nava and L. Carraresi. *Study of atmospheric aerosols by IBA techniques: The LABEC experience*. *Nucl. Instr. Meth. Phys. B*, 417:121, 2018. URL https://www.sciencedirect.com/science/article/pii/S0168583X17307747.

[55] D. Sokaras and E. Bistekos and L. Georgiou and J. Salomon and M. Bogovac and E. Aloupi-Siotis and V. Paschalis and I. Aslani and S. Karabagia and A. Lagoyannis and S. Harissopulos and V. Kantarelou and A.-G. Karydas. *The new external ion beam analysis setup at the Demokritos Tandem accelerator and first applications in cultural heritage*. *Nucl. Instrum. Meth. Phys. Res. B*, 269(5):519, 2011. URL https://www.sciencedirect.com/science/article/pii/S0168583X11000139.

[56] S. Ashraf and M. Sood and J.D. Bandral and M. Trilokia and M. Manzoor. *Food irradiation: A review*. *Int. J. Chem. Stud.*, page 131, 2019. URL https://www.chemijournal.com/archives/?year=2019&vol=7&issue=2&ArticleId=5139&si=false.

[57] W.A. Reed . *Nondestructive testing and inspection using electron linacs*, page 307. World Scientific, 2012. URL https://www.worldscientific.com/doi/abs/10.1142/9789814307055_0008.

[58] P.-M. Hillenbrand, S. Hagmann, Y.S. Kozhedub, E.P. Benis, C. Brandau, R.J. Chen, D. Dmytriiev, O. Forstner, J. Glorius, R.E. Grisenti, A. Gumberidze, M. Lestinsky, Yu.A. Litvinov, E.B. Menz, T. Morgenroth, S. Nanos, N. Petridis, Ph. Pfäfflein, H. Rothard, M.S. Sanjari, R.S. Sidhu, U. Spillmann, S. Trotsenko, I.I. Tupitsyn, L. Varga, and Th. Stöhlker. *Single and double K-shell vacancy production in slow* $Xe^{54+,53+} - Xe$ *collisions*. *Phys. Rev. A*, 105: 022810, 2022. URL https://link.aps.org/doi/10.1103/PhysRevA.105.022810.

[59] S.A. King and L.J. Spieß and P. Micke and A. Wilzewski and T. Leopold and E. Benkler and R. Lange and N. Huntemann and A. Surzhykov and V.A. Yerokhin and J.R.C. López-Urrutia and P.O. Schmidt. *An optical atomic clock based on a highly charged ion*. *Nature*, 611:43, 2022. URL https://doi.org/10.1038/s41586-022-05245-4.

[60] D. Schury, A. Méry, J.M. Ramillon, L. Adoui, J.-Y. Chesnel, A. Lévy, S. Macé, C. Prigent, J. Rangama, P. Rousseau, S. Steydli, M. Trassinelli, D. Vernhet, A. Gumberidze, Th. Stöhlker, A. Bräuning-Demian, C. Hahn, U. Spillmann, and E. Lamour. *The low energy beamline of the FISIC experiment: current*

status of construction and performance. *J. Phys. Conf. S.*, 1412(16):162011, 2020. URL https://dx.doi.org/10.1088/1742-6596/1412/16/162011.

[61] D.H. Jakubaßa-Amundsen. *Theoretical models for atomic charge transfer in ion-atom collisions*. *Int. J. Mod Phys. A*, 4:769, 1989. URL https://doi.org/10.1142/S0217751X89000376.

[62] A.S. Schlachter and J.W. Stearns and W.G. Graham and K.H. Berkner and R.V. Pyle and J.A. Tanis. *Electron capture for fast highly charged ions in gas targets: An empirical scaling rule*. *Phys. Rev. A*, 27:3372, 1983. URL https://link.aps.org/doi/10.1103/PhysRevA.27.3372.

[63] W.L. Fite and R.T. Brackmann and W.R. Snow. *Charge Exchange in Proton-Hydrogen-Atom Collisions*. *Phys. Rev.*, 112:1161, 1958. URL https://link.aps.org/doi/10.1103/PhysRev.112.1161.

[64] W.L. Fite and R.F. Stebbings and D.G. Hummer and R.T. Brackmann. *Ionization and Charge Transfer in Proton-Hydrogen Atom Collisions*. *Phys. Rev.*, 119:663, 1960. URL https://link.aps.org/doi/10.1103/PhysRev.119.663.

[65] H.B. Gilbody and G. Ryding. *An experimental study of charge transfer in proton-atomic hydrogen collisions at impact energies above 40 keV*. *Proc. Roy. Soc. A*, 291:438, 196. URL https://doi.org/10.1098/rspa.1966.0104.

[66] C.E. Kuyatt and T. Jorgensen, T. *Energy and Angular Dependence of the Differential Cross Section for Production of Electrons by 50-100 keV Protons in Hydrogen Gas*. *Phys. Rev.*, 130:1444, 1963. URL https://link.aps.org/doi/10.1103/PhysRev.130.1444.

[67] J.R. Macdonald and C.L. Cocke and W.W. Eidson. *Capture of Argon K-Shell Electrons by 2.5- to 12-MeV Protons*. *Phys. Rev. Lett.*, 32:648, 1974. URL https://link.aps.org/doi/10.1103/PhysRevLett.32.648.

[68] A.K. Edwards and M.E. Rudd. Excitation of Auto-Ionizing Levels in Neon by Ion Impact. *Phys. Rev.*, 170:140, 1968. URL https://link.aps.org/doi/10.1103/PhysRev.170.140.

[69] V.A. Belyaev and B.G. Brezhnev and E.M. Erastov. *Resonant Charge Transfer of Low-energy Carbon and Nitrogen Ions*. *J. Exp. Theor. Phys.*, 27(6):924, 1968. URL http://jetp.ras.ru/cgi-bin/e/index/e/27/6/p924?a=list.

[70] A. Müller and E. Salzborn. Single and double electron transfer in $Ar^{i+} - He$ collisions. *Phys. Let. A*, 59(1):19, 1976. URL https://doi.org/10.1016/0375-9601(76)90338-8.

[71] F.W. Meyer and C.J. Anderson and L.W. Anderson. *Total charge-transfer cross sections for* H^+, H_2^+, H_3^+, He^+, N^+, N_2^+, Ne^+, Ar^+, Kr^+, *and* Xe^+ *incident on* Cs. *Phys. Rev. A*, 15:455, 1977. URL https://link.aps.org/doi/10.1103/PhysRevA.15.455.

[72] V.P. Shevelko. *One-electron Capture in Collisions of Fast Ions with Atoms V. Z. Physik A*, 287:19, 1978. URL https://doi.org/10.1007/BF01408355.

[73] M.E. Rudd. *Mechanisms of electron production in ion-atom collisions*. *Radiat. Res.*, (1):153, 1975. URL https://www.osti.gov/biblio/4106628.

[74] N. Stolterfoht. *High Resolution Auger Spectroscopy in Energetic Ion-Atom Collisions*. *Phys. Scr.*, 146(6):315, 1987. URL https://apapes.physics.uoc.gr/references/Stolterfoht_PR146_315_1987.pdf.

[75] J. Newcomb and T.R. Dillingham and J. Hall and S.L. Varghese and P.L. Pepmiller and P. Richard. *Electron capture by metastable projectiles on* He *and* Ne. *Phys. Rev. A*, 29:82, 1984. URL https://link.aps.org/doi/10.1103/PhysRevA.29.82.

[76] T.J.M. Zouros and D.H. Lee. Chapter 13 - *Zero-Degree Auger Electron Spectroscopy of Projectile Ions*. In S.M. Shafroth and J.C. Austin, editor, *Accelerator-based atomic physics techniques and applications*, page 426. American Institute of Physics Conference Series, New York, 1997. URL https://www.researchgate.net/publication/282274732_Zero-Degree_Auger_Electron_Spectroscopy_of_Projectile_Ions.

[77] E.P. Benis and I. Madesis and A. Laoutaris and S. Nanos and T.J.M. Zouros. *Mixed-State Ionic Beams: An Effective Tool for Collision Dynamics Investigations*. *Atoms*, 6:66, 2018. URL https://doi.org/10.3390/atoms6040066.

[78] A. Laoutaris and S. Nanos and I. Madesis and S. Passalidis and E.P. Benis and A. Dubois and T.J.M. Zouros. *Coherent treatment of transfer-excitation processes in swift ion-atom collisions*. *Phys. Rev. A*, 106:022810, 2022. URL https://doi.org/10.1103/PhysRevA.106.022810.

[79] R. Abrines and I.C. Percival. *Classical theory of charge transfer and ionization of hydrogen atoms by protons*. *Proc. Phys. Soc.*, 88(4):861, 1966. URL https://dx.doi.org/10.1088/0370-1328/88/4/306.

[80] E.M. Mack. *Electron capture to autoionizing states of multiply charged ions.* PhD thesis, Rijksuniversiteit te Utrecht, 1987 (unpublished). URL https://inis.iaea.org/collection/NCLCollectionStore/_Public/19/042/19042610.pdf.

[81] T. Kirchner and M. Keim and A. Achenbach and H.J. Lüdde and O.J. Kroneisen and R.M. Dreizler. *Basis Generator Method Study of Collisions Between Alpha Particles and Lithium-like Ions*. *Phys. Scr.*, T80:270, 1999. URL https://doi.org/10.1238/Physica.Topical.080a00270.

[82] W. Fritsch and C.D. Lin. *The semiclassical close-coupling description of atomic collisions: Recent developments and results*. *Phys. Rep.*, 202:1, 1991. URL https://doi.org/10.1016/0370-1573(91)90008-A.

[83] G.B. Crooks and M.E. Rudd. *Experimental Evidence for the Mechanism of Charge Transfer into Continuum States*. *Phys. Rev. Lett.*, 25:1599, 1970. URL https://doi.org/10.1103/PhysRevLett.25.1599.

[84] N. Stolterfoht and R.D. DuBois and R.D. Rivarola. *Electron Emission in Heavy Ion-Atom Collisions.* Springer Berlin Heidelberg, Berlin, Heidelberg, 1997. URL https://doi.org/10.1007/978-3-662-03480-4.

[85] L.H. Thomas. On the Capture of Electrons by Swiftly Moving Electrified Particles. *Proc. R. Soc. London S. A*, 114(768):561, 1927. URL http://www.jstor.org/stable/94828.

[86] W. Meckbach and I.B. Nemirovsky and C.R. Garibotti. *Resolution dependence and asymmetry of electron capture to the continuum spectra*. *Phys. Rev. A*, 24: 1793, 1981. URL https://link.aps.org/doi/10.1103/PhysRevA.24.1793.

[87] A. Skutlartz and S. Hagmann and H. Schmidt-Bocking. *Correlated electron capture in the impact parameter and final projectile charge-state dependence of ECC cusp production in 0.53 MeV* u^{-1} $F^{8+} + Ne$. *J. Phys. B At. Mol. Phys.*, 21(21):3609, 1988. URL https://dx.doi.org/10.1088/0953-4075/21/21/016.

[88] Th. Weber and Kh. Khayyat and R. Dörner and V.D. Rodríguez and V. Mergel and O. Jagutzki and L. Schmidt and K.A. Müller and F. Afaneh and A. Gonzalez and H. Schmidt-Böcking. *Abrupt Rise of the Longitudinal Recoil Ion Momentum Distribution for Ionizing Collisions*. *Phys. Rev. Lett.*, 86:224, 2001. URL https://link.aps.org/doi/10.1103/PhysRevLett.86.224.

[89] P.-M. Hillenbrand and S. Hagmann and D. Atanasov and D. Banaś and K.-H. Blumenhagen and C. Brandau and W. Chen and E. De Filippo and A. Gumberidze and D.L. Guo and D.H. Jakubassa-Amundsen and O. Kovtun and C. Kozhuharov and M. Lestinsky and Yu.A. Litvinov and A. Müller and R.A. Müller and H. Rothard and S. Schippers and M.S. Schöffler and U. Spillmann and A. Surzhykov and S. Trotsenko and N. Winckler and X.L. Yan and V.A. Yerokhin and X.L. Zhu and Th. Stöhlker. *Radiative-electron-capture-to-continuum cusp in* $U^{88+} + N_2$ *collisions and the high-energy end-point of electron-nucleus bremsstrahlung*. *Phys. Rev. A*, 90:022707, 2014. URL https://link.aps.org/doi/10.1103/PhysRevA.90.022707.

[90] P.-M. Hillenbrand and S. Hagmann and A.B. Voitkiv and B. Najjari and D. Banaś and K.-H. Blumenhagen and C. Brandau and W. Chen and E. De Filippo and A. Gumberidze and D.L. Guo and C. Kozhuharov and M. Lestinsky and Yu.A. Litvinov and A. Müller and H. Rothard and S. Schippers and M.S. Schöffler and U. Spillmann and S. Trotsenko and X.L. Zhu and Th. Stöhlker. *Electron-loss-to-continuum cusp in* $U^{88+} + N_2$ *collisions*. *Phys. Rev. A*, 90:042713, 2014. URL https://link.aps.org/doi/10.1103/PhysRevA.90.042713.

[91] P.-M. Hillenbrand and S. Hagmann and D.H. Jakubassa-Amundsen and J.M. Monti and D. Banaś and K.-H. Blumenhagen and C. Brandau and W. Chen and P.D. Fainstein and E. De Filippo and A. Gumberidze and D.L. Guo and M. Lestinsky and Yu.A. Litvinov and A. Müller and R.D. Rivarola and H. Rothard and S. Schippers and M.S. Schöffler and U. Spillmann and S. Trotsenko and X.L. Zhu and Th. Stöhlker. *Electron-capture-to-continuum cusp in* $U^{88+} + N_2$ *collisions*. *Phys. Rev. A*, 91:022705, 2015. URL https://link.aps.org/doi/10.1103/PhysRevA.91.022705.

[92] P.-M. Hillenbrand and S. Hagmann and J.M. Monti and R.D. Rivarola and K.-H. Blumenhagen and C. Brandau and W. Chen and R.D. DuBois and A.

Gumberidze and D.L. Guo and M. Lestinsky and Yu.A. Litvinov and A. Müller and S. Schippers and U. Spillmann and S. Trotsenko and G. Weber and Th. Stöhlker. *Strong asymmetry of the electron-loss-to-continuum cusp of multielectron* U^{28+} *projectiles in near-relativistic collisions with gaseous targets*. *Phys. Rev. A*, 93:042709, 2016. URL https://link.aps.org/doi/10.1103/PhysRevA.93.042709.

[93] N.J. Esponda and M.A. Quinto and R.D. Rivarola and J.M. Monti. *Dynamic screening and two-center effects in neutral and partially dressed ion-atom collisions*. *Phys. Rev. A*, 105:032817, 2022. URL https://doi.org/10.1103/PhysRevA.105.032817.

[94] M.E. Rudd and J.H. Macek. Chapter 2 - *Mechanisms of Electron Production in Ion—Atom Collisions*. In E.W. McDaniel and M.R.C. McDowell, editors, *Case Studies in Atomic Physics*, page 47. Elsevier, 1974. URL https://doi.org/10.1016/B978-0-7204-0292-6.50006-6.

[95] D. Burch and N. Stolterfoht and D. Schneider and H. Wieman and J.S. Risley. *Projectile Charge-State Dependence of* Ne*K-Shell Ionization and Fluorescence Yield in 50-MeV* Cl^{n+} + Ne *Collisions*. *Phys. Rev. Lett.*, 32:1151, 1974. URL https://doi.org/10.1103/PhysRevLett.32.1151.

[96] A. Itoh and D. Schneider and T. Schneider and T.J.M. Zouros and G. Nolte and G. Schiwietz and W. Zeitz and N. Stolterfoht. *Selective production of* Li-, Be-, *and* B*-like K vacancy states in fast Ne projectiles studied by zero-degree Auger spectroscopy*. *Phys. Rev. A*, 31:684, 1985. URL https://doi.org/10.1103/PhysRevA.31.684.

[97] A. Itoh and T. Schneider and G. Schiwietz and Z. Roller and H. Platten and G. Nolte and D. Schneider and N. Stolterfoht. *Selective production of Auger electrons from fast projectile ions studied by zero-degree Auger spectroscopy*. *J. Phys. B: At. and Mol. Phys.*, 16(21):3965, 1983. URL https://doi.org/10.1088/0022-3700/16/21/016.

[98] N. Stolterfoht and C.C. Havener and R.A. Phaneuf and J.K. Swenson and S.M. Shafroth and F.W. Meyer. *Evidence for correlated double-electron capture in low-energy collisions of* O^{6+} *with* He. *Phys. Rev. Lett.*, 57:74, 1986. URL https://doi.org/10.1103/PhysRevLett.57.74.

[99] Y. Yamazaki and P.D. Miller and H.F. Krause and P.L. Pepmiller and S. Datz and I.A. Sellin and N. Stolterfoht. *Observation of Strong Forward-Backward Asymmetries in Electron Emission from Overlapping Resonance States Produced by Transfer Excitation in 2.5-3.5-MeV* C^{3+}+ He *Collisions*. *Phys. Rev. Lett.*, 57:992, 1986. URL https://doi.org/10.1103/PhysRevLett.57.992.

[100] J.K Swenson and Y. Yamazaki and P.D. Miller and H.F. Krause and P.F. Dittner and P.L. Pepmiller and S. Datz and N. Stolterfoht. *Observation of Resonant Transfer and Excitation to Specific* LS*-Coupled States in* O^{5+}+ He *Collisions by High-Resolution, 0° Auger-Electron Spectroscopy*. *Phys. Rev. Lett.*, 57:3042, 1986. URL https://doi.org/10.1103/PhysRevLett.57.3042.

[101] F.W. Meyer and D.C Griffin and C.C. Havener and M.S. Huq and R.A. Phaneuf and J.K. Swenson and N. Stolterfoht. *Population of high–angular-momentum states in low-energy double-electron-capture collisions of* O^{6+} *with* He. *Phys. Rev. Lett.*, 60:1821, 1988. URL https://doi.org/10.1103/PhysRevLett.60.1821.

[102] Y. Yamazaki and N. Stolterfoht and P.D. Miller and H.F. Krause and P.L. Pepmiller and S.Datz and I.A. Sellin and J.N. Scheurer and S. Andriamonje and D. Bertault and J.F. Chemin. *Angular Momentum Distributions of Autoionizing States Produced by 1.5-5-MeV* C^+ *Ions in Carbon Foils*. *Phys. Rev. Lett.*, 61:2913, 1988. URL https://doi.org/10.1103/PhysRevLett.61.2913.

[103] J.K. Swenson and C.C. Havener and N. Stolterfoht and K. Sommer and F.W. Meyer. *Observation of Coulomb focusing of autoionization electrons produced in low-energy* $He^+ + He$ *collisions*. *Phys. Rev. Lett.*, 63:35, 1989. URL https://doi.org/10.1103/PhysRevLett.63.35.

[104] T.J.M. Zouros and D.H. Lee and P. Richard. *Projectile 1s→2p excitation due to electron-electron interaction in collisions of* O^{5+} *and* F^{6+} *ions with* H_2 *and* He *targets*. *Phys. Rev. Lett.*, 62:2261, 1989. URL https://doi.org/10.1103/PhysRevLett.62.2261.

[105] T.J.M. Zouros and C.P. Bhalla and D.H. Lee and P. Richard. *Effects of alignment and interference in resonant transfer and excitation for* F^{6+} *and* O^{5+} *collisions with* H_2 *in 0° Auger measurements*. *Phys. Rev. A*, 42:678, 1990. URL https://doi.org/10.1103/PhysRevA.42.678.

[106] D.H. Lee and P. Richard and J.M. Sanders and T.J.M. Zouros and J.L. Shinpaugh and S.L. Varghese. *KLL resonant transfer excitation to* F^{6+} *(1s2l2l') intermediate states*. *Phys. Rev. A*, 44:1636, 1991. URL https://doi.org/10.1103/PhysRevA.44.1636.

[107] J.K. Swenson and J. Burgdörfer and F.W. Meyer and C.C. Havener and D.C. Gregory and N. Stolterfoht. *Coulomb "path" interference in low-energy ion-atom collisions*. *Phys. Rev. Lett.*, 66:417, 1991. URL https://doi.org/10.1103/PhysRevLett.66.417.

[108] D.H. Lee and T.J.M. Zouros and J.M. Sanders and P. Richard and J.M. Anthony and Y.D. Wang and J.H. McGuire. *K-shell ionization of* O^{4+} *and* C^{2+} *ions in fast collisions with* H_2 *and He gas targets*. *Phys. Rev. A*, 46:1374, 1992. URL https://doi.org/10.1103/PhysRevA.46.1374.

[109] E.P. Benis and K. Zaharakis and M.M. Voultsidou and T.J.M. Zouros and M. Stöckli and P. Richard and S. Hagmann. *A new hemispherical analyser with 2-D-PSD and focusing lens for use in* 0^o *electron spectroscopy*. *Nucl. Instrum. Meth. Phys. Res. B*, 146:120, 1998.

[110] E.P. Benis and T.J.M Zouros and H. Aliabadi and P. Richard. *Hemispherical Analyser with 2-D PSD for Zero-degree Auger Projectile Spectroscopy*. *Phys. Scr.*, 1999(T80B):529, 1999. URL https://doi.org/10.1238/Physica.Topical.080a00529.

[111] E.P. Benis and T.J.M. Zouros and P. Richard. *High resolution RTE measurements at 0° using a hemispherical analyser with lens and 2-D PSD*. *Nucl. Instrum. Meth. Phys. Res. B*, 154(1):276, 1999. URL https://doi.org/10.1016/S0168-583X(99)00028-2.

[112] A. Laoutaris. *Study and implementation of a system of ion poststrippers for use at the 5.5 MV Tandem Van de Graaff accelerator of the National Center for Science and Research Demokritos*. Master's thesis, Dept. of Physics, National Technical University of Athens, 2015 (unpublished). URL https://apapes.physics.uoc.gr/thesis/Laoutaris_diplomatiki_partial.pdf.

[113] I. Madesis, A. Dimitriou, A. Laoutaris, A. Lagoyannis, M. Axiotis, T. Mertzimekis, M. Andrianis, S. Harissopulos, E.P. Benis, and B. Sulik. *Atomic Physics with Accelerators: Projectile Electron Spectroscopy (APAPES)*. *J. Phys: Conf. Ser.*, 583:012014, 2015. URL https://doi.org/10.1088/1742-6596/583/1/012014.

[114] A. Dimitriou and A. Laoutaris and I. Madesis and S. Doukas and E.P. Benis and B. Sulik and O. Sise and A. Lagoyannis and M. Axiotis and T.J.M. Zouros. *High Resolution Auger Projectile Electron Spectroscopy of* Li*-like Ions Produced by Electron Capture in collision of* He*-like ions with Gaseous targets*. *J. Atom. Mol. Cond. Nano Phys.*, 3:125, 2016. URL https://doi.org/10.26713/jamcnp.v3i2.523.

[115] I. Madesis and A. Laoutaris and S. Doukas and A. Dimitriou and E.P. Benis and T.J.M. Zouros. *Separation and solid angle correction of the metastable* $1s2s2p\ ^4\mathrm{P}$ *Auger yield produced in ion-atom collisions using the biased gas cell technique: A tool for the determination of the population mechanisms*. *J. Phys: Conf. Ser.*, 635:052082, 2015. URL https://doi.org/10.1088/1742-6596/635/5/052082.

[116] E.P. Benis and T.J.M. Zouros. *The hemispherical deflector analyser revisited. II. Electronoptical properties*. *J. El. Spec. and Rel. Phen.*, 163:28, 2008. URL https://doi.org/10.1016/j.elspec.2008.02.001.

[117] E.P. Benis and T.J.M. Zouros. *Improving the energy resolution of a hemispherical spectrograph using a paracentric entry at a nonzero potential*. *Nucl. Instrum. Meth. Phys. Res. A*, 440:462, 2000. URL https://doi.org/10.1016/S0168-9002(99)00954-7.

[118] T.J.M. Zouros and E.P. Benis. *The hemispherical deflector analyser revisited. I. Motion in the ideal 1/r potential, generalized entry conditions, Kepler orbits and spectrometer basic equation*. *J. El. Spec. Rel. Phen.*, 125:221, 2002. URL https://doi.org/10.1016/S0368-2048(02)00137-8.

[119] O. Sise and T.J.M. Zouros and M. Ulu and M. Dogan. *Novel and traditional fringing field correction schemes for the hemispherical analyzer: Comparison of 1rst order focusing and energy resolution*. *Meas. Sci. Tech.*, 18:1853, 2007. URL https://doi.org/10.1088/0957-0233/18/7/009.

[120] T.J.M. Zouros and O. Sise and M. Ulu and M. Dogan. *Using the fringing fields of a hemispherical spectrograph to improve its energy resolution*. *Meas. Sci. Tech.*, 17:N81, 2006. URL https://doi.org/10.1088/0957-0233/17/12/N02.

[121] N.L.S. Martin and A. von Engel. *The reflection of slow electrons from a soot-covered surface*. *J. Phys D: Appl. Phys.*, 10:863, 1977. URL https://doi.org/10.1088/0022-3727/10/6/008.

[122] L.M. Conecici, C. Munteanu, and I.M. Purcar. *Study of the shielding performances of different materials regarding Electromagnetic Field Interference*. *IOP Conf. Ser.: Mater. Sci. Eng.*, 200:012045, 2017. URL https://doi.org/10.1088/1757-899X/200/1/012045.

[123] T.J.M. Zouros and E.P. Benis and J. E. Schauer. *Charged particle trajectories in an ideal paracentric hemispherical deflection analyser*. In J.L. Duggan and I.L. Morgan, editor, *Application of Accelerators in Research and Industry*, page 76. American Institute of Physics Conference Series, New York, 2005. URL https://doi.org/10.1063/1.1395253.

[124] T.J.M. Zouros and E.P. Benis. *Optimal energy resolution of a hemispherical analyzer with virtual entry*. *Ap. Phys. Let.*, 86(9), 2005. URL https://doi.org/10.1063/1.1871339.

[125] T.J.M. Zouros and E.P. Benis. *The hemispherical deflector analyser revisited. I. Motion in the ideal 1/r potential, generalized entry conditions, Kepler orbits and spectrometer basic equation*. *J. El. Spec. Rel. Phen.*, 125(3):221, 2002. URL https://doi.org/10.1016/S0368-2048(02)00137-8.

[126] M. Dogan and M. Ulu and G.G. Gennarakis and T.J.M. Zouros. *Experimental energy resolution of a paracentric hemispherical deflector analyzer for different entry positions and bias*. *Rev. Sci. Instr.*, 84(4):043105, 2013. URL https://doi.org/10.1063/1.4798592.

[127] T.J.M. Zouros and A. Kanellakopoulos and I. Madesis and A. Dimitriou and M. Fernàndez-Martìn and G. Martinez and T.J. Mertzimekis. *The optimization of a 4-element input lens on a hemispherical deflector analyzer using SIMION*. *Micros. Microanal.*, 21:148, 2015. URL https://doi.org/10.1017/S143192761501329X.

[128] O. Sise and T.J.M. Zouros. *Position, Energy, and Transit Time Distributions in a Hemispherical Deflector Analyzer with Position Sensitive Detector*. *J. Spec.*, 53513, 2005. URL http://dx.doi.org/10.1155/2015/153513.

[129] G. Martínez and M. Fernández-Martín and O. Sise and I. Madesis and A. Dimitriou and A. Laoutaris and T.J.M. Zouros. *Voltage optimization of a 4-element injection lens on a hemispherical spectrograph with virtual entry aperture*. *Nucl. Instr. Meth. Phys. B*, 369:92, 2016. URL https://www.sciencedirect.com/science/article/pii/S0168583X15009891.

[130] O. Sise and G. Martínez and I. Madesis and A. Laoutaris and A. Dimitriou and M. Fernández-Martín and T.J.M. Zouros. *The voltage optimization of a four-element lens used on a hemispherical spectrograph with virtual entry for highest energy resolution*. *J. El. Spec. Rel. Phen.*, 211:19, 2016. URL https://www.sciencedirect.com/science/article/pii/S0368204816300573.

[131] Quantar Technology. *3300/2400 Series System Installation and Operation Manual*, 2012.

[132] Hahn-Meitner-Institut, HelmholtzZentrum Berlin für Materialien und Energie Hahn-Meitner-Platz 1 (formerly Glienicker Str. 100), 14109 Berlin. *HV-Versorgung N 97*, May 1979. URL https://apapes.physics.uoc.gr/equipment/documentation/N97_Manual.pdf.

[133] Tennelec, Inc, 107 Union Valley Rd, Oak Ridge, TN. *Instruction Manual TC 952 High Voltage Power Supply*, September 1983. URL https://apapes.physics.uoc.gr/equipment/documentation/TC952.pdf.

[134] Applied KiloVolts, Woods Way, Goring by Sea, BN12 4QY. United Kingdom. *HPZ Series Data Sheet*, May 2012. URL https://apapes.physics.uoc.gr/equipment/documentation/Applied_kV_HPZ-Iss3.pdf.

[135] Applied KiloVolts, Woods Way, Goring by Sea, BN12 4QY. United Kingdom. *LS Series Data Sheet*, May 2012. URL https://apapes.physics.uoc.gr/equipment/documentation/Applied_kV_LS-Iss3.pdf.

[136] Oerlikon Leybold Vacuum GmbH. *Operating Instructions GA05118 1502*, 2006.

[137] Oerlikon Leybold Vacuum GmbH. *TRIVAC B: D 16 B / D 25 B*, 2011.

[138] Oerlikon Leybold Vacuum GmbH. *Leybold SC 5D, SC 15D, SC 30D, Dry Scroll Vacuum Pump*, 2004.

[139] Oerlikon Leybold Vacuum GmbH. *TURBOVAC SL 80, WideRange Turbomolecular Pump with Integrated or External Frequency Converter*, 2009.

[140] PFEIFFER VACUUM. *HIPACE 700 Turbopump*, 2020.

[141] E.P. Benis and others. *Emmanouil (Manolis) P. Benis web page*, Accessed: 30-06-2023. URL https://sites.google.com/uoi.gr/manolis-benis/projects/ikyda-2020?authuser=0.

[142] Scientific Instrument Services (SIS) by Adaptas Solutions, LLC. *SIMION: The field and particle trajectory simulator - Industry standard charged particle optics software* , Accessed: 30-06-2023. URL https://simion.com/.

[143] Atomki. *ATOMKI - Debrecen*, Accessed: 18-09-2023. URL https://www.atomki.hu/en/.

[144] H.I. Hidmi and P. Richard and I. Ben-Itzhak. *Energy calibration of an accelerator using cusp electron spectroscopy*. *Nucl. Instrum. Meth. Phys. Res. B*, 88(3):313, 1994. URL https://doi.org/10.1016/0168-583X(94)95330-9.

[145] M. Rodbro and R. Bruch and P. Bisgaard. *High-resolution projectile Auger spectroscopy for* Li, Be, B *and* C *excited in single gas collisions. I. Line energies for prompt decays*. *J. Phys. B At. Mol. Phys.*, 12(15):2413, 1979. URL https://dx.doi.org/10.1088/0022-3700/12/15/009.

[146] R. Bruch and K.T. Chung and W.L. Luken and J.C. Culberson. *Recalibration of the KLL Auger spectrum of carbon*. *Phys. Rev. A*, 31:310, 1985. URL https://doi.org/10.1103/PhysRevA.31.310.

[147] R. Bruch and N. Stolterfoht and S. Datz and P.D. Miller and P.L. Pepmiller and Y. Yamazaki and H.F. Krause and J.K. Swenson and K.T. Chung and B.F. Davis. *High-resolution KLL Auger spectra of multiply ionized oxygen projectiles studied by zero-degree electron spectroscopy*. *Phys. Rev. A*, 35:4114, 1987. URL https://doi.org/10.1103/PhysRevA.35.4114.

[148] MKS Instruments Inc. *MA 018102449, Type: 390/590 Absolute 398 Differential High Accuracy Pressure Transducers*, 1990.

[149] MKS Instruments Inc. *MA 018102449, MKS Type 248A/B/C Control Valve*, 2006.

[150] MKS Instruments Inc. *MA 018102449, MKS Type 250E Pressure/Flow Controller*, 1997.

[151] MKS Instruments Inc. *MA 018102449, MKS Type 270D High Accuracy Signal Conditioner*, 1998.

[152] E. Rutherford, F.R.S. *LXXIX. The scattering of α and β particles by matter and the structure of the atom*. *The London, Edinburgh, and Dublin Philosophical Magazine and Journal of Science*, 21(125):669, 1911. URL https://doi.org/10.1080/14786440508637080.

[153] N.J. Esponda and S. Nanos and M.A. Quinto and T.J.M. Zouros and R.D. Rivarola and E.P. Benis and J.M. Monti. *Binary Encounter Electrons in Fast Dressed-Ion-H_2 Collisions: Distorted Wave Theories and Experiment*. *Atoms*, 11:2, 2023. URL https://doi.org/10.3390/atoms11020017.

[154] C.W. Woods and R.L. Kauffman and K.A. Jamison and N. Stolterfoht and P. Richard. *K-shell Auger-electron production cross sections from ion bombardment*. *Phys. Rev. A*, 13:1358, 1976. URL https://doi.org/10.1103/PhysRevA.13.1358.

[155] D. Schneider and R. Bruch and W. Butscher and W.H.E. Schwarz. *Prompt and time-delayed electron decay-in-flight spectra of gas-excited carbon ions*. *Phys. Rev. A*, 24:1223, 1981. URL https://doi.org/10.1103/PhysRevA.24.1223.

[156] D. Röhrbein and T. Kirchner and S. Fritzsche. *Role of cascade and Auger effects in the enhanced population of the* $C^{3+}(1s2s2p\ ^4P)$ *states following single-electron capture in* $C^{4+}(1s2s\ ^3S) - He$ *collisions*. *Phys. Rev. A*, 81:042701, 2010. URL https://doi.org/10.1103/PhysRevA.81.042701.

[157] E.P. Benis and M. Zamkov and P. Richard and T.J.M. Zouros. *Technique for the determination of the* $1s2s\ ^3\mathrm{S}$ *metastable fraction in two-electron ion beams*. *Phys. Rev. A*, 65:064701, 2002. URL https://doi.org/10.1103/PhysRevA.65.064701.

[158] M. Zamkov and H. Aliabadi and E.P. Benis and P. Richard and H. Tawara and T.J.M. Zouros. *Energy dependence of the metastable fraction in* B^{3+}*(*$1s^2\ ^1\mathrm{S}$, $1s2s\ ^3\mathrm{S}$*) beams produced in collisions with thin-foil and gas targets*. *Phys. Rev. A*, 64:052702, 2001. URL https://doi.org/10.1103/PhysRevA.64.052702.

[159] E.P. Benis and S. Doukas and T.J.M. Zouros. *Evidence for the non-statistical population of the* $1s2s2p\ ^4\mathrm{P}$ *metastable state by electron capture in 4MeV collisions of* B^{3+}*(*$1s2s\ ^3\mathrm{S}$*) with* H_2 *targets*. *Nucl. Instrum. Meth. Phys. Res. B*, 369:83, 2016. URL https://doi.org/10.1016/j.nimb.2015.10.010.

[160] M. Terasawa and T.J. Gray and S. Hagmann and J. Hall and J. Newcomb and P. Pepmiller and P. Richard. *Electron capture by and electron excitation of two-electron fluorine ions incident on helium*. *Phys. Rev. A*, 27:2868, 1983. URL https://doi.org/10.1103/PhysRevA.27.2868.

[161] I. Madesis and A. Laoutaris and T.J.M. Zouros and S. Nanos and E.P. Benis. Chapter 1 - *Projectile electron spectroscopy and new answers to old questions: Latest results at the new atomic physics beamline in Demokritos, Athens*. In Dž. Belkić, I. Bray, and A. Kadyrov, editors, *State-of-the-Art Reviews on Energetic Ion-Atom and Ion-Molecule Collisions*, page 1. World Scientific, 2019. URL https://doi.org/10.1142/9789811211614_0001.

[162] J. Doerfert and E. Träbert and A. Wolf and D. Schwalm and O. Uwira. *Precision Measurement of the Electric Dipole Intercombination Rate in* C^{2+}. *Phys. Rev. Lett.*, 78:4355, 1997. URL https://doi.org/10.1103/PhysRevLett.78.4355.

[163] E. Träbert and A. Wolf and G. Gwinner. *Measurement of EUV intercombination transition rates in* Be*-like ions at a heavy-ion storage ring*. *Phys. Let. A*, 295(1):44, 2002. URL https://doi.org/10.1016/S0375-9601(02)00135-4.

[164] A. Müller and S. Schippers and R.A. Phaneuf and A.L.D. Kilcoyne and H. Bräuning and A.S. Schlachter and M. Lu and B.M. McLaughlin. *Fine-structure resolved photoionization of metastable* Be*-like ions* C III*,* N IV*, and* O *V*. *J. Phys: Conf. Ser.*, 58(1):383, 2007. URL https://doi.org/10.1088/1742-6596/58/1/087.

[165] D. Strohschein and D. Röhrbein and T. Kirchner and S. Fritzsche and J. Baran and J.A. Tanis. *Nonstatistical enhancement of the* $1s2s2p\ ^4\mathrm{P}$ *state in electron transfer in* $0.5 - 1.0$ *MeV/u* $\mathrm{C}^{4,5+}$ + He *and* Ne *collisions*. *Phys. Rev. A*, 77:022706, 2008. URL https://link.aps.org/doi/10.1103/PhysRevA.77.022706.

[166] E.P. Benis and T.J.M. Zouros. *Determination of the* $1s2l2l'$ *state production ratios* $^4\mathrm{P}^\circ/^2\mathrm{P}$, $^2\mathrm{D}/^2\mathrm{P}$ *and* $^2\mathrm{P}_+/^2\mathrm{P}_-$ *from fast (*$1s^2$, $1s2s\ ^3\mathrm{S}$*) mixed-state*

He-*like ion beams in collisions with* H_2 *targets*. *J. Phys. B: At. and Mol. Phys.*, 49(23):235202, 2016. URL https://doi.org/10.1088/0953-4075/49/23/235202.

[167] D.H. Jakubaßa-Amundsen. *Radiative electron capture to continuum in relativistic ion–atom collisions*. *J. Phys. B At. Mol. Phys.*, 36(10):1971, 2003. URL https://dx.doi.org/10.1088/0953-4075/36/10/308.

[168] D. Burch, H. Wieman, and W.B. Ingalls. *Electron Loss in High-Energy Oxygen-Ion Collisions. Phys. Rev. Lett.*, 30:823, 1973. URL https://link.aps.org/doi/10.1103/PhysRevLett.30.823.

[169] M.E. Rudd and C.A. Sautter and C.L. Bailey. *Energy and Angular Distributions of Electrons Ejected from Hydrogen and Helium by 100- to 300-keV Protons*. *Phys. Rev.*, 151:20, 1966. URL https://link.aps.org/doi/10.1103/PhysRev.151.20.

[170] A. Salin. *Ionization of atomic hydrogen by proton impact*. *J. Phys. B At. Mol. Phys.*, 2(6):631, 1969. URL https://dx.doi.org/10.1088/0022-3700/2/6/301.

[171] J. Macek. *Theory of the Forward Peak in the Angular Distribution of Electrons Ejecteed by Fast Protons*. *Phys. Rev. A*, 1:235, 1970. URL https://link.aps.org/doi/10.1103/PhysRevA.1.235.

[172] R. Shakeshaft. *Coupled-state calculations of proton—hydrogen-atom scattering using a scaled hydrogenic basis set*. *Phys. Rev. A*, 18:1930, 1978. URL https://link.aps.org/doi/10.1103/PhysRevA.18.1930.

[173] R. Shakeshaft and L. Spruch. *Asymmetry in the Cusp of the Cross Section for Electron Capture to the Continuum for a Fast Bare Ion on a Hydrogenlike Atom*. *Phys. Rev. Lett.*, 41:1037, 1978. URL https://link.aps.org/doi/10.1103/PhysRevLett.41.1037.

[174] R. Shakeshaft and L. Spruch. *Mechanisms for charge transfer (or for the capture of any light particle) at asymptotically high impact velocities*. *Rev. Mod. Phys.*, 51:369, 1979. URL https://link.aps.org/doi/10.1103/RevModPhys.51.369.

[175] C.R. Vane and I.A. Sellin and M. Suter and G.D. Alton and S.B. Elston and P.M. Griffin and R.S. Thoe. *Z, Velocity, and Charge Dependence of Zero-Degree Electron C̈uspsf̈rom Charge Transfer to Continuum States of Bare and Highly Ionized Projectiles*. *Phys. Rev. Lett.*, 40:1020, 1978. URL https://link.aps.org/doi/10.1103/PhysRevLett.40.1020.

[176] M. Breinig and S.B. Elston and S. Huldt and L. Liljeby and C.R. Vane and S.D. Berry and G.A. Glass and M. Schauer and I.A. Sellin and G.D. Alton and S. Datz and S. Overbury and R. Laubert and M. Suter. *Experiments concerning electron capture and loss to the continuum and convoy electron production by highly ionized projectiles in the 0.7 - 8.5-MeV/u range transversing the rare gases, polycrystalline solids, and axial channels in gold*. *Phys. Rev. A*, 25:3015, 1982. URL https://doi.org/10.1103/PhysRevA.25.3015.

[177] Andersen, L. H. and Frost, M. and Hvelplund, P. and Knudsen, H. and Datz, S. *Correlated Two-Electron Effects in Highly Charged Ion-Atom Collisions: Transfer Ionization and Transfer Excitation in 20-MeV* Au^{15+}+He *Collisions*. *Phys. Rev. Lett.*, 52:518, 1984. URL https://link.aps.org/doi/10.1103/PhysRevLett.52.518.

[178] S. Datz and R. Hippler and L.H. Andersen and P.F. Dittner and H. Knudsen and H.F. Krause and P.D. Miller and P.L. Pepmiller and T. Rosseel and R. Schuch and N. Stolterfoht and Y. Yamazaki and C.R. Vane. *Coincidence studies of capture and ionization in highly charged* I^{q+} − He *and* U^{q+} − He *collisions at medium velocities*. *Phys. Rev. A*, 41:3559, 1990. URL https://link.aps.org/doi/10.1103/PhysRevA.41.3559.

[179] L. Sarkadi and J. Pálinkás and A. Kövér and D. Berényi and T. Vajnai. *Observation of electron capture into continuum states of neutral atoms*. *Phys. Rev. Lett.*, 62:527, 1989. URL https://link.aps.org/doi/10.1103/PhysRevLett.62.527.

[180] C.O. Reinhold and D.R. Schultz. *Anticusp and binary peak structures in the electronic spectra arising from proton- and antiproton-helium collisions*. *Phys. Rev. A*, 40:7373, 1989. URL https://link.aps.org/doi/10.1103/PhysRevA.40.7373.

[181] P.-M. Hillenbrand and S. Hagmann and M.E. Groshev and D. Banaś and E.P. Benis and C. Brandau and E. De Filippo and O. Forstner and J. Glorius and R.E. Grisenti and A. Gumberidze and D.L. Guo and B. Hai and M.O. Herdrich and M. Lestinsky and Yu.A. Litvinov and E.V. Pagano and N. Petridis and M.S. Sanjari and D. Schury and U. Spillmann and S. Trotsenko and M. Vockert and G. Weber and V.A. Yerokhin and Th. Stöhlker. *Radiative electron capture to the continuum in* $U^{89+} + N_2$ *collisions: Experiment and theory*. *Phys. Rev. A*, 101:022708, 2020. URL https://link.aps.org/doi/10.1103/PhysRevA.101.022708.

[182] P.-M. Hillenbrand and K.N. Lyashchenko and S. Hagmann and O.Yu. Andreev and D. Banaś and E.P. Benis and A.I. Bondarev and C. Brandau and E. De Filippo and O. Forstner and J. Glorius and R.E. Grisenti and A. Gumberidze and D.L. Guo and M.O. Herdrich and M. Lestinsky and Yu.A. Litvinov and E.V. Pagano and N. Petridis and M.S. Sanjari and D. Schury and U. Spillmann and S. Trotsenko and M. Vockert and A.B. Voitkiv and G. Weber and Th. Stöhlker. *Electron-loss-to-continuum cusp in collisions of* U^{89+} *with* N_2 *and* Xe. *Phys. Rev. A*, 104:012809, 2021. URL https://link.aps.org/doi/10.1103/PhysRevA.104.012809.

[183] M. Rodbro and F.D. Andersen. *Charge transfer to the continuum for 15 to 1500 keV* H^+ *in* He, Ne, Ar *and* H_2 *gases under single-collision conditions*. *J. Phys. B At. Mol. Phys.*, 12:2883, 1979. URL https://doi.org/10.1088/0022-3700/12/17/017.

[184] J.B. Crooks and M.E. Rudd. *Angular and energy distribution of cross sections for electron production by 50-300-keV-proton impacts on* N_2, O_2, Ne, *and*

Ar. *Phys. Rev. A*, 3:1628, 1971. URL https://link.aps.org/doi/10.1103/PhysRevA.3.1628.

[185] L. Sarkadi and J. Bossler and R. Hippler and H.O. Lutz. *Electron capture to continuum states from inner shells*. *Phys. Rev. Lett.*, 53:1551, 1984. URL https://link.aps.org/doi/10.1103/PhysRevLett.53.1551.

[186] G. Bernardi and P. Fainstein and C.R. Garibotti and S. Suarez. *Projectile charge dependence of the ionisation spectra for* H^+ *and* $^3He^{2+}$ *ions on* He *and* Ne *atoms*. *J. Phys. B At. Mol. Phys.*, 23(9):L139, 1990. URL https://doi.org/10.1088/0953-4075/23/9/004.

[187] T.J. Gay and M.W. Gealy and M.E. Rudd. *Projectile- and target-charge dependent effects in ionizing collisions of* H^+ *and* He^{2+} *with* He, Ne *and* Ar *atoms*. *J. Phys. B At. Mol. Phys.*, 23(24):L823, 1990. URL https://doi.org/10.1088/0953-4075/23/24/003.

[188] S. Suárez and C. Garibotti and W. Meckbach and G. Bernardi. *Experimental evidence of the asymmetry of the soft electron peak in ion-atom ionization*. *Phys. Rev. Lett.*, 70:418, 1993. URL https://link.aps.org/doi/10.1103/PhysRevLett.70.418.

[189] S. Biswas and D. Misra and J.M. Monti and C.A. Tachino and R.D. Rivarola and L.C. Tribedi. *Energy and angular distribution of electrons in ionization of* He *and* Ne *by 6-MeV/u bare carbon ions: Comparison with continuum-distorted-wave eikonal-initial-state calculations in prior and post forms*. *Phys. Rev. A*, 90:052714, 2014. URL https://link.aps.org/doi/10.1103/PhysRevA.90.052714.

[190] R. Ben-shlomi and R. Vexiau and Z. Meir and T. Sikorsky and N. Akerman and M. Pinkas and O. Dulieu and R. Ozeri. *Direct observation of ultracold atom-ion excitation exchange*. *Phys. Rev. A*, 102:031301, 2020. URL https://doi.org/10.1103/PhysRevA.102.031301.

[191] A. Gumberidze and D.B. Thorn and A. Surzhykov and C.J. Fontes and D. Banaś and H.F. Beyer and W. Chen and R.E. Grisenti and S. Hagmann and R. Hess and P.-M. Hillenbrand and P. Indelicato and C. Kozhuharov and M. Lestinsky and R. Märtin and N. Petridis and R.V. Popov and R. Schuch and U. Spillmann and S. Tashenov and S. Trotsenko and A. Warczak and G. Weber and W. Wen and D.F.A Winters and N. Winters and Z. Yin and T. Stöhlker. *Angular Distribution of Characteristic Radiation Following the Excitation of He-Like Uranium in Relativistic Collisions*. *Atoms*, 9:2, 2021. URL https://doi.org/10.3390/atoms9020020.

[192] S. Schippers and S. Stock and T. Buhr and A. Perry-Sassmannshausen and S. Reinwardt and M. Martins and A. Müller and S. Fritzsche. *Near K-edge Photoionization and Photoabsorption of Singly, Doubly, and Triply Charged Silicon Ions*. *Astrophys. Journ.*, 931:100, 2022. URL https://doi.org/10.3847/1538-4357/ac6874.

[193] Z. Huang and S. Wang and W. Wen and H. Wang and W. Ma and C. Chen amd C. Zhang and D. Chen and H. Huang and L. Shao. *Absolute dielectronic recombination rate coefficients of highly charged ions at the storage ring CSRm and CSRe*. *Chi. Phys B*, 32(7):073401, 2023. URL https://doi.org/10.1088/1674-1056/acbc69.

[194] B. Cunha de Miranda and C. Romanzin and S. Chefdeville and V. Vuitton and J. Žabka and M. Polášek and C. Alcaraz. *Reactions of State-Selected Atomic Oxygen Ions* $O^+(^4S, ^2D, ^2P)$ *with Methane*. *J. Phys Chem A.*, 119:6082, 2015. URL https://doi.org/10.1021/jp512846v.

[195] R. Hubele and A. LaForge and M. Schulz and J. Goullon and X. Wang and B. Najjari and N. Ferreira and M. Grieser and V.L.B. de Jesus and R. Moshammer and K. Schneider and A.B. Voitkiv and D. Fischer. *Polarization and Interference Effects in Ionization of* Li *by Ion Impact*. *Phys. Rev. Lett.*, 110: 133201, 2013. URL https://doi.org/10.1103/PhysRevLett.110.133201.

[196] M.A. Quinto and P.R. Montenegro and J.M. Monti and O.A. Fojón and R.D. Rivarola. *Electron capture by swift ions from molecules of biological interest*. *J. Phys. B At. Mol. Phys.*, 51(16):165201, 2018. URL https://dx.doi.org/10.1088/1361-6455/aad152.

[197] C. Champion and M.A. Quinto and J.M. Monti and M.E. Galassi and P.F. Weck and O.A. Fojón and J. Hanssen and R.D. Rivarola. *Water versus DNA: new insights into proton track-structure modelling in radiobiology and radiotherapy*. *Phys. Med. Biol.*, 60(20):7805, 2015. URL https://dx.doi.org/10.1088/0031-9155/60/20/7805.

[198] J.M. Monti and C.A. Tachino and J. Hanssen and O.A. Fojón and M.E. Galassi and C. Champion and R.D. Rivarola. Distorted wave calculations for electron loss process induced by bare ion impact on biological targets. *Ap. Rad. Isot.*, 83:105, 2014. URL https://www.sciencedirect.com/science/article/pii/S0969804312006069.

[199] Dž Belkić . *A quantum theory of ionisation in fast collisions between ions and atomic systems*. *J. Phys. B At. Mol. Phys. At. Mol. Phys.*, 11:3529, 1978. URL https://doi.org/0.1088/0022-3700/11/20/015.

[200] I.M. Cheshire. *Continuum distorted wave approximation; resonant charge transfer by fast protons in atomic hydrogen*. *Proc. Phys. Soc.*, 84(1):89, 1964. URL https://doi.org/10.1088/0370-1328/84/1/313.

[201] D. Belkić and R. Gayet and A. Salin. *Electron capture in high-energy ion-atom collisions*. *Phys. Rep.*, 56:279, 1979. URL https://doi.org/10.1016/0370-1573(79)90035-8.

[202] P.D. Fainstein and V.H. Ponce and R.D. Rivarola. *A theoretical model for ionisation in ion-atom collisions. Application for the impact of multicharged projectiles on helium*. *J. Phys. B At. Mol. Phys.*, 21:287, 1988. URL https://doi.org/10.1088/0953-4075/21/2/013.

[203] P.D. Fainstein and V.H. Ponce and R.D. Rivarola. *Two-centre effects in ionization by ion impact*. *J. Phys. B At. Mol. Phys.*, 24:3091, 1991. URL https://doi.org/10.1088/0953-4075/24/14/005.

[204] J.M. Monti and O.A. Fojón and J. Hanssen and R.D. Rivarola. *Single electron ionization of multishell atoms: dynamic screening and post-prior discrepancies in the CDW-EIS model*. *J. Phys. B At. Mol. Phys.*, 46(14):145201, 2013. URL https://doi.org/10.1088/0953-4075/46/14/145201.

[205] J.M. Monti and O.A. Fojón and J. Hanssen and R.D. Rivarola. *Influence of the dynamic screening on single-electron ionization of multi-electron atoms*. *J. Phys. B At. Mol. Phys.*, 43(20):205203, 2010. URL https://doi.org/10.1088/0953-4075/43/20/205203.

[206] J.M. Monti and M.A. Quinto and R.D. Rivarola. A Complete CDW theory for the single ionization of multielectronic atoms by bare ion impact. *Atoms*, 9(1):3, 2021. URL https://doi.org/10.3390/atoms9010003.

[207] D.S.F. Crothers and J.F. McCann. *Ionisation of atoms by ion impact*. *J. Phys. B At. Mol. Phys.*, 16:3229, 1983. URL https://doi.org/10.1088/0022-3700/16/17/015.

[208] L. Gulyas and P.D. Fainstein and A. Salin. *CDW-EIS theory of ionization by ion impact with Hartree-Fock description of the target*. *J. Phys. B At. Mol. Phys.*, 28(2):245, 1995. URL https://doi.org/10.1088/0953-4075/28/2/013.

[209] J.M. Monti and R.D. Rivarola and P.D. Fainstein. *Distorted wave theories for dressed-ion–atom collisions with* GSZ *projectile potentials*. *J. Phys. B*, 44 (19):195206, 2011. URL https://dx.doi.org/10.1088/0953-4075/44/19/195206.

[210] N.V. Novikov. *New method of the approximation of hartree-fock wave function*. *Int. J. of Math. and Comp. Sc.*, 1(2):55, 2015. URL http://files.aiscience.org/journal/article/html/70400005.html.

[211] D. Fregenal and J.M. Monti and J. Fiol and P.D. Fainstein and R.D. Rivarola and G. Bernardi and S. Suárez. *Experimental and theoretical results on electron emission in collisions between* He *targets and dressed* $\mathrm{Li}^{q+}(q = 1, 2)$ *projectiles*. *J. Phys. B*, 47(15):155204, 2014. URL https://doi.org/10.1088/0953-4075/47/15/155204.

[212] J.M. Monti and O.A. Fojón and J. Hanssen and R.D. Rivarola. *Ionization of helium targets by proton impact: a four-body distorted wave-eikonal initial state model and electron dynamic correlation*. *J. Phys. B At. Mol. Phys.*, 42(19):195201, 2009. URL https://doi.org/10.1088/0953-4075/42/19/195201.

[213] L. Gulyás and T. Kirchner. *Ionization of* Ar *by energetic proton impact*. *Phys. Rev. A*, 70:022704, 2004. URL https://doi.org/10.1103/PhysRevA.70.022704.

[214] M. Kuzel and L. Sarkadi and J. Pálinkás and P.A. Závodszky and R. Maier and D. Berényi and K.O. Groeneveld. *Observation of enhanced emission of cusp electrons at impact of excited metastable neutral* He *projectiles*. *Phys. Rev. A*, 48(3):R1745, 1993. URL https://doi.org/10.1103/PhysRevA.48.R1745.

[215] O. Heil and J.Kemmler and K. Kroneberger and A. Kövér and Gy. Szabó and L. Gulyás and R. DeSerio and S. Lencinas and N. Keller and D. Hofmann and H. Rothard and D. Berényi and K.O. Groeneveld. *Electron loss and capture to continuum from* He *and* Ne *atoms bombarded with* He^+*-Ions*. *Z. Phys. D At. Mol. Clust.*, 9:229, 1988. URL https://doi.org/10.1007/BF01438294.

[216] K.F. Man and W. Steckelmacher and M.W. Lucas. *Electron loss to the continuum for* H_2^+ *and* He^+ *ions colliding with* H_2, He, Ne *and* Ar. *I. Electron cusp widths and shapes*. *J. Phys. B At. Mol. Phys.*, 19(4):401, 1986. URL https://dx.doi.org/10.1088/0022-3700/19/4/008.

[217] H.F. Beyer and V.P. Shevelko. *Introduction to the Physics of Highly Charged Ions*. CRC Press, Bristol and Philadelphia, 2002. URL https://doi.org/10.1201/9781420034097.

[218] A.K. Pradhan and S.N. Nahar. *Atomic Astrophysics and Spectroscopy*. Cambridge University Press, Cambridge, England, 2011. URL https://ui.adsabs.harvard.edu/abs/2011aas..book.....P.

[219] P. Beiersdorfer. *Laboratory X-Ray Astrophysics*. *Ann. Rev. Astr. Astr.*, 41:343, 2003. URL https://doi.org/10.1146/annurev.astro.41.011802.094825.

[220] V. Shevelko and H. Tawara. *Atomic Processes in Basic and Applied Physics*. Springer Berlin Heidelberg, Berlin, Heidelberg, 2014. URL https://doi.org/10.1007/978-3-642-25569-4.

[221] J.A. Tanis and A.L. Landers and D.J. Pole and A.S. Alnaser and S. Hossain and T. Kirchner. *Evidence for Pauli Exchange Leading to Excited-State Enhancement in Electron Transfer*. *Phys. Rev. Lett.*, 92:133201, 2004. URL https://link.aps.org/doi/10.1103/PhysRevLett.92.133201.

[222] T.J.M. Zouros and B. Sulik and L. Gulyás and K. Tőkési. *Selective enhancement of* $1s2s2p\ ^4P_J$ *metastable states populated by cascades in single-electron transfer collisions of* $F^{7+}(1s^2/1s2s\ ^3S)$ *ions with* He *and* H_2 *targets*. *Phys. Rev. A*, 77:050701, 2008. URL https://link.aps.org/doi/10.1103/PhysRevA.77.050701.

[223] O.J. Kroneisen and H.J. Lüdde and T. Kirchner and R.M. Dreizler. *The basis generator method: optimized dynamical representation of the solution of time-dependent quantum problems*. *J. Physics A Math. Gen.*, 32(11):2141, 1999. URL https://dx.doi.org/10.1088/0305-4470/32/11/009.

[224] M. Zapukhlyak and T. Kirchner and H.J. Lüdde and S. Knoop and R. Morgenstern and R. Hoekstra. *Inner- and outer-shell electron dynamics in proton collisions with sodium atoms*. *J. Phys. B At. Mol. Opt. Phys.*, 38(14):2353, 2005. URL https://dx.doi.org/10.1088/0953-4075/38/14/003.

[225] E.P. Benis and I. Madesis and A. Laoutaris and S. Nanos and T.J.M. Zouros. *Experimental determination of the effective solid angle of long-lived projectile states in zero-degree Auger projectile spectroscopy*. *J. El. Spec. Rel. Phen.*, 222: 31, 2018. URL https://www.sciencedirect.com/science/article/pii/S0368204817301792.

[226] R.D. Cowan. *The Theory of Atomic Structure and Spectra*. University of California Press, Berkeley, Los Angeles, London, 1981.

[227] N. Sisourat and I. Pilskog and A. Dubois. *Nonperturbative treatment of multielectron processes in ion-molecule scattering: Application to* $He^{2+} - H_2$ *collisions*. *Phys. Rev. A*, 84:052722, 2011. URL https://link.aps.org/doi/10.1103/PhysRevA.84.052722.

[228] W. Mehlhorn and K. Taulbjerg. *Angular distribution of electrons from autoionising states with unresolved fine structure*. *J. Phys. B At. Mol. Phys.*, 13 (3):445, 1980. URL https://dx.doi.org/10.1088/0022-3700/13/3/007.

[229] S. M. Younger and W. L. Wiese. *Theoretical simulation of beam-foil decay curves for resonance transitions of heavy ions*. *Phys. Rev. A*, 17:1944, 1978. URL https://link.aps.org/doi/10.1103/PhysRevA.17.1944.

[230] J. Burgdörfer. *Final-state angular momentum distributions in charge transfer collisions at high energies*. *Nucl. Instr. Meth. Phys. Res. Sect. A*, 240(3):519, 1985. URL https://doi.org/10.1016/0168-9002(85)90675-8.

[231] H.D. Betz. *Charge states and charge-changing cross sections of fast heavy ions penetrating through gaseous and solid media*. *Rev. Mod. Phys.*, 44:465, 1972. URL https://doi.org/10.1103/RevModPhys.44.465.

[232] I.S. Dmitriev and V.S. Nikolaev. *Semi-empirical method for the calculation of the equilibrium distribution of charges in a fast-ion beam*. *Sov. Phys.*, 20:409, 1964. URL http://jetp.ras.ru/cgi-bin/dn/e_020_02_0409.pdf.

[233] R.O. Sayer. *Semi-empirical formulas for heavy-ion stripping data*. *Rev. Phys. Ap.*, 12:1543, 1977. URL https://doi.org/10.1051/rphysap:0197700120100154300.

[234] G. Schiwietz and P.L. Grande. *Improved charge-state formulas*. *Nucl. Instrum. Methods Phys. Res. B*, 175:125, 2001. URL https://doi.org/10.1016/S0168-583X(00)00583-8.

[235] K.P.Nesteruk and L. Ramseyer and T.S. Carzaniga and S Braccini. *Measurement of the Beam Energy Distribution of a Medical Cyclotron with a Multi-Leaf Faraday Cup*. *Atoms*, 3(4), 2019. URL https://doi.org/10.3390/instruments3010004.

[236] R.M. Nazhmudinov and A.S. Kubankin and P.V. Karataev and I.A. Kishin and A.V. Vukolov and A.P. Potylitsyn and P.N. Zhukovaa and V.A. Nasonova. *A multi-wirescanner test setup utilizing characteristic X-rays for charged particle and photon beam diagnostics*. *J. Instr.*, 13(12):P12012, 2018. URL https://doi.org/10.1088/1748-0221/13/12/P12012.

[237] S. Harissopulos and C. Chronidou and K. Spyrou and T. Paradellis and C. Rolfs and W. H. Schulte and H. W. Becker. *The* ^{27}Al$(p,\gamma)^{28}$Si *reaction: direct capture cross-section and resonance strengths at* E_p *=0.2–1.12 MeV*. *Eur. Phys. J. A*, 9:479, 2020. URL https://doi.org/10.1007/s100500070006.

[238] V. Paneta and M. Kokkoris and A. Lagoyannis and K. Preketes-Sigalas. *Accurate accelerator energy calibration using selected resonances in proton elastic scattering and in* (p,γ) *and* $(\mathrm{p},\mathrm{p}'\gamma)$ *reactions*. *Nucl. Instrum. Methods Phys. Res. B*, 406:108, 2017. URL https://doi.org/10.1016/j.nimb.2017.03.040.

[239] M.H. Chen and B. Crasemann and H. Mark. *Deexcitation of light* Li*-like ions in the* $1s2s2p$ *state*. *Phys. Rev. A*, 27:544, 1983. URL https://link.aps.org/doi/10.1103/PhysRevA.27.544.

[240] E.M. Asimakopoulou and I. Madesis and T.J.M. Zouros and T.J. Mertzimekis and A. Lagoyannis and M. Axiotis. *Incorporation of Ion Post Stripper in the APAPES Experimental Setup*. *Proc. 23rd HNPS*, 22:122, 2014. URL https://doi.org/10.12681/hnps.1918.

[241] J. Sanders. *FROTRAN program CHARGE*, 1991 (unpublished).

[242] Fasmatech. *Fasmatech web page*, Accessed: 30-06-2023. URL https://fasmatech.com/.

[243] PySimpleGUI. *Python GUIs for Humans*, Accessed: 30-06-2023. URL https://www.pysimplegui.org/en/latest/.

[244] O.A. Asbjornsen. Chapter 10 - *System Life Cycle Optimization Under Uncertainty*. In B.M. Ayyub and M.M. Gupta, editors, *Uncertainty Analysis in Engineering and Sciences: Fuzzy Logic, Statistics, and Neural Network Approach*, pages 143–156. Springer US, Boston, MA, 1998. ISBN 978-1-4615-5473-8. URL https://doi.org/10.1007/978-1-4615-5473-8_10.

[245] R. Kissell and J. Poserina. Chapter 4 - *Advanced Math and Statistics*. In R. Kissell and J. Poserina, editor, *Optimal Sports Math, Statistics, and Fantasy*, page 103. Academic Press, 2017. URL https://doi.org/10.1016/B978-0-12-805163-4.00004-9.

[246] G. Pólya. *Ü*ber den zentralen Grenzwertsatz der Wahrscheinlichkeitsrechnung und das Momentenproblem. *Mathematische Zeitschrift*, 8:171, 1920. URL https://doi.org/10.1007/BF01206525.

Dissemination

Ph.D. Publications

1. *Cusp-electron production in collisions of open-shell He-like oxygen ions with atomic targets*, S. Nanos, N. J. Esponda, P.-M. Hillenbrand, A. Biniskos, A. Laoutaris, M. A. Quinto, N. Petridis, E. Menz, T.J.M. Zouros, T. Stölker, R. D. Rivarola, J. M. Monti and E.P. Benis, Phys. Rev. A 107, 062815 (2023)

2. *Determination of the ion beam energy width in tandem Van de Graaff accelerators via Auger projectile spectroscopy*, S. Nanos, A. Biniskos, A. Laoutaris, M. Andrianis, T.J.M. Zouros, A. Lagoyannis and E.P. Benis, Nucl. Instrum. Methods Phys. Res. Sect. B541, 93 (2023)

3. *Subshell contributions to electron capture into the continuum in MeV/u collisions of deuterons with multielectron targets*, S. Nanos, M. A. Quinto, I. Madesis, A. Laoutaris, T.J.M. Zouros, R.D. Rivarola, J.M. Monti, E.P. Benis, Phys. Rev. A 105, 022806 (2022)

Closely Related Publications

1. *Binary Encounter Electrons in Fast Dressed-Ion - H_2 Collisions: Distorted Wave Theories and Experiment*, N.J. Esponda, S. Nanos, M.A. Quinto, T.J.M. Zouros, R.D. Rivarola, E.P. Benis, and J.M. Monti, Atoms 11, 17 (2023)

2. *Coherent treatment of transfer-excitation processes in swift ion-atom collisions*, A. Laoutaris, S. Nanos, I. Madesis, S. Passalidis, E.P. Benis, A. Dubois and T. J. M. Zouros, Phys. Rev. A 106, 022810 (2022)

3. *State-resolved differential cross sections of single-electron capture in swift collisions of $C^{4+}(1s2s\ ^3S)$ ions with gas targets*, I. Madesis, A. Laoutaris, S. Nanos, S. Passalidis, A. Dubois, T. J. M. Zouros and E.P. Benis, Phys. Rev. A 105, 062810 (2022)

4. *Radiative cascade repopulation of $1s2s2p\ ^4P$ states formed by single electron capture in 2-18 MeV collisions of $C^{4+}(1s2s\ ^3S)$ with He*, T.J.M. Zouros, S. Nikolaou, I. Madesis, A. Laoutaris, S. Nanos, A. Dubois, E. P. Benis, Atoms 2, 61 (2020)

5. *Projectile electron spectroscopy: new answers to old questions. Latest results at the new atomic physics beamline in Demokritos, Athens*, I. Madesis, A. Laoutaris, T.J.M. Zouros, S. Nanos, E.P. Benis, in State-of-the-Art Reviews

on Energetic Ion-Atom and Ion-Molecule Collisions, Interdisciplinary Research on Particle Collisions and Quantitative Spectroscopy, Vol. 2, edited by Dž. Belkić, I. Bray, and A. Kadyrov, World Scientific (2019)

Invited Talks

1. *Cusp electron studies in MeV collisions of dressed projectiles with gas targets*, S. Nanos, N.J. Esponda, P-M. Hillenbrand, A. Biniskos, A. Laoutaris, M.A. Quinto, , N. Petridis, E. Menz, T.J.M. Zouros, , T. Stöhlker, R.D. Rivarola, J.M. Monti, E.P. Benis, 20th SPARC workshop, Edinburgh, Scotland, 5-9 September 2023

2. *Mechanisms of electron capture, excitation, and ionization in fast ion-atom collisions*, S. Nanos, A. Laoutaris, A. Biniskos, P-M. Hillenbrand, N. Petridis, T.J.M. Zouros and E.P. Benis, *Seminar talk*, University of Sorbonne, Paris, 27 March 2023

3. *Cusp Electron Studies in MeV Collisions of Pre Excited* $1s2s\,^3S$ *Ions with Gas Targets: A Progress Report*, S. Nanos, A. Lagoyiannis, A. Laoutaris, A. Biniskos, T.J.M. Zouros, E. Menz, L. Varga, U. Spillmann, P-M. Hillenbrand, N. Petridis, S. Hagman, T. Stöhlker, and E.P. Benis, 18th SPARC workshop, virtual meeting, 6-9 September 2021

Oral Presentations

1. *Single electron capture in fast collisions of He-like ions with gas targets*, S. Nanos, A. Laoutaris, A. Biniskos, T.J.M. Zouros, S. Passalidis, A. Dubois, E.P. Benis, HNPS2021: 29th Symposium of the Hellenic Nuclear Physics Society, University of Ioannina, Ioannina, Greece, 7-8 October 2022

2. *Upgrading the APAPES installation at the tandem accelerator laboratory of NCSR "Demokritos" by developing coincidence techniques*, S. Nanos, A. Lagoyannis, A. Laoutaris, A. Biniskos, E. Menz, L. Varga, U. Spillmann, P-M. Hillenbrand, N. Petridis, T. Stöhlker, E.P. Benis, HNPS2021: 29th Symposium of the Hellenic Nuclear Physics Society, NCSR "Demokritos", Athens, Greece, 24-25 September 2021

3. *Shell Effects on Electron Capture to the Continuum in MeV/u Collisions of Deuteron Ions with Multielectron Targets*, S. Nanos, I. Madesis, A. Laoutaris, T.J.M. Zouros, J.M. Monti, R.D. Rivarola, E.P. Benis, ISIAC 2021: XXVII Int. Symposium on Ion-Atom Collisions, virtual meeting, 14-16 July 2021

Poster Presentations

1. *Cusp electron production in collisions of open-shell* $O^{6+}(1s2s)$ *ions with He*, S. Nanos, N.J. Esponda, P-M. Hillenbrand, A. Biniskos, A, Laoutaris, M.A. Quinto, N. Petridis, E. Menz, T.J.M. Zouros, T. Stöhlker, R.D. Rivarola,

J.M. Monti, E.P. Benis, ICPEAC 2023: XXXIII International Conference on Photonic, Electronic and Atomic Collisions, Ottawa, Canada, July 25 - August 1 2023 - [*Presented by N.J. Esponda*]

2. *Cusp electron studies in MeV/u collisions of $O^{6+}(1s2s\,^3S)$ ions with He targets*, S. Nanos, A. Laoutaris, A. Biniskos, T.J.M. Zouros, E. Menz, U. Spillmann, P-M. Hillenbrand, N. Petridis, S. Hagmann, N.J. Esponda, M.A. Quinto, J.M. Monti, R.D. Rivarola, T. Stöhlker, E.P. Benis, ECAMP14: 14th European Conference on Atoms Molecules and Photons, Vilnius, Lithuania, June 27 - July 1 2022 - [*Presented by P-M. Hillenbrand*]

3. *State-resolved KLL cross sections of single electron capture in collisions of swift $C^{4+}(1s2s\,^3S)$ ions with gas targets*, I. Madesis, A. Laoutaris, S. Nanos, T.J.M. Zouros, A. Dubois, E.P. Benis, ICPEAC 2021: XXXII International Conference on Photonic, Electronic and Atomic Collisions, July 20-23 2021, virtual meeting - [*Presented by S. Nanos*]

4. *Electron Capture to Continuum in 0.5 – 4.5 MeV/u Collisions of Protons and Deuterons with Gas Targets*, S. Nanos, A. Laoutaris, I. Madesis, T.J.M. Zouros and E.P. Benis, 16th SPARC Topical Workshop, Friedrich-Schiller-Universitat & Helmholtz Institute Jena, Jena, Germany, Septemper 8-13 2019 - [*Presented by E.P. Benis*]

5. *Cusp Electron Measurements at the NCSR "Demokritos" Tandem Accelerator Laboratory*, S. Nanos, A. Laoutaris, I. Madesis, T.J.M. Zouros and E.P. Benis, 1st TUMIEE Training School, Rethymno (Crete), Greece, September 22 - October 4 2019 - [*Presented by S. Nanos*]